The pedestal structure in high performance JET plasmas

Matthew John Leyland

Doctor of Philosophy

University of York
Physics

July 2014

Abstract

The ITER baseline scenario is foreseen to be a type I ELMy H-mode. This mode of operation is characterised by a steep pressure gradient at the plasma edge termed the pedestal. Quantifying the pedestal structure and its role on confinement for current Tokamaks, such as JET, is key to gaining an insight into the operation of future devices. Furthermore, to identify the physical mechanism(s) governing the pedestal structure, it is essential to compare measurements to modelling results. This thesis focuses on the JET high resolution Thomson scattering (HRTS) system, a key diagnostic, as it provides radial electron temperature and density profiles.

This thesis first presents how the performance of the HRTS system polychromators was improved by performing a realignment and optimisation. Consequently, all the electron temperature profile data after the installation of the JET ITER-Like-Wall are independently calibrated (instead of cross-calibrated via the ECE diagnostic).

The JET pedestal structure is quantified by performing a modified hyperbolic tangent fit to the HRTS profiles. The JET pedestal fitting tool incorporates the diagnostic measurement accuracy (the instrument function) resulting in a deconvolved fit. This is necessary in order to accurately determine the pedestal width. It has previously been shown that the systematic error in the fit parameters due to the deconvolution technique is negligible in comparison to the statistical error, as long as the pedestal is wider than the instrument function. Furthermore, this thesis shows that the systematic error due to ELM synchronisation is also negligible by replicating the fitting process and performing a Monte-Carlo simulation using synthetic HRTS-like profiles.

The JET pedestal fitting tool has been used to quantify the variation in pedestal structure for a database of JET baseline type I ELMy H-mode deuterium fuelling and nitrogen seeding plasmas before and after the installation of the ITER-like wall. Across a high triangularity deuterium fuelling scan for JET plasmas with a carbon wall there is a widening of the pedestal and an increase in the pedestal height, which accounts for the improvement in edge performance. After the installation of the ITER-like-wall, the energy confinement of equivalent JET plasmas was degraded by up to 40% due to a reduction in pedestal performance and a strong pedestal-core coupling. However, this performance could be partially recovered with nitrogen seeding. Measurements of the pedestal structure show that with increasing nitrogen seeding there is an increase in both the pedestal height and width, which is not yet captured by the EPED model. A key result of this thesis is, with increasing deuterium fuelling, the pedestal now widens whilst the pedestal height remains constant. These measurements pose the biggest challenge for the EPED model as they deviate from the square root relation between the pedestal width and normalised pedestal height acting as the kinetic ballooning constraint.

Contents

List of Figures

List of Tables

Acknowledgments

I would first like to thank my supervisors, Dr. Marc Beurskens and Prof. Kieran Gibson, for their unwavering support, advice and enthusiasm throughout my PhD. I am fortunate to have had the opportunity to work on such an engaging, interesting project which has enabled me to publish, travel to new places and meet many new people. I am also grateful for their encouragement, comments and particularly their patience whilst I have been writing this thesis.

I would like to acknowledge the role of the York Plasma Institute, CCFE and JET, all of which have hosted me throughout my PhD. This work has been jointly funded by EPSRC and CCFE. I would also like to praise the Fusion Doctoral Training Network (FDTN) for providing me with a broad fusion academic background during the first six months of my PhD and promoting wider scientific professional development.

There are many people who have helped me throughout my PhD, too many to name all here. Nevertheless, I would particularly like to thank the JET-TS Team; Joanne Flanagan, Mikhail Maslov and Mark Kempenaars for providing high quality HRTS data and welcoming me into the group; Lorenzo Frassinetti for providing a robust pedestal fitting tool; Carine Giroud for providing interesting JET plasmas to study; Samuli Saarelma and Phil Snyder for their pedestal modelling expertise; Alberto Loarte for sharing his enthusiasm and sheer wealth of expertise on all things Tokamak related; and Rory Scannell for being another TS expert I can rely on for help and being my undergraduate placement supervisor, which is when I first got interested in fusion research. I would like to thank Joanne Flanagan for carefully reading chapters of this thesis and Mathew Banks, Chad Heys, Stuart Morris and Russell Perry for helping to provide the best quality figures.

I would like to thank all the students I have encountered throughout my PhD for making it a more enjoyable experience. In particular; Stuart Henderson, Rich Lake, Sarah Elmore, Nick Walkden and Tom Fox. I would also like to thank those whom I have shared an office with; Tom Farley, Amelia Nunn, Jamie Beal, Alex Cackett and Sarah Medley for at least pretending to be interested in our conversations.

Finally, I would like to thank my family, in particular my parents, who have unconditionally supported and encouraged me throughout my education.

Declaration

The work presented in this thesis was performed at the Culham Centre for Fusion Energy whilst working on JET under the joint supervision of Dr. M.N.A. Beurskens and Prof. K.J. Gibson. I declare that this work is my own except where indicated by an appropriate citation and with the exceptions given below.

The optimisation of the HRTS polychromators, as detailed in Chapter 2, was jointly performed by Dr. J. C. Flanagan, Dr. M. Maslov and M.J. Leyland.

The JET HRTS pedestal fitting routine has been developed and maintained by Dr. L. Frassinetti and Dr. M.N.A. Beurskens.

MISHKA-1 PB stability analysis has been performed by Dr. S. Saarelma.

EPED model predictions have been provided by Dr. P.B. Snyder.

The study presented in Chapter 4 is the result of a joint project as published in the following article:

- M.J. Leyland, M.N.A. Beurskens, L. Frassinetti, T. Osborne, P.B. Snyder, C. Giroud, S. Jachmich, G. Maddison, P. Lomas, C. Perez von Thun, S. Saarelma, G. Saibene, K.J. Gibson and JET-EFDA Collaborators, Nuclear Fusion 53, 083028, (2013).

The study presented in Chapter 5 is the result of a joint project accepted to be published as detailed below:

- M.J. Leyland, M.N.A. Beurskens, L. Frassinetti, C. Giroud, S. Saarelma, P.B. Snyder, J.C. Flanagan, S. Jachmich, M. Kempenaars, P. Lomas, G. Maddison, R. Neu, I. Nunes, K.J. Gibson and JET-EFDA Collaborators, accepted to Nuclear Fusion.

Some of the results presented in Chapter 5 have also been included as part of the following article which has a broader scope as also considers ASDEX Upgrade measurements:

- M.N.A. Beurskens, J. Schweinzer, C. Angioni, A. Burckhart, C.D. Challis, I. Chapman, R. Fischer, J. Flanagan, L. Frassinetti, C. Giroud, J. Hobirk, R. Jof-

frin, A. Kallenbach, M. Kempenaars, M. Leyland, P. Lomas, G. Maddison, M. Maslov, R. McDermott, R. Neu, I. Nunes, T. Osborne, F. Ryter, S. Saarelma, P.A. Schneider, P. Snyder, G. Tardini, E. Viezzer, E. Wolfrum, the ASDEX Upgrade Team and JET-EFDA Contributors, Plasma Physics and Controlled Fusion 55, 124043, (2013).

The figures shown in Chapters 4 and 5 have been re-drawn by Mathew Banks, Chad Heys and Stuart Morris from the Culham Publications Service to conform with the JET publication rules required for the publications listed above.

The analysis of the JET measurements presented in Appendix A is part of a wider study as convened by Dr. A. Loarte and published in the following article:

- A. Loarte, M.J. Leyland, J.A. Mier, M.N.A. Beurskens, I. Nunes, V. Parail, P.J. Lomas, G.R. Saibene, R.I.A. Sartori, L. Frassinetti and JET-EFDA Contributors, Nuclear Fusion 53, 083031, (2013).

Chapter 1

Introduction

1.1 The global energy challenge

In July 2013 the total global population was estimated at 7.2 billion and is predicted to increase to 9.6 billion by 2050 [1]. This will further increase demand for key resources such as energy, with the global energy demand expected to more than double by 2050 in comparison to recent consumption (2012) [2].

Furthermore, energy consumption is not uniformly distributed worldwide and is traditionally concentrated in developed Western OECD[1] countries. In 1973 OECD countries accounted for 60.4 % of the global energy consumption [3]. However, in 2011 this reduced to 41.0 % due to the rapid growth of emerging economies such as China, India and the Middle East which drive global energy consumption one third higher [3, 4].

In 2011 fossil fuels (coal, gas and oil) accounted for nearly 80 % of the energy demand equating to the release of over 10^{13} kg of CO_2 [3]. The release of CO_2 (a greenhouse gas) has been comprehensively monitored since 1950 with results showing a 25 % increase in atmospheric CO_2 concentration over 50 years. Although the carbon cycle is a complex system with multiple sources and sinks it is clear that there is a net warming of the climate with consequences such as melting of the polar ice caps and increased sea levels [5]. The environmental impact of the continued use of fossil fuels is unacceptable. In addition, the reserves of fossil fuels are fast diminishing. For example, an estimate for the most abundant fossil fuel, coal, predicts that it could last for approximately 150 years at the current consumption rate [6].

Alternatives to fossil fuels are required to meet this rising demand whilst also being environmentally sustainable. Possible options include nuclear fission and renewable

[1] Organisation for Economic Co-operation and Development (OECD)

energy such as wind, solar, biofuel and hydroelectric. However these all have limitations.

Nuclear fission is capable of large-scale energy production with power stations typically producing of the order of 1 GW [7]. There are significant (but limited) reserves of the fuel (uranium) and fission is carbon-free (no direct release of CO_2). Despite these positive factors there are a number of challenges including the disposal of long lived[2] high level nuclear waste, the capital cost of building a power station and the negative perception to the public.

Renewable energy methods are regarded as carbon-free. However, in general, they require a substantial initial financial spend, offering a low energy return and are intermittent. For example, the current generation of wind turbines, with a diameter of 100 m, produce 5 MW, thus requiring 200 to produce a 1 GW facility [9]. Such a large number is expensive and requires a substantial amount of land with the turbines highly visible to the surrounding countryside. Nevertheless, the most fundamental limitation is that the turbines do not produce energy when there is too little or too much wind. Similarly, solar cells do not work when there is no sunlight. In the future, this intermittency challenge could be over come by developing efficient large scale electricity storage or by means of long distance grids to even out fluctuations (but both these solutions are themselves a considerable challenge).

Although renewable energy can significantly contribute to the primary energy need, it will be a major feat to replace fossil fuels entirely. Therefore, the most pragmatic solution to the energy challenge is utilising a combination of alternative fuels. This would mean the acceptance of nuclear fission with the contribution of renewables increasing as efficiency improves and the technology becomes more affordable. Another possible alternative option is nuclear fusion. However, it is not yet commercially available.

1.2 Nuclear fusion

Fusion is the combination of nuclei. When combining light elements such as hydrogen (or isotopes of hydrogen) the mass of the resulting nucleus is lighter than the sum of the constituent nuclei. The difference in mass is released as kinetic energy[10]. Fusion reactions are ubiquitous throughout the universe, occuring naturally in stars such as the Sun. In the Sun, the proton-proton chain, a series of reactions staring with Hydrogen and ending with Helium, dominates. The premise behind fusion research is to produce an economically viable fusion reactor on Earth. However, using the

[2]The half life of long lived high level radioactive waste can range from thousands up to millions of years [8]

proton-proton chain is not suitable as the reaction rate is too small. Equation 1.1 is the hard-sphere reaction rate (number of fusion reactions per second) between two species of density n_1 and n_2 [10].

$$R_{12} = n_1 n_2 < \sigma\upsilon > V \tag{1.1}$$

σ is the cross-section of interaction, v is the relative velocity of the reactants, $< \sigma\upsilon >$ is referred to as the reactivity and V is the volume. The reactivity can be considered as a proportionality constant, dependent on the reactant species and reactant temperature. When the density and volume are constant, the reactivity determines the reaction rate. The first step of the proton-proton chain has a very small reactivity [11]. Fusion reactions with a higher reactivity, more suitable for a reactor include the Deuterium-Tritium (D-T), Deuterium-Deuterium (D-D) and Deuterium-Helium (D-He) reactions, where Deuterium and Tritium are isotopes of Hydrogen.

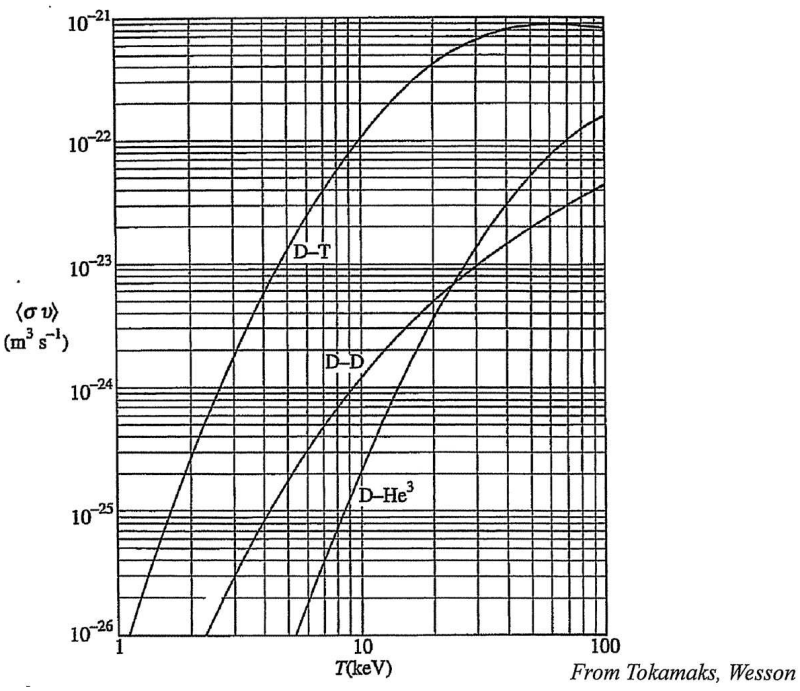

Figure 1.1: Reactivity $< \sigma\upsilon >$ for $D - T$, $D - D$ and $D - He^3$ reactions as a function of temperature [12].

The most suitable reaction is the D-T reaction as it has the highest reactivity at relatively low temperatures (see figure 1.1). The D-T reaction releases 17.6 MeV; 14.1 MeV carried by a neutron and 3.5 MeV carried by a Helium ion as shown in equation 1.2,[10, 12].

$$D + T \rightarrow He^4(3.5\text{MeV}) + n(14.1\text{MeV}) \tag{1.2}$$

1.3 Definition of a plasma

The core temperature of a fusion reactor must be in excess of ≈ 10 keV (≈ 100 million °C) to achieve a sufficient reaction rate to make the reactor viable. This is equivalent to a temperature 10 times hotter than the centre of the Sun (≈ 10 million °C). At temperatures this high, the gaseous fuel will exist as a plasma; a partially ionised gas, as the electrons have sufficient energy to dissociate from the nucleus. An ionised gas can be referred to as a plasma subject to three basic parameters; the Debye length (λ_D), the plasma parameter (Λ_D) and the frequency of collisions (ω). The conditions are summarised by equation 1.3.

$$\lambda_D << L \tag{1.3a}$$

$$\Lambda_D >> 1 \tag{1.3b}$$

$$\omega\tau_c >> 1 \tag{1.3c}$$

The Debye length (λ_D) is a characteristic length describing the size of a shielding cloud of charge within an ionised gas. L is the system length (the spatial extent of a plasma). Λ_D is the plasma parameter, the number of particles within a sphere of radius λ_D (the Debye sphere). ω is the total frequency of all types of collisions and τ_c is the time period between neutral-charged particle collisions.

Condition 1.3a and 1.3b ask if the ionised gas is sufficiently dense to be a plasma. Condition 1.3c asks if the neutral concentration is sufficiently low such that the motion is governed by electrostatic forces over hydrodynamic forces [13]; i.e. is the ionised gas sufficiently hot. To summarise, Chen [13] describes a plasma as 'a quasineutral gas of charged and neutral particles which exhibits collective behaviour'.

1.4 Ignition and fusion gain

Fusion reactor concepts rely on capturing and harnessing the D-T fusion products. In principle, the proposed method is the 14.1 MeV neutrons are used to generate electricity as they pass through the plasma and deposit their energy in a surrounding blanket. Whereas, the other product of the D-T reaction, the 3.5 MeV alpha particles, deposit their energy in the plasma which further heats the plasma [12]. Initially external heating of the fusion reactants is required to reach temperatures greater than 10 keV. However, once D-T fusion occurs a plasma can become self-sustaining; burn without the aid of external heating, which is termed ignition. To initiate

ignition, as well as the particles being heated to a sufficient temperature, there must be a sufficient number of particles confined for a sufficient amount of time. This is quantified by the fusion triple product, a condition for ignition, see equation 1.4 [12].

$$n\tau_E T > 3 \times 10^{21} m^{-3} \text{keVs}, \tag{1.4}$$

where n is the density, τ_E is the energy confinement time and T is the temperature. A measure of the efficiency of a reactor is the physics gain factor (Q). This is defined as the net thermal power out ($P_{OUT,NET}$) to the heating power in (P_{IN}) [10].

$$Q = \frac{P_{OUT,NET}}{P_{IN}} \tag{1.5}$$

There is no gain when $Q < 1$, it is breakeven when $Q = 1$ and there is gain when $Q > 1$. Ignition (also termed full ignition) is when $Q \approx \infty$ as the input power required to sustain the plasma burn falls to zero. Achieving a net gain poses major technical, engineering and physics challenges. Nonetheless, once over the initial hurdle of the cost of research and development, fusion has many advantages in comparison to other energy alternatives. It has a small carbon footprint. There is minimal low level and short lived radioactive waste. It will be able to replace GW power stations and hence produce energy on a sufficiently large scale. It is not directly dependent on factors beyond human control such as the weather (solar/wind). Most notably, the potential fuel resources could last for thousands of years in contrast to the few hundred at most for fossil fuels [10].

1.5 Confinement methods

There are two popular confinement techniques extensively researched throughout the international scientific community: Inertial Confinement Fusion (ICF) and Magnetic Confinement Fusion (MCF). Both are briefly described below.

1.5.1 Inertial Confinement Fusion

Inertial fusion utilises high-powered lasers incident on a pellet with a diameter typically of the order of 1 mm. The pellet contains approximately a milligram of D-T fuel, which compresses resulting in a hot central spot. This spot initiates a burn wave propagating out through the pellet into the denser cooler fuel layers. The National Ignition Facility (NIF) at the Lawrence Livermore National Laboratory (LLNL) in

the USA is the largest inertial confinement experiment with 192 beams. NIF aims to achieve ignition in the near future with projected yields of $5 - 10$ MJ for a laser energy of 1.3 MJ [14]. Nevertheless, inertial fusion faces a number of challenges including directly or indirectly irradiating the target with sufficient uniformity to mitigate the formation of instabilities, for example, the Rayleigh-Taylor instability. This instability mixes different density layers of the target which ultimately impedes the symmetric compression and ignition of target.

1.5.2 Magnetic Confinement Fusion

Magnetic fusion exploits the interaction between charged particles and magnetic fields. The motion of a single charged particle within a fusion plasma is governed by the Lorentz force [10, 12, 13], as described in equation 1.6.

$$\begin{aligned} m\frac{d\underline{v}}{dt} &= Ze(\underline{E} + \underline{v} \times \underline{B}) \\ \frac{d\underline{r}}{dt} &= \underline{v} \end{aligned} \tag{1.6}$$

Where m is the mass of the particle, $\underline{v}$ is the velocity, Ze is the charge of the particle, $\underline{E}$ is the electric field and $\underline{B}$ is the magnetic field. In the case where $\underline{E} = 0$ and assuming $\underline{B}$ is uniform in time and space a charged particle will simply gyrate about the magnetic field at the gyro frequency [10, 12, 13], as described in equation 1.7.

$$\Omega = \frac{ZeB}{m} \tag{1.7}$$

The radius of orbit is called the gyro radius[3] [10, 12, 13], as defined in equation 1.8.

$$r_L = \frac{v_\perp}{\Omega} = \frac{mv_\perp}{ZeB} \tag{1.8}$$

$v_\perp$ is the velocity of the particle perpendicular to the magnetic field. This gyro motion describes the circular motion of charged particles on a plane perpendicular to the magnetic field. A charged particle can move parallel to the magnetic field if there is an E field parallel to B or a gradient in B parallel to B [12].

The gyro motion of a charged particle along a field can be perturbed by a perpendicular force ($\underline{F}_\perp$) due to, for example, a perpendicular $\underline{E}$ field. The equation of

[3] Also known as the Larmor radius.

motion, equation 1.6, can be modified to include $\underline{F}_\perp$, as shown in equation 1.9.

$$m\frac{d\underline{v}}{dt} = \underline{F}_\perp + Ze(\underline{v} \times \underline{B}) \tag{1.9}$$

It can be shown that the charged particle drifts at a constant velocity perpendicular to $\underline{F}_\perp$ and $\underline{B}$ as given by equation 1.10.

$$\underline{v}_\perp = \frac{1}{Ze}\frac{\underline{F}_\perp \times \underline{B}}{B^2} \tag{1.10}$$

The important drifts when considering magnetic fusion devices are: $\underline{E}\times\underline{B}$, curvature, ∇B, polarization and the diamagnetic drifts, all described by Chen [13]. The diamagnetic drift arises from a fluid description of a plasma, i.e. multiple particles instead of a single particle [13].

A measure of how effective a magnetic fusion device is at confining a plasma is Beta (β). Beta is defined as the ratio of particle pressure to magnetic pressure, as described by equation 1.11 [10, 12, 13].

$$\beta = \frac{p}{B^2/2\mu_0} = \frac{\text{Particle Pressure}}{\text{Magnetic Pressure}} \tag{1.11}$$

p is the particle pressure, B is the magnitude of the magnetic field, μ_0 is the permeability of free space and $B^2/2\mu_0$ is the magnetic pressure. Ideally, beta should be large implying that a high particle pressure is achieved for minimal magnetic pressure. Equivalently, large beta implies high confinement for low investment of magnetic fusion energy [15].

1.6 The Tokamak

The gyro motion of charged particles about a magnetic field can be utilised when conceiving a magnetic fusion device that guides and confines a plasma, such as a Tokamak. A Tokamak is a torus shaped device [12]. A toroidal field is generated by multiple toroidal field coils surrounding the torus, see figure 1.2.

R is major radius, a is the minor radius and $\hat{\phi}$ and $\hat{\theta}$ are the unit vectors defining the toroidal and poloidal directions respectively. The toroidal field B_ϕ, is in the direction of $\hat{\phi}$. The magnetic field strength is not uniform across the major radius of a Tokamak. It can be shown via integrating Ampere's Law [11] that the magnetic field varies with the inverse of the major radius, as illustrated by figure 1.3.

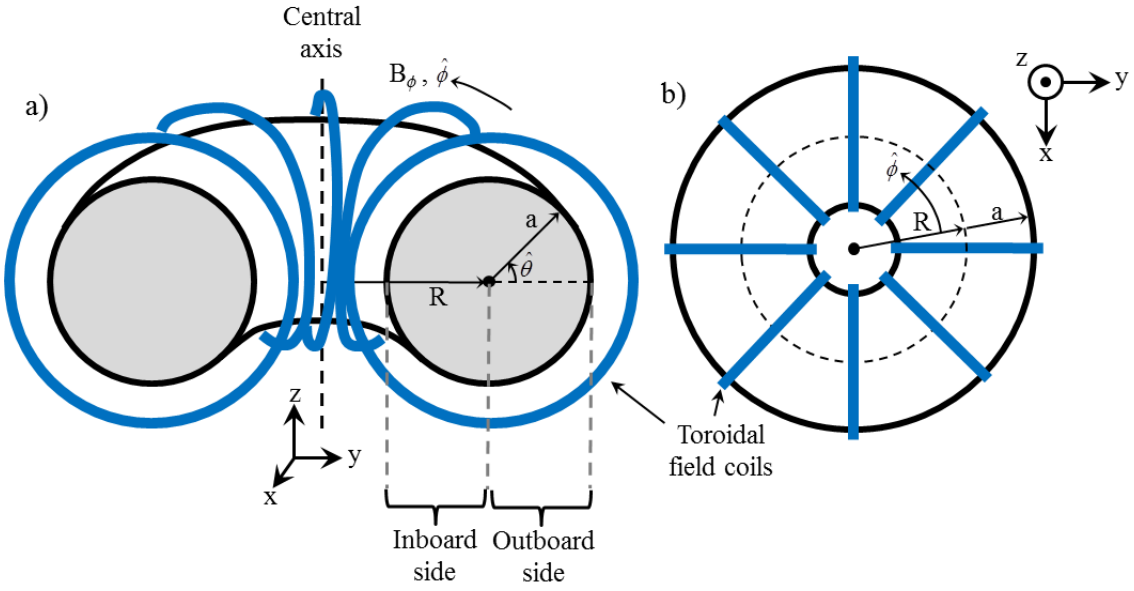

Figure 1.2: a) 3-dimensional and b) top down view schematic of a Tokamak showing toroidal field coils (blue).

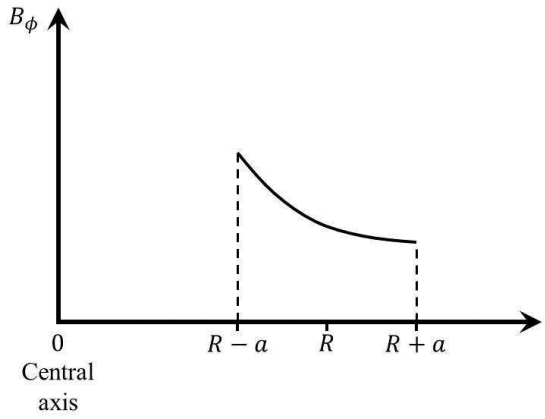

Figure 1.3: Variation of toroidal magnetic field with respect to the major radius, R.

A plasma confined by a purely toroidal field by will exhibit vertical charge separation due to the curvature and $\nabla \underline{B}$ drift. This generates a vertical $\underline{E}$ field and combined with the toroidal magnetic field results in a radially outward $\underline{E} \times \underline{B}$ drift, compromising confinement, see figure 1.4.

To overcome the charge separation a poloidal field is required to provide a poloidal rotational transform, mixing the ions and electrons. The poloidal field is produced by a toroidal plasma current. The plasma current is driven by transfomer action. According to Faraday's Law a changing magnetic flux through the centre of the Tokamak $d\underline{B}/dt$ by ramping the current in the central solenoid results in an induced current in the secondary winding, the plasma, see figure 1.5.

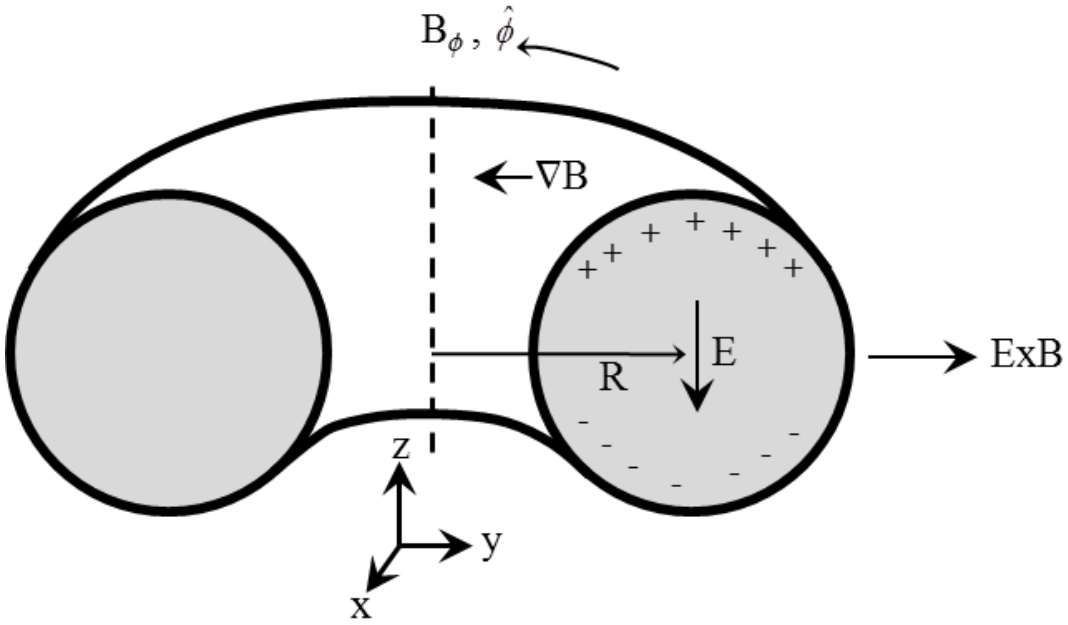

Figure 1.4: Vertical $\underline{E}$ field generated by charge separation due to curvature and $\nabla \underline{B}$ drift resulting in $\underline{E} \times \underline{B}$ drift.

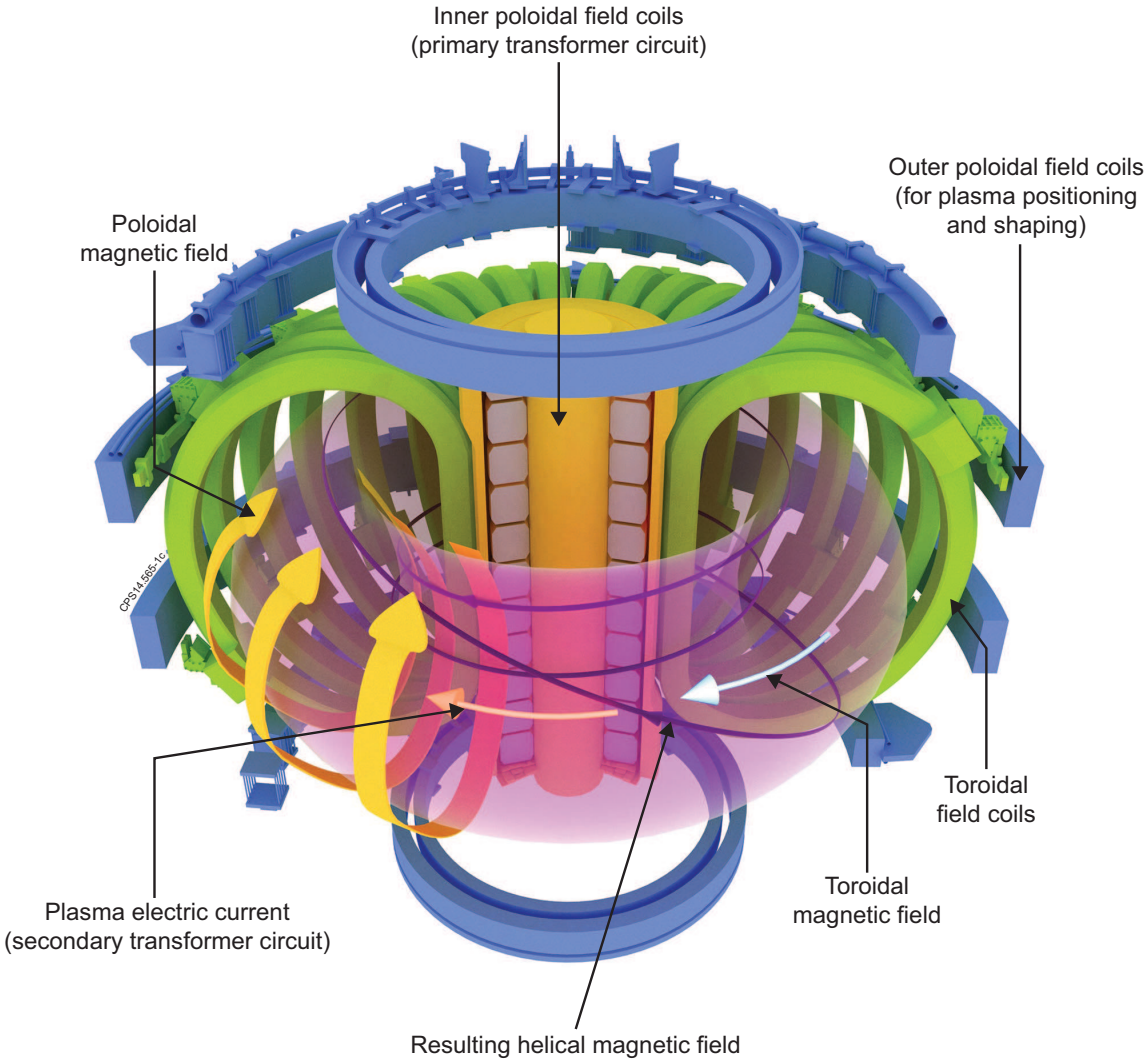

Figure 1.5: Schematic of conventional Tokamak toroidal, poloidal and net helical fields, plasma current and magnetic coils. Image provided by Russell Perry, Culham Publication Services.

The toroidal and poloidal magnetic fields combine to form a net helical magnetic field. To generate the change in magnetic flux for the transformer action, the current is ramped from $-I_{max}$ to $+I_{max}$ through a central solenoid. This process is inherently pulsed hence imposing a major limitation for the Tokamak. Non-solenoid start-up is an area of Tokamak research [12].

There are many operational research Tokamaks worldwide such as the Joint European Torus (JET, UK), DIII-D (USA), ASDEX-Upgrade (AUG, Germany), JT-60 (Japan) and Alcator C-Mod (USA). The Tokamak to date is the most advanced proven magnetic fusion device as JET achieved the record ratio of fusion power to input power (Q) of ≈ 0.6 in 1997 during a D-T phase of operation [16]. This pulse produced a maximum fusion power of 16.1 MW. ITER is the next large Tokamak to be built, with a major radius approximately double the radius of JET ($R_{ITER} \approx 6$ m). ITER is a collaboration between China, Europe, India, Japan, Korea, Russia and the USA. The project aims to achieve a net fusion gain of $Q \approx 10$ [17]. ITER is under construction in Cadarache, France and the first plasmas are foreseen in 2019. ITER is an essential experiment on the road to a demonstration fusion power plant.

There exist alternative magnetic fusion devices such as the stellarator. The stellarator exploits a complex set of modular coils, computationally designed to produce a magnetic field with a rotational transform whilst minimising plasma currents [10]. Minimising currents is advantageous as they drive instabilities within a Tokamak, which requires a plasma current for the poloidal field. As a result, a Stellarator design is less prone to instabilities in comparison to a Tokamak. On the other hand, the challenge for Stellarators is the complexity of the design and the manufacturing precision required. Depending on the outcome of the Wendelstein 7-X project, a Stellarator could be favoured over a Tokamak for a demonstration fusion power plant, the step after ITER.

1.7 H-mode and Edge Localised Modes (ELMs)

The ultimate goal of a fusion powerplant has not yet been realised as the magnetic confinement is not perfect. The energy confinement time τ_E is a characteristic timescale describing how long it takes for energy to leak out of a device such as a Tokamak. The three conventional modes of operation in within a Tokamak are ohmic, low confinement mode (L-mode) and high confinement mode (H-mode) [10]. The energy confinement time varies between each mode of operation.

Ohmic mode operation relies on the plasma being resistive such that coulomb collisions between particles to dissipate the energy provided by the central solenoid in the plasma. Ohmically heating the plasma will not be sufficient for the high tem-

perature operation required for D-T fusion as the resistivity and collisionality (the frequency of collisions where $\nu* \propto n/T^2$) both decrease with increasing temperature so not enough energy would be deposited in the plasma.

Ohmic heating can be supplemented by additional heating systems. The two types of conventional heating systems widely used on Tokamaks are Neutral Beam Injection (NBI) and Radio Frequency[4] (RF) heating. In 1982 a bifurcation of Tokamak confinement performance was discovered when applying auxiliary heating (NBI) to ohmic plasmas on the ASDEX Tokamak [15] as shown in Figure 1.6 which shows the change in poloidal beta and internal inductance $\Delta\left(\beta_p + \frac{1}{2}l_i\right)$ (a measure of confinement) as a function of NBI input power. At higher P_{NBI} there are two branches corresponding to L-mode (closed circles) and H-mode (open circles). NBI heated L-modes while showed an increase in the temperature gradient, the energy and particle confinement time was degraded in comparison to ohmic plasmas; hence the name L-mode or low confinement mode. Fortunately, there was another sub-set of results which showed a very different response to heating as the confinement time doubled; hence the name H-mode or high confinement mode [15]. It is thought for a given heating power if there is sufficient power passing through the plasma edge the plasma will be in H-mode.

It has subsequently been established that H-mode is characterised by the formation of an Edge Transport Barrier (ETB) resulting in a steep pressure gradient at the edge called the pedestal. Figure 1.7 shows the normalised pressure profile for an L-mode and H-mode plasma. The formation of the pedestal is due to the suppression of anomalous turbulence at the edge. The mechanism for this suppression is not well understood despite there being a number of theories. For example, [18] proposes the ion flux drives a negative radial electric field, a characteristic of H-mode. [19] presents measurements of the negative radial electric field E_r during H-mode on MAST (a spherical Tokamak[5], smaller in comparison to JET). [20] suggests the Scrape-Off-Layer[6] (SOL) flows play a controlling role in the L-H transition.

Operation in H-mode is highly attractive as the increase in edge pressure with the formation of the pedestal aids core confinement. Consequently, H-mode is the ITER baseline scenario. However, H-mode does have drawbacks, the most prominent of which is the susceptibility of the pedestal region to instabilities such as Edge Localised Modes (ELMs). ELMs are a periodic crash of the pressure pedestal due to reaching a critical gradient, see figure 1.7. At each ELM crash there is an outward

[4]RF heating can be sub-catergorised by frequencies: Ion Cyclotron Resonant Heating (ICRH); Lower Hybrid (LH); and Electron Cyclotron Resonant Heating (ECRH) [10].

[5]A Spherical Tokamak has a smaller aspect ratio (R/r) in comparison to a conventional Tokamak such as JET

[6]The Scrape-Off-Layer is the region beyond the last closed flux surface where open field lines connect with the divertor

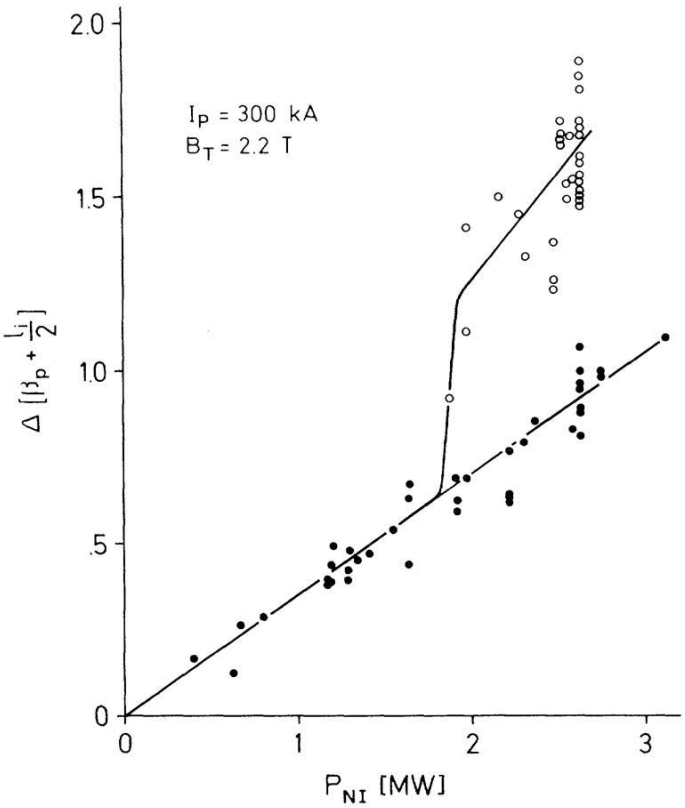

Figure 1.6: The change in poloidal beta and internal inductance as a function of NBI heating power demonstrating the bifurcation of plasma performance from L-mode (closed circles) to H-mode (open circles). Figure taken from [15].

radial burst of energy characterised by a spike in deuterium alpha (D_α) emission due to the interaction of the expelled energetic particles with neutrals in the Scrape-Off-Layer (SOL) region.

There are different types of ELMs, including Type I, Type II and Type III ELMs, which are discussed throughout this thesis and, in particular, in Chapter 4.3. Type I ELMs are large in amplitude and periodic with a relatively small frequency. Type III ELMs are small in amplitude and of a frequency such that the occurance is almost continuous. Type II ELMs are between Type I and III when considering both the amplitude and frequency. Type I and II ELMs do not degrade confinement, unlike type III ELMs, but instead result in large transient heat leads on plasma facing components. This causes unacceptable damage, resulting in impurities in the plasma, which can, in turn, degrade performance and, in extreme cases, lead to instabilities and even disruptions [10].

As well as ELMs (the origins of which are discussed in the next section) there are a number of other limits to Tokamak operation [10]. One such phenomenon, which is particularly relevant in the context of this thesis, is the density limit. The physical mechanism responsible for the density limit in heated H-mode plasmas is not well understood. It is thought when fuelling to high density, such that the temperature

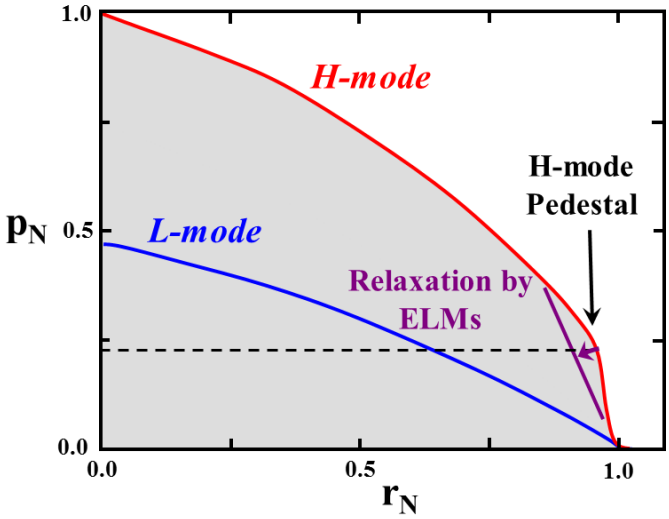

Figure 1.7: Normalised pressure profile for an L-mode (blue) and H-mode (red) plasma. The H-mode profile shows a steep pressure gradient at the plasma edge called the pedestal [21].

pedestal cools below 10 eV, results in: detachment, increased divertor radiation, impurity influx, increased susceptibility to core instabilities and ultimately a disruption [10, 22]. An empirical scaling for the maximum achievable plasma density, as first shown by [23], is given by,

$$n_{GW} = \frac{I_P}{\pi a^2}. \tag{1.12}$$

Where n_{GW} is the Greenwald density in $10^{20}\mathrm{m}^{-3}$, I_P is the plasma current in MA and a is the minor radius in m. The Greenwald density is particularly insightful when normalising the measured line-integral density or the density pedestal height. The resulting fractional density is independent of the machine dimensions and hence is a convenient way to order data. The fractional density is used throughout this thesis.

1.8 The Peeling-Ballooning limit

An ELM is a type of magnetohydrodynamic (MHD) instability. In general, MHD can be considered to be an extension of fluid dynamics that takes into account the electrostatic and magnetic response of a plasma. A branch of MHD that assumes the plasma is not resistive is called ideal MHD [10]. There are three categories of ideal MHD instabilities: internal/external; conducting/non-conducting wall; and pressure/current driven, as described in detail by [10].

It is thought an ELM occurs due exceeding the Peeling-Ballooning (PB) MHD sta-

bility limit [85]. This limit is a combination of three ideal MHD instabilities as now described. An external instability involves the motion of the entire plasma volume. As a result, the plasma surface can strike the wall causing impurity influx and damage to the first wall due to high heat loads. A kink mode is a current driven instability resulting in a physical kink in the plasma. A ballooning mode is a pressure driven instability which manifests at bad curvature; at the low field side of a Tokamak. Bad curvature is where the curvature of the magnetic field and pressure gradient are in the same direction ($\underline{\kappa} \cdot \nabla p > 0$). The PB limit is the combination of an edge localised external kink (peeling) mode with a ballooning mode, as discussed in more rigorous detail by [24–26].

The two drivers of PB instability are the edge current (J_{ped}) and the pressure gradient (p'_{ped}). With this in mind, the PB stability boundary can be represented on a plot of J_{ped} versus p'_{ped} as illustrated in Figure 1.8. Below the boundary, the plasma edge is stable. Above the boundary, at high J_{ped}, the plasma edge is peeling unstable. Similarly, at high p'_{ped} the plasma edge is ballooning unstable. The region between peeling and ballooning limited plasmas at high J_{ped} and p'_{ped} is referred to as the PB corner or nose. The stability boundary corresponds to a specific pedestal width. If, for example, the pedestal was wider, the edge region would be able to accommodate more modes and would, therefore, be relatively more unstable. Consequently, this would result in an unfavourable shift in the PB stability boundary and a reduction in the operational space.

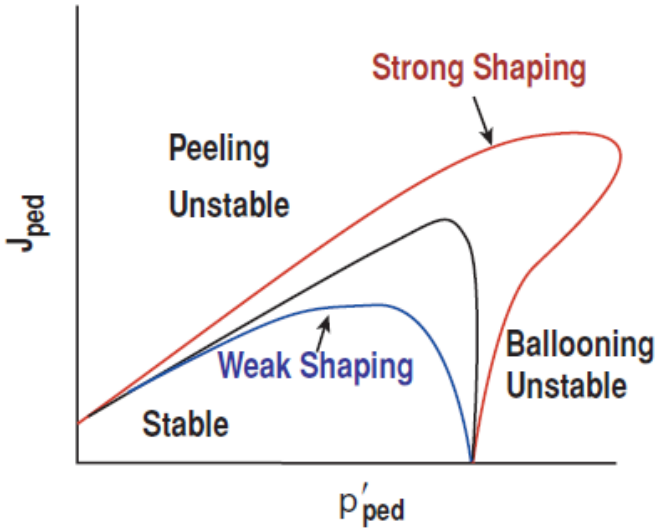

Figure 1.8: Schematic of stability boundaries for Peeling-Ballooning limit as a function of pedestal pressure gradient (p'_{ped}) and edge current (J_{ped}). Three limits are shown; blue represents a more weakly shaped plasma relative to the black line. The red line represents a strongly shaped plasma. When above the stability boundary at relatively low p'_{ped} and high J_{ped}, the plasma is referred to as peeling unstable. Similarly, when over the boundary at high p'_{ped} and low J_{ped} the plasma is referred to as ballooning unstable [26].

The PB stability boundary can be modified by varying the strength of the plasma shaping as also illustrated in Figure 1.8. The plasma shaping refers to the elongation κ (ellipticity), triangularity δ and indentation b (bean-like). A larger pressure gradient and current density can be maintained with high shaping as this favorably moves the PB stability boundary. High performance, high triangularity ELMy H-mode JET plasmas are extensively discussed throughout this thesis.

The PB stability boundary is evaluated using an ideal MHD eigenvalue solver, such as MISHKA-1 [27] or ELITE [24]. A detailed description of the analysis process is provided by [28], as now summarised. First, a plasma equilibrium characteristic of a specified J_{ped} and p'_{ped} is calculated by HELENA, an equilibrium solver. MISHKA-1 evaluates the growth rate (eigenvalue) and mode structure (eigenfunction) for a given toroidal mode number and equilibrium. This is repeated over a range of toroidal mode numbers to find the eigenfunction that minimises the change in potential energy. If, over all n values, the change in stored energy is positive ($\delta W > 0$), then the plasma equilibrium is stable and the growth rate is zero. Conversely, if, for any n value, the change in stored energy is negative ($\delta W < 0$), then the plasma equilibrium is unstable and the growth rate is non-zero. The eigenfunction corresponding the highest growth rate defines the most unstable/limiting toroidal mode number. The eigenfunction defines the nature of the limiting mode (i.e. peeling or ballooning). Furthermore, this process can be repeated for different values of J_{ped} and p'_{ped} over a 2D grid to define the stable and unstable regions. Typically, the peeling mode is unstable to low n (<5) modes, whereas the ballooning mode is unstable to high n (>20) modes. The PB mode is unstable to intermediate n values (5-20). The PB mode is usually the limiting instability in the pedestal that results in an ELM crash [26].

An operational point, representing the edge stability of an experimental plasma, can be compared to the calculated PB stability boundary. To calculate the experimental equilibrium, the pressure gradient is determined from radial temperature and density profile measurements. The edge current is assumed to be dominated by the bootstrap current and can be calculated using the expression given in [29]. The radial position of the kinetic profiles is corrected such that the separatrix temperature is ≈ 100 eV (to be consistent with the two-point model, as discussed in more detail in Section 4.4.3). The proximity of the operation point to the PB stability boundary indicates if the plasma edge is stable or unstable. Furthermore, the position of the operation point relative to the PB corner indicates if the plasma edge is peeling or ballooning limited.

It is important to note that the PB stability calculation provides the maximum achievable pedestal height for a given pedestal width. When analysing experimental plasmas this is provided from kinetic profile measurements. However, to predict the

pedestal height more information is required.

1.9 Kinetic Ballooning modes

It can be argued that Kinetic Ballooning (KB) modes provide another relation between the pedestal width and height, which, when combined with the PB constraint enables a predictive model for the pedestal structure. A description of this argument is given in [30], as now summarised.

The onset of strong turbulence in the pedestal is found in electromagnetic gyrofluid and gyrokinetic simulations at a threshold close to the KB mode [31, 32]. $E_r \times B$ flow shearing, discussed in Section 1.7, is a possible mechanism for turbulent suppression resulting in the formation of the pedestal. However, the KB mode turbulence, as just described, is independent of $E_r \times B$ as even for large radial electric fields the KB mode turbulence cannot be fully suppressed. Therefore, KB modes are proposed as the gradient limiting instability in the pedestal region and so determine the pedestal width. Combining an expression for the normalised pressure gradient linear threshold for KB mode turbulence (α_{KB}) and an expression for the normalised pedestal pressure gives,

$$\Delta = c_1 \cdot \sqrt{\beta_{pol,ped}}. \tag{1.13}$$

Δ is the pressure pedestal width in normalised poloidal flux and $\beta_{pol,ped}$ is the normalised poloidal pedestal pressure ($\beta_{pol,ped}$). A detailed description of the steps formulating Equation 1.13 are given by [30] and concisely summarised by [33]. c_1 can be simply considered a constant and is expected to be of the order 0.1.

Experimental observations in support of the supposition that pedestal width scales with the square root of the poloidal pedestal beta have been shown on a number of devices. On DIII-D, as suggested by regression analysis [34], the electron pressure pedestal width measured in real space scales with $(\beta_{pol,ped})^{0.5}$ [35]. Furthermore, the average of the electron temperature and electron density pedestal width in normalized poloidal flux also scale with $(\beta_{pol,ped})^{0.5}$ [30, 36]. A multi-machine database incorporating data from AUG, DIII-D and JET shows that the electron temperature width measured in real space scales with $(\beta_{pol,ped})^{0.5}$, but that the electron density width does not [33]. In terms of the mean pedestal width on AUG, it again scales with $(\beta_{pol,ped})^{0.5}$ but only in normalized poloidal flux space and not real space [37]. Although, after the inclusion of DIII-D and JET data in another multi machine comparison the mean pedestal width in real space could be considered to scale with $(\beta_{pol,ped})^{0.5}$ [37]. Other studies which support the pedestal width scaling with

$(\beta_{pol,ped})^{0.5}$ include [38–40], which present results from JT-60U as well as spherical Tokamaks such as MAST and NSTX. The value of c_1, for example on DIII-D, is 0.076 [30] as expected. However, it is important to note that the constant c_1 is higher for spherical machines than for medium aspect ratio tokamaks (for NSTX $c_1 = 0.17$) [40].

1.10 Predictive pedestal modelling: EPED1 and EPED1.62

The EPED model is designed to predict the pressure pedestal structure of a Tokamak plasma. EPED assumes that the pedestal pressure will rise until constrained by the onset of two key instabilities; PB modes and KB modes. These instabilities provide two calculable constraints which, when combined, can be solved for the two unknowns; the pedestal height and width [30, 41–43]. The inputs to the model are eight scalar parameters, B_t (T) the toroidal magnetic field, I_p (MA) the plasma current, R (m) the major radius, a (m) the minor radius, δ the triangularity , κ the elongation, $n_{e,ped}$ ($\times 10^{19}$ m^{-3}) the pedestal density and $\beta_{N,global}$ the global Troyon normalised β. In the context of EPED the PB stability boundary is evaluated by ELITE [25, 43] as opposed to MISHKA-1, see Section 1.8. Furthermore, the EPED model assumes the pressure pedestal width is the average of the temperature and density pedestal width.

There are two versions of the model, EPED1 [30] and EPED1.62 [42]. A key difference between the two versions is the treatment of the KB constraint, defined in Equation 1.13. The simpler version, EPED1, assumes c_1 is a constant at a value of 0.076 [30]. The full EPED1.62 model has a more sophisticated implementation of the KB constraint as detailed in [42]. In EPED1.62, c_1 is calculated directly using the Ballooning Critical Pedestal (BCP) technique which treats c_1 as a weakly varying function of parameters such as collisionality ($\nu*$) and aspect ratio (ϵ) [42]. The calculated values of c_1 are generally found to be in the range 0.06-0.09 for medium aspect ratio tokamaks.

The normalised poloidal pedestal pressure ($\beta_{pol,ped}$) is discussed in the context of EPED predictions shown in this thesis. A useful expression to calculate $\beta_{pol,ped}$ from measurements, for a specific pulse, is given by e.g [37],

$$\beta_{pol,ped} = \frac{p_{ped}}{B_p^2/2\mu_0} = \frac{p_{ped}}{\left(\mu_0 I_p/C\right)^2/2\mu_0} = \frac{2C^2 p_{ped}}{\mu_0 I_p^2} \tag{1.14}$$

Where p_{ped} is the plasma pressure in Pa, B is the magnetic field strength in T, I_p is

the plasma current in A and C is the plasma circumference in m.

1.11 Motivation and thesis outline

The motivation behind this thesis is to exploit electron temperature and density radial profiles as measured by the JET High Resolution Thomson Scattering (HRTS) system. More specifically, this thesis is primarily focused on using the JET pedestal fitting tool to quantify the pedestal structure and contribute towards the understanding of the physical mechanism(s) which govern the H-mode pedestal.

Chapter 2 introduces the JET HRTS system, describing the hardware and how measurements of temperature and density are determined. A study into the optimisation of the HRTS polychromators is also presented.

To quantify the pedestal structure from the HRTS electron temperature and density profiles, a modified hyperbolic tangent (mtanh) function is fitted to ELM synchronised HRTS profiles. Chapter 3 introduces the JET pedestal fitting routine that has been extensively used throughout this thesis. In addition, Chapter 3 also presents a study that quantifies the systematic error introduced the pedestal width due to ELM synchronising the profiles.

Chapter 4 considers a database of dense highly shaped (high trianglarity) ELMy H-mode JET plasmas with the carbon wall. In comparison to previous studies which were limited by diagnostic capabilities, this database has good quality high resolution HRTS data. This study presents the pre-ELM pedestal structure as well as providing a comparison to the leading predictive pedestal model, EPED. Predictions from both versions of the model, EPED1 and EPED1.62 are presented in Chapter 4. Furthermore, the inter-ELM dynamics are presented along with the evolution of the PB stability.

Measurements from recent JET campaigns with the new ITER-Like Wall (ILW) offers an invaluable opportunity to investigate how the pedestal structure changes with the presence of a metallic wall and its role on confinement. The results from a new database consisting of deuterium and nitrogen fuelled Type I ELMy H-mode plasmas on JET with the ILW (JET-ILW) are presented. Chapter 5 focuses on pre-ELM measurements and the comparison to EPED1 predictions.

As well as using the HRTS profiles to quantify the pedestal structure, these profiles are also insightful when considering the timescale of core and edge build-up in density and temperature from L-mode to H-mode. Appendix A details the variation of the build-up timescale, as determined by an *mtanh* fit, across a low and high δ JET carbon wall database spanning a range of plasma currents. This analysis has

facilitated modeling focused on the implications for ITER of which a brief summary is provided.

Chapter 2

The JET High Resolution Thomson Scattering (HRTS) system

2.1 Thomson scattering diagnostic principle

Thomson scattering describes the process where by relatively low energy ($\hbar\omega << mc^2$) electromagnetic radiation incident upon a charged particle, such as an electron, is elastically scattered. The electric and magnetic fields of incident linearly polarised electromagnetic wave accelerate the charged particle which absorbs and then re-emits the wave such that the 3-dimensional polar distribution of the time average radiated power resembles a torus [44]. Incoherent Thomson scattering, where the motion of electrons is independent of the surrounding electrons, is a key diagnostic technique for measuring electron temperature and density within Tokamak plasmas. This diagnostic technique was first demonstrated by [45] in 1963. Later, in 1968, incoherent Thomson scattering came to fruition when used to confirm world leading electron temperatures within the T-3 Tokamak [46]. Thomson scattering systems are widely used on present-day Tokamaks such as JET [47, 48], DIII-D [49, 50], ASDEX [51, 52], JT-60U [53], Alcator C-MOD [54, 55], MAST [56, 57] and NSTX [58].

In general a Thomson scattering diagnostic system typically requires a high powered laser ($\approx$ 1 GW) to produce a sufficient number of scattered photons. This is due to a small scattering cross section as typically only 10^{-8} of the incident photons are scattered and furthermore the collection optics only capture a fraction of the scattered photons [44].

The number of scattered photons, as calculated by integrating the scattered spectrum with respect to wavelength, is proportional to the electron density. The scattered

spectrum is Doppler broadened and blue shifted relative to the laser wavelength. This is more pronounced at higher temperatures and therefore the shape of the scattered spectrum can be used to determine the temperature. Figure 2.1 shows the variation with temperature, at fixed density, of the Selden-Naito expression [59]; an analytical expression that well describes the observed Thomson scattered spectrum.

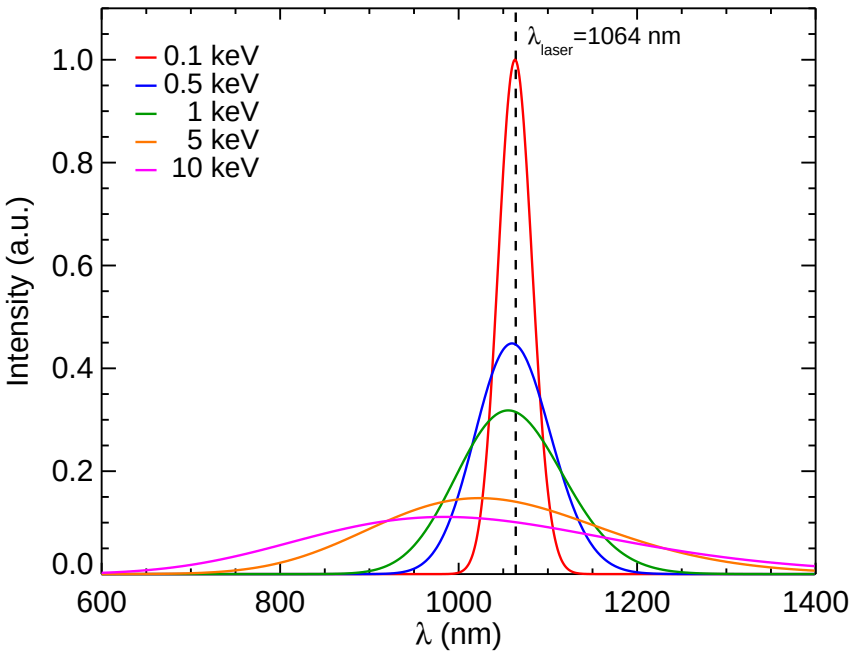

Figure 2.1: Variation of analytical expression (Selden-Naito) for Thomson scattering spectrum as a function of wavelength with temperature, $T \approx 0.1$ keV (red), 0.5 keV (blue), 1.0 keV (green), 5.0 keV (orange), 10.0 keV (magenta), at fixed density. At higher temperature the scattered spectrum has a greater doppler broadening and blue shift relative to the laser wavelength (1064 nm).

Physically the scattered spectrum is Doppler broadened due to the thermal motion of the electrons which blue or red shifts the scattered light depending on the relative velocity. In addition, the net blue shift is due to the relativistic aberration of the scattered light. More specifically, as the velocity of the electron approaches a non negligible fraction of the speed of light, the laser light is preferentially scattered in the direction of motion of the electron. Consequently, the number of scattered photons collected by the lens are more likely to have been scattered from an electron also travelling towards the lens, resulting in a net blue shift. This is also termed the headlight effect as all discussed in [60]. A summary of the nuances of Thomson scattering theory in the context of a fusion diagnostics can be found in [61]. This chapter continues by describing in detail the JET High Resolution Thomson Scattering system.

2.2 System Overview

The High Resolution Thomson Scattering (HRTS) system on JET measures radial electron temperature and density profiles. The system was installed in 2005 and started routine operation in 2007. A key requirement of the system was to better resolve steep gradients such as those seen in the H-mode pedestal (on JET typically $|dT_e/dr| \approx 50$ keVm^{-1} and $|dn_e/dr| \approx 500 \times 10^{19}$ m^{-4}). The HRTS system complements the two other Thomson scattering systems on JET, the main and edge light detection and ranging (LIDAR) systems which produce profiles by means of a time-of-flight method [48]. Figure 2.2 shows the set-up for the HRTS system which is discussed in detail by [48].

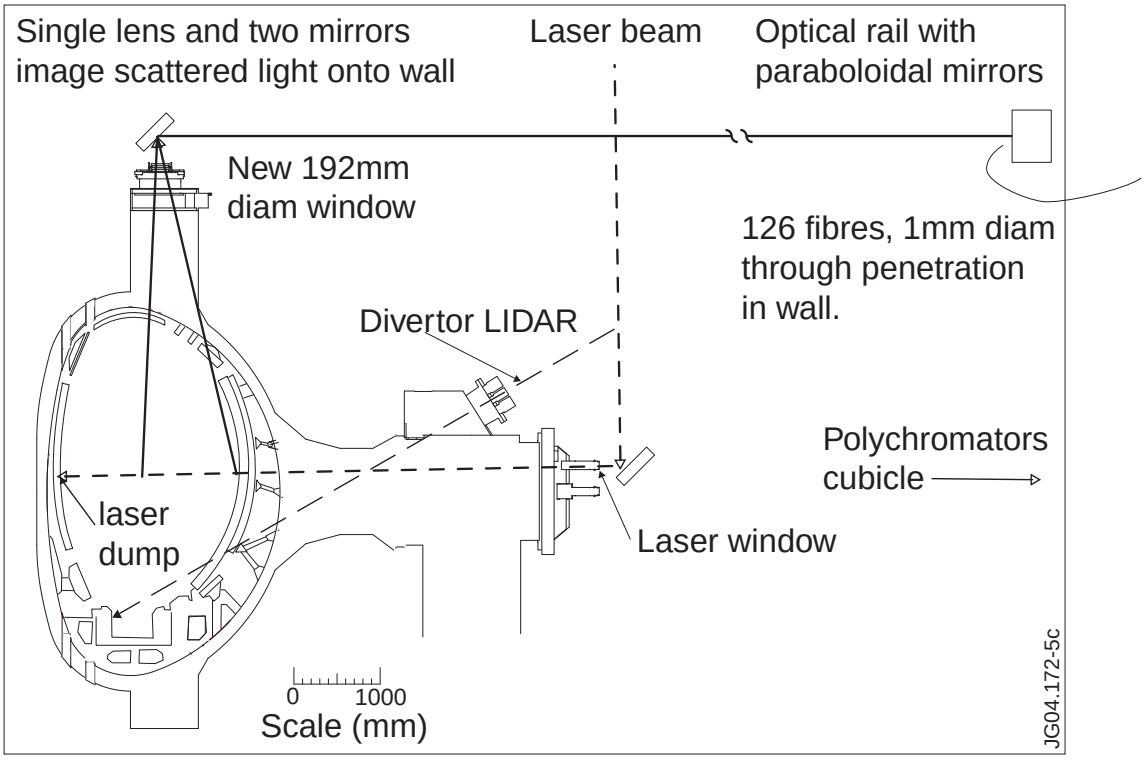

Figure 2.2: Schematic of optical hardware for JET HRTS system and the JET vessel. The black dashed line indicates the path of the laser beam that travels from the roof lab and is directed into the vessel. The un-scattered light is dissipated on a beam dump tile on the inner wall. The scattered light is collected by a lens situated at the top of the vessel, which directs the light to an array of parabolic mirrors. These mirrors focus the light into fibres which are connected to the polychromators situated outside the torus hall as described in [48].

To summarise, the system utilises a 5 J Q-switched linearly polarised Nd:YAG laser ($\lambda = 1064$ nm) with a 20 ns pulse duration and a 20 Hz repetition rate throughout the entire JET pulse ($\approx$ 800 profiles). This custom built laser is situated in the roof laboratory above the torus hall. The laser beam is directed down into the torus hall and then horizontally into the vessel at a beam dump on the inner wall. The resulting Thomson scattered light is collected by a large diameter lens in a vertical

port at 90° to the path of the laser beam. This lens images the scattered light from the laser chord within the vessel onto an array of 150 parabolic mirrors. Each mirror couples the scattered light into a 1 mm core optical fibre. These fibres lead to a bank of 21 spectrometers, situated outside the biological shielding surrounding the torus hall.

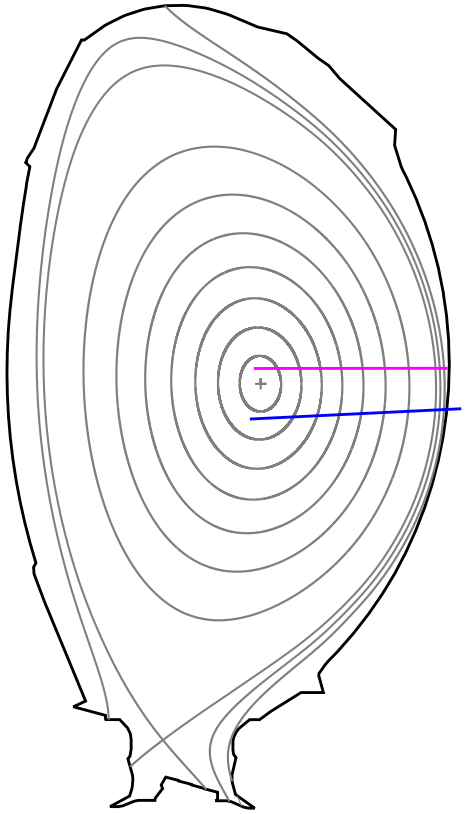

Figure 2.3: Magnetic equilibrium reconstruction for JET Pulse Number 79503 (JET-C plasma) at $t \sim 22.0s$ showing the lower (magenta) HRTS line-of-sight. The upper HRTS line-of-sight as also shown, in blue, as used for the first JET-ILW campaign.

During JET operations with the carbon wall (JET-C), after the installation of HRTS, the upper beam dump was a carbon plate only sufficient, in terms of power handling, for the LIDAR laser whereas the lower beam dump was a higher specification knife edge beam dump made from inconel steel. The HRTS system required the knife edge beam dump and therefore was configured to the lower line of sight for all JET-C plasmas. As shown in Figure 2.3, the lower line of sight (blue) for a high triangularity ELMy H-mode typically passes below the central axis. While the profiles can be mapped onto the mid-plane, it is not possible to measure the peak core density and temperature for this configuration.

The upper beam dump was upgraded to a knife edge variant during the installation of the ITER-Like-Wall (ILW) and for the subsequent campaign period, HRTS was switched to the upper line of sight. Figure 2.3 shows that the upper line of sight (magenta) is typically closer to the plasma core for a high triangularity ELMy H-

mode. However, since the first JET-ILW campaign the HRTS system has been configured back onto the lower line of sight as the view of the edge region is better resulting in higher quality edge measurements. All JET-ILW pulses discussed within this thesis are from the first JET-ILW campaign on the upper beam dump.

2.3 HRTS Polychromators

A polychromator is an optical device used to isolate different wavelength bands of light. The JET HRTS polychromators separates the Thomson scattered signal into four wavelength bands (channels) using interference filters. The signal strength of each channel is measured by an avalanche photo diode (APD). Figure 2.4 is a schematic of a JET HRTS polychromator showing the position of the optical fibre input, lenses, interference filters and APDs. The input fibre launches the Thomson scattered signal into the polychromator which is focused onto the interference filter for channel 1 by the input lens. The wavelengths selected by the channel 1 interference filter are transmitted and focused on the corresponding APD by a detector lens. The wavelengths rejected by the channel 1 interference filter are reflected onto the next interference filter where the process of selecting and rejecting a specific range of the Thomson scattered wavelength distribution is repeated for channel 2, then channel 3 and 4.

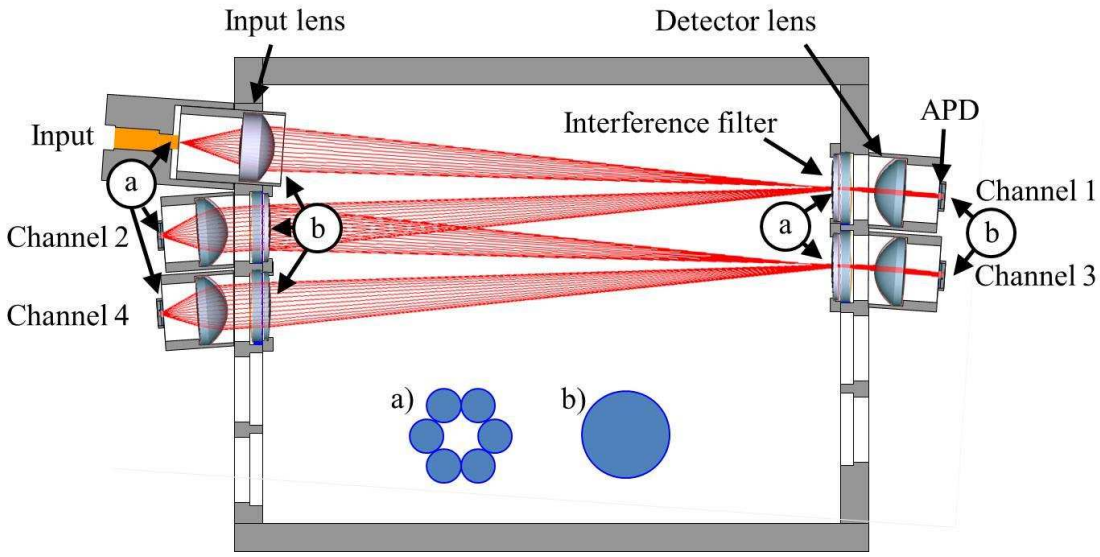

Figure 2.4: Schematic of optical box for JET HRTS polychromators showing the optical fibre input, lenses, interference filters and APDs. The blue labels demonstrate where the a) input fibre and b) input lens are imaged. The red lines represent the path of the scattered light through the polychromator using a ray tracing software package (Zeemax).

Figure 2.5 shows the spectral transmission of two different sets of interference filters in use within the JET HRTS system. The interference filters for the core polychro-

mators extend to lower wavelengths ($\approx 650 - 1064$ nm) to detect the higher energy scattered photons expected from the core. In comparison, the interference filters for edge polychromators cover a narrower range of wavelengths ($\approx 800 - 1064$ nm). The order of the channels in the edge polychromators is reversed, relative to the core polychromators, so that the channel closest to the laser wavelength is the last (in terms of striking order) to aid stray laser light rejection.

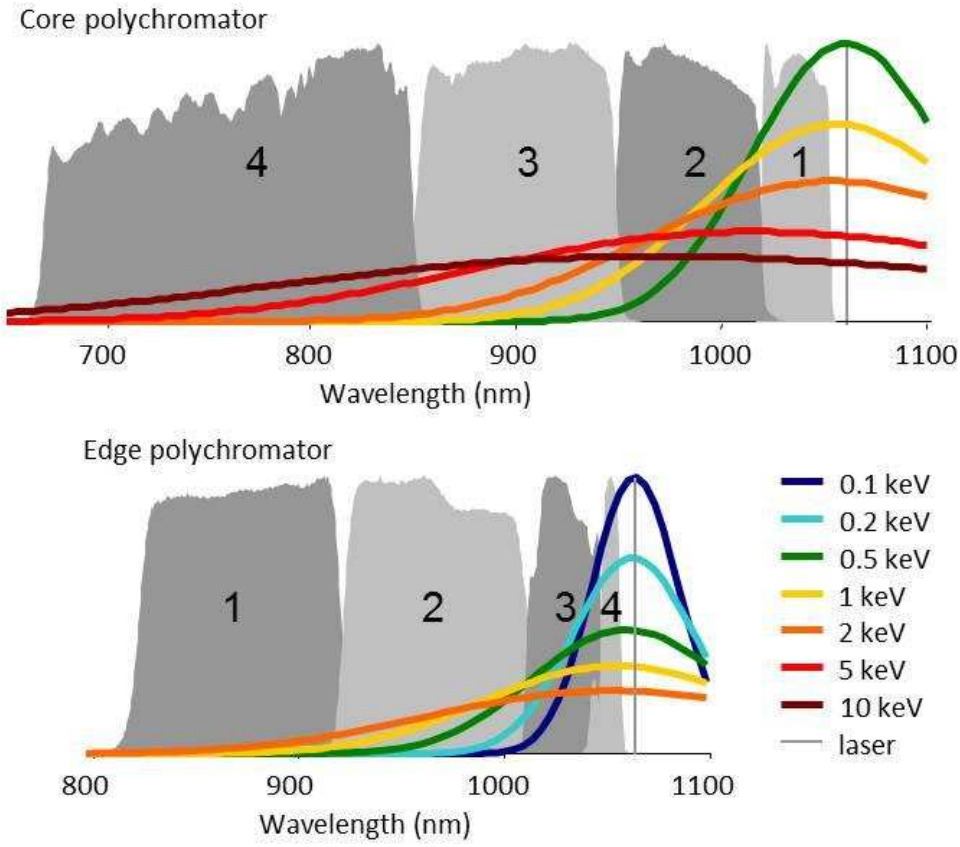

Figure 2.5: Spectral response of each HRTS polychromator channel for core and edge polychromators. The variation with temperature of the Thomson scattered spectrum for a 90° scattering angle, as given by the Selden-Naito expression [59], is overlaid. Refer to legend for more information. Image taken from [62]

A polychromator uses the response of four APDs to determine the temperature and density for a spatial point along the radial profile. In principle the absolute height of each channel indicates the density and the relative height of each channel indicates the temperature. In practice, the HRTS system uses a least squares minimisation technique to compare the channel intensities to a pre-determined table of intensities, calculated with the Selden-Naito expression. This is computationally faster than directly fitting the Selden-Naito expression; an important consideration for inter-shot analysis.

The JET HRTS system has 21 polychromators each multiplexed via optical delay lines. The delay lines stagger the arrival of the Thomson scattered light resulting

in three spatial points per polychromator, hence a maximum of 63 spatial points per profile. For a single polychromator the first spatial point has no delay line, the second has a delay line of 30 m and the third 60 m. There are six off-axis optical inputs into each polychromator, as shown in figure 2.4. Core polychromators use all six input fibres and combine the signals from two adjacent optical fibres resulting in a resolution of $\approx$ 1.6 cm. In the edge region, most of the polychromators are configured so that each spatial point corresponds to a single fibre and therefore only three of the six inputs are utilised. This results in a higher spatial resolution of 1.0 cm, desirable for measuring the steep gradients at the outboard edge.

The optical path for each spatial point in the HRTS profile is similar but not identical from the parabolic mirror array to the polychromator cubical. The delay lines are stored in a compartment within the cubical itself. The optical fibres are connected to a patchpanel at the side of the cubical via SMA connectors. The 30 m delay line is made up of a 10 m and 20 m length requiring an extra SMA connection relative to the 60 m delay line path. As a result the overall attenuation of the signal in the two delayed lines is comparable, with a loss of $\approx$ 15 % relative to the un-delayed signal.

Figure 2.6 demonstrates the layout of the patchboard. The SMA connections on the patchboard are numbered one to six from the central line outwards. The polychromators are labelled from A to U. The fibres along the parabolic mirror array are numbered from 1 to 150 although typically only 111 are used. The fibres are connected to the appropriate SMA connectors according to the delay required and the polychromator.

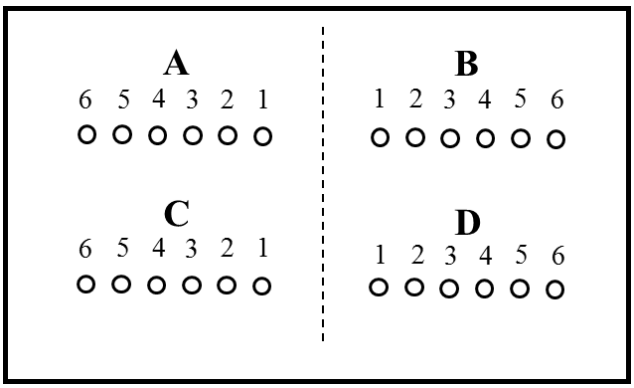

Figure 2.6: Diagram showing the layout of the patchpanel at side of polychromator cubical. Each circle represents an SMA connection. There are six SMA connections for each polychromator. The connection numbering starts at one in the middle of the patchpanel and increase to six outwards. Polychromators are labelled from A to U.

The JET HRTS polychromator optical boxes are provided on loan by General Atomics, (San Diego, CA). The amplifiers and detectors are provided by Princeton Plasma Physics Laboratories, (Princeton, NJ) [48]. The polychromators and amplifier units

can be seen in figure 2.7 (a). One amplifier unit is required per channel. Figure 2.7 (b) shows two detector and amplifier units detached from the optical box revealing the avalanche photo diode (APD). There is a lens between the amplifier unit (APD) and the polychromator referred to as the detector lens. The amplifier unit sends the signal from the APD to analogue to digital converters (ADCs) to digitise the data.

Figure 2.7: JET HRTS polychromator a) optical box and amplifier units as positioned on the shelves within the HRTS cubical and b) amplifier units with the detector lens block detached to reveal APD.

2.4 Optimising the polychromator spectral response

To accurately determine the temperature, a calibration using a monochromator is performed in order to accurately determine the spectral transmission of each channel, as shown by the grey regions on figure 2.5. Prior to the ILW campaigns an investigation showed that there was a strong variation in the polychromator response between the six optical fibre inputs and also in response to varying the input numerical aperture (NA). In particular the strong variation with input NA introduced a significant systematic uncertainty for each channel signal level and, consequently, the calculated temperature. These variations also meant a loss of signal.

A brief description of the factors contributing to the sub-optimal performance which was determined as part of this project is now provided. First, the input lens for the majority of polychromators, all except E, had a sub-optimal focal behaviour with two fuzzy 'focal' positions, see figure 2.8 (a) and (b). Figure 2.8(a) shows a fuzzy larger focus with a small halo whereas figure 2.8 (b) shows a smaller, sharper, focus with a large halo. Neither focus was ideal and results in some loss of signal. It was determined that a larger proportion of signal was lost in the large halo in Figure 2.8 (b). Figure 2.8 (c) shows the lens from polychromator E exhibits a clear sharp focus with no halo; this is the design lens.

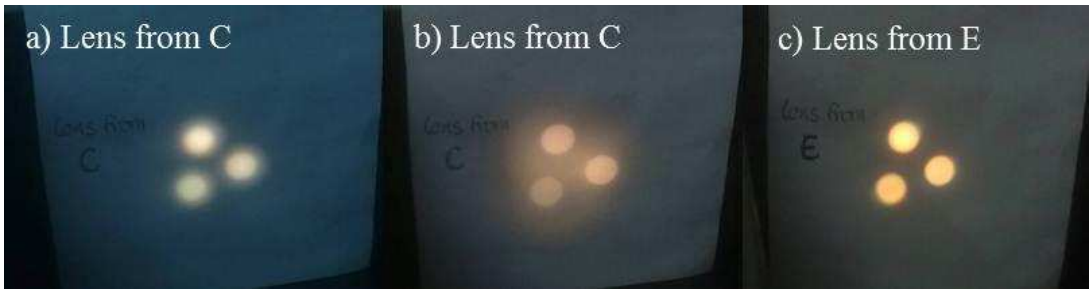

Figure 2.8: Image of fibre bundle at first interference filter position for a), b) polychromator C and c) polychromator E. Images obtained by back illuminating the polychromators with a white light source and demonstrate the focal behaviour to the input lens.

Second, the images on the interference filters were misaligned resulting in a loss of signal. An image of the input fibre bundle is incident on the interference filters for channel 1 and 3 and if this image is misaligned it results in fibre-to-fibre variation. Similarly, an image of the input lens is incident on the interference filters for channels 2 and 4 and if these images are misaligned this results in NA sensitivity.

Third, the APDs were not positioned at the focal position of the detector lens; they were too close. Consequently, there was again a loss of signal introducing a combination of fibre-to-fibre sensitivity and NA sensitivity similar to the misalignment of the polychromators.

An improvement in performance of the HRTS polychromators was obtained by first realigning the polychromator and setting the input lens focus to match Figure 2.8 (a). In addition, the position of the APDs was corrected using plastic shims to move the APD back to the focal point of the detector lens. It is important to note that any improvement had to be reversible as the polychromators are on loan. The shims were inserted between the polychromator and the detector lens block, see figure 2.9 (b). The shims have six holes in total: four at the corners for the screws, one at the centre top and the other at the centre bottom both for the guiding pins, see figure 2.9. Shims with a thickness of 1.0 mm and 1.5 mm were manufactured from high density polyethylene (HDPE).

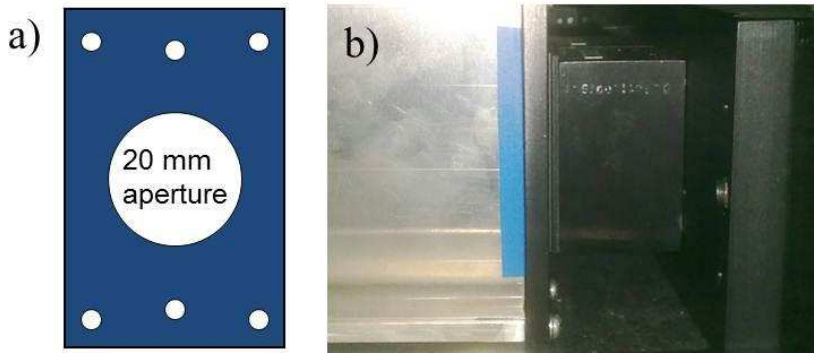

Figure 2.9: a) Plastic shim and b) photograph of shim in position between lens block and optical box

Figure 2.10 demonstrates the change in spectral response during the procedure used to realign and optimise the polychromators. First, after the realignment there is typically an improvement in optical throughput for all channels, as shown by comparing the green and red traces on Figure 2.10 (b) and (d). Second, Figure 2.10 demonstrates the iterative process to optimise the spacing between the APDs and detector lenses for channels 1 and 3. For polychromator E the initial step of this optimisation was performed simultaneously to the realignment and therefore the change in spectral response as shown by the green and red traces is a combination of both the realignment and addition of a shim. Whilst optimising channels 1 and 3, channels 2 and 4 are kept unchanged to provide a reference (red and black overlap). At least one channel is required to remain unchanged from one iteration to the next so that if the light source intensity did change the signal could be normalised.

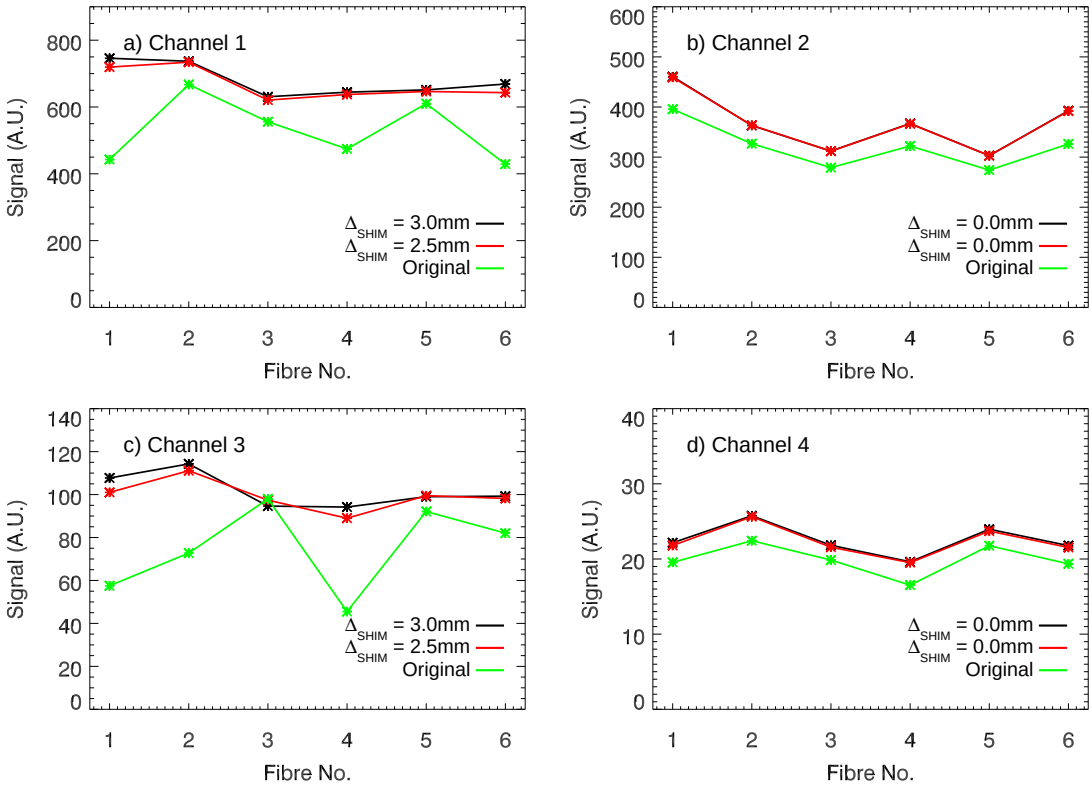

Figure 2.10: Demonstration of the optimization procedure used to correct APD position, shown for channel 1 and 3 on polychromator E for an input NA of 0.35. The response of each channel is shown in (a) to (d) as a function of input fibre. Each curve corresponds to a different stage of the realignment and optimisation procedure (see legend for details).

To install a shim to a single channel, the pre-amplifier and lens block both have to be removed and re-installed after which the measurements are repeated to reassess the polychromator throughput. There is no significant difference in the response of channel 1 and 3 with shims where the total thickness is 2.5 mm (red) and 3.0 mm (black) respectively. The configuration with the best overall throughput is chosen as

the final spacing. In this case for channel 1 and 3 the throughput is sufficiently similar that it is assumed the APD is close enough to the focal position so no further iteration is required. The addition of the shims typically resulted in a larger improvement in throughput in comparison to the realignment.

This method was repeated for all 21 polychromators. For all polychromators, channel 1 and 3 generally show the largest improvement in throughput with an average increase of the signal (over the six input fibres) of 39 % and 38 % respectively. Channel 2 and 4 show a smaller average increase of 14 % and 13 % respectively. The numerical aperture sensitivity and fibre-to-fibre variation has been minimised. It is possible to get a feeling for the impact of this optimisation by looking at the temperature profiles as shown by Figure 2.11 which, compares the average HRTS electron temperature profile (a) before and (b) after the realignment and optimisation of the polychromators as calculated using independent calibrations. The temperature for each channel has been averaged over the stationary ELMy H-mode phase of both pulses to highlight the reduction in systematic errors. Furthermore, Figure 2.11 also shows there is good agreement with the average temperature profiles as measured by the ECE system. The ECE system has repetition rate up to 5 kHz (dependent on diagnostic setup) compared to 20Hz for the HRTS system. The ECE profiles closest in time to the HRTS profiles are selected for the averaged ECE profile so as to use the same number of profiles. Note that due to these large systematic fluctuations in the HRTS electron temperature profile before the realignment of the polychromators, an additional cross-calibration was implemented by the HRTS responsible officer. Cross calibration to ECE data was used to better determine the channel-to-channel sensitivities of the polychromator. This calibration method is unaffected by the NA sensitivity.

The realignment and optimisation of the polychromators was performed in parallel to the installation of the new JET ITER-Like-Wall (between November 2009 and May 2011). The HRTS electron temperature profiles for all JET pulses with the carbon wall (e.g. Figure 2.11(a)) are calibrated via cross comparison to ECE data on a few dedicated JET pulses. Whereas the temperature profiles for JET pulses with the ITER-Like-Wall (e.g. Figure 2.11(b)) are independently calibrated.

Further to the reduction in systematic errors, on comparison of the JET HRTS averaged electron profiles in Figure 2.11 it can be seen that there is a change in the radial extent of the profiles. This is due to a combination of a change in the HRTS line of sight (see Figure 2.3) and a change in the fibre configuration to improve the resolution at the plasma edge. The upper line of sight used for the JET-ILW plasma (Figure 2.11 (b)) extends further into the core relative to the carbon wall lower line of sight used for the JET-C plasma (Figure 2.11 (a)). However, this is not reflected in the profiles as the spatial points in the core region were sacrificed

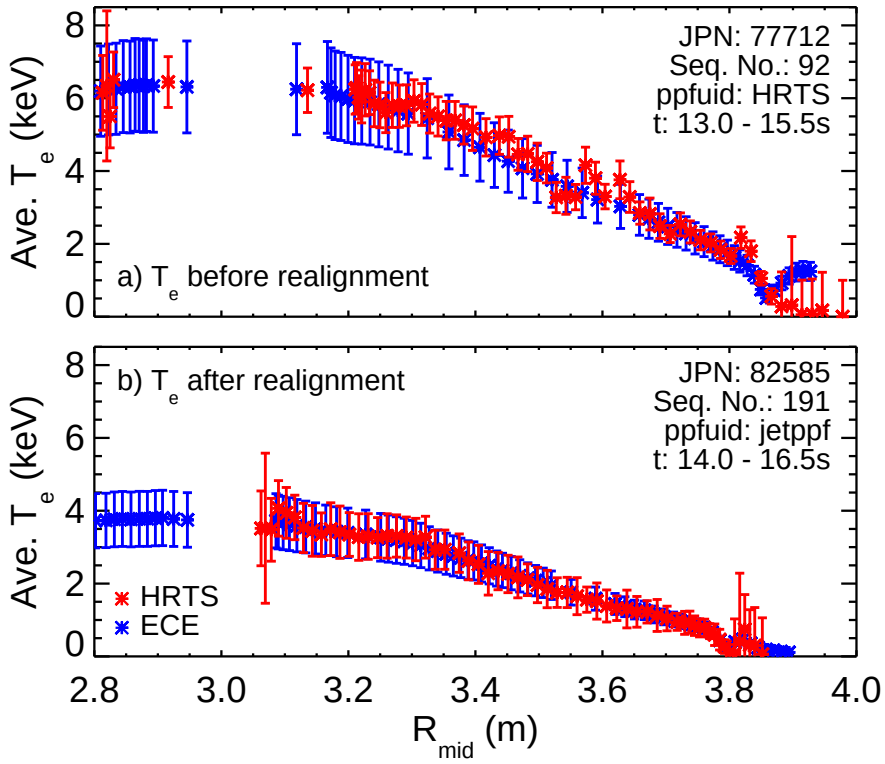

Figure 2.11: Comparison of HRTS (red) electron temperature profile (a) before and (b) after realignment and optimisation of the polychromators as calculated using independent calibrations. (a) JPN: 77712, JET pulse with the carbon wall (JET-C) and (b) JPN: 82585, JET pulse with ITER-Like-Wall (JET-ILW). The averaged ECE (blue) electron temperature profiles are overlaid for comparison. It is noted that the overall reduction in electron temperature between the two pulses is due to a variation in plasma performance.

to improved the spatial resolution at the plasma edge (spatial points visibly closer together between $R \approx 3.7 - 3.85$ for Figure 2.11 (b)). The improvement in JET HRTS spatial resolution at the plasma edge was performed before the start of the final JET-C experimental campaign (between JPN 78157 and 78281) so there also do exist JET-C pulses with the better JET HRTS spatial resolution. Furthermore, the decision to change optics that led to the improvement in spatial resolution was a consequence of a study to calculate the JET HRTS instrument function [63] as discussed in detail in the next chapter.

2.5 Summary

The JET High Resolution Thomson Scattering (HRTS) system provides electron temperature and density profiles across a large part of the plasma radius. It was found that the HRTS polychromators under-performed due to a loss of signal, fibre-to-fibre sensitivity and input numerical aperture sensitivity. This compromised the

ability to provide independently calibrated temperature profiles. However, this has been resolved by realigning the polychromators and installing plastic shims to correct the position of the APDs relative the the focal position of the detector lens. A comparison of averaged temperature profiles before and after realignment and optimisation demonstrate that systematic fluctuations have been reduced. All HRTS electron temperature data for JET pulses after the installation of the new ITER-Like-Wall are independently calibrated (instead of cross calibrated to ECE profiles).

To summarise the significant changes in the JET HRTS system setup since installation in 2004, first the edge spatial resolution was improved before the last JET-C campaign (early 2009) as a consequence of a study to calculate the JET HRTS instrument function [63] (see Chapter 3). Second, during the installation of the ILW (late 2009-2011) the realignment of the polychromators and installation of plastic shims was performed to reduce the systematic errors in independently calibrated temperature measurements. Furthermore, for the first JET-ILW campaign the HRTS system was moved from the lower to the upper line of sight to measure closer to the plasma core. However for subsequent JET-ILW campaigns the HRTS system reverted back to the lower line of sight as there is less vignetting.

Chapter 3

Pedestal fitting

3.1 Motivation

Quantifying the H-mode pedestal structure, the width, gradient and height, has been the focus of numerous studies addressing the physical processes governing the plasma edge. Fitting a modified hyperbolic tangent (mtanh) function to radial kinetic profiles is a common technique used on many machines such as JET [37, 64], AUG [33, 65], DIII-D [36, 66], Alcator C-Mod [67, 68], MAST [39, 69–71], NSTX [40] and JT-60 [72]. The mtanh function is given by [67, 73, 74],

$$\begin{aligned} mtanh\left(r' : \vec{a}\right) &= \frac{a_2 - a_4}{2}\left[\left(\frac{\left(1 + a_3 r'\right) e^{r'} - e^{-r'}}{e^{r'} + e^{-r'}}\right) + 1\right] + a_4 \\ r' &= \frac{a_0 - r}{2a_1} \end{aligned} \tag{3.1}$$

where $\vec{a}$ is a vector containing all the mtanh parameters. These parameters can be related to the pedestal, where a_0 is the pedestal position along the abscissa, a_1 is the pedestal width, a_2 is the pedestal height, a_3 is the core slope and a_4 is the Scrape-Off-Layer (SOL) offset.

This chapter is organised as follows: Section 3.2 gives an introduction to the JET mtanh pedestal fitting routine as developed by L. Frassinetti and M. Beurskens; Section 3.3 describes how the HRTS instrument function is calculated [63]; Section 3.4 summarises the deconvolution technique and corresponding systematic error [73]; Section 3.5 describes new work detailing how, with knowledge of the HRTS system, a synthetic profile can be generated. The synthetic HRTS-like profiles are used in Section 3.6 to evaluate, for the first time, the systematic error introduced to pedestal width caused by ELM synchronising the profiles and assuming an error of the profile

position correction. Section 3.7 describes the procedure adopted to perform an mtanh fit using the JET mtanh pedestal fitting routine.

3.2 The JET mtanh pedestal fitting routine

JET Type I ELMy H-modes typically have an ELM period ranging from $25 - 150$ ms. For example consider the JET-C database detailed in [75]. The HRTS laser fires every 50 ms therefore on average there are one to two profiles per ELM period. Furthermore HRTS electron temperature and density profiles typically have two to three spatial points defining the pedestal region as can be seen in Figure 3.1. Figure 3.1 shows an example of an HRTS electron (a) temperature and (b) density profile during the stationary Type I ELMy H-mode phase of JET Pulse No. 79498 at $t = 20.176$ s. Figure 3.1 focuses on the pedestal region where $R = 3.7 - 3.9$ m). The profiles are representative of the pre-ELM state of the plasma, see Figure 3.2.

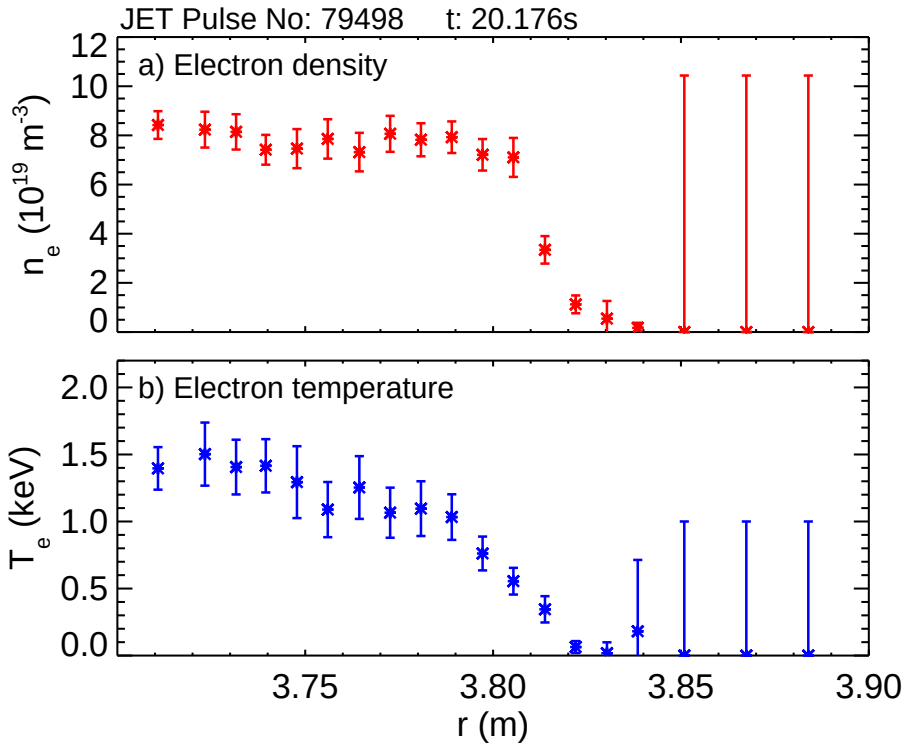

Figure 3.1: Example of single HRTS electron (a) temperature and (b) density profiles for pedestal region ($R = 3.7 - 3.9$ m) towards the end of an ELM cycle (pre-ELM state). JET Pulse No. 79498 at t=20.176s during stationary ELMy H-mode phase of the pulse.

To maximise the number of points defining the pedestal, profiles from the same phase of the ELM cycle are overlapped (referred to as ELM synchronisation) and the mtanh function is fitted to a composite profile. Typically on JET, HRTS profiles within the last 70-99 % of the ELM cycle, (from a window spanning the stationary phase of a pulse, typically ≈ 2 s), are used to determine pre-ELM fits [37, 63]. For

example, Figure 3.2 demonstrates the timings of the HRTS profiles relative to the last 70-99 % of the ELM cycle for JPN 79498 between $t = 19.8$ to 20.4 s. To account for the dynamic variation of the plasma position during the pulse when overlaying the selected profiles the radial position of each profile is adjusted according to the edge of the plasma (the last closed flux surface) as determined using the JET fast equilibrium reconstruction with a time resolution of ≈ 0.4 ms.

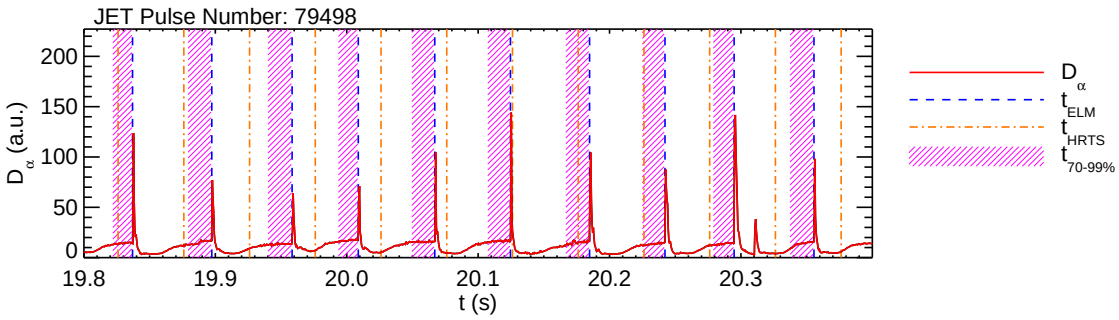

Figure 3.2: Evolution of deuterium alpha emission (red) during a stationary ELMy H-mode phase for JET pulse number 79498. The timing of the HRTS laser is shown in orange toegether with the start of the ELMs in blue and the pre-ELM region 70-99 % (magenta).

3.3 The JET HRTS instrument function

The JET mtanh pedestal fitting routine determines a deconvolved pedestal fit using a forward deconvolution technique and incorporating the numerically calculated instrument function [63]. The JET HRTS instrument function is determined from the geometrical layout of the laser beam, collection optics and the orientation of the magnetic flux surfaces in the pedestal region. This section summarises the key results from [63] incorporated into the JET mtanh pedestal fitting routine.

Figure 3.3 demonstrates the geometrical layout of the HRTS hardware relevant for the instrument function calculation. The HRTS laser beam is focused into the vessel along a near horizontal line-of-sight by a spherical and cylindrical lens. The Thomson scattered light is captured by collection optics positioned at $\approx 90^{o}$ to laser beam on top of vessel. The scattered light entering each optical fibre corresponds to a scattering volume within the plasma. The scattering volume is where the laser beam intersects the collection optics cone of view corresponding to a single spatial point, as shown in figure 3.4. The HRTS laser beam intensity profile has two peaks as the total beam is made up of two beams stacked vertically one on top of the other, separated by ≈ 4.0 cm, as shown in figure 3.4 and [63].

The JET instrument function is calculated by evaluating multiple line integrals of the laser intensity along the magnetic field lines within the scattering volume for a single

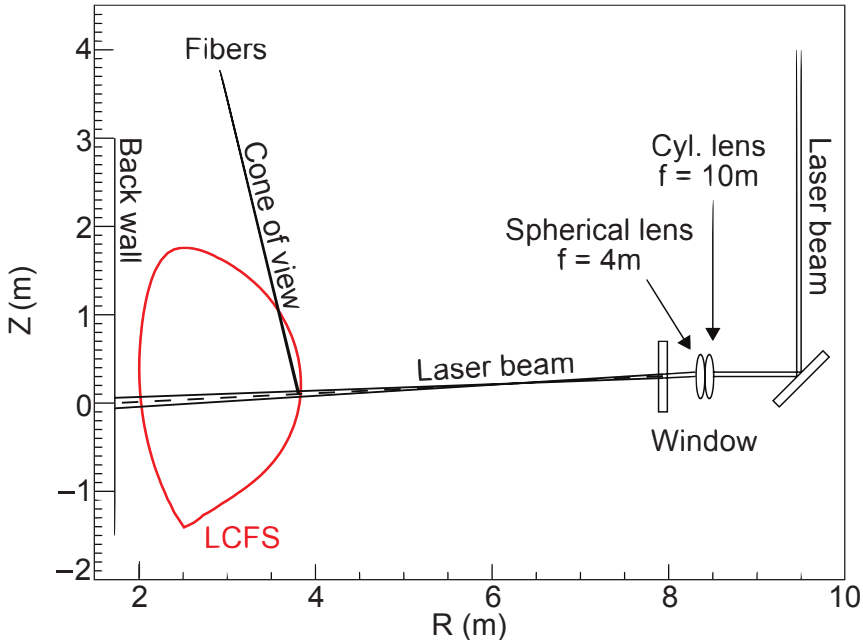

Figure 3.3: Geometrical layout of the relevant HRTS hardware with respect to the instrument function. The spherical and cylindrical lenses used to focus the laser beam into the vessel are positioned at $R \approx 8.5$ m. The HRTS laser beam passes through the JET plasma between $R \approx 2.0-4.0$ m. The collection optics are on top of the vessel. Taken from [63].

spatial point, see Figure 3.4. Each line integral results in an intensity corresponding to a position along a radial chord perpendicular to the magnetic field lines. The resulting profile of intensity versus radial position is the instrument function, see Figure 3.5.

Figure 3.5 shows the instrument function for three JET pulses, for (a) the original system configuration, where the Full Width Half Maximum (FWHM) is 22 mm. Towards the end of the last JET campaign with the carbon wall the HRTS system configuration was modified to decrease the FWHM. First, the laser beam was reduced in vertical width by using a cylindrical lens with a shorter focal length and second, the resolution in the pedestal region was increased by only using a single fibre for each spatial point where both changes reduce the scattering volume. Consequently, the instrument function FWHM decreased to 11 mm, see Figure 3.5 (b).

Figure 3.5 (c) shows the instrument function FWHM remains at 11 mm after the installation of the ILW even though the HRTS system configuration was changed from the lower to upper line-of-sight (discussed in Chapter 2, see Figure 2.3) altering the laser beam angle of intersection with the collection optics cone of view and B-field. However, Figure 3.5 shows this change did alter the shape of the instrument function; most notably at the peak. The HRTS instrument function was not affected by the optimisation and realignment of the polychromators (see Chapter 2).

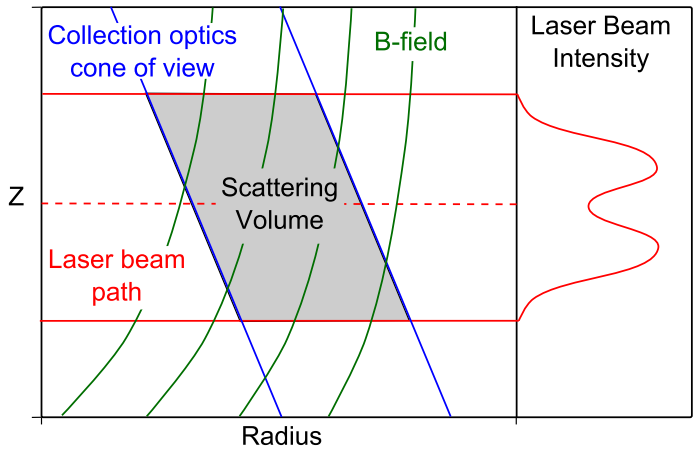

Figure 3.4: Schematic of two vertically stacked laser beams (red) intersecting collection optics cone of view (blue) defining scattering volume (grey) in edge region of JET plasma. Orientation of magnetic field lines (green) in relation to scattering volume. Adapted from [63].

The HRTS instrument function varies with increasing major radius due to a relative change in the angle of intersection of the collection optics cone of view with the laser beam and the angle at which the magnetic field intersects the scattering volume. Towards the centre of the plasma, the collection cone is perpendicular to the laser beam and the magnetic field lines are more vertical. Consequently, the FWHM is $6 - 10$ mm smaller in the core relative to the edge for double and single fibre configurations respectively. The variation of the instrument function is negligible in the pedestal region for both HRTS system configurations [63]. Nevertheless the HRTS instrument function utilised within the pedestal fitting routine is taken at $R = 3.8$ m towards the plasma edge.

The error on the FWHM for both HRTS configurations is $\approx \pm 1$ mm, as determined assessing the uncertainties in the laser beam height, collection optics cone of view and angle of the field lines intersecting the scattering volume, [63].

3.4 Determining a deconvolved 'mtanh' pedestal fit

Deconvolution is the process of calculating the underlying profile with the knowledge of the measured profile and the instrument function. Deconvolution is only necessary when the feature of interest has a radial scale length less than or equivalent to the instrument function FWHM. The JET HRTS temperature and density profiles are not deconvolved due to the potential of introducing artifacts. Instead, the JET pedestal fitting code determines a deconvolved mtanh fit using a forward convolution technique requiring knowledge of only the profiles and the instrument function. This section summarises the implementation of the deconvolution technique incor-

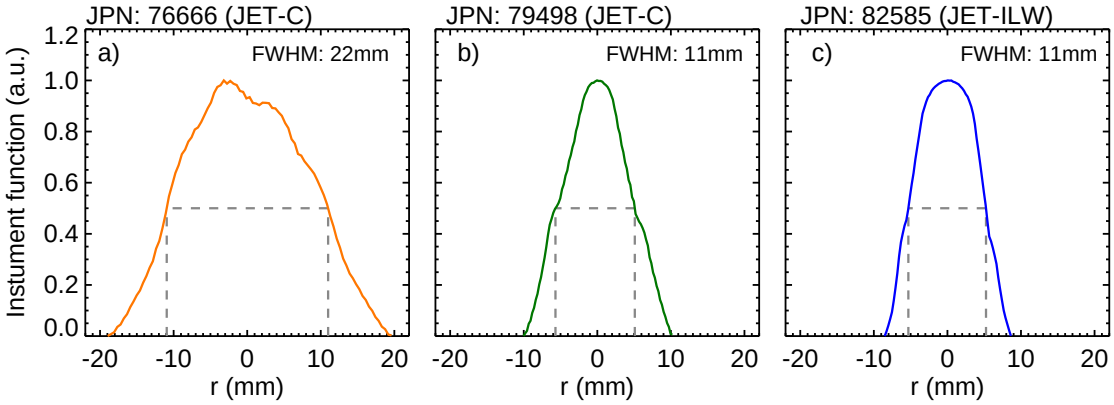

Figure 3.5: The JET HRTS instrument function, as taken at $R = 3.8$ m in the pedestal region, for carbon wall plasmas (a) before and (b) after the optimisation of the laser beam focal length and edge spatial resolution. (c) The HRTS instrument function for the first JET campaign with the ITER-Like-Wall. The Full Width Half Maximum (FWHM) decreases from (a) 22 mm to (b), (c) 11 mm after the optimisation of the laser focal length and edge spatial resolution. The difference in the instrument function shape from (b) to (c) is due to shifting from the lower to upper line-of-sight.

porated into the JET mtanh pedestal fitting routine as originally documented in [63, 73].

First consider a radial density profile as measured by the JET HRTS system. The measured density profile ($n_{e,measured}(r)$) is a convolution of the underlying profile ($n_{e,underlying}(r)$) and the instrument function of the diagnostic ($I_{HRTS}(r)$). Figure 3.1 shows the density pedestal width is approximately between $\approx 20-40$ mm which is equivalent to the HRTS instrument function and hence deconvolution is necessary [63, 73].

A forward deconvolution method is performed by assuming a model for the underlying profile, which, in the case of the density pedestal, is an mtanh function ($n_{e,mtanh}(r)$). The model profile is convolved with the instrument function ($I_{HRTS}(r)$) in an attempt to reproduce the measured profile ($n_{e,measured}(r)$). This process is repeated adjusting the model, the *mtanh* parameters, to minimise the squared difference between the model ($n_{e,mtanh}(r)$) and measured ($n_{e,measured}(r)$) profile; commonly referred to as a least squares fit [76]. This process is summarised below [73],

$$n_{e,mtanh}(r) \otimes I_{HRTS}(r) \leftrightarrow n_{e,measured}(r) \tag{3.2}$$

where $\leftrightarrow$ represents the iterative minimisation process. Once the minimisation process is complete it is assumed that the model, $n_{e,mtanh}$, (within error) is representative of the underlying profile ($n_{e,underlying}(r)$).

$$n_{e,mtanh}(r) \sim n_{e,underlying}(r) \tag{3.3}$$

This forward deconvolution method is referred to as classical deconvolution by [63, 73] where it is described in detail. Furthermore [73] shows classical deconvolution works well for density profiles however this is not the case for the temperature profiles in the pedestal region where there are steep gradients. This discrepancy is due to the variation of density across the scattering volume skewing the width of the resulting scattered spectrum such that the temperature profile is weighted radially outwards. Equation 3.2 describes the forward deconvolution method for the density profile can be modified to account for the variation in density across the scattering volume for the temperature profile as,

$$\frac{n_{e,mtanh}(r)T_{e,mtanh}(r) \otimes I_{HRTS}(r)}{n_{e,mtanh}(r) \otimes I_{HRTS}(r)} \leftrightarrow T_{e,measured}(r) \tag{3.4}$$

This modified deconvolution method for the temperature is referred to as the weighted deconvolution by [63, 73].

To summarise, the mtanh JET pedestal fitting routine provides a deconvolved fit of the density using the classic deconvolution technique and the temperature using the weighted deconvolution technique [63, 73]. Figure 3.6 shows an example fit to a pre-ELM (70-99 %) electron density and temperature profiles. The errors associated with the mtanh parameters are representative of the statistical uncertainty in the fit. However, systematic errors also contribute to the uncertainty in the mtanh fit as now discussed.

The systematic error introduced to the pedestal width by the deconvolution techniques has been quantified by [63, 73]. In the current HRTS system configuration (where the instrument function has a FWHM $\approx$ 11 mm), this systematic error, in most cases, is below the statistical error. The systematic error on the temperature pedestal width due to the weighted deconvolution technique is more noticeable and this increases to 10 % when the pedestal width approaches the FWHM.

Another source of systematic error when performing this fit arises from ELM synchronisation; more specifically the inaccuracies in the process of identifying the HRTS profiles from the same region of the ELM cycle and overlaying the profiles by adjusting the radial position relative to the plasma edge. This is to account for small scale fluctuations in the plasma position during the ELM cycle so that the steep gradient region of the profiles accurately overlay. The uncertainty in the profile position, and thus a misalignment when overlaying the profiles, will introduce a systematic error into the pedestal fit. The following two sections describe new work detailing an approach used to quantify the systematic error introduced to the pedestal width.

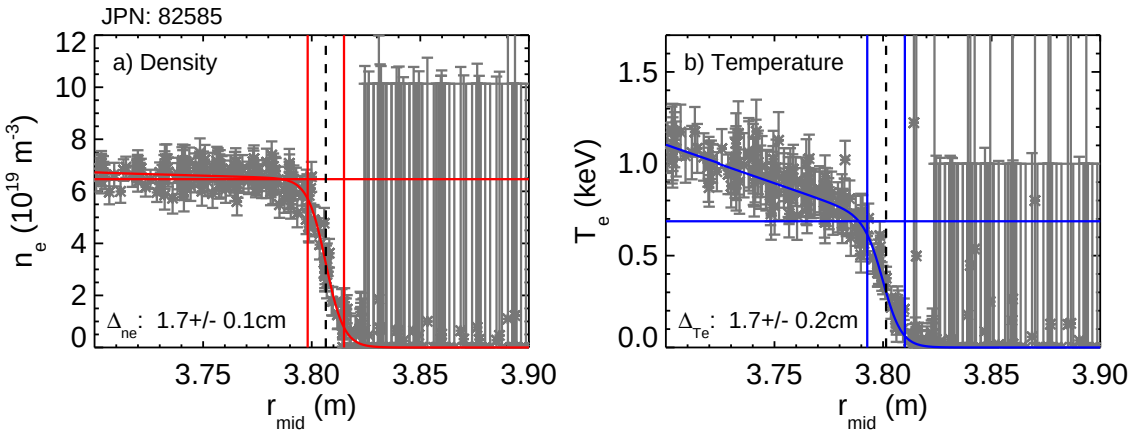

Figure 3.6: Example of (a) classic deconvolved mtanh pedestal fit to electron density(red) and (b) weighted deconvolved mtanh pedestal fit to electron temperature (blue) for JET Pulse Number 82585. HRTS profiles (grey) selected from stationary ELMing phase of pulse between 14.1 − 16.7 s. The pedestal position is given by the black dashed vertical line, the pedestal width by the solid vertical lines and the pedestal height by the horizontal solid line.

First, the process of generating synthetic HRTS profiles from known underlying temperature and density profiles is described. Second, the results from replicating the fitting process for synthetic profiles to quantify the deviation of the mtanh fit from the underlying profile is presented. The intention is, for the first time, to assess the validity of the ELM synchronisation technique.

3.5 Generating a synthetic HRTS profile

The advantage of using synthetic HRTS profiles when quantifying the systematic error due to ELM synchronisation is that the underlying profile is known. This section details how knowledge of the HRTS system can be used to generate profiles with noise and error bars representative of real profiles.

3.5.1 Number of Thomson scattered photons

The number of Thomson scattered photons collected by the HRTS system is given by [77, 78],

$$N_{ph,scat} = n_e \cdot \frac{E_{laser}}{h\nu_0} \cdot \frac{d\sigma_{TS}}{d\Omega} \cdot \Delta L \cdot \Delta\Omega \cdot T_{sys} \cdot T_{N,vig}(r) \cdot EQE, \tag{3.5}$$

where n_e is the electron density, E_{laser} is the laser energy (5 J), $h\nu_0$ is the energy of a photon (1.9×10^{-19} J), $\frac{E_{laser}}{h\nu_0}$ is the total number of photons in a signal laser pulse,

ΔL is the scattering length (12 mm or 20 mm depending on whether single or double fibre configuration is used [63]), $\Delta\Omega$ is the solid angle of collection optics ($\sim 2.2\times10^{-3}$ sr), $d\sigma_{TS}/d\Omega$ is Thomson scattering cross section ($= r_0^2 \approx 8.0 \times 10^{-30}$ m^2), T_{sys} is the system transmission, $T_{N,vig}(r)$ is the normalised spatial variation in transmission due to the system vignetting and EQE is the effective quantum efficiency of the avalanche photo diodes (APDs) within the polychromators.

The system transmission can be broken down into seven components;

$$T_{sys} = T_{laser} \cdot T_{port} \cdot T_{window} \cdot T_{lens} \cdot T_{mirrors} \cdot T_{fibres} \cdot T_{filters}, \tag{3.6}$$

where T_{laser} is the transmission of the laser, typically 0.65. $T_{port} \approx 0.70$ is the transmission due to the port having a finite diameter and depth. The scattered photons pass through a double window as they exit the vessel with a transmission of $T_{window} \approx 0.96^4$. The collection lens has an anti-reflection coating resulting in an average transmission (T_{lens}) ≈ 0.99 from $670 - 1100$ nm as measured for light normally incident on the lens. Three aluminum mirrors, with an individual transmission of $T_{mirror} \approx 0.85$, direct the collected scattered signal into the optical fibres. The total mirror transmission is $T_{mirrors} \approx 0.85^3$. The transmission of the single core optical fibres is, on average, $T_{fibres} \approx 0.6$. The transmission of the filters is $T_{filters} \approx 0.80$. The wavelength averaged total system transmission is $T_{sys} \approx 0.19$. The normalised spatially dependent vignetting transmission coefficient $T_{N,vig}(r)$ is evaluated via performing a Raman calibration. This calibration is described in the following section.

3.5.2 Raman calibration

As summarised in [78], Raman scattering is the inelastic scattering of electromagnetic radiation off a molecule resulting in scattered light at discrete wavelengths about the incident laser wavelength (λ_L). The change in scattered photon wavelength and energy corresponds to a change in the rotational (or vibrational) state of the scattering molecule. A molecule that loses energy results in a higher energy, lower wavelength, scattered photon with corresponding Raman lines below λ_L, referred to as anti-Stokes lines. Raman lines above λ_L are referred to as Stokes lines and correspond to the scattered photons having relinquished energy to the scattering molecule.

The spectral channels of the HRTS polychromators are designed to detect blue-shifted wavelengths and, consequently, the system can only detect anti-Stokes lines. At the temperatures at which this calibration is performed ($300 - 500$ K), signal is seen only in the few channels closest to the laser wavelength. Figure 3.7 shows

the Raman spectra in relation to (a) channel 4 for an edge HRTS polychromator and (b) channel 1 for a core HRTS polychromator. Channel 4 for an edge polychromator is closer to the laser wavelength in comparison to channel 1 for a core polychromator and therefore it collects more of the anti-Stokes scattered Raman signal. Consequently, the measured Raman signal is larger for an edge polychromator despite the spectral width of channel 4 for an edge polychromator being narrower in comparison to channel 1 from a core polychromator and the smaller scattering length for an edge polychromator ($\approx$ 12 mm in comparison to $\approx$ 20 mm for a core polychromator). Furthermore, the Raman signal for edge polychromators is further reduced for the spatial points effected by vignetting.

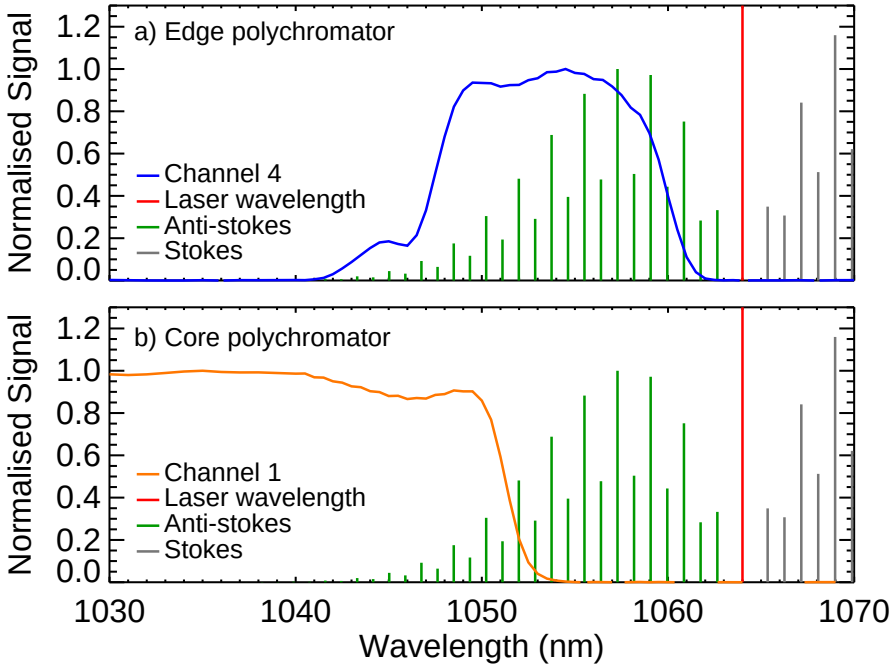

Figure 3.7: Raman stokes and antistokes spectra about the HRTS laser wavelength (λ_L = 1064 nm) together with the spectral response of (a) channel 4 for an edge HRTS polychromator and (b) channel 1 for a core polychromator. The raman spectra are determined for Nitrogen gas and assuming a vessel temperature of 294 K.

Typically on JET the vessel is filled with Nitrogen gas ranging from 0 to 400 mbar at room temperature ($\approx$ 20 °C) for a Raman calibration. The gas pressure is constant throughout the entire vessel resulting in the same number of Raman scattered photons per scattering volume across the HRTS line-of-sight. The difference in measured Raman intensity across the HRTS line of sight thus quantifies the differences in coupling and transmission for each light path [79].

Figure 3.8 shows the normalised spatially dependent transmission coefficient $T_{N,vig}(r)$ for the upper and lower line of sight mapped onto the magnetic mid-plane. $T_{N,vig}(r)$ is curved for both lines of sight with a maximum at $R_{mid} \approx 3.35$ m due to vignetting of the collection optics field of view by the vertical port. The vignetting is most

prominent at the plasma edge where the vertical port significantly obstructs the collection optics field of view. Comparing the upper and lower transmission curves it can be seen that fewer spatial points are impaired for the lower line of sight.

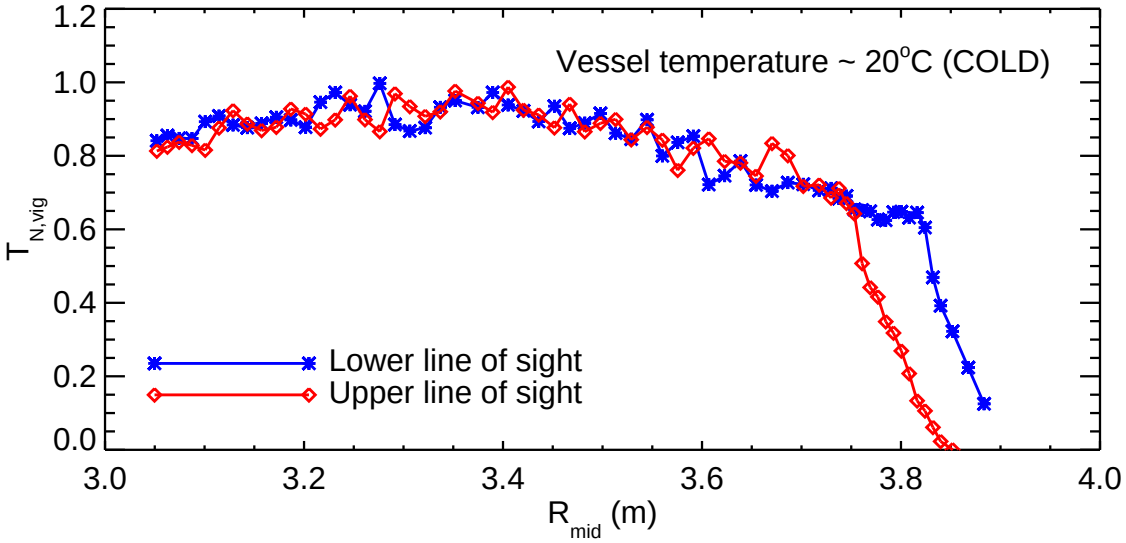

Figure 3.8: Transmission curve for the HRTS upper line of sight (red) and lower line of sight (blue) both mapped onto the magnetic mid plane. Mapping performed using magnetic equilibrium reconstruction for JET Pulse Number 82814 during stationary ELMy H-mode phase. $T_{N,vig}$ determined by variation of Raman scattering intensity across HRTS line of sight when the vessel is filled with Nitrogen at 200 mBar. The vessel temperature is at room temperature at $\approx$ 20 °C (cold).

$T_{N,vig}(r)$, as shown in Figure 3.8, is typically measured when the JET vessel is at room temperature, $\approx$ 20 °C (cold). However, during operations, the vessel is held between $\approx$ 200 – 300 °C (hot) [79]. The expansion of the vessel at operational temperatures accounts for the notable reduction in vignetting ($\approx$ 10 % increase in $T_{N,vig}$) at the plasma edge, as shown in Figure 3.9, in which a hot and cold Raman curve for the lower line of sight are shown. Consequently, it can be seen that the Raman, as measured in a cold vessel (as shown in Figure 3.8) is a over estimate of the signal loss at the edge. Hot Raman measurements only exist for the lower line of sight (this is a relatively new measurement for JET) and therefore the cold vignetting curves are used when generating synthetic profiles.

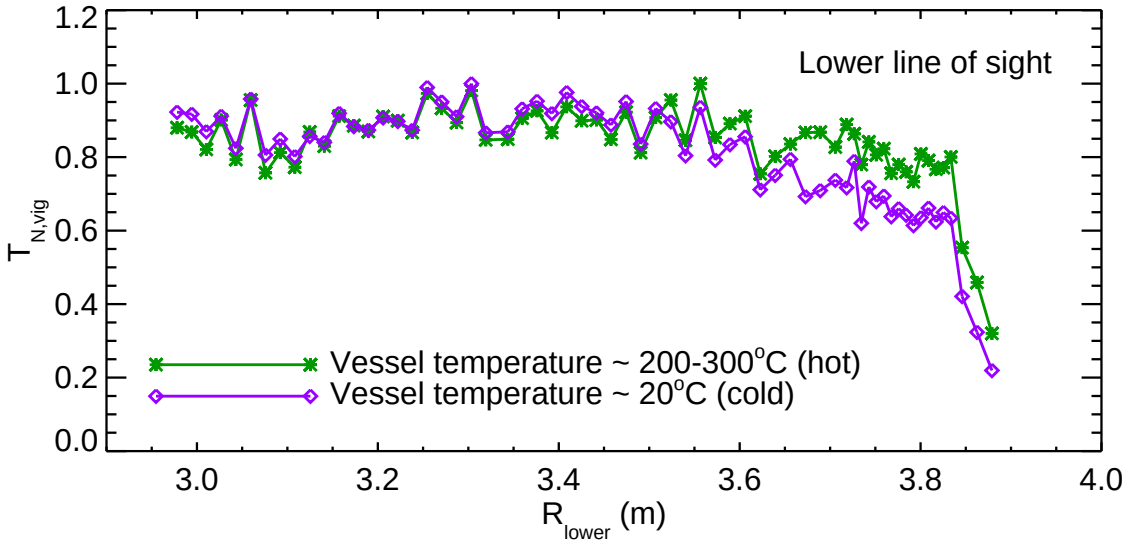

Figure 3.9: Transmission curve along the lower line of sight at a vessel temperature of ≈ 20 °C (purple) and $\approx 200 - 300$ °C (green). Determined by variation of Raman scattering intensity across HRTS line of sight when the vessel is filled with Nitrogen at 200 mBar.

At the top of the pedestal ($R_{mid} \approx 3.77$ m for JET Pulse Number 82814), the cold Raman data gives $T_{N,vig} \approx 0.65$. Evaluating Equation 3.5 results in ≈ 840 Thomson scattered photons per 10^{19} electrons m^{-3}, assuming a scattering length of 0.012 m and EQE ≈ 0.2. The expected number of Thomson scattered photons can be verified by further consideration of the signal-to-noise ratio of the Raman calibration data, as detailed in the following.

Figure 3.10 shows the Raman signal intensity as measured by HRTS polychromator C throughout a Raman calibration JET pulse. The HRTS laser starts firing before $t = 0$ s as during normal plasma operation this is required to obtain stray light measurements before the formation of a plasma. The Raman signal is proportional to the gas pressure, as can be seen by the data in 3.10. The data in Figure 3.10 also demonstrates that there is a variation in Raman intensity across the 800 laser pulses. The Raman calibration data for a range of pressures is summarised by Figure 3.11 which shows the average Raman signal as a function of nitrogen gas pressure where the ordinate error bar is the standard deviation of the Raman signal. Figure 3.11 furthermore demonstrates the linearity (increase in signal with pressure) incorporating multiple Raman JET pulses. The difference in the slope of the dashed lines shown in Figure 3.11 is due to a variation in system throughput as a result of independent Raman calibrations at the beginning of each JET campaign.

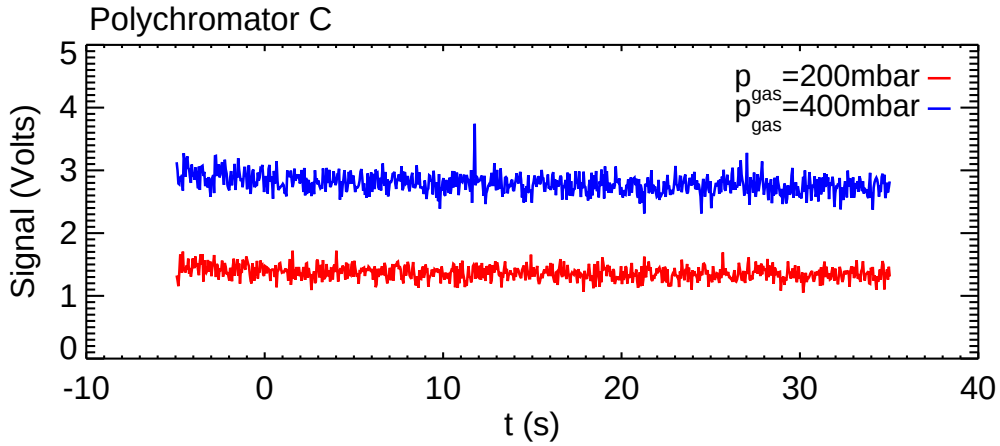

Figure 3.10: Raman signal over 800 laser pulses as measured by channel 4 of HRTS polychromator C when the JET vessel is filled with nitrogen gas at 200 mbar (red) and 400 mbar (blue) at $T_{Vessel} \approx 20$ °C.

Assuming a Poisson distribution ($\sigma = \sqrt{N}$), the average Raman signal ($\overline{S}$) and corresponding standard deviation (σ_S) can be used to estimate the number of Raman scattered photons ($N_{Ram,meas}$) as,

$$\frac{\sqrt{N_{Ram,meas}}}{N_{Ram,meas}} = \frac{\sigma_S}{\overline{S}} \tag{3.7}$$

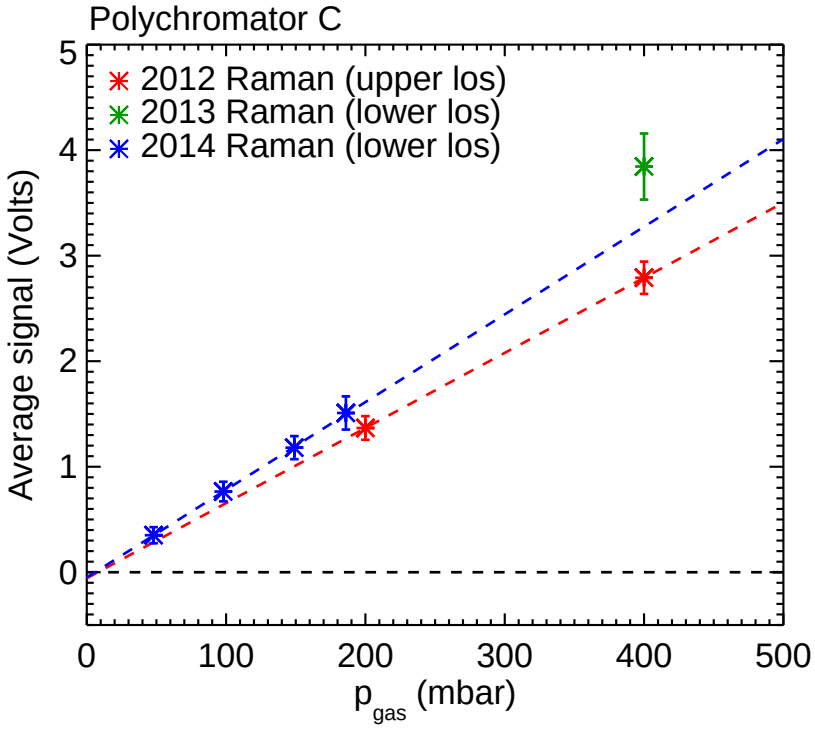

Figure 3.11: Average Raman signal as a function of nitrogen gas pressure in the JET vessel for Raman calibration pulses from 2012 on the upper line of sight (red), 2013 on the lower line of sight (green) and 2014 on the lower line of sight (blue).

It is important to note that the values of $\overline{S}$ and σ_S will be inaccurate when the Raman signal is affected by stray light. Consequently, when evaluating $\overline{S}$ and σ_S, the Raman signals suffering from stray light are excluded. This estimate of $N_{Ram,meas}$ can be compared to the number of expected Raman scattered photons ($N_{Ram,calc}$) as calculated using a similar expression to Equation 3.5 and given by;

$$N_{Ram,calc} = \frac{p_{gas}}{k_B T_{vessel}} \cdot \frac{E_{laser}}{h\nu_0} \cdot \frac{d\sigma_{Raman}}{d\Omega} \cdot \Delta L \cdot \Delta\Omega \cdot T_{sys} \cdot T_{N,vig}(r) \cdot EQE, \qquad (3.8)$$

where p_{gas} is the nitrogen gas pressure (18600 Pa $\equiv$ 186 mbar), k_B is Boltzmann's constant (1.38×10^{-23} Pam^{3}K^{-1}), T_{vessel} is the temperature of the vessel ($\approx$ 294 K), $d\sigma_{Raman}/d\Omega$ is the Raman cross section (of the order 1×10^{-35} m^2) and the remaining parameters are as previously defined for Equation 3.5.

Figure 3.12(a) compares the calculated (expected) number of Raman scattered photons ($N_{Ram,calc}$) with the measured Raman scattered photons ($N_{Ram,meas}$) for each HRTS spatial point. The point-to-point variation in the calculated number of photons is due to evaluating $d\sigma_{Raman}/d\Omega$ for each spatial point using the corresponding spectral response and the variation in $T_{N,vig}$, as determined from Raman calibration data for the lower line of sight. As previously described, the step changes in the number of

calculated Raman scattered photons ($N_{Ram,calc}$), as shown by Figure 3.12(a), is due to the changes in scattering length ($l_{scat} = 12$ mm for single fibre configuration and $l_{scat} = 20$ mm for double fibre configuration), differences in the overlap between the spectral channel closest to the laser wavelength with the Raman spectra (see Figure 3.7) and the vignetting curve.

Figures 3.12 (a) and (b) demonstrate there is good agreement between the measured and calculated number of photons with a difference of $\approx \times 1.7$ relating to the crude way that the transmission was estimated. Figure 3.12 (a) also shows, in general, there is good relative agreement in the number of Raman scattered photons across the line of sight (apart from for polychromators affected by stray light such as polychromator G corresponding to $R_{mid} \approx 3.68 - 3.72$). This good relative agreement implies that it is correct to assume a Poisson distribution.

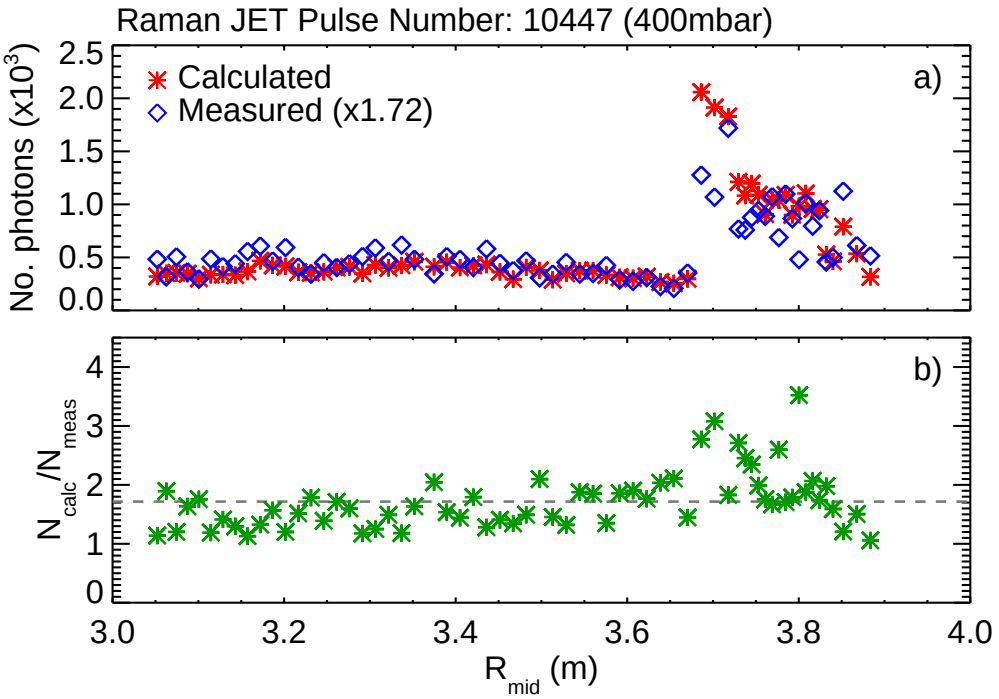

Figure 3.12: (a) Comparison of the calculated number of Raman scattered photons ($N_{Ram,calc}$) to the measured number of Raman scattered photons ($N_{Ram,meas}$) for each HRTS spatial point. The number of photons is shown as a function of radial position, mapped onto the midplane. (b) shows the ratio of the calculated to measured Raman scatter photons ($N_{Ram,calc}/N_{Ram,meas}$).

To summarise, the measured number of Raman scattered photons is a factor of ≈ 1.7 less than expected. This factor is used to correct the number of calculated Thomson scattered photons when generating a synthetic profile.

3.5.3 Simulating an HRTS polychromator

An HRTS polychromator separates out the total number of scattered photons into four wavelength bands (channels). The response of each channel is dependent on the spectral transmission ($\phi(\lambda)$), the scattered spectrum as given by the Selden-Naito expression ($S(\lambda, \theta, T_e)$) and the quantum efficiency of the photodiodes (assume EQE constant for all channels at ≈ 0.2). The Selden-Naito expression is normalised to unity [80],

$$S_N(\lambda, \theta, T_e) = \int_0^\infty \frac{S(\lambda, \theta, T_e)}{\lambda_0} d\lambda = 1, \tag{3.9}$$

where $S_N(\lambda, \theta, T_e)$ is the normalised Selden-Naito expression. The number of photons detected by each channel (i) is given by integrating the product of the spectral transmission of each polychromator channel ($\phi_i(\lambda)$) and the scattered spectrum, as given by

$$N_{ph,dect,chn=i} = N_{ph,scat} \int \phi_i(\lambda) \frac{S_N(\lambda, \theta, T_e)}{\lambda_0} d\lambda \tag{3.10}$$

The spectral response for each fibre and polychromator is used when determining the electron temperature and density from HRTS measurements as there is some variation fibre-to-fibre and polychromator-to-polychromator even though the optical components are nominally identical (due to differences in alignment and high sensitivity of filters to angle of incidence). However, when generating synthetic profiles a single spectral response is assumed for all edge and core polychromators, for simplicity, as shown by Figure 3.13(a) and (b). The edge polychromators channels are closer to the laser wavelength and consequently, the highest wavelength channel is more susceptible to laser stray light. This analysis focuses on the pedestal region and therefore the examples below utilise the spectral response of an edge polychromator.

Figure 3.14 shows the scattered spectrum and the product of the scattered spectrum with the edge polychromator spectral response, as shown in Figure 3.13(a), for a range of electron temperatures (T_e = 0.5, 1.0, 3.0 and 10.0 keV). Figure 3.14 demonstrates the change in relative intensities of the polychromator channels as the temperature increases. At higher temperatures the intensity of lower wavelength channels increases due to the blue shift of the scattered spectrum relative to the laser wavelength.

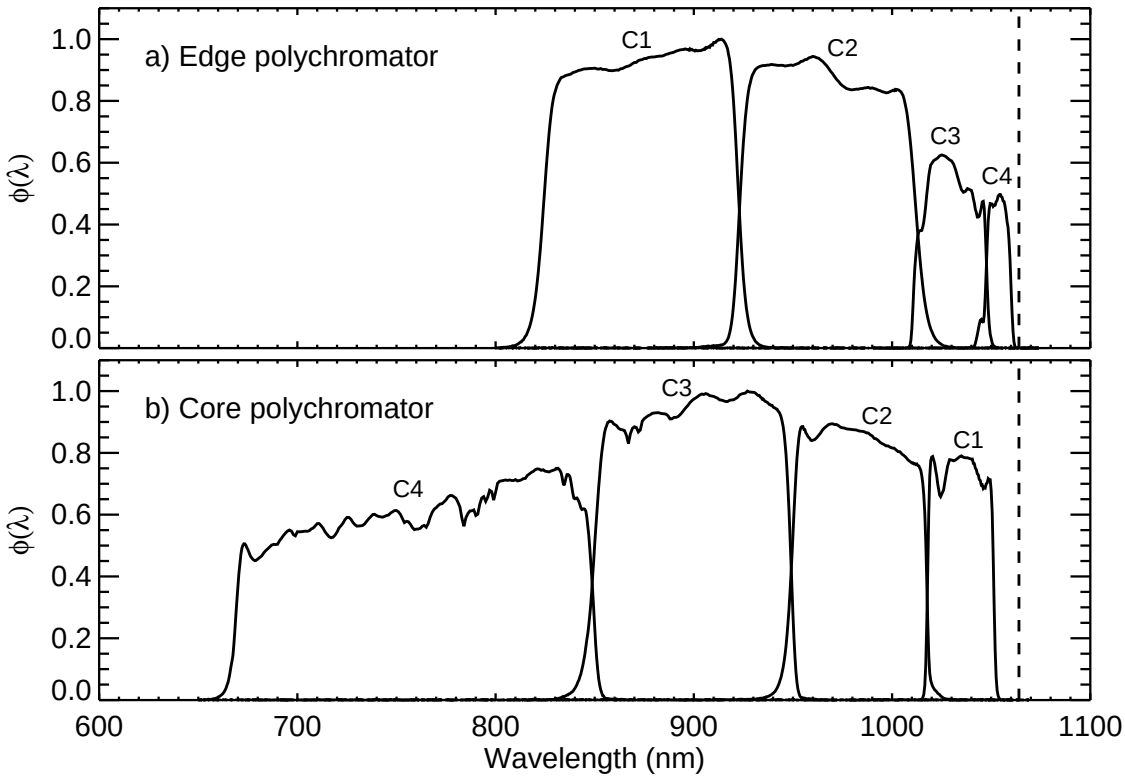

Figure 3.13: The normalised spectral response of (a) an edge polychromator (Polychromator C, Fibre 2) and (b) a core polychromator (Polychromator P, Fibre 2) relative to the laser wavelength at 1064 nm (black dashed line). Channel 1 (C1) is closest to the laser wavelength for the core polychromator but is furthest away from the laser wavelength for the edge polychromator.

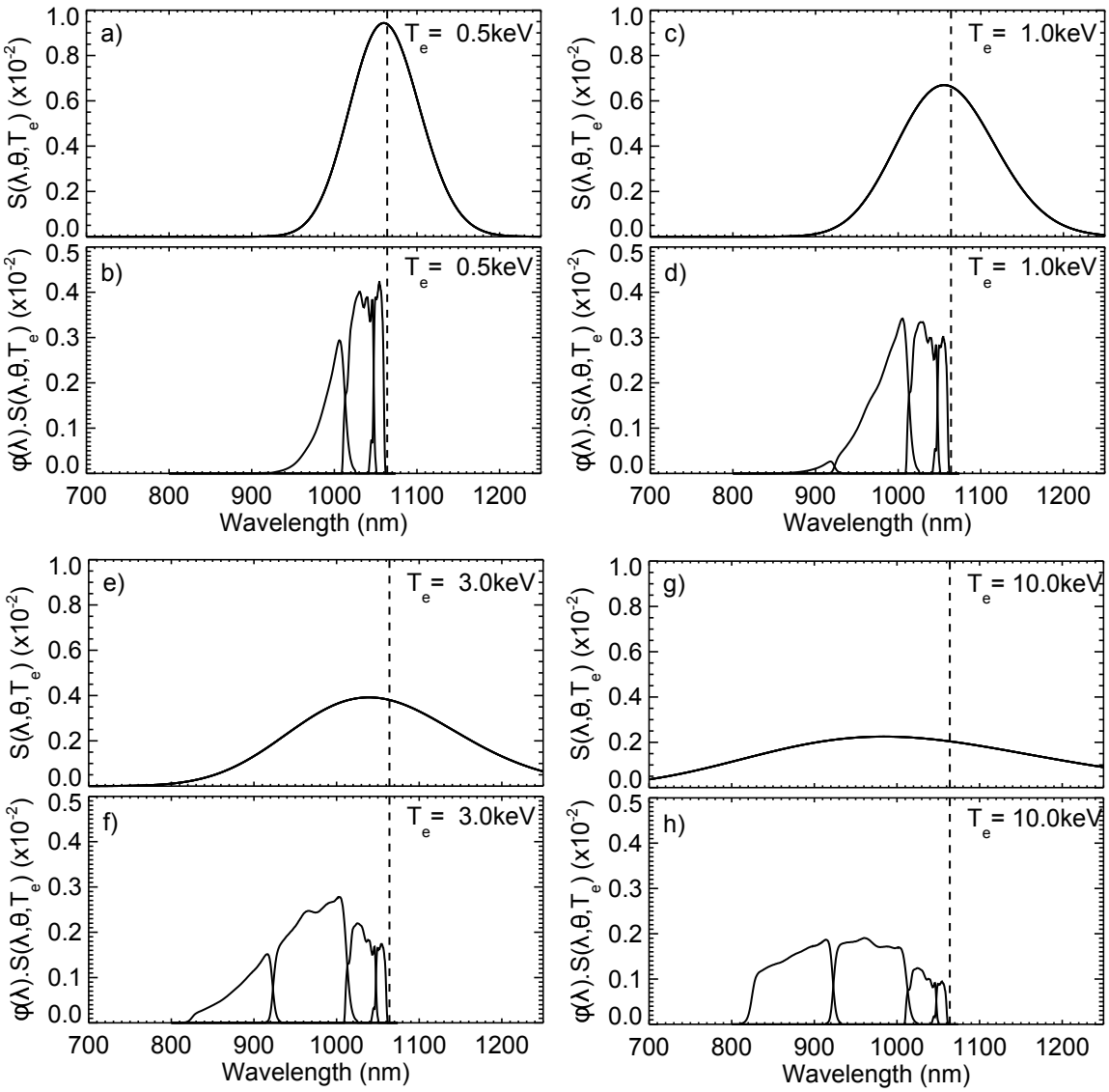

Figure 3.14: Scattered Thomson spectrum ($S(\lambda, \theta, T_e)$) for (a) $T_e = 0.5$ keV, (c) $T_e = 1.0$ keV, (e) $T_e = 3.0$ keV and (g) $T_e = 10.0$ keV. Product of scattered spectrum and the spectral response for an edge polychromator ($\phi(\lambda) \cdot S(\lambda, \theta, T_e)$) for (b) $T_e = 0.5$ keV, (d) $T_e = 1.0$ keV, (f) $T_e = 3.0$ keV and (h) $T_e = 10.0$ keV where the laser wavelength is 1064 nm (black dashed line).

The number of detected Thomson scattered photons ($N_{ph,dect,chn=i}$) can be expressed as the product of electron density (n_e) and the temperature dependent response of the polychromators ($F_i(T_e)$) given by,

$$N_{ph,dect,chn=i} = n_e \cdot F_i(T_e) \tag{3.11}$$

More specifically, $F_i(T_e)$ details the relative intensity of each channel for a specific temperature and independent of density. Instead of fitting the Selden-Naito expression directly to the signal, the HRTS system has a pre-determined table of $F_i(T_e)$ values for a range of electron temperatures. A least squares minimisation technique is used to determine the electron temperature, as shown in Equation 3.12.

$$\begin{aligned}\chi^2 &= \sum_{i=1-4} w_i[N_{ph,dect,chn=i} - n_e \cdot F_i(T_e)]^2 \\ &= \sum_{i=1-4} w_i[N_{ph,dect,chn=i} - \frac{\sum_{i=1-4} w_i N_{ph,dect,chn=i} F_i}{\sum_{i=1-4} w_i F_i^2} \cdot F_i(T_e)]^2,\end{aligned} \tag{3.12}$$

where $w_i = (\sigma_{N_{ph,dect,chn=i}}/N_{ph,dect,chn=i})^{-2}$ is a weighting factor that results in the least squares minimisation being dominated by the more reliable channels with a relatively low error. The electron density is determined by evaluating Equation 3.13 for F_i values corresponding to the minimum χ^2; the sum of the squared differences.

$$n_e = \frac{\sum_{i=1-4} w_i N_{ph,dect,chn=i} F_i(T_{e,min(\chi^2)})}{\sum_{i=1-4} w_i F_i(T_{e,min(\chi^2)})^2} \tag{3.13}$$

The measured HRTS profiles have a vertical scatter in temperature and density due to the error on the number of photons detected by each channel. More specifically, these errors correspond to a set of F_i values deviating from the underlying F_i (temperature and density). The contributions to the total error in number of detected photons is given by [80],

$$\sigma^2_{N,tot} = \sigma^2_{Poisson} + \sigma^2_{background} + \sigma^2_{amplifier} \tag{3.14}$$

where $\sigma_{Poisson} \sim \sqrt{N}$ is the Poisson error. In general, the Poisson distribution quantifies the probability of a number of events, such as photon counts for a given mean. $\sigma_{background}$ is the uncertainly introduced by the background plasma light and $\sigma_{amplifier}$ is the noise introduced by the electronic components. In the scrape off layer region, where there is typically minimal Thomson scattered photons detected, the contribution of $\sigma^2_{Poisson}$ is small in comparison to $\sigma^2_{background}+\sigma^2_{amplifier}$. To accurately

replicate a JET HRTS profile beyond the foot of the pedestal, an order of magnitude estimate for $\sigma^2_{background} + \sigma^2_{amplifier}$ is required. This is obtained by considering the measured HRTS signal intensity for a single laser pulse.

Figure 3.15 shows the measured signal intensity for polychromator C, for JET Pulse Number 82585 at $t = 15.72$ s. The acquisition time of 500 ns captures three Thomson scattering troughs as each polychromator measures three spatial points using delay lines to stagger the signal. For this particular pulse the first Thomson scattering trough at ≈ 90 ns corresponds to a spatial point at the top of the pedestal where $n_e \sim 5.2 \times 10^{19}$ m^{-3} and $T_e \approx 0.5$ keV. At this temperature Figure 3.15 (a) shows that there is no appreciable Thomson scattering signal in Channel 1 as expected from Figure 3.14 (a) and (b).

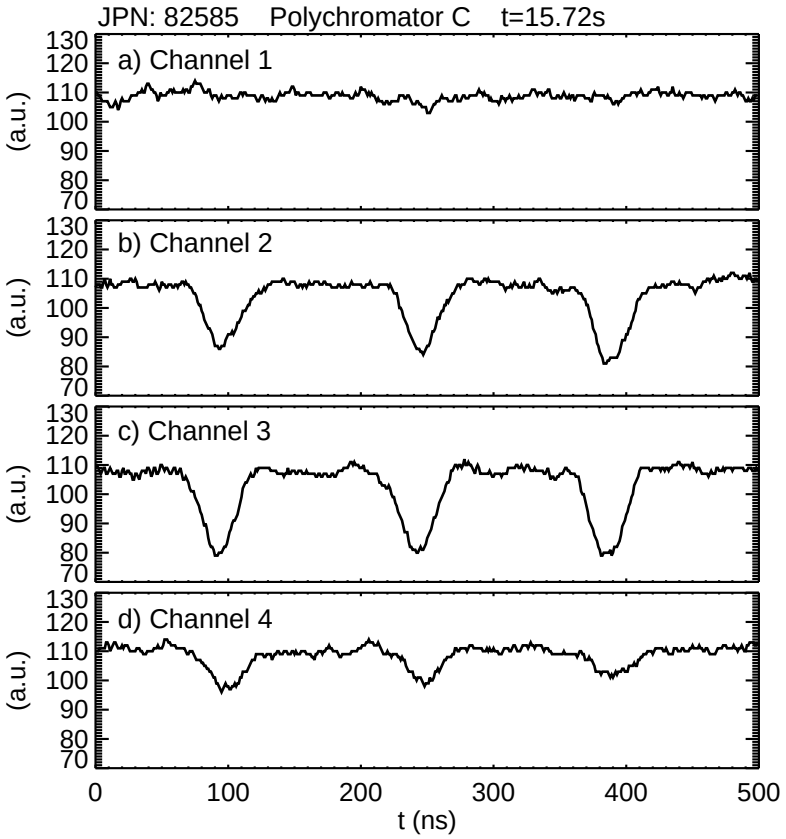

Figure 3.15: Measured signal for JET Pulse Number 82585 for channels 1-4 of polychromator C at $t = 15.72$ s. Recall that each polychromator measures the signal from three adjacent spatial points due to optical multiplexing by means of delay line fibres.

The magnitude of the noise between the Thomson scattering troughs is a combination of measurements of background plasma light and amplifier noise. To convert the signals into units of photons, a baseline and stray light subtraction is performed centring the signal about zero. The JET HRTS system baseline light level is determined by averaging the 99 laser pulses corresponding to 99 acquisitions before the plasma is formed. Since the electron temperature and density is already known

from the measured profile, the number of expected photons in each channel can be determined. This is then used to scale the peak of the first Thomson scattering signal as shown by Figure 3.16.

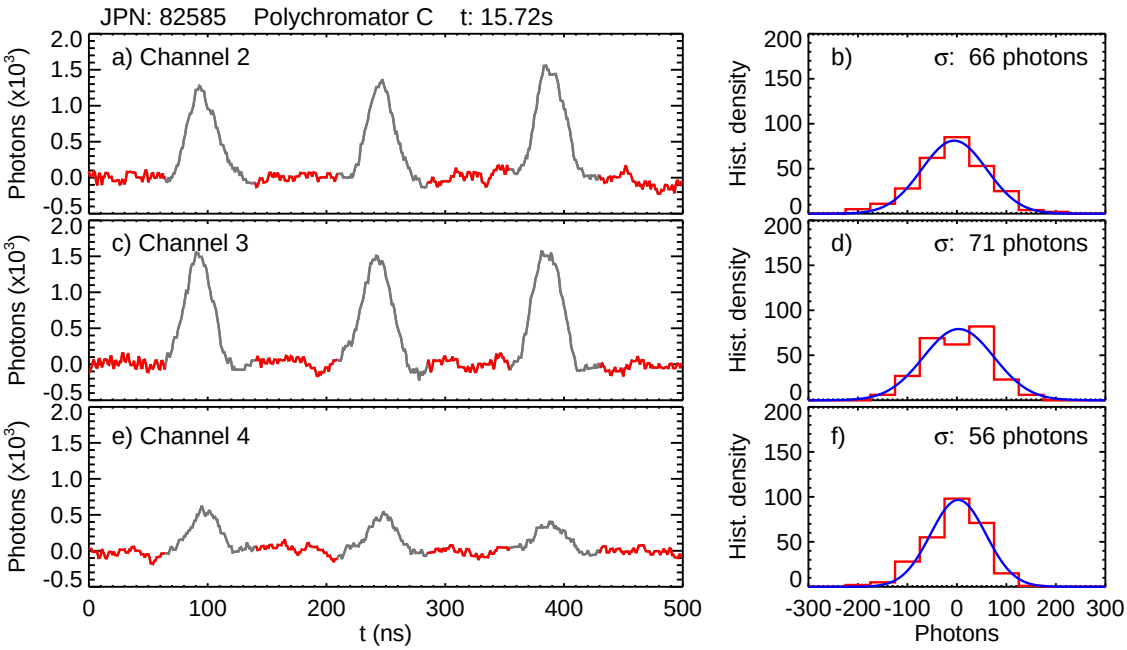

Figure 3.16: Measured signal converted into units of photons for JET Pulse Number 82585 for polychromator C channel (a) 2, (c) 3 and (e) 4 at $t = 15.72$ s. The number of photons is calculated for each channel at $n_e \approx 5.2 \times 10^{19}$ m^{-3} and $T_e \approx 0.5 \times 10^3$ keV using $T_{N,vig} \approx 0.65$ from the cold lower line-of-sight vignetting curve. The histogram shows the signal between the Thomson scattering peaks (red) for channel (b) 2, (d) 3, (f) 4 and the corresponding Gaussian fit (blue). Channel 1 is not shown as a negligible number photons are expected in this channel.

Figure 3.16 also shows histograms of the signal between the Thomson scattering peaks and a corresponding Gaussian fit. The standard deviation gives an estimate for $\sigma^2_{background} + \sigma^2_{amplifier}$, ranging from 55 photons for channel 4 up to 71 photons for channel 2. It is important to note that this method is not valid for channel 1 as a negligible number of photons are expected in this channel. It is expected that $\sigma^2_{background} + \sigma^2_{amplifier}$ is larger for a wider spectral channel as more background light is collected. Furthermore, core polychromators have a larger scattering volume and so will also collect more background light, resulting in a larger uncertainty. $\sigma^2_{background} + \sigma^2_{amplifier}$ is fixed at 70 for all single fibre polychromators and 140 for all double fibre polychromators.

Figure 3.17 (a) shows an example of the χ^2 minimisation for a vignetted spatial point near the plasma edge at the top of the pedestal, where the underlying temperature and density is $n_e \approx 5.2 \times 10^{19}$ m^{-3} and $T_e \sim 0.5 \times 10^3$ keV and $T_{N,vig} \approx 0.65$. The underlying signal (green), as inferred from the underlying temperature and density,

with the addition of random errors is termed the synthetic signal (red). The additional error is sampled from a normal distribution of width $\sigma_{N,tot}$. Performing the χ^2 minimistaion results in the fitted signal (blue) in Figure 3.17 corresponding to a temperature and density of $n_{e,fit} = 5.29 \pm 0.23 \times 10^{19}$ m^{-3} and $T_{e,fit} = 0.47 \pm 0.03$ keV. A Monte Carlo technique is used to determine the error on the temperature and density by repeating this minimisation process 100 times for different synthetic signals, as varied according to the random error, and taking the standard deviation.

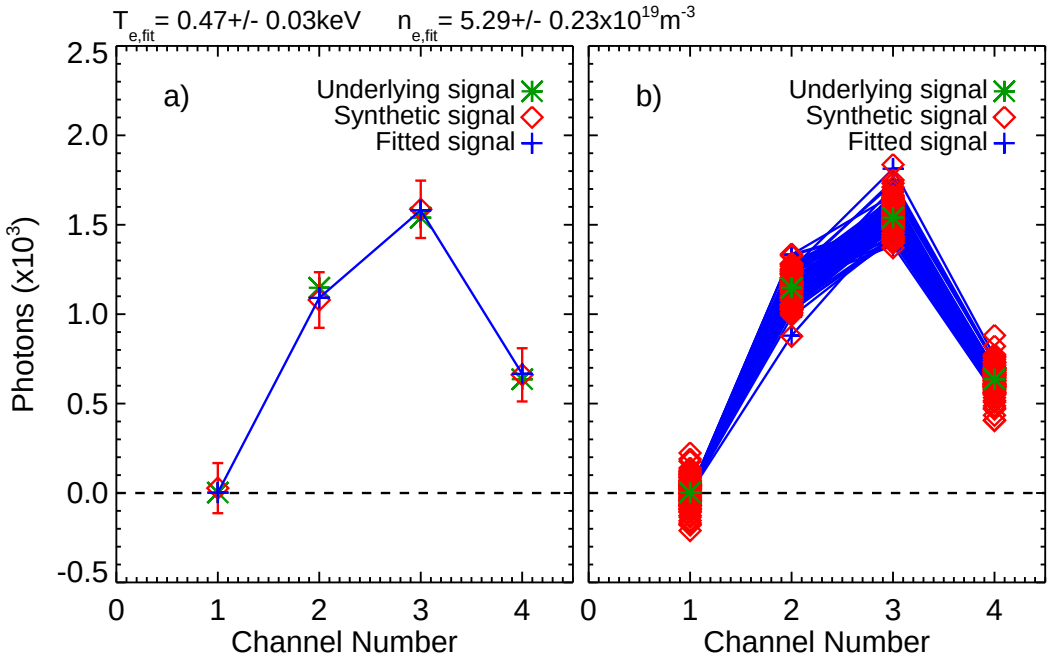

Figure 3.17: (a) Example of an underlying signal (green), an underlying signal with noise (also termed synthetic signal) (red) and fitted signal (blue) for an underlying electron density and temperature of $n_e \sim 5.2 \times 10^{19}$ m^{-3} and $T_e \sim 0.5 \times 10^3$ keV where $T_{N,vig} \sim 0.65$. The resulting fitted electron density and temperature being $n_{e,fit} = 5.29 \pm 0.23 \times 10^{19}$ m^{-3} and $T_{e,fit} = 0.47 \pm 0.03$ keV. (b) The error is determined performing the fit 100 times with different synthetic signals.

3.5.4 Example synthetic HRTS profiles

Figure 3.18 and Figure 3.19 show an example of a radial synthetic profiles along the magnetic mid-plane. The pre-ELM pedestal fit for JET Pulse Number 82585 is taken as the underlying profile. The cold transmission curve for both the upper and lower line-of-sight mapped onto the magnetic mid plane (as shown in Figure 3.8) are incorporated into the calculation of the number of photons for the profiles shown in Figures 3.18 and 3.19 respectively. Both the upper and lower line-of-sight are considered to demonstrate the difference in vignetting has on the synthetic profiles. Figure 3.18 and Figure 3.19 (a) and (c) show the entire extent of the synthetic profile, while (b) and (d) focus on the pedestal region.

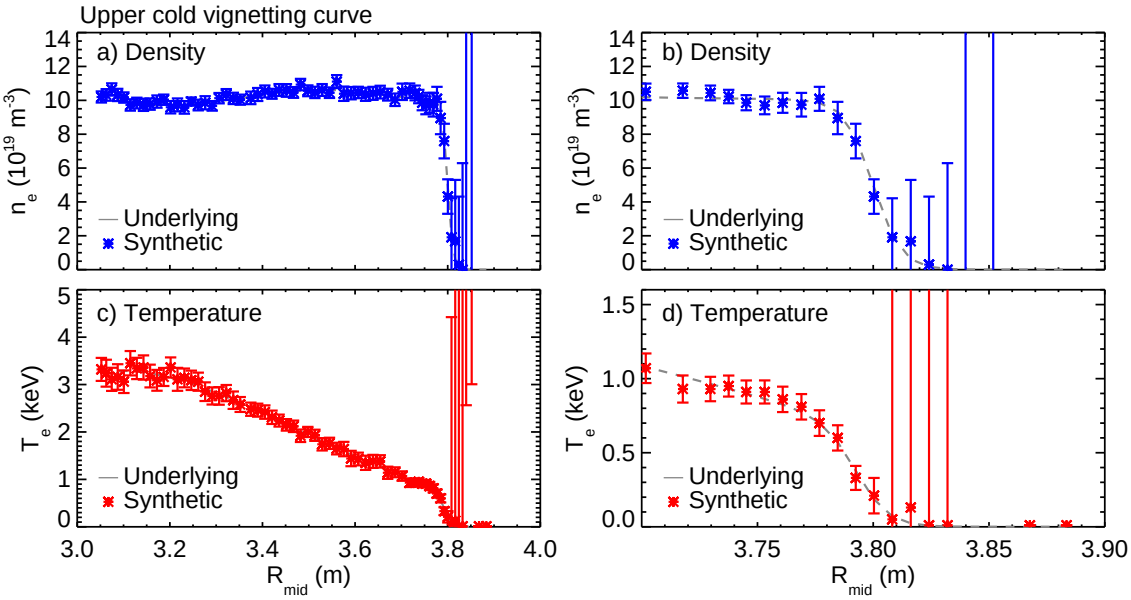

Figure 3.18: Underlying (dashed line) and synthetic (asterisk symbol) profiles for electron (a),(b) density (blue) and (c),(d) temperature (red). Upper cold vignetting curve incorporated into photon calculation. (a) and (c) show the entire profile, whereas (b) and (d) focus on the pedestal region.

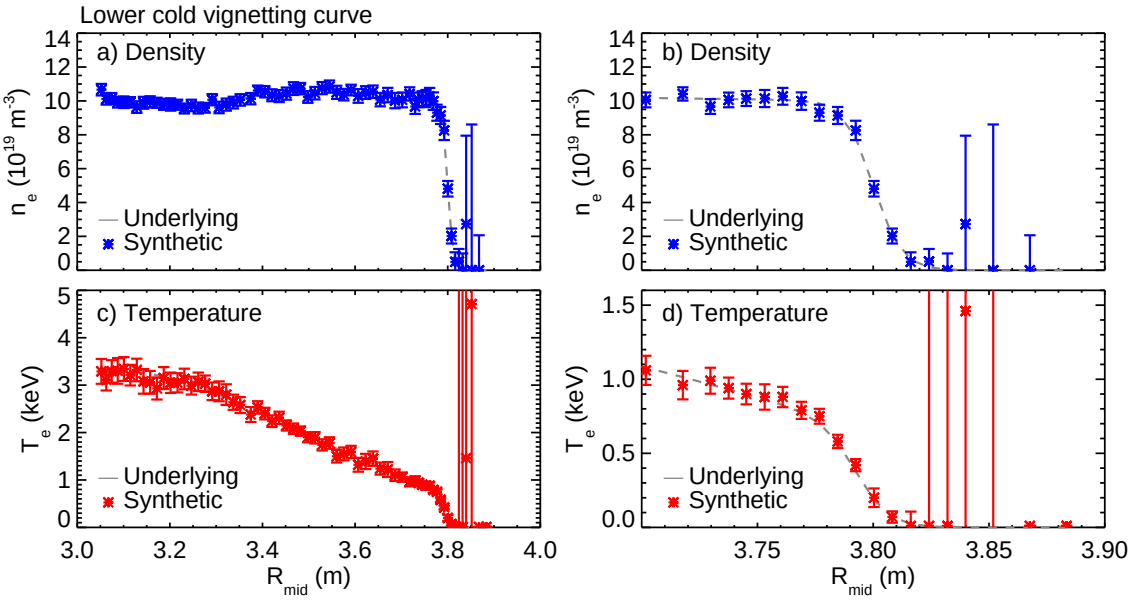

Figure 3.19: Underlying (dashed line) and synthetic (asterisk symbol) profiles for electron (a),(b) density (blue) and (c),(d) temperature (red). Lower cold vignetting curve incorporated into photon calculation. (a) and (c) show the entire profile, whereas (b) and (d) focus on the pedestal region.

In the Scrape Off Layer (SOL) region of a plasma, the temperature and density are at the limit of the dynamic range of the HRTS diagnostic as the system suffers from a low number of detected photons. In other words, the detected number of photons falls below the background and amplifier photon error. Consequently, in this instance, the fitted temperature and density is a reflection of the random noise and not the detected signal. This effect results in a rapidly increase in the uncertainty within the SOL of the order $\sigma_{Te} \approx 3$ keV and $\sigma_{Te} \sim 1 \times 10^{19}$ m^{-3}.

Comparison of Figures 3.18 and 3.19 demonstrates that the rapid increase in uncertainty occurs at $R \approx 3.82$ m for the lower line of sight in comparison to $R \approx 3.80$ m for the upper line of sight. The upper line of sight compromises two to three more spatial points relative to the lower line of sight.

3.6 Quantifying the systematic error due to ELM synchronisation

This section quantifies the systematic error introduced due to the radial shift when overlaying the JET HRTS profiles. The profiles are shifted according to the last closed flux surface as determined by the magnetic equilibrium. This is to account for small scale fluctuations in plasma position and any error in the position of the last closed flux surface. It is inconsequential whether this uncertainty in profile position is a real movement of the plasma or an artifact of the magnetic equilibrium reconstruction as what is important is to accurately overlay the steep gradient region of the profiles.

Figure 3.20 shows a schematic diagram describing the method used to assess the systematic uncertainty in the radial shift. There are three steps; (1) an underlying profile is defined (grey), (2) a composite profile is generated (blue) by overlaying multiple HRTS like profiles with different pedestal positions (the error on the pedestal position is sampled from a normal distribution) and (3) an mtanh is fitted to the composite profile. The difference between the fitted and the original underlying parameters is then assessed.

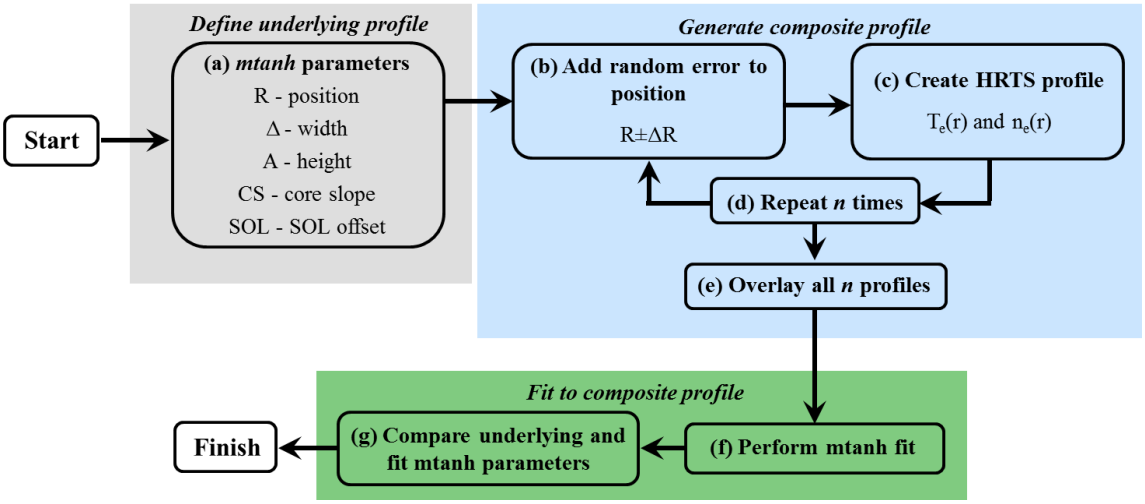

Figure 3.20: Schematic of method to access systematic uncertainty introduced by ELM synchronisation. First an underlying profile is defined (grey). Second a composite profile is generated consisting of n HRTS like profiles (blue). To finish, an mtanh fit is performed to the composite profile and the difference between the resulting parameters in comparison the original underlying parameters is accessed (green).

Figure 3.21 shows the fit to a composite of 10 synthetic temperature and density HRTS profiles, which incorporate the vignetting curve for the lower line of sight for (a), (b) $\sigma_R = 0.1$ cm, (c), (d) $\sigma_R = 0.2$ cm, (e), (f) $\sigma_R = 0.3$ cm and (a), (b) $\sigma_R = 0.4$ cm. The error bars on the temperature and density points above $R \approx 3.80$ m are large in comparison to the measured value. Figure 3.21 (a) and (b) shows that the density and temperature pedestal width is accurately recovered within the statistical error. However, as σ_R increases (for example consider Figure 3.21 (e) and (f) where $\sigma_R = 0.3$ cm) the fitted width systematically deviates from the underlying width beyond the statistical error. The density pedestal width is recovered more accurately than the temperature pedestal width. This is partially due to the fact that the density has a shallower core slope, which better constrains the pedestal top. In addition the error bars at the foot of the density pedestal (for $R \approx 3.81$ m) are smaller than those at the foot of the temperature pedestal.

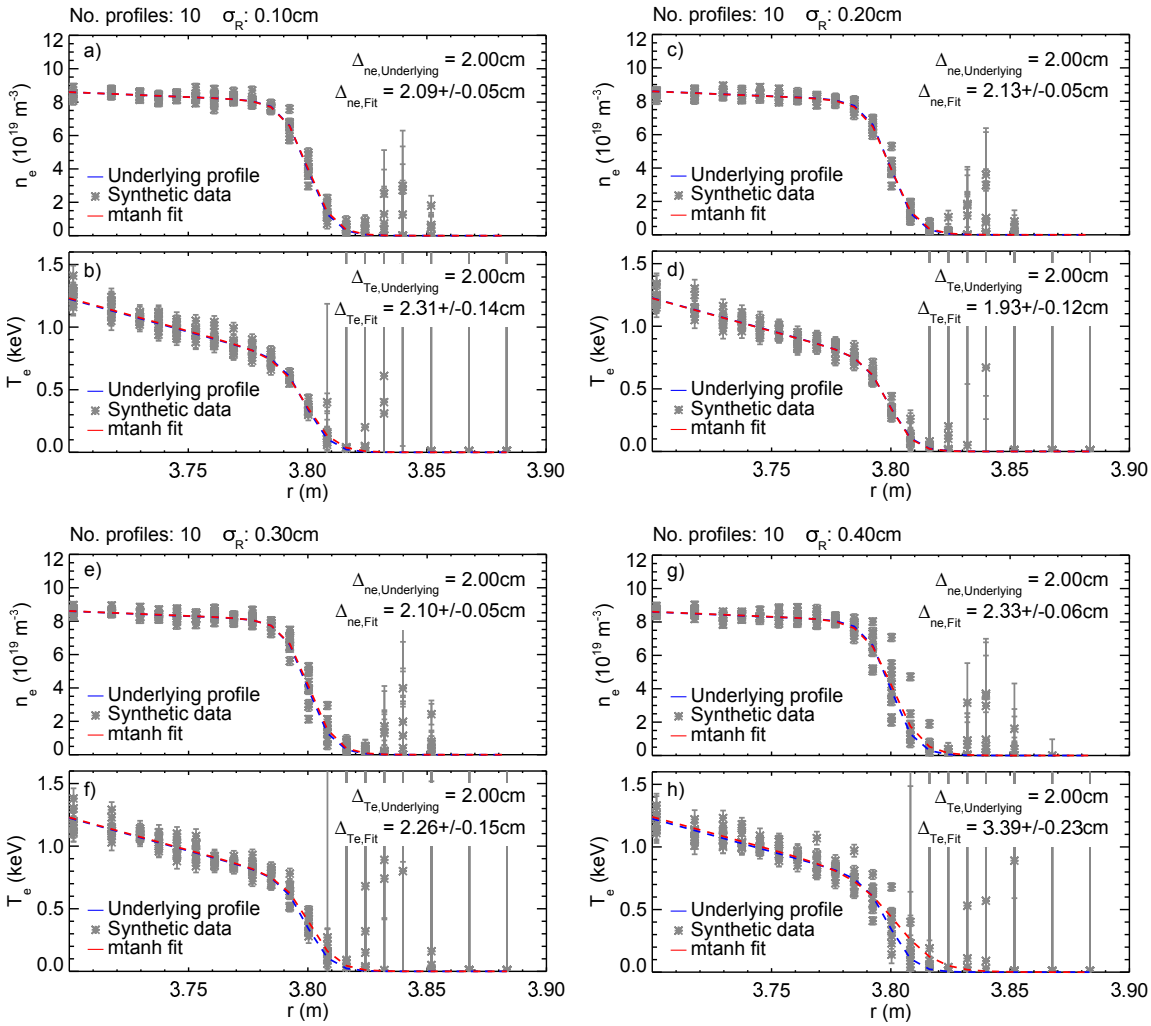

Figure 3.21: Underlying mtanh profile (blue), synthetic data (grey) and mtanh fit to a composite of 10 synthetic profiles (blue). The random error is sampled from a normal distribution of width (a), (b) $\sigma_R \approx 0.1$ cm, (c), (d) $\sigma_R \approx 0.2$ cm, (e), (f) $\sigma_R \approx 0.3$ cm and (g), (h) $\sigma_R \approx 0.1$ cm.

Figure 3.22 shows the average systematic deviation over 20 Monte-Carlo runs of the temperature and density pedestal width over a scan of σ_R from 0.0 to 0.5 cm. For the composites of 10 temperature and density synthetic profiles, the systematic deviation in pedestal width increases with σ_R. For small σ_R (< 0.15) the systematic error is negligible in comparison to the statistical error. The systematic deviation in the temperature pedestal width increases more rapidly than for density. As just described in the context of Figure 3.21, this results from the density profile having a shallower core slope (and thus better constraining the pedestal top). Figure 3.22 also shows that the statistical error in pedestal width increases with σ_R, most notably for the temperature. However, the systematic deviation in pedestal width is greater than the statistical error at high $\sigma_R > 0.3$.

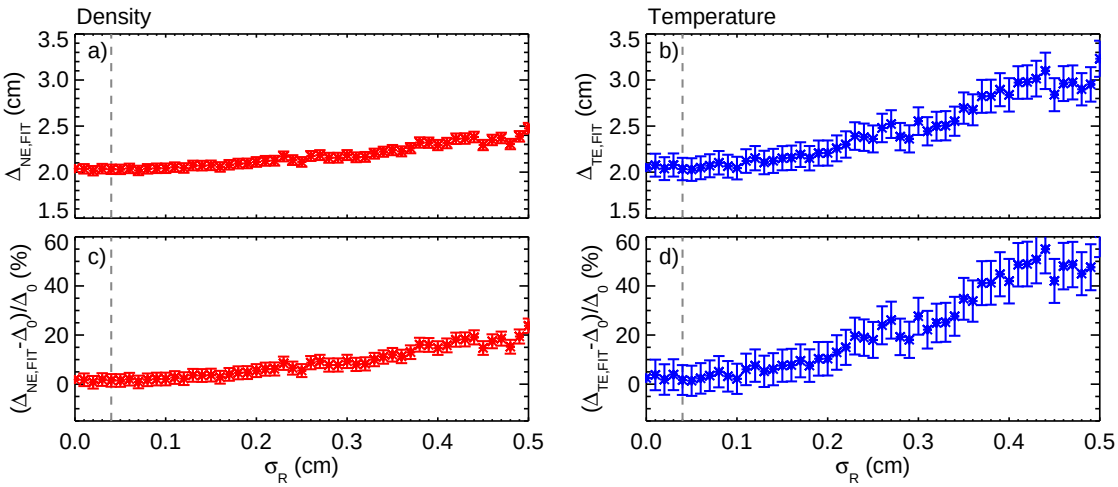

Figure 3.22: Scan of σ_r ranging from 0.0 cm to 0.5 cm for (a) temperature pedestal width, (b) density pedestal width, (c) percentage error in temperature pedestal width and (d) percentage error in density pedestal width as determined by fitting to composite profile (Figure 3.21) consisting of HRTS like profiles, see Section 3.5.

The Last Closed Flux Surface (LCFS) position, used to correct the radial position of the real HRTS profiles when forming the composite profile, is calculated using the high time resolution magnetic reconstruction. The Radial Outer Gap (ROG), which is the distance between the plasma edge and wall, is converted into the LCFS position using geometric information. The ROG can be used to quantify the variation in position by smoothing the time trace and evaluating the residuals. Figure 3.23 shows a histogram of the residuals during the inter-ELM stationary phase (excluding the ELM crash; the rapid collapse of the steep pressure gradient resulting in the lose of energy and particles) of a JET-ILW pulse along with a corresponding Gaussian fit. The width of this Gaussian is $\sigma_R = 0.4$ cm, an estimate of the uncertainty in profile position for real HRTS measurements.

The vertical lines in Figure 3.22 show how the experimental estimate for σ_R relates to the scan of σ_R. Assuming $\sigma_R \approx 0.4$ cm and the composite profile consists of 10

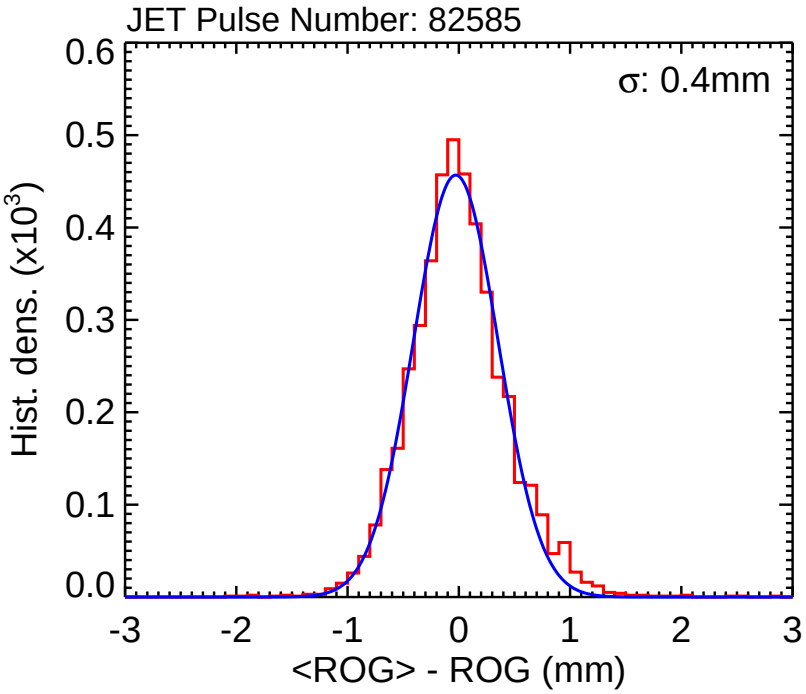

Figure 3.23: Histogram of the difference between the un-smoothed and smoothed Radial Outer Gap (ROG) as a function of time (red) and a corresponding gaussian fit (blue).

profiles, the expected systematic error is found to be negligible for both the density and temperature pedestal width in comparison to the corresponding statistical error.

The method described in Figure 3.20 can be adapted to investigate how the statistical error varies with the number of profiles within the composite profile. Figure 3.24 shows how the statistical error (in cm and as a percentage of the underlying temperature and density pedestal width) varies with the number of profiles in the composite profile. The value of σ_R is fixed at 0.04 cm. The statistical error is large (± 20 %), for one profile but reduces as the number of profiles increases. The data in Figure 3.24 also shows that the reduction in the statistical error plateaus above five profiles. Consequently, this should be considered as a minimum number of profiles required for a fit, which typically equates to a stationary ELMy phase of $1.5 - 2.0$ s.

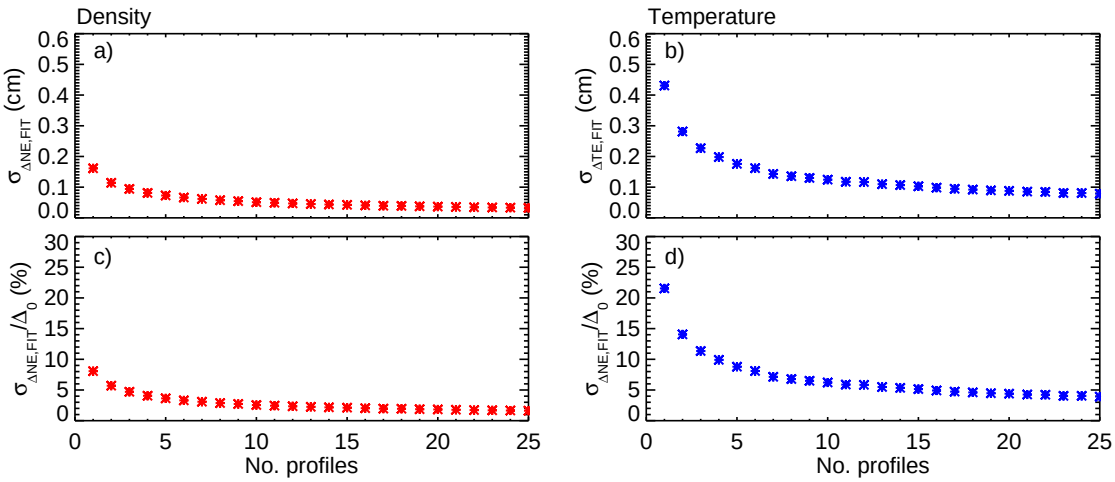

Figure 3.24: Variation in pedestal width for (a) temperature and (b) density. Percentage error in pedestal width for (c) temperature and (d) density as determined from mtanh fits to a composite profile where $\sigma_R = 0.4$ cm.

3.7 Performing a pedestal fit

This section describes in some detail, the procedure required to perform a fit using the JET pedestal fitting tool. Assuming the pulse of interest has reliable calibrated HRTS data there are thress steps. The stationary phase of a pulse is first selected and then the timing of the ELMs are selected. Following this, the quality of the resulting composite profile and fit are evaluated. If necessary, in order to improve the quality of the fit, the two former steps can be repeated with some modifications to the criteria used to select the profiles.

The stationary phase of the plasma is evaluated by considering a range of time dependent plasma parameters such as the core line integral density, the edge line integral density, the neutral beam input power P_{NBI}, the normalised toroidal beta ($\beta_{\phi,N}$ a measure of normalised pressure), the confinement enhancement factor (H_{98}), the gas fuelling rate and the intensity of an emission line (Deuterium alpha for JET with the carbon wall and beryllium for JET with the ITER-Like-Wall). Other parameters may also be considered depending on the specifics of the plasma discharge and experiment.

Figure 3.25 shows a selection of plasma parameters and the stationary phase (red) chosen for analysis for JET Pulse Number 81586. The HRTS system produces 20 profiles per second and so for a sufficient number of profiles in each phase of the ELM cycle, the stationary phase is ideally $1.5 - 2.0$ s, as previously mentioned. It is important to note that the initial phase after the transition into H-mode (characterised by a ramp in density, normalised beta and H_{98} as shown in Figure 3.25(b), (d) and (e)) should not be included in the analysis windows. Other considerations include avoiding steps in heating power, changes in gas fuelling and clear changes in ELM behaviour (frequency). Essentially what we are looking for is a stationary, unvarying phase of a plasma with a regular ELM frequency.

As previously mentioned, the JET pedestal fitting tool determines the timing of the ELMs by considering the intensity of a relevent spectral line. An ELM is a periodic collapse of the steep gradient at the plasma edge expelling energy and particles into the Scrape Off Layer (SOL) towards the first wall. Consequently there is a peak in emission as the ejected energetic particles interact of the surrounding neutral particles in the SOL. Each peak in emission above the threshold is defined as an ELM. The full footprint of an ELM is more extensive and it is insightful to also consider, for example, magnetic signals, change in stored energy, evolution of temperature and density. There exist more complex methods to determine ELM timings, however the simplicity of a threshold technique means that it is inherently robust and it also provides a good level of flexibility.

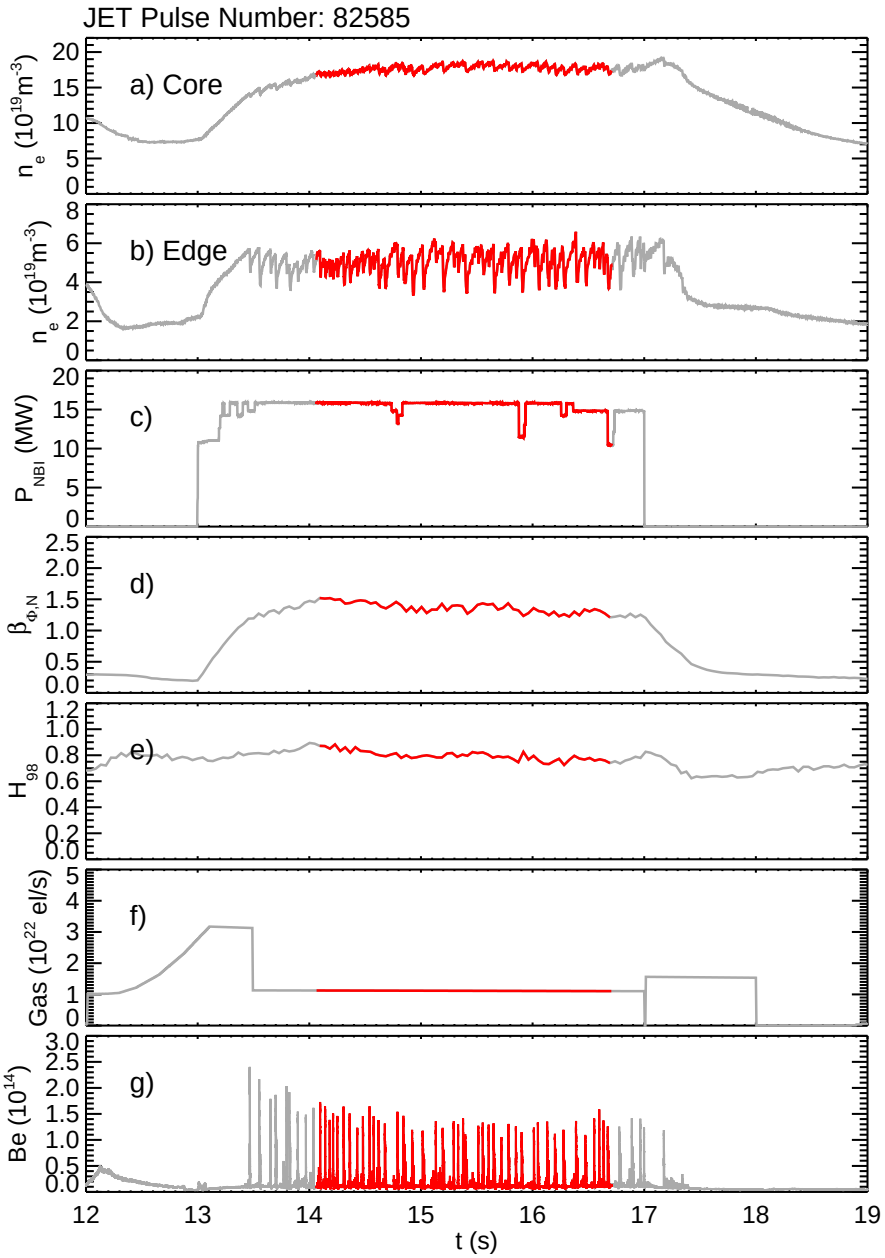

Figure 3.25: Variation of plasma parameters for JET Pulse Number 85186 and the stationary phase of pulse selected for pedestal fit. (a) Core integral line density, (b) edge integral line density, (c) neutral beam input power, (d) normalised beta, (e) confinement enhancement factor, (f) gas fuelling rate, (g) error correction field coil kick amplitude and (h) beryllium emission.

The ELM selection is relatively trivial for regular, stationary Type I ELMy H-mode discharges with clear distinct peaks in emission and no pre or post fluctuations in emission, as demonstrated by Figure 3.26 (a) for JET Pulse number 82814. However, this is not so clear for all discharges, as shown by Figure 3.26 (b) for JET Pulse number 82585. Here, the ELM period is more irregular as reflected in the standard deviation of the ELM frequency where $f_{ELM} = 18.8 \pm 8.2$ Hz. Furthermore, in some instances ELMs are followed by a near immediate peak, for example at $t \sim 15.4$ s. By considering the full ELM footprint, it is possible the subsequent peak is an ELM,

however, the pedestal will have not recovered to the typical pre-ELM state in this case. This could therefore introduce an uncharacteristic profile into the a fit biasing the resulting parameters and so can be ignored if necessary.

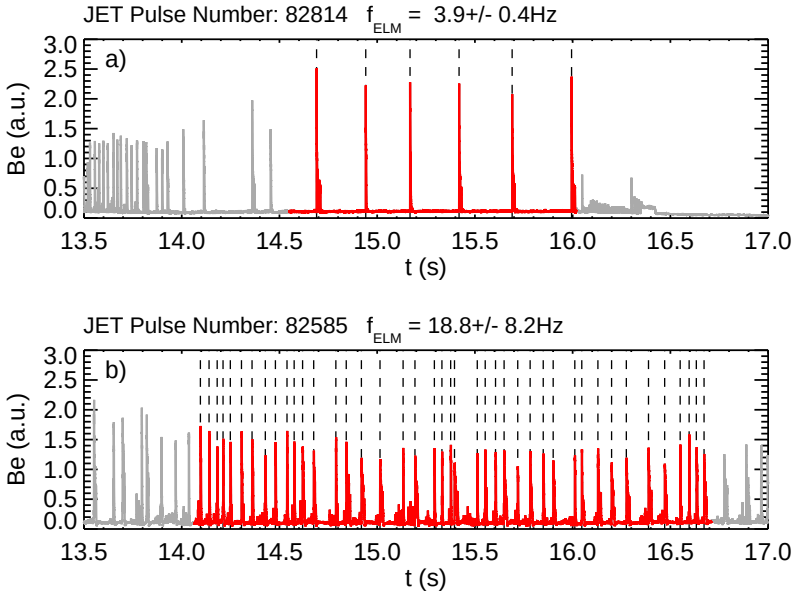

Figure 3.26: Beryllium emission for JET Pulse Number (a) 82814 and (b) 82585 between $t = 13.5 - 17.0$ s. (a) and (b) show selection for stationary phase of each pulse (blue) and the timing of selected ELMs (black dashed lines).

The final step is to assess the quality of the fit. This can be done by checking that there is a sufficient number of pulses in the selected analysis region (ideally at least five profiles are required as shown in Section 3.6). The ELM selection can also be optimised to exclude uncharacteristic profiles from a fit. Sometimes it is also necessary to exclude obviously noisy data, such as those at the foot of the pedestal and towards the SOL region, where signal is low.

Further confidence in the result can be provided by considering multiple fits from different regions of the ELM cycle. Figure 3.27 shows the evolution of the temperature and density pedestal height and width over the normalised ELM cycle for fits incorporating profiles selected from 10 %, 20 % and 30 % windows of the normalised ELM cycle. Figure 3.27 helps identify which fits may not be as reliable, by showcasing those that do not fit the overall trend throughout the ELM cycle or, where the error bar is relatively large.

For example, the temperature and density width for the 10 % window fit centred about 0.15 has a relatively large error in comparison to the other 10 % window fits as it only uses one profile (see Figure 3.28 (a)). Figure 3.28 shows the distribution of the HRTS profiles across the normalised ELM cycle for (a) 10 %, (b) 20 % and (c) 30 % windows. As the percentage window size increase, the number of selected profiles increases and the variation in the number of profiles between windows decreases.

For this particular pulse the distribution of HRTS profiles results in not all the 10 % window fits being reliable. Furthermore, consider the 10 % window fit centred about 0.75. This fit deviates from the trend in temperature width and has a larger relative error bar for both temperature width and height. The ELM selection in this case results in a post-ELM HRTS profile within a near pre-ELM fit.

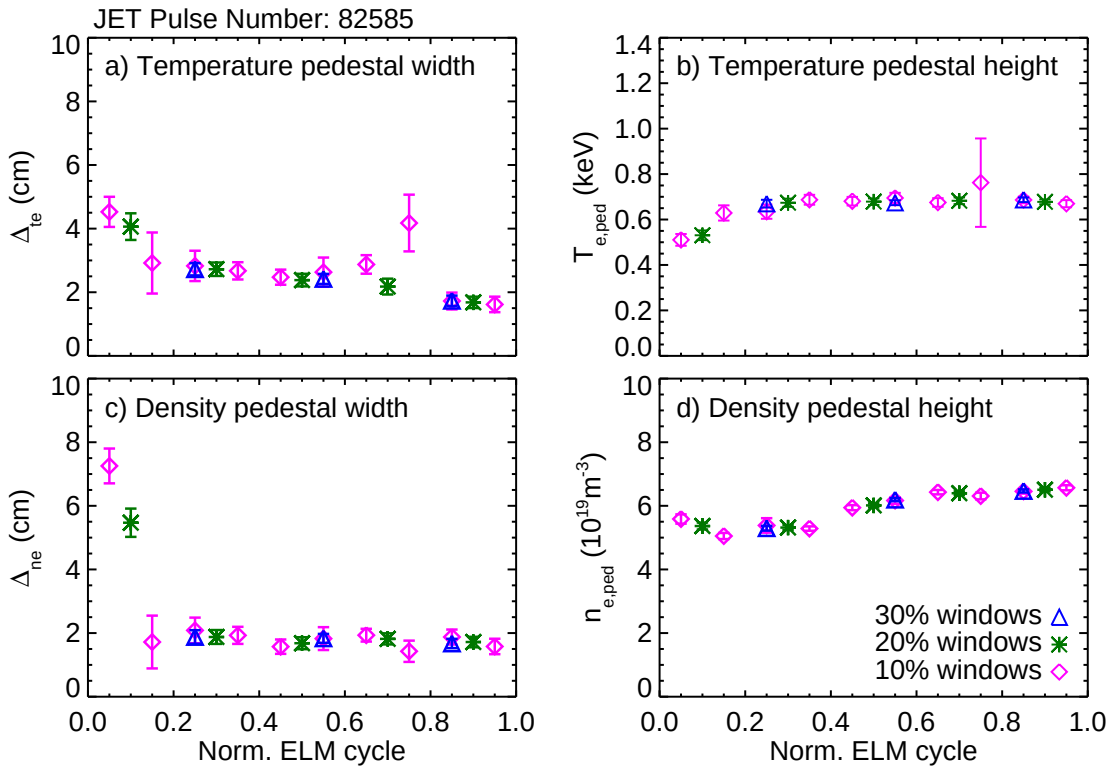

Figure 3.27: Inter ELM evolution of (a) temperature pedestal width, (b) temperature pedestal height, (c) density pedestal width and (d) density pedestal height where profiles are selected from 10 % (magenta), 20 % (green) and 30 % (blue) windows of the normalised ELM cycle.

Figure 3.27 (a) and (c) show that the temperature and density pedestal width is initially wide ($\Delta_{te} \approx 4.0$ cm and $\Delta_{ne} \approx 7.0$ cm) due to a loss of the steep gradient after an ELM. The temperature and density pedestal recover after 20 % of the ELM cycle where $\Delta_{te} \approx 2.5$ cm and $\Delta_{ne} \approx 2.0$ cm. The temperature pedestal width narrows throughout the rest of the ELM cycle whereas the density pedestal width saturates. Figure 3.27 (b) shows the pedestal temperature initially rises from $T_{e,ped} \approx 0.5$ to 0.7 keV in the first 20 % of the ELM cycle and then saturates. The density pedestal height rises from $n_{e,ped} \approx 5.0$ to 6.5×10^{19} m^{-3} throughout the entire ELM cycle. JET Pulse number 82585 is a deuterium fuelled high triangularity Type I ELMy H-mode JET-ILW plasma. The inter-ELM evolution of the pedestal structure described here will be discussed in detail in following the chapters.

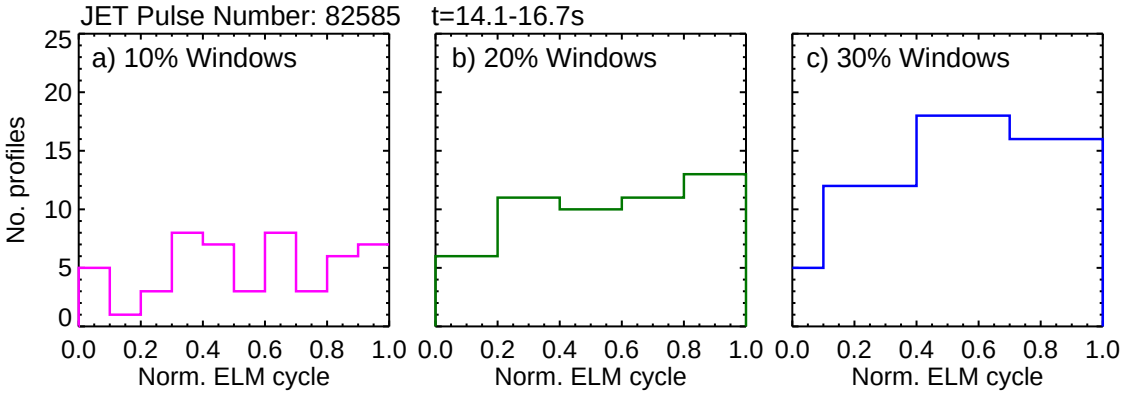

Figure 3.28: Histograms showing the distribution of number of HRTS profiles across a normalised ELM cycle for (a) 10 % (magenta), (b) 20 % (green) and (c) 30 % (blue) windows. The 30 % window histogram has a 10 % window at the beginning of the ELM cycle and then three subsequent 30 % windows.

3.8 Summary

Fitting a modified hyperbolic tangent (mtanh) function to the steep temperature and density gradient at the plasma edge, the pedestal, is a common technique for extracting the pedestal width, gradient and height. This assumes an mtanh function is a good description of the radial profile (which is a reasonable assumption).

The JET pedestal fitting tool performs a fit to ELM synchronised HRTS profiles selected from a specified region of the ELM cycle over the stationary phase of a plasma. The fitting routine determines a deconvolved fit using an instrument function calculated using the system geometry, more specifically; the orientation of the collection optics cone of view, the laser line of sight and the angle at which the magnetic field lines intersect the scattering volume. The density uses a classic deconvolution technique whereas the temperature fit is weighted by the density fit (and is termed a weighted deconvolution technique). This weighting is important in the pedestal where the density changes across the scattering volume.

The total error in the pedestal structure is found to be dominated by the statistical error in the fit. The systematic error due to the deconvolution technique has been quantified by [63] and is negligible, particularly in the high resolution HRTS configuration. A first order approach has been used to estimate the systematic error due to ELM synchronisation by replicating the fitting process using synthetic HRTS profiles. The systematic error on the density and temperature pedestal width due to ELM synchronisation is found to be negligible in comparison to the statistical error, assuming σ_R for experimental profiles is ≈ 0.4 cm.

Finally, a description of the procedure undertaken to perform a single fit and check the reliability of this fit is described. There are three steps to performing a fit. First, selecting the stationary phase of a pulse. Second, selecting the timing of the ELMs. Then, assessing the quality of the resulting fits and repeating the initial steps if necessary. To further assess the reliability of the resulting fit it is insightful to compare it with fits covering different regions of the ELM cycle. This will highlight if the mtanh parameters conform with the overall trend.

Chapter 4

Pedestal study across a deuterium fuelling scan for high triangularity ELMy H-mode plasmas on JET with the carbon wall

This Chapter focuses on a database of 14 high triangularity ELMy H-mode plasmas on JET with the carbon wall (JET-C) across a deuterium fuelling scan. This study describes the ELM behaviour, quantifies the pedestal structure (pre-ELM and inter-ELM) and then goes onto compare the pre-ELM measurements with models. The models are MISHKA-1, which evaluates the Peeling Ballooning stability and the leading predictive model, EPED, for the pedestal width and height. The results from this Chapter are presented in [75].

4.1 Introduction

The ITER baseline scenario is a Type I ELMy H-mode [81]. An H-mode is a high confinement mode of operation that is believed to arise due to the suppression of edge turbulence, resulting in an Edge Transport Barrier (ETB) [82–84]. A consequence of the ETB is the formation of a steep pressure gradient at the plasma edge called the pedestal. The pressure pedestal height is limited by Edge Localised Modes (ELMs). ELMs are a periodic relaxation of the pedestal due to reaching a critical pedestal width and height, thought to be associated with crossing the Peeling Ballooning (PB) stability boundary [85]. The plasma core performance is strongly linked to the pressure pedestal height [86, 87].

ITER will be considerably larger than current machines, operating at higher tem-

perature and density. ITER will also be the first machine to have a significant fusion alpha particle fraction, contributing towards plasma heating [81]. To improve the understanding of the ITER baseline scenario, research on current machines is focused on characterising regimes approaching the operational parameters of ITER. On JET, a discharge cannot simultaneously achieve ITER-like temperature and density. Instead separate studies investigate each operational parameter. For example, high temperature, low collisionality JET plasmas have been addressed [88]. Also of interest are dense plasmas, comparable to the Greenwald density.

Reference [89] states that at high density, with gas puff fuelling, it is difficult to maintain confinement in the Type I ELMy H-mode. A possible solution is to increase the degree of plasma shaping; more specifically the triangularity [87]. Dense, high triangularity ITER-like plasmas have been investigated by [90] on JET and are the focus of this study. The key findings in [90] are, first, there was little degradation of stored energy when fuelled up to a pedestal density normalised to the Greenwald density ($n_{e,ped}/n_{GW} \approx 1$). Second, the Type I ELM frequency decreased with increasing pedestal density. And finally, the inter-ELM heat losses increased at high pedestal density, $n_{e,ped}/n_{GW} > 0.7$, thought to be due to a transition from a pure Type I to a mixed Type I/II ELMy regime.

The 2002 study was limited by diagnostic capabilities and consequently there remained some unanswered questions with respect to the role of pedestal structure to the change in performance. This has now be addressed using the JET High Resolution Thomson Scattering (HRTS) system [48], installed in 2005. In this Chapter, a new JET-C database is presented consisting of 14 dense high triangularity ELMy H-mode JET plasmas, comparable to [90], with good diagnostic coverage. The aim of this study is to utilise the HRTS electron temperature and density profiles to quantify the pre-ELM pedestal structure and the pedestal evolution during the ELM cycle. These measurements facilitate a PB stability analysis and a comparison to the leading predictive pedestal structure model, EPED [30, 42].

Measurements of radial kinetic pedestal profiles, like the results presented in this study, have been the focus of numerous studies. These studies have the collective aim of contributing towards the understanding of the physical processes governing the H-mode pedestal structure and therefore providing a basis for predictive models. The scaling of the pedestal structure with dimensionless parameters, such as normalized ion gyroradius ($\rho* = \rho_i/a$), gives an indication of the possible pedestal structure on future devices such as ITER. A positive scaling of the pedestal width with normalized gyroradius $\rho*$ was a concern for ITER as it will operate at comparatively low $\rho*$ however this has been addressed by [34, 37, 38, 64, 91, 92] and all show a weak scaling. Another important parameter is the normalised poloidal pedestal pressure ($\beta_{pol,ped}$) as studied in detail by [30, 33–40, 93]. The average of the electron temperature and

density pedestal width in normalized poloidal flux is shown to scale with $(\beta_{pol,ped})^{0.5}$. This scaling relationship was discussed in more detail in Section 1.9 and acts as one of the two constraints within the EPED model. Also of interest is how the pedestal structure evolves during the ELM cycle. The electron temperature and density pedestal width widens during the ELM cycle on DIII-D [36, 66] and MAST [69, 70]. This behaviour is considered typical and is well described by EPED [30, 42].

In this chapter, the focus of Section 4.2 and Section 4.3 is to show that the 2002 and new JET-C databases are comparable before going on, to present the new pedestal measurements. In Section 4.2, there is a detailed description and comparison of the two databases. Then the plasma performance of the new JET-C database is presented. Section 4.3 focuses on the transition from a pure Type I to a mixed Type I/II ELMy regime at high fuelling, as originally observed in the 2002 study [90].

Section 4.4 studies the electron temperature and density pedestal width and height determined by fitting a modified hyperbolic tangent (mtanh) function to HRTS profiles. Furthermore the inter-ELM evolution of the pedestal structure is studied by fitting to profiles selected from a temporal window in various phases of the ELM cycle.

Section 4.5 presents the result of a pedestal stability code, MISHKA-1 [27]. MISHKA-1 calculates the position of the PB stability boundary and the proximity of the plasma edge to this boundary, using the experimental profiles. A sensitivity analysis to quantify the uncertainties associated with the operational points relative to the stability boundary is also presented. Then section 4.5 goes on to present a comparison of the pedestal measurements to the results from the EPED1 model [30, 42]. EPED1 is designed to predict the pressure pedestal width and height for present and future devices. This comparison helps further test that model and interpret the observations. Section 4.6 discusses the conclusions.

4.2 Description of database

4.2.1 Plasma scenarios

The JET pulses within the new JET-C database were obtained during experiments with a carbon fibre composite (CFC) wall before the installation of the current Be/W ITER-Like-Wall (ILW) [94]. A D_2 fuelling scan from $\Gamma_D \approx 0.2$ to 6.1×10^{22} electrons per second (el/s) was performed over 14 single null, Type I ELMy H-mode plasmas as described in [95, 96]. The high triangularity plasma scenarios for the 2002 and new JET-C databases are compared in Table 4.1.

Table 4.1: Comparison of plasma scenario for 2002 and present day scenario. The current divertor configuration is termed load bearing septum replacement plate (LBSRP) [97]

	2002	new JET-C
$(\delta_{up} + \delta_{low}) = \delta$	$(0.49 + 0.45)/2 = 0.47$	$(0.43 + 0.39)/2 = 0.41$
I_p/B_t	2.5 MA/2.7 T	2.5 MA/2.7 T
P_{NBI}	< 15 MW	< 15 MW
Γ_D	$(0 - 5) \times 10^{22}$ el s^{-1}	$(0.2 - 6.1) \times 10^{22}$ el s^{-1}
Divertor config.	Septum Divertor (carbon)	LBSRP Divertor (carbon)

The two scenarios have similar plasma current, toroidal magnetic field strength, Neutral Beam Injection (NBI) heating power and gas fuelling capabilities. There is a small variation in triangularity due to the most notable difference between the two scenarios, the divertor configuration.

Figure 4.1 shows the EFIT equilibrium reconstruction for JET Pulse Number (JPN): 52014, from the 2002 study; and 79503, from the new JET-C database. The divertor geometry shown by Figure 4.1 (b) is the Septum Divertor (SD) configuration, used in the 2002 study. The divertor geometry shown by Figure 4.1 (a) and (c) is the Load Bearing Septum Replacement Plate (LBSRP) divertor configuration, as used in the new JET-C database. When operating with the LBSRP divertor an optimisation of plasma volume was possible due to achieving magnetic configurations with a lowered X-point position. The configuration chosen for this study is optimised for both volume and a choice of triangularity ($\delta \approx 0.41$) at which good confinement at high density was found. Also as shown by the arrow on Figure 4.1 (c) the variation in D_2 fuelling from 0.2 to 6.1×10^{22} el/s is provided by a gas injection model located at the inner divertor [95].

4.2.2 Diagnostic setup

As previously mentioned, the 2002 study [90] was limited by diagnostic capabilities. The maximum electron density of the plasmas in [90] was $\approx 10^{20}$ m^{-3}, which is greater than the density cut-off for ECE emission, $\approx 8.5 \times 10^{19}$ m^{-3}. As a result the ECE heterodyne radiometer could not provide pre-ELM temperature profiles. However, currently the JET HRTS system can measure temperature and density profiles throughout the ELM cycle. As discussed in Chapter 2 the system utilises a 5 J Q-switched Nd:YAG laser ($\lambda = 1064$ nm) with a 20 ns pulse duration and a 20 Hz repetition rate across the entire JET pulse (≈ 800 profiles) [48, 63]. The HRTS line-of-sight in the outer midplane is indicated by the green line in Figure 4.1 (a).

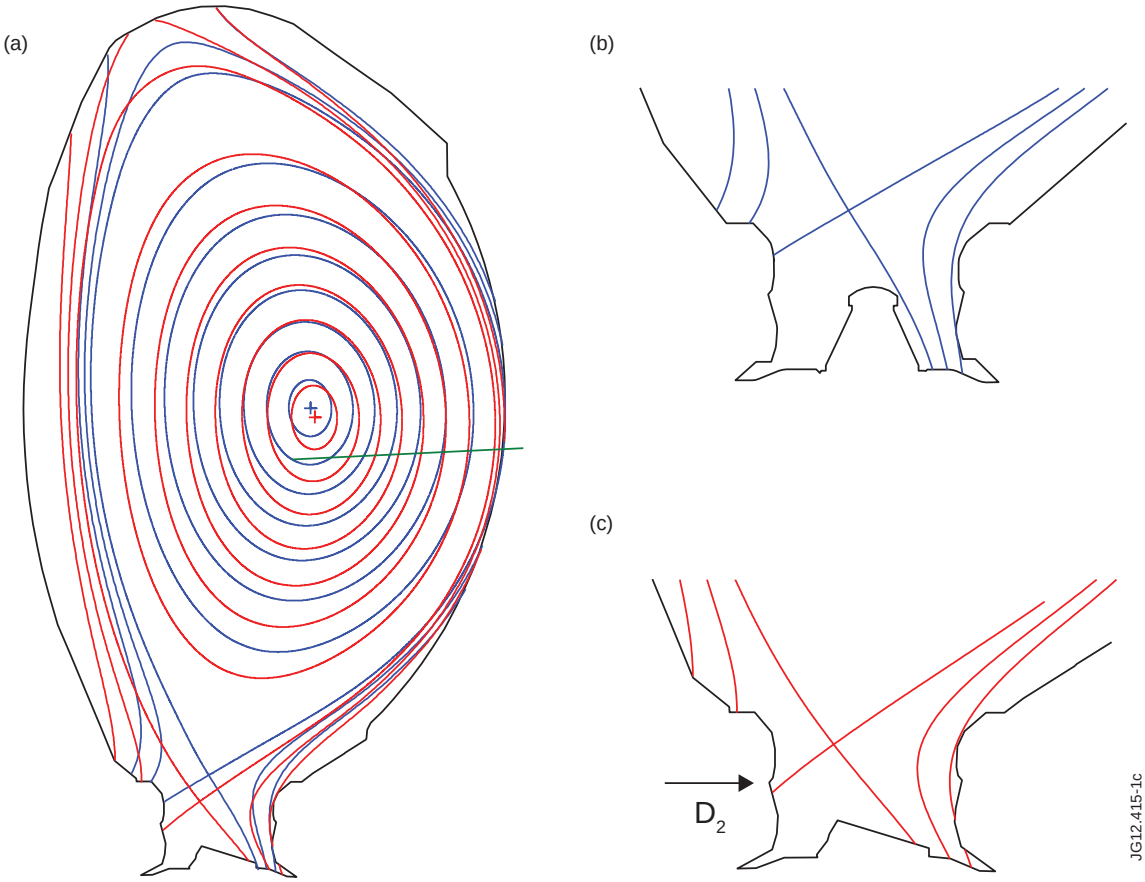

Figure 4.1: (a) Comparison of EFIT equilibrium reconstruction for JET Pulse Number 52014 blue line (t = 23.1 s) [90] and JET Pulse Number 79503 red line (t = 22.0 s) where the green line is the HRTS line of sight. Divertor configuration for (b) JET Pulse Number 52014 (Septum Divertor) and (c) JET Pulse Number 79503 (LBSRP Divertor).

As previously discussed (Chapter 2, during the campaign the spatial resolution of the HRTS system was improved from a Full Width Half Maximum (FWHM) instrument function of $\sim$ 22 mm to $\sim$ 11 mm [63]. Three out of the 14 plasmas have higher spatial resolution and are indicated by different coloured symbols in the rest of the Chapter. It is also important to note the HRTS electron temperature data for the pulses presented in this study are calibrated via cross-comparison to ECE data on a few dedicated shots. In this instance the ECE temperature data uses the 1995 calibration as opposed to the more recent calibration detailed by [98].

4.2.3 Plasma confinement

Figure 4.2 shows the evolution of key plasma parameters for a low fuelling (0.2×10^{22} el/s, in blue) and a high fuelling pulse (2.6×10^{22} el/s, in red) where both have high resolution HRTS coverage. And therefore these same two pulses will later be used for detailed profile analysis 4.4.

The selected stationary region of a pulse is indicated by the coloured region of each trace in Figure 4.2. Plasma parameters are averaged over this region and as discussed later, HRTS profiles are selected for further analysis within this region.

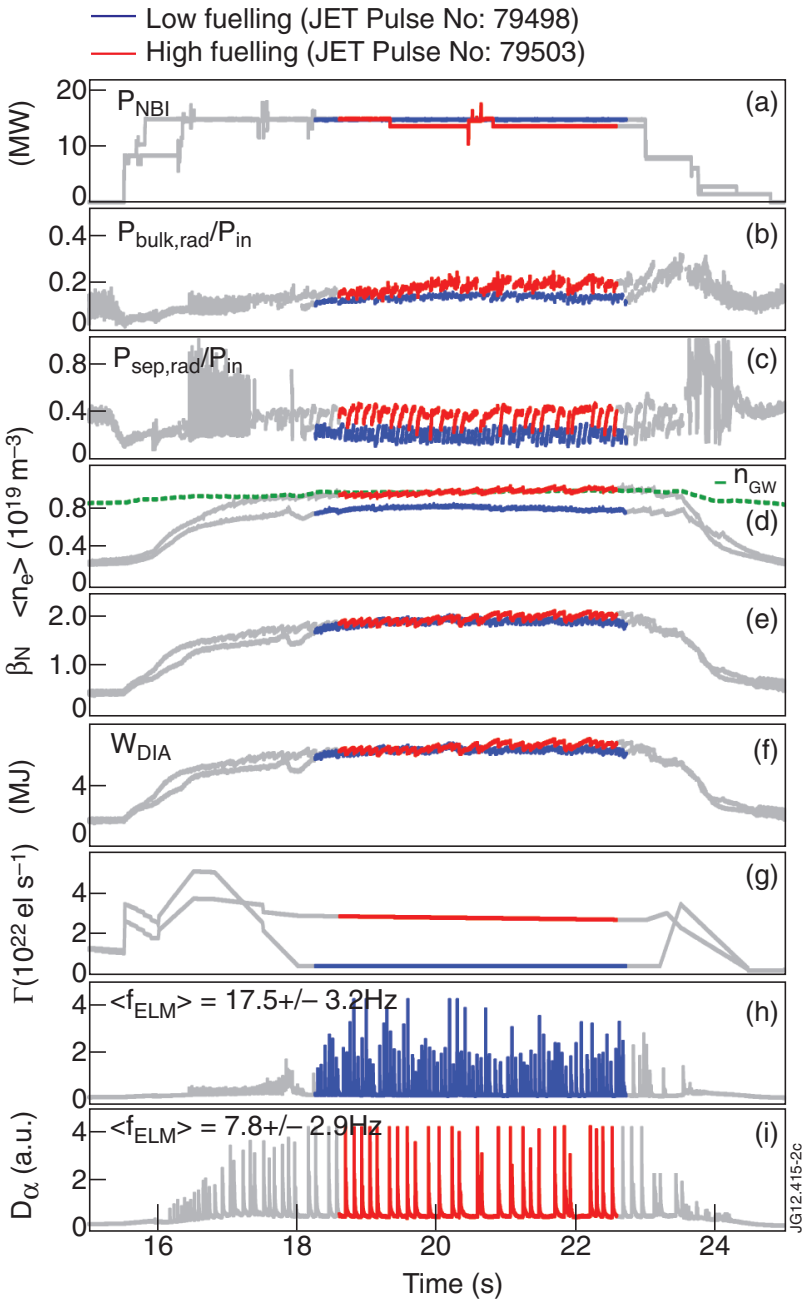

Figure 4.2: Low (blue) and high (red) fuelling pulses showing (a) NBI power, (b) bulk radiated power fraction, (c) separatrix radiated power fraction, (d) line averaged density n_e and n_{GW}, (e) normalised toroidal beta, (f) stored energy, (g) gas fuelling rate, (h) D_α emission for low fuelling and (i) D_α emission for high fuelling.

Figure 4.2 shows for a similar input power ($P_{NBI} \approx 15$ MW) both pulses have a comparable normalised beta ($\beta_N \approx 1.9$) and stored energy ($W_{DIA} \approx 6$ MW). The two pulses have line averaged densities of 8.0 and 9.5×10^20 m^{-3} which is respectively 75 % and 100 % of the Greenwald density limit. As a consequence the confinement enhancement factor (H_{98}) for these two pulses differ slightly ($H_{98} = 1.0$ and $H_{98} = 0.95$) due to the density dependence in the confinement scaling law (Figure 4.3). Figure 4.2 (h) and 4.2 (i) show that the ELM frequency reduces when the fuelling level in increased, as is typical for dense high triangularity plasmas in JET [90].

The 2002 and more recent JET-C optimised high δ Type I ELMy H-mode plasma scenarios, although different, both exhibit similar ELM behaviour and comparable confinement. The confinement enhancement factor (H_{98}) as defined [99] is used as a measure of the confinement performance. More specifically H_{98} is the ratio of the energy confinement time for a specific pulse as determined from measured quantities to the energy confinement time calculated from a scaling relation which is a function of geometry and basic plasma parameters. The scaling relation is determined via regression analysis of the ITER H-mode confinement database consisting of data from 12 different Tokamaks [99]. Figure 4.3 (a) and 4.3 (b) show H_{98} as a function of fuelling rate and the pedestal density normalised to the Greenwald density respectively.

Figure 4.3 (a) shows H_{98} decreases by less than 10 % up to a fuelling rate of $\Gamma_e \approx 4.8 \times 10^{22}$ el/s. Above this fuelling rate there is a transition to a lower confinement state, so called compound ELMs [100], as indicated by a further reduction of H_{98} (≈ 20 %). The ELM frequency of the compound ELMy pulse is ≈ 100 Hz, whereas all the other pulses within the fuelling scan are between $5 - 25$ Hz. The ELM frequency is discussed further in section 4.3.

The variation of H_{98} for a given level of fuelling, see Figure 4.3 (a), implies the fuelling level does not sort the performance for these plasmas well. To achieve similar plasma parameters on different operational days the fuelling level has to be fine-tuned. This is to account for variations in wall conditioning and fuelling port location. A better sorting of the data is found with the pedestal density normalised to the Greenwald density ($n_{e,ped}/n_{GW}$), a plasma parameter, rather than the fuelling level (Γ_D), a machine parameter, as shown by Figure 4.3 (b). As pedestal density increases, H_{98} remains approximately constant within error between $n_{e,ped}/n_{GW} \approx 0.65$-$0.75$. Above $n_{e,ped}/n_{GW} \approx 0.8$, H_{98} increases again, due to an apparent confinement improvement, up to a pedestal density of $n_{e,ped}/n_{GW} \approx 1.0$. The degraded performance of the compound ELMy pulse results in an intermediate pedestal density ($n_{e,ped}/n_{GW} \approx 0.82$). Comparison of Figure 4.3 (a) and 4.3 (b), indicate as the fuelling is increased the pedestal density initially increases, peaking at $n_{e,ped}/n_{GW} \approx 1.0$, corresponding to a fuelling rate of 2.6×10^{22} el/s. As the fuelling is further increased up to $\Gamma_D \approx 6.1 \times$

10^{22} el/s, the pedestal density decreases due to the compound ELM transition.

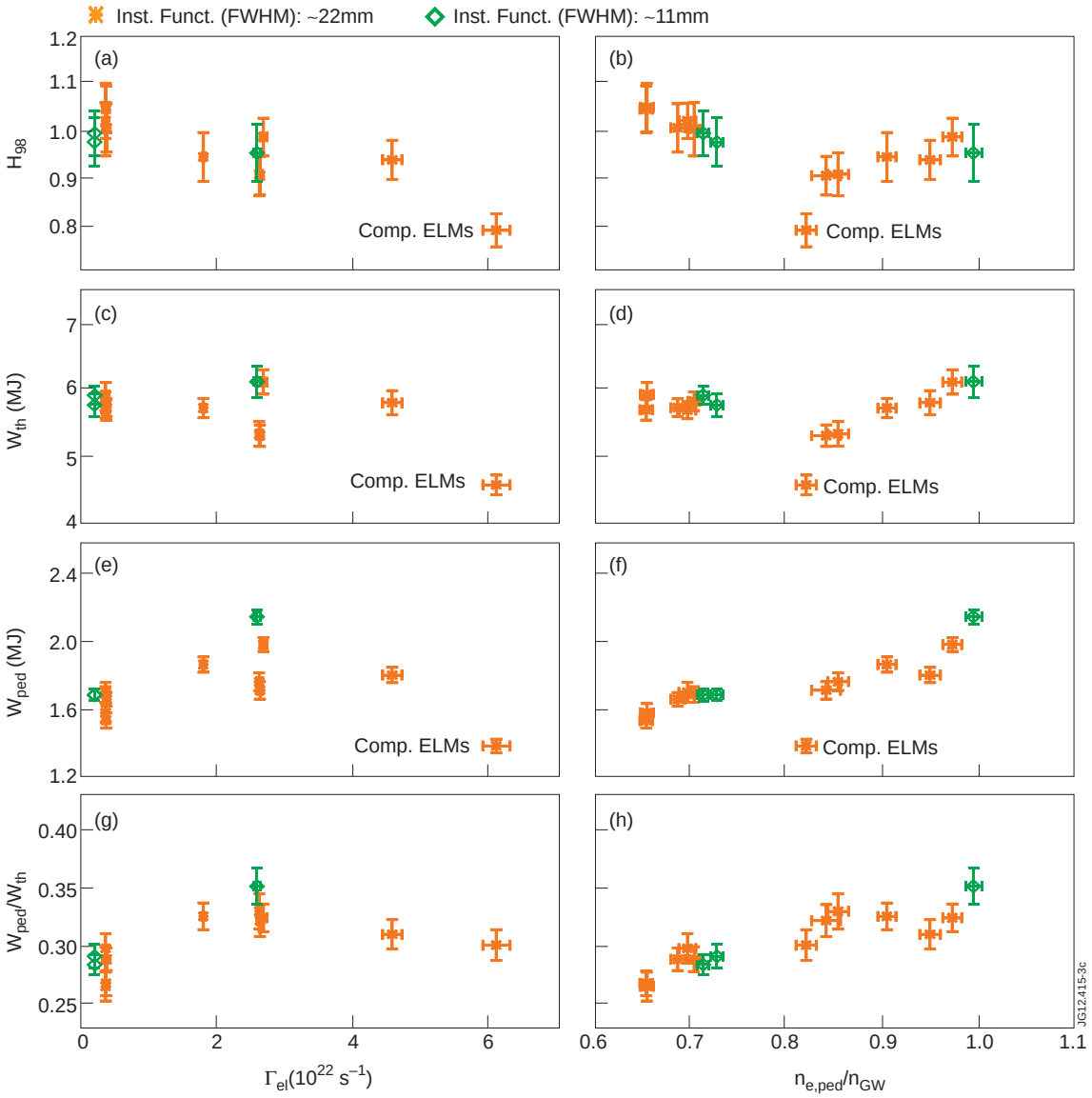

Figure 4.3: H_{98} as a function of (a) fuelling rate and (b) pedestal density. Total stored thermal energy (W_{th}) as a function of (c) fuelling rate and (d) pedestal density. Pedestal stored energy (W_{ped}) as a function of (e) fuelling rate and (f) pedestal density. Ratio of pedestal stored energy to total stored thermal energy (W_{ped}/W_{th}) as a function of (g) fuelling rate and (h) pedestal density. Figure distinguishes between pulses with low (orange) and high (green) resolution HRTS data. The pulse labelled Comp. ELMs has a compound ELMy regime.

Figure 4.3 (c) and 4.3 (d) show the total stored thermal energy (W_{th}) as a function of fuelling rate and pedestal density respectively. The stored thermal energy is calculated by correcting the measured diamagnetic energy (W_{DIA}) with the energy of the fast ions (W_{PET}) given by [101],

$$W_{th} = W_{DIA} - \frac{3}{2} W_{PET} \tag{4.1}$$

Similar to Figure 4.3 (a), Figure 4.3 (c) shows a minimal degradation of stored thermal energy as fuelling increases until the compound ELM transition. Like H_{98} as shown in Figure 4.3 (b), Figure 4.3 (d) shows W_{th} is approximately constant between $n_{e,ped}/n_{GW} \approx 0.65 - 0.75$, increases at higher fuelling and then degrades for the compound ELM transition.

The pedestal stored energy, W_{ped}, is calculated by evaluating the volume integral of the pressure profile capped at the pressure pedestal height. The integral is given by:

$$\begin{aligned} W_{ped}(J) &= \frac{3}{2}\int_V (p_i + p_e)\, dV \\ &= \frac{3}{2}\int_V e\,(n_i T_i + n_e T_e)\, dV \\ &\approx \frac{1}{4}\int_V e\,(13 - Z_{eff})\, n_e T_e dV \end{aligned} \tag{4.2}$$

where p_i and p_e are the ion and electron pressure profiles respectively in Pa; V is the plasma volume in m^3; e is a constant required for the conversion from eV to J and is equal to the elementary charge ($\approx 1.602 \times 10^{-19}$); n_i and n_e are the ion and electron density profiles respectively in m^{-3}; T_i and T_e are the ion and electron temperature profiles respectively in eV; and Z_{eff} is the average effective atomic charge. The pressure profile is calculated from the product of an mtanh fit [37] to the density and temperature HRTS data. The HRTS data selected for the fits in Figure 4.3 (e) and 4.3 (f) are ELM averaged over the stationary phase of a pulse. Equation 4.2 assumes $T_i \sim T_e$, justified for all pulses discussed here due to their high density and therefore strong ion-electron heat exchange coupling. Z_{eff} is averaged over the stationary phase of each pulse within the fuelling database and is assumed constant in radius. Z_{eff} ranges from 1.5 to 2.1. The expression for W_{ped} utilises the following relationship between n_i and n_e assuming carbon is the sole impurity,

$$n_i = \left(\frac{7 - Z_{eff}}{6}\right) n_e \tag{4.3}$$

The pedestal stored energy as calculated by Equation 4.2 is shown in Figures 4.3 (e) and 4.3 (f). In contrast to Figure 4.3 (a), Figure 4.3 (e) shows as the fuelling is increased, the pedestal stored energy also increases and peaks at a fuelling rate of $\Gamma_D \approx 2.6 \times 10^{22}$ el/s. At higher fuelling the pedestal stored energy then decreases. Figure 4.3 f shows the low fuelling pulses have low pedestal density and pedestal stored energy. The pedestal density and pedestal stored energy both peak at a fuelling of $\Gamma_D \sim 2.6 \times 10^{22}$ el/s. As the fuelling is further increased, towards the compound ELM transition, the pedestal density and pedestal stored energy both

degrade.

Figure 4.3 (g) and 4.3 (h) show the ratio of the pedestal stored energy to the total thermal stored energy (W_{ped}/W_{th}) as a function of fuelling rate and the pedestal density respectively. This ratio gives an indication of the profile peaking, which is the relative edge and core performance. The greater the core performance relative to the edge, the more peaked the profile. The profile peaking is not constant across the fuelling scan as W_{ped}/W_{th} ranges from 0.27 at low pedestal density ($n_{e,ped}/n_{GW} \approx 0.65$) to 0.35 at high pedestal density ($n_{e,ped}/n_{GW} \approx 1.0$). To summarise, Figure 4.3 (b) and 4.3 (d) show for Type I ELMy pulses there is minimal degradation in overall performance (H_{98} and W_{th}) up to $n_{e,ped}/n_{GW} \approx 1$, in agreement with [90].

4.3 ELM characterisation

The ELM type for the 2002 study was characterised as Type I ELMs at low fuelling and as mixed Type I/II ELMs at high fuelling levels [90].

A pure Type II ELMy regime is classified by the absence of large transient heat loads (Type I ELMs) and a minimal decrease in confinement (H_{98}) when compared to a Type I ELMy regime [102]. Type II ELMs produce a continuous power load on plasma facing components, similar to that of Type III ELMs. The degradation in confinement due to Type II ELMs is typically less than 10 %, distinguishing them from a larger reduction in confinement of $\approx 20 - 30$ % found in Type III ELMy regimes [100].

A transition from a Type I to a pure Type II ELMy regime is observed on AUG in single null configurations [103]. This transition is achieved by applying strong fuelling to exceed a collisionality threshold. Gas fuelling and plasma shaping, more specifically the proximity to Double Null (DN), are the two main methods of controlling the Type I to Type II transition [102].

JET results do thus far not show a pure Type II ELM regime in a single null configuration [28], but instead there is evidence for a mixed Type I/II ELMy regime for pulses with a high pedestal density where $n_e \geq 0.7 n_{GW}$, as seen by [90]. A mixed Type I/II ELMy regime exhibits increased inter-ELM losses (Type II) between Type I ELMs. The key findings from the new fuelling scan database, which exhibits the same mixed Type I/II behaviour, are presented below focusing on the ELM frequency dependence, inter-ELM build up of stored energy, the LH power threshold and magnetic fluctuations.

Figure 4.2 (h) and 4.2 (i) show the D_α emission for the low and high fuelling case respectively. The ELM frequency for a low and high fuelling pulse is 17.5 Hz and

7.8 Hz respectively. Figure 4.4 shows the ELM frequency for the entire database as a function of pedestal density. As observed by [90], the ELM frequency for the new database of high triangularity pulses decreases with increasing pedestal density.

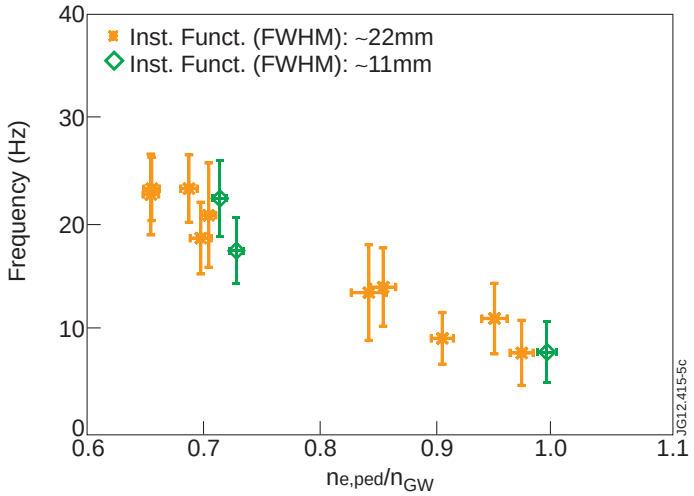

Figure 4.4: ELM frequency as a function of pedestal density normalised to the Greenwald density.

The explanation given by [90] for the decrease in ELM frequency is that increased inter-ELM losses (Type II activity) at higher pedestal density, increases the time taken to reach the critical pressure and therefore reduces the Type I ELM frequency.

For the mixed Type I/II ELMy regime to account for the ELM frequency variation, it would be expected that the energy build-up for a pulse exhibiting Type II inter-ELM activity, a high fuelling pulse, would be slower in comparison to a low fuelling pulse. Figure 4.5 compares the inter-ELM stored energy build-up of a high and low fuelling pulse as calculated from magnetic diagnostics. The build up after multiple ELM collapses are overlaid to improve temporal resolution, see Figure 4.5 (a). Figure 4.5 (b) shows the result of normalising the ELM synchronised data to a $5 - 10ms$ post-ELM window and then applying a moving average. Figure 4.5 (a) and (b) both show there is a difference in the build up between the two pulses and also that the build up of stored energy does not saturate.

The existence of mixed Type I/II ELMs is consistent with the decrease in ELM frequency across the fuelling scan although another factor which could influence the ELM frequency is the proximity to the LH power threshold, above which a transition from L to H-mode occurs. In, for example, [104] the ELM frequency is shown to reduce when the input power approaches the LH power threshold for a JET ELMy H-mode fuelling database.

The LH power threshold has been determined using the scaling derived from a multi machine database for P_{LH-08}, [105]. The total loss power is defined [105],

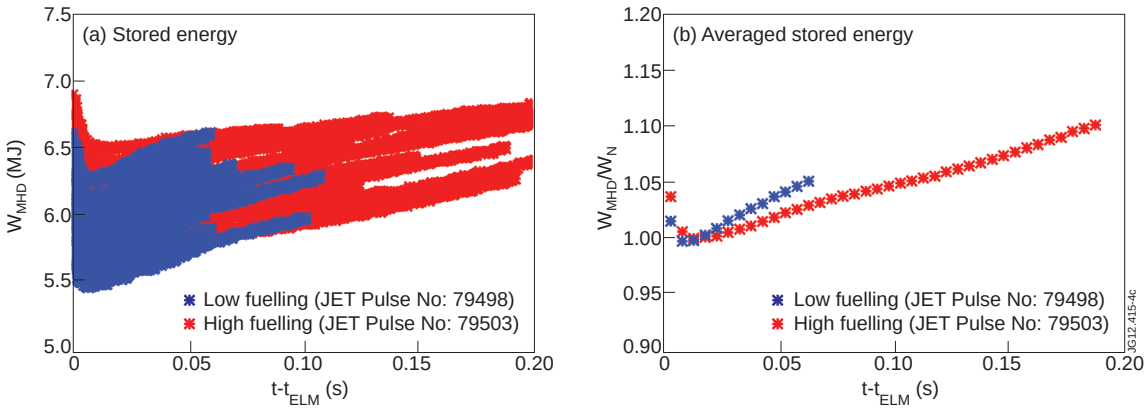

Figure 4.5: Build-up of stored energy (W_{MHD}) for the low and high fuelling cases as a function of time from the previous ELM. (a) shows the ELM synchronised data and (b) shows the result of first normalising the ELM synchronised data to a $5-10$ ms post-ELM window and then applying a moving average.

$$P_{loss} = P_{NET} - \frac{dW}{dt} \tag{4.4}$$

where P_{NET} is the total net input power and dW/dt is the rate of change in plasma stored energy. P_{NET} in MW is given by [101],

$$P_{NET} = P_{CX} + P_{ICRH} + P_{OHM} - P_{SHI} \tag{4.5}$$

$$P_{CX} = P_{NBI}\left(1 - \frac{1}{100}\exp\left(3.35 - 0.667 \cdot abs\left|I_p\right| - 0.2n_{e,la}\right)\right) \tag{4.6}$$

where P_{CX} in MW is the power deposited in the plasma due to NBI heating taking into account all losses, P_{ICRH} in MW is the input power due to Ion Cyclotron Resonant Heating (ICRH), P_{OHM} in MW is the input power due to ohmic heating, P_{SHI} in MW is the power lost due to NBI shine-through, P_{NBI} in MW is the input NBI power not taking into account losses, I_P in MA is the plasma current and $n_{e,la}$ in $\times 10^{-19}$ m^{-3} is the line average electron density.

The LH threshold power described by [105] refers to the power required to access H-mode. In the calculation of P_{loss} in stationary H-modes, the term dW/dt varies strongly during the ELM cycle. For this reason dW/dt at the end of the ELM cycle (70-99 %) has been used in the calculation as considered most relevant with respect to the ELM event.

Figure 4.6 shows the ratio of the total loss power (P_{loss}) to the LH threshold power (P_{LH-08}). Figure 4.6 shows that the ratio of P_{loss}/P_{LH-08} remains approximately constant, ≈ 1.1 from low to high fuelling (comparing green data-points) implying the ELM frequency is most likely independent of the proximity to the LH threshold.

The important comparison in Figure 4.6 is between the low and high fuelling pulses with high resolution HRTS data (green data points). However, it is noted the pulses with intermediate $n_{e,ped}/n_{GW}$ have a relatively high ratio of P_{loss} to P_{LH-08}. The heating power is fixed across the scan and there is no significant variation in dw/dt. A possible explanation is these pulses are the highest fuelling where the ELM behaviour transitions from mixed Type I/II towards Type III. Therefore P_{LH-08} may not be as relevant. Both P_{loss} and P_{LH-08} increase with $n_{e,ped}/n_{GW}$. It is also noted in terms of absolute values, the large ratio for the intermediate $n_{e,ped}/n_{GW}$ pulses is due to P_{loss} begin equivalent to the high $n_{e,ped}/n_{GW}$ pulses whereas P_{LH-08} is equivalent to low $n_{e,ped}/n_{GW}$ pulses.

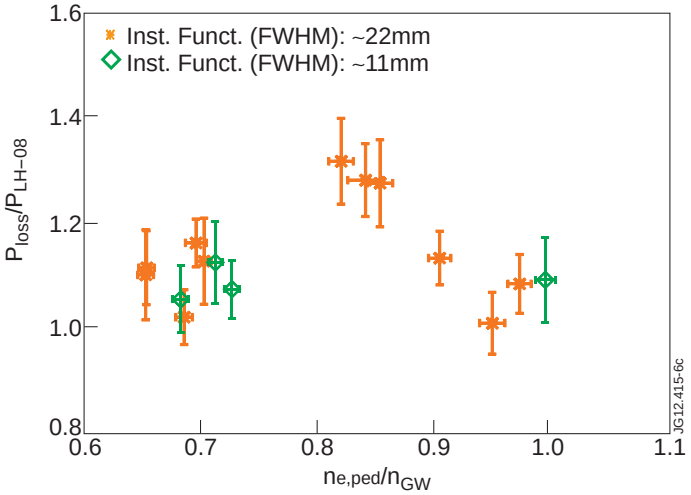

Figure 4.6: Ratio of P_{loss} to P_{LH-08} as a function of pedestal density normalised to Greenwald density where the ELM dependent parameter dW/dt is averaged over 70-99 % of ELM cycle during steady state phase of pulse.

Furthermore previous studies, [90, 102, 106, 107], have considered magnetic fluctuations when establishing the characterisation of mixed Type I/II ELMs. The Type II ELM activity between the Type I ELMs on JET coincides with an increase of the intensity of broadband magnetic fluctuations at low frequency ($< 40kHz$) and these MHD events are termed washboard modes. A detailed study by [106] discusses the causal link between washboard modes and increased inter-ELM transport referred to as Type II ELMs. It is thought washboard modes regulate the build up of pressure (stored energy) by enhanced inter-ELM transport (Type II ELMs).

The magnetic fluctuation behaviour of the new JET-C database presented in this study is consistent with [90]. Figure 4.7 shows the MHD fluctuation intensity for the high fuelling pulse in comparison to the low fuelling pulse increases at low frequency ($0 - 40$ kHz) consistent with an increase in washboard mode activity. There is also

a decrease in MHD fluctuation intensity at high frequency (above 40 kHz). This is visible from the spectrograms for the low and high fuelling pulses as shown by Figure 4.8 (a) and (b) respectively.

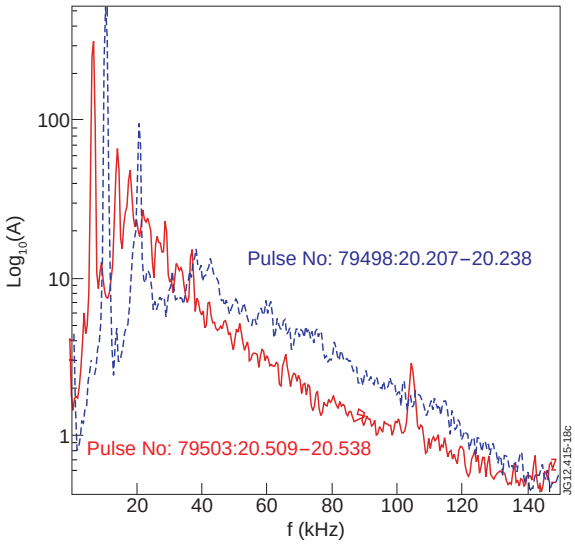

Figure 4.7: Comparison of MHD fluctuation intensity for a low (blue) and high fuelling (red) JET pulse as determined by averaging a Fourier spectra, vertical slices of the corresponding spectrogram (Figure 4.8), within a specified time interval ($t = 20.207 - 20.238$ s for the low fuelling pulse and $t = 20.509 - 20.538$ s for the high fuelling pulse). The intense low frequency peaks, for example for the low fuelling pulse (blue) at 12 kHz and 21 kHz, are associated with core MHD activity and should be disregarded when comparing of the broadband magnetic fluctuation behaviour associated with washboard modes.

In summary, the observations on the ELM regime in this study are consistent with those in [90] and a transition from the pure Type I ELMs to a mixed Type I/II ELMy regime is a most likely reason for the non-standard ELM behaviour. Following the convention as laid out in [90], the low and high fuelling example pulses referred to within this study are termed as pure Type I and mixed Type I/II ELMy H-modes.

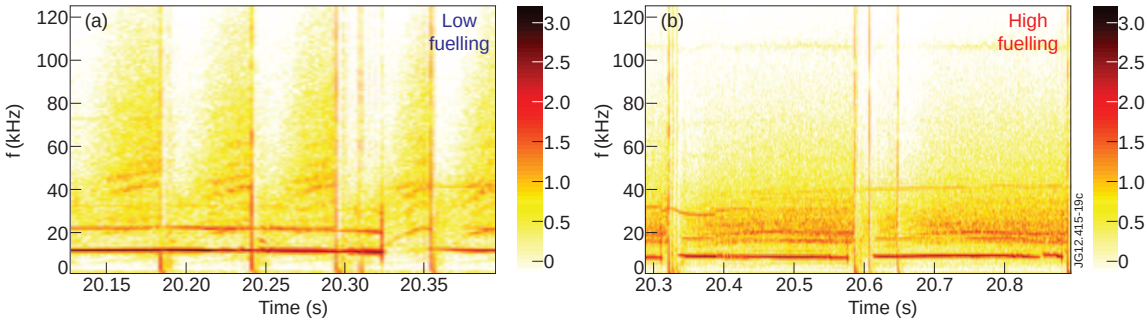

Figure 4.8: Magnetic frequency spectrograms from a coil low-field side for (a) low fuelling (JPN: 79498) and (b) high fuelling (JPN: 79503) pulses. The numbers to the right of the colour scale denote log_{10} of the amplitude [106]. The narrow intense red vertical lines are the Type I ELMs and the narrow intense red horizontal lines are associated with core MHD activity. The washboard mode activity is indicated by the inter-ELM more broadband ubiquitous yellow/orange features. There is washboard mode activity in both low and high fuelling pulses however the difference is the relative intensity of low and high frequency components of these washboard modes. For the low fuelling pulse the toroidal mode number (n) for the easily distinguishable individual bands are $n = -1$ to -6. For the high fuelling pulse n ranges from -2 for the lower frequency broad band end of the spectrum to -6 for the higher frequency end of the spectrum.

4.4 Pedestal measurements

In section 4.2.3 we saw that the increase in stored thermal energy above $n_{e,ped}/n_{GW} = 0.8$ is largely due to an increase of the pedestal stored energy. To understand why the pedestal performance improves when the fuelling level is increased this section quantifies the behaviour of the H-mode pedestal within the new JET fuelling database, utilising electron temperature (T_e) and density (n_e) profiles produced by the JET HRTS system. The pedestal structure, i.e. the width and height, and pedestal dynamics are quantified by least squares mtanh fits to ELM synchronised HRTS profiles, see Chapter 3. The mtanh fits to the JET HRTS profiles presented in this section are used in Section 4.5.2 when evaluating the Peeling Ballooning stability and comparing experimental results to EPED1 predictions for the pedestal pressure.

4.4.1 Pedestal fitting: mtanh and linear forms

Figure 4.9 shows the result of a least squares mtanh fit to determine the pedestal width and height. Figure 4.9 (a)-(d) show the selected overlaid HRTS temperature and density profiles (open circles) and the corresponding mtanh fits (dashed lines) for the pure Type I pulse and mixed Type I/II pulse respectively as shown in Figure 4.2. Comparison of the pure Type I and mixed Type I/II pulses detailed in Figure 4.9 show both the temperature and density pedestals are wider for the mixed Type I/II pulse in comparison to the pure Type I pulse. Further still, the pedestal temperature is smaller by ≈ 0.1 keV (12 %) whereas the pedestal density is significantly larger by $\approx 2.6 \times 10^{19}$ m^{-3} (37 %), as a consequence the pedestal pressure increases by 20 %.

Beyond the extent of the foot of the mtanh fit function, see Figure 4.9, there is minimal data (as discussed in the context of the upper and lower HRTS line of sight in Chapter 3) weakening the validity of the mtanh fit in this region. Least squares linear fits were performed on the same data selected for the mtanh fits to provide a comparison, see Figure 4.10 [33]. Figure 4.10 (a)-(d) show the linear fit to the selected overlaid HRTS temperature and density profiles for the pure Type I and mixed Type I/II pulse respectively. In agreement with the mtanh fit, the linear fits suggest the temperature and density pedestal is wider for the mixed Type I/II pulse in comparison to the pure Type I pulse. Further still, the pedestal temperature and pedestal density, determined from the linear fit, show a similar small decrease and significant increase respectively. In comparison to the mtanh fit the linear fit width is larger for both the temperature and density pedestal. The temperature pedestal height from the linear fit is marginally larger in comparison to the mtanh

fit. Interestingly the density pedestal height is similar for the mtanh and linear fit due to the relatively flat core gradient accurately constraining the knee of the profile.

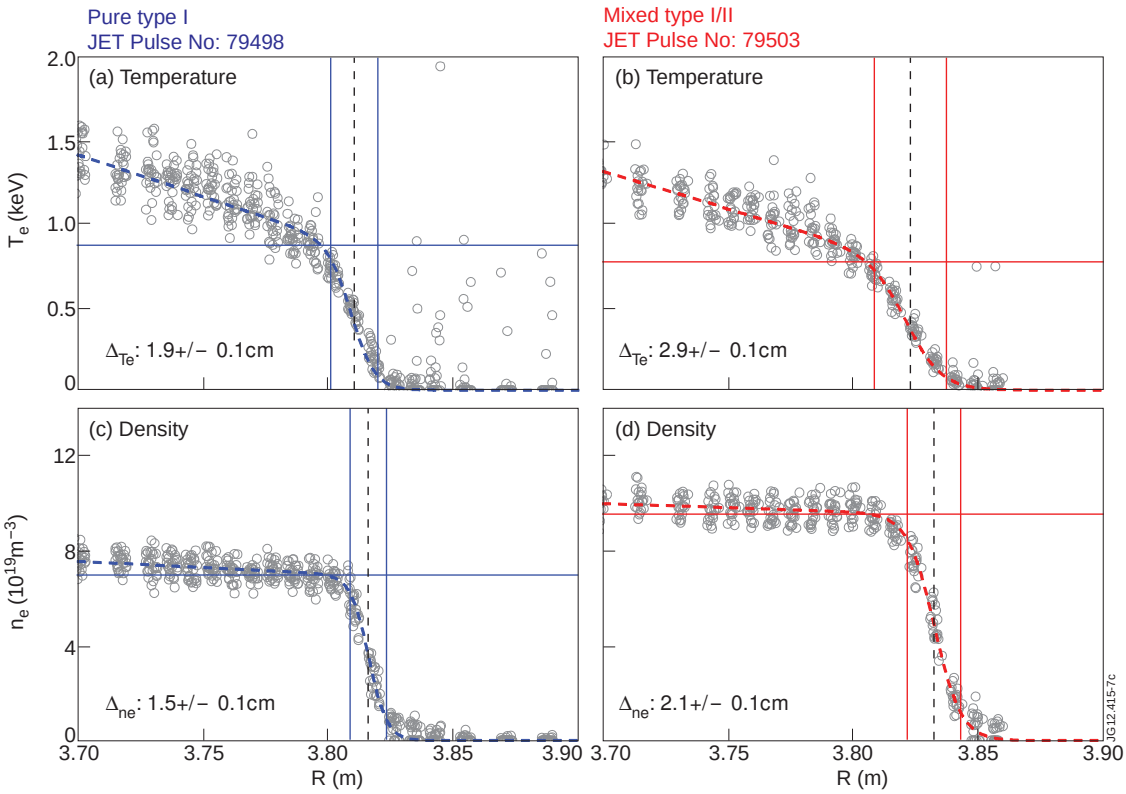

Figure 4.9: Example of mtanh fits for temperature and density JET HRTS profiles for (a), (c) low (blue) and (b), (d) high (red) fuelling pulses.

Figure 4.11 details a comparison of linear and mtanh fits for the temperature pedestal width, the density pedestal width, the temperature pedestal height and the density pedestal height. This comparison includes all pulses within the new JET fuelling database. As well as considering HRTS profiles from the last 70-99 % of the ELM cycle, profiles within 0-10 %, and 0-100 % (i.e. all time windows) of the ELM cycle were also considered.

The linear density and temperature pedestal width is larger than the corresponding mtanh widths as shown by Figure 4.11 (a) and (b) respectively, due to a difference in the definition of the pedestal widths for both fits. Similarly Figure 4.11 (c) shows the linear temperature pedestal height is larger than the mtanh pedestal height. Figure 4.11 (d) shows the density pedestal heights for the linear and mtanh fits are in good agreement. To summarise there are some deviations between pedestal widths and heights when comparing linear and mtanh fits, see Figure 4.11. These deviations are purely a consequence of the different fit functions. The data trends are still consistent.

Figure 4.11 (a) and (b) show the post-ELM widths (orange data points) are larger than the pre-ELM widths (red data points) indicating both the density and tem-

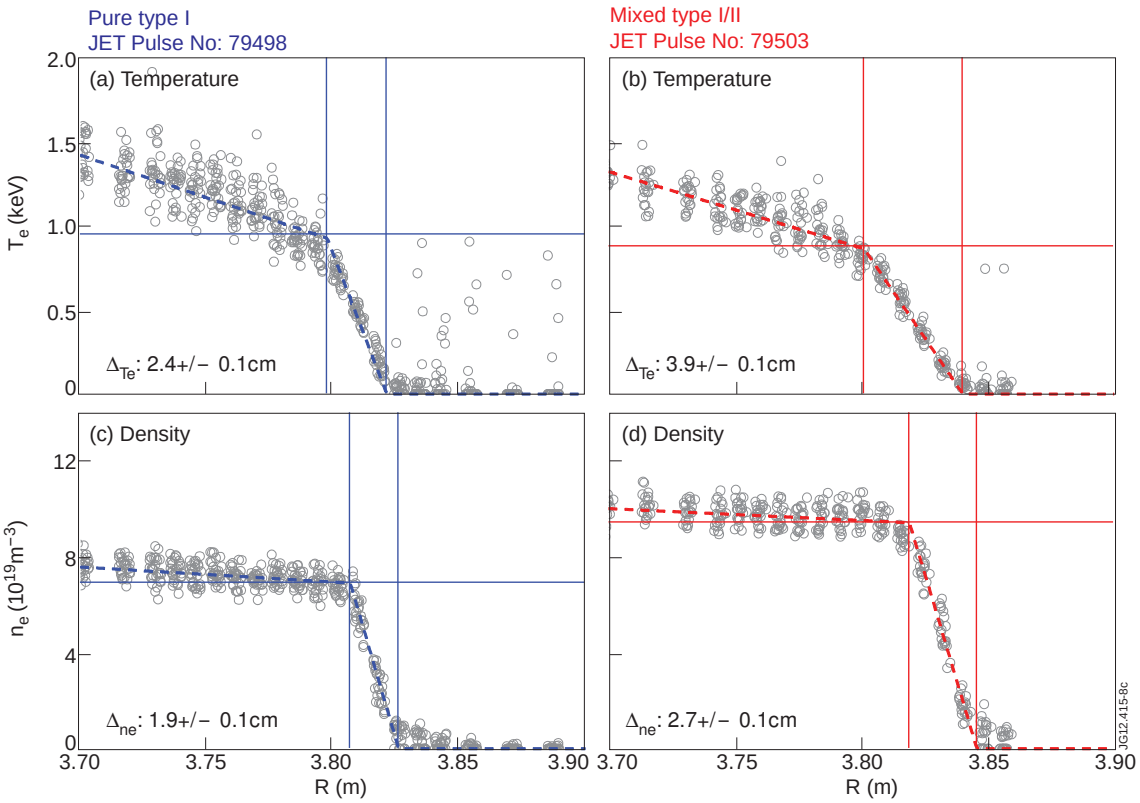

Figure 4.10: Example of linear fits for temperature and density JET HRTS profiles for (a), (c) low (blue) and (b), (d) high (red) fuelling pulses.

perature pedestal width narrows during the ELM cycles. The pedestal structure evolution is discussed in more detail in section 4.4.3.

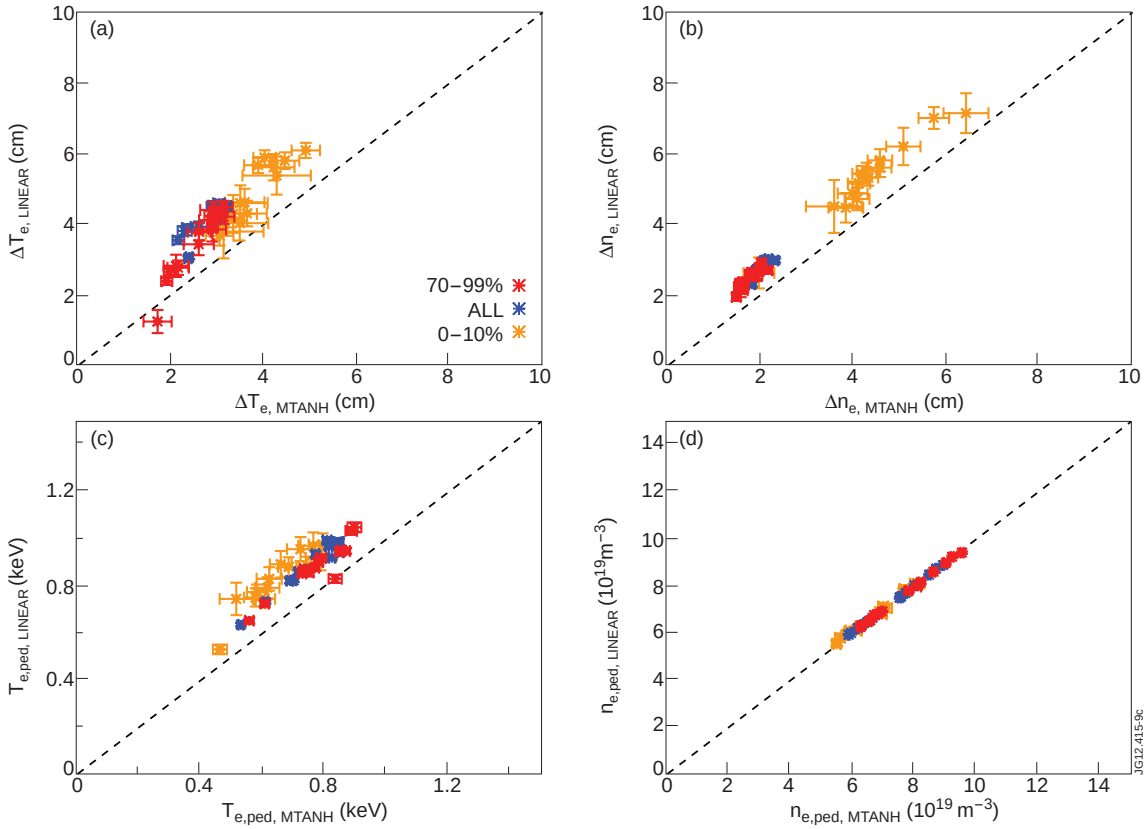

Figure 4.11: Comparison of linear and mtanh fit results for (a) temperature pedestal width, (b) the density pedestal width, (c) the temperature pedestal height and (d) the density pedestal height for all pulses within the new JET fuelling database.

4.4.2 Pedestal structure

In this study we refer to the pedestal structure as the width and height of the pedestal. The examples of mtanh and linear fits in the previous section, Figure 4.9 and 4.10 respectively, show for the mixed Type I/II pulse in comparison to the pure Type I pulse: the temperature and density pedestal widens; the pedestal temperature is lower and the pedestal density is higher. This section presents the measurements of the pre-ELM (70-99 %) pedestal structure for all pulses within the new fuelling scan database.

Figure 4.12 shows the variation of pedestal width with respect to the pedestal density. The temperature and density widths for pulses with low (FWHM $\approx$ 22 mm) resolution HRTS profiles, the orange points, are more scattered and have larger error bars in comparison to the pulses with high ($\approx$ 11mm) resolution HRTS pulses, the green points. This is understandably so as the actual pedestal width, i.e. $1.5 - 2.0$ cm for the density and $2.0 - 3.0$ cm for the temperature pedestal is of the same order as the width of the instrument function for the lower resolution cases [63]. The comparison of relative scatter between low and high resolution HRTS pulses may be misleading due to there being more low resolution HRTS pulses. The low resolution HRTS pulses for the temperature pedestal width are particular scattered and this may be due to larger errors associated with the weighted deconvolution technique [73]. The high resolution data from Figure 4.12 (a) and 4.12 (b) shows evidence for the temperature and density pedestal widening as the pedestal density increases. The data set is limited due to no pulses with intermediate pedestal densities.

Figure 4.13 shows the pedestal temperature versus pedestal density for all pulses within the current fuelling database. The two main groups of pulses correspond to pure Type I (low fuelling) and mixed Type I/II (high fuelling) ELMy H-modes. The mixed Type I/II pulses have a lower pedestal temperature and higher pedestal density relative to the pure Type I pulses, see Figure 4.9. Further still, as indicated by the isobars, black dashed lines, the mixed Type I/II pulses have higher pedestal pressure. The pure Type I pulses are all between the lower (p_L) and central (p_C) isobars whereas the mixed Type I/II pulses are between the central (p_C) and upper (p_U) isobars. The degraded performance of the compound ELMy pulse is reflected in the lowest pressure pedestal due to a reduction in both T_e ($T_{e,ped} \approx 0.55$ keV) and n_e ($n_e \approx 7.8 \times 10^{19}$ m^{-3}).

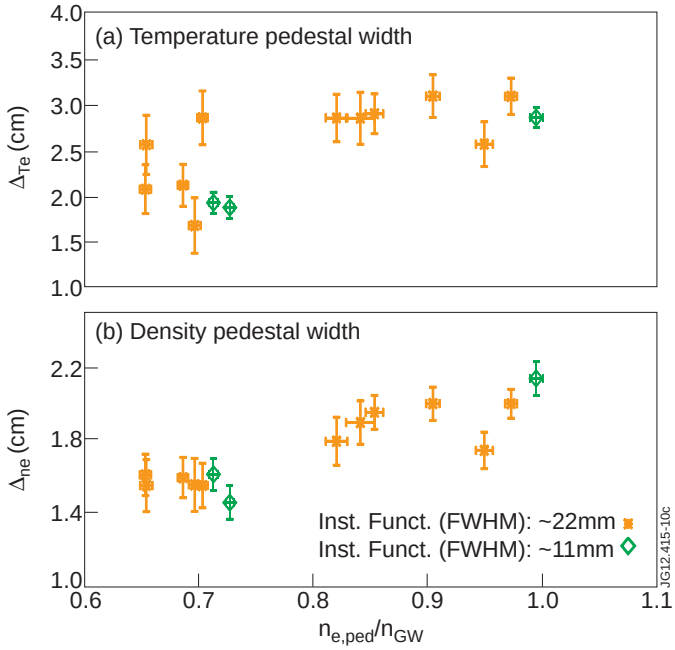

Figure 4.12: (a) Temperature pedestal width and (b) density pedestal width as a function of density pedestal height normalised to Greenwald density. Pedestal widths determined from mtanh fits incorporating a weight deconvolution technique for the electron temperature [73] and classic deconvolution technique for the electron density.

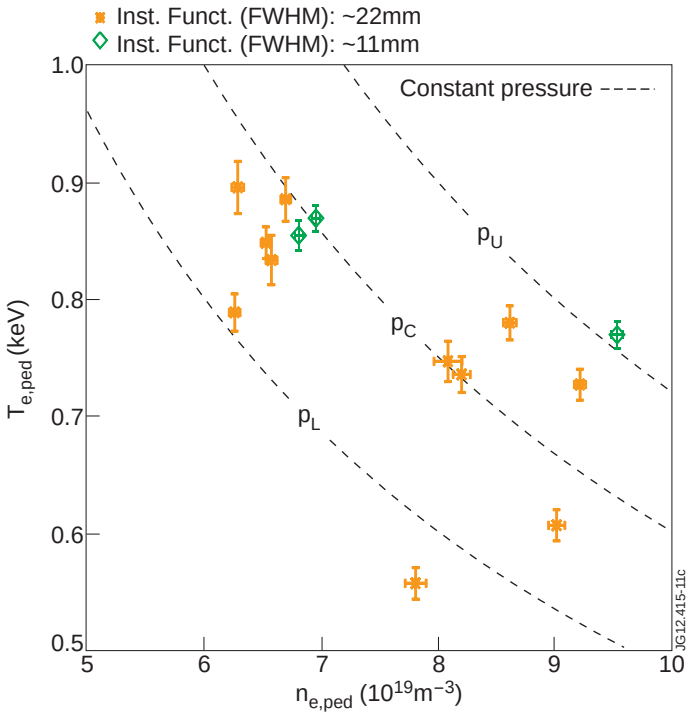

Figure 4.13: Pedestal temperature versus pedestal density for all 14 discharges within the new fuelling database. There are three isobars indicated by black dashed lines. p_C is the central isobar. The lower isobar, p_L is a 20 % decrease with respect to p_C and the upper isobar, p_U a 20 % increase, also with respect to p_C.

4.4.3 Pedestal dynamics

The HRTS profiles for two plasmas with high resolution data; a pure Type I and a mixed Type I/II pulse from the new JET fuelling database, have been windowed from 0-10 %, 10-40 %, 40-70 % and 70-99 % of the ELM cycle. The corresponding mtanh fits quantify the pedestal width and height for each region of the ELM cycle. The initial 0-10 % of the ELM cycle can be considered as a transient recovery phase after the ELM crash. As a result the pedestal width and height from the fit corresponding to 0-10 % of the ELM cycle may not follow a trend described by the rest of the data.

Figure 4.14 (a) shows the evolution of the temperature and density pedestal width for a pure Type I and mixed Type I/II pulse. For both pulses the temperature and density pedestals jump from large post-ELM pedestal widths ($\Delta_{ne} \approx 5.0 - 5.7$ cm, $\Delta_{Te} \approx 4.0 - 4.5$ cm), corresponding to profiles from 0-10 % of the ELM cycle, to smaller intermediate values ($\Delta_{ne} \approx 2.0$ cm, $\Delta_{Te} \approx 3.0$ cm). The pure Type I pulse then progressively narrows during the rest of the ELM cycle to pre-ELM widths of $\Delta_{ne} = 1.5$ cm and $\Delta_{Te} = 1.9$ cm. In comparison, the pre-ELM widths for the mixed Type I/II pulse are $\Delta_{ne} = 2.1$ cm and $\Delta_{Te} = 2.9$ cm as the pedestal widths remain approximately constant for 10-40 %, 40-70 % and 70-99 % of the ELM cycle. The inter-ELM evolution of the density pedestal width, as observed using HRTS, has been verified using Li-beam measurements at the plasma edge for a pure Type I ELMy pulse and mixed Type I/II ELMy pulse [108].

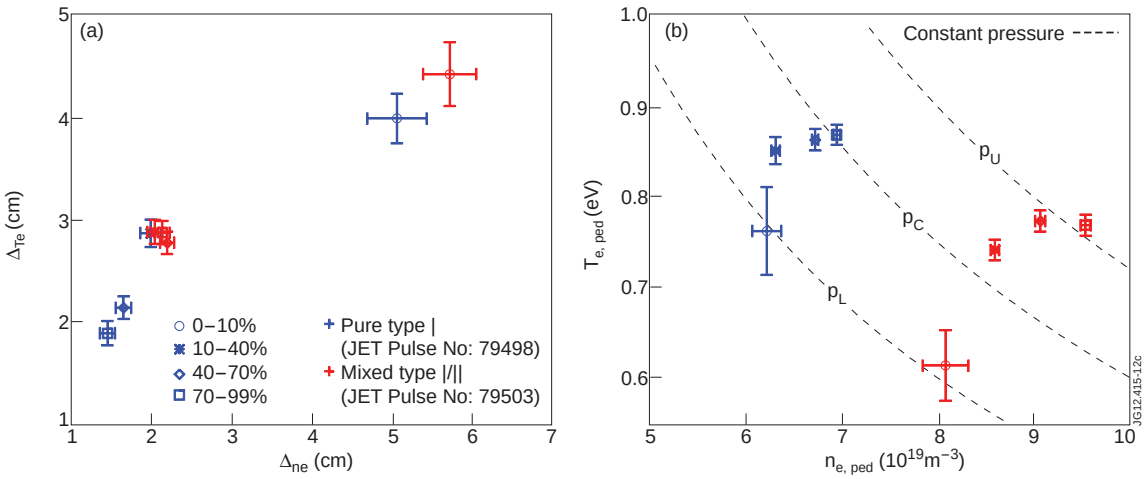

Figure 4.14: Evolution of (a) temperature and density pedestal width, and (b) temperature and density pedestal height for low (blue) and high (red) fuelling pulses. Identical to Figure 4.13, there are three isobars indicated by black dashed lines. p_C is the central isobar. The lower isobar, p_L is a 20 % decrease with respect to p_C and the upper isobar, p_U a 20 % increase, also with respect to p_C.

The evolution of the temperature and density pedestal height during the ELM cycle for a pure Type I and mixed Type I/II pulse is shown by Figure 4.14 (b). Initially

the temperature pedestal height rapidly grows, slowing down towards the end of the ELM cycle and for the mixed Type I/II pulse the temperature pedestal height saturates. The density pedestal height, for both pulses, increases throughout the ELM cycle. Overall the pedestal pressure increases, for both pulses, during the ELM cycle. The pure Type I pulse is at relatively high temperature and low density in comparison to the mixed Type I/II pulse.

Figure 4.15 (a) and (b) show the pressure profiles determined from the temperature and density mtanh fits corresponding to 0-10 %, 10-40 %, 40-70 % and 70-99 % of the ELM cycle. Figure 4.15 (c) and (d) show the derivative of these pressure profiles with respect to normalised flux. Figure 4.15 focuses on the two pulses considered throughout this Chapter. Figure 4.15 (a) and (c) corresponds to the pure Type I pulse. Figure 4.15 (b) and (d) corresponds to the mixed Type I/II pulse. The trends shown by Figure 4.14 can also been seen in Figure 4.15.

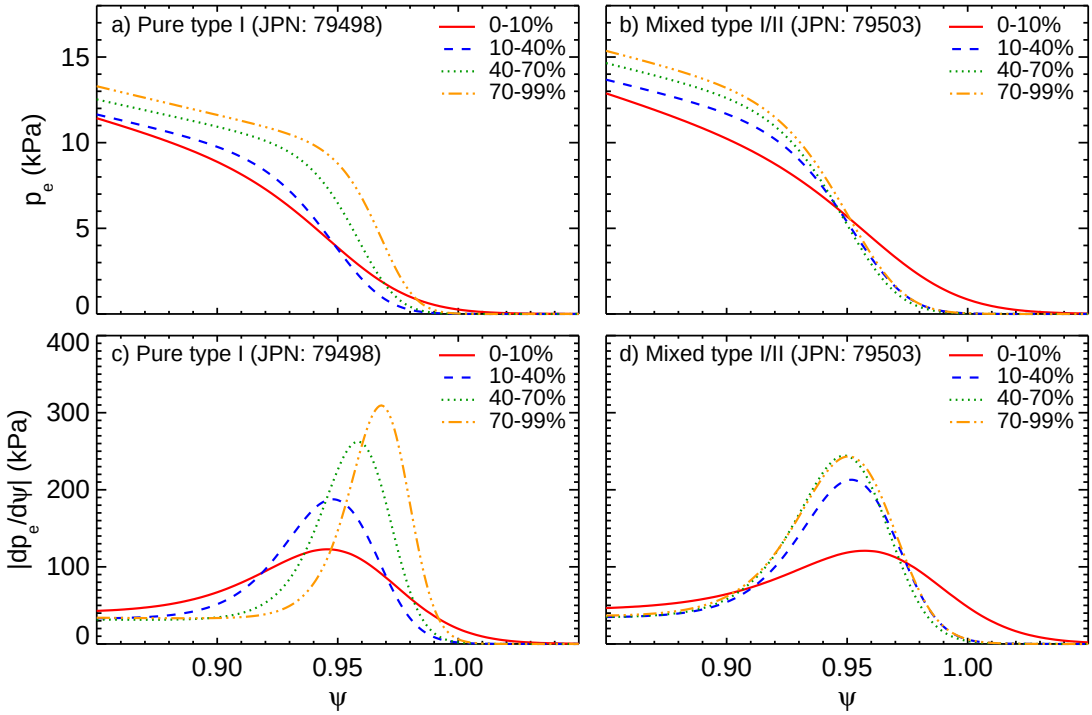

Figure 4.15: (a), (b) Pressure profiles and (c), (d) derivative of pressure profiles corresponding to 0-10 % (red), 10-40 % (blue), 40-70 % (green) and 70-99 % (orange) of the ELM cycle for (a), (c) pure Type I and (b), (d) mixed Type I/II JET pulses.

The pressure pedestal for the pure Type I pulse narrows during the ELM cycle, as clearly seen in Figure 4.15 (c). This is consistent with Figure 4.14 (a). The peak pressure gradient does not saturate during the ELM cycle. The position of the peak pressure gradient shifts radially outwards by ≈ 0.25 % of Ψ during the ELM cycle suggesting the entire pedestal also moves radially outwards.

Disregarding the profile for the initial 0-10 % of the ELM cycle, the pressure pedestal

width is relatively constant for the mixed Type I/II pulse, see Figure 4.15 (d). Once again this is consistent with Figure 4.14 (a). The peak pressure gradient increases from 10-40 % to 40-70 % and then remains constant from 40-70 % to 70-99 %. The lack of variation in peak pressure gradient position suggests a minimal shift in pedestal position during the ELM cycle.

The evolution of the pedestal, as described above, can be compared to observations on other devices. At DIII-D a widening of the electron density, temperature and pressure pedestal during the ELM cycle was observed in plasmas with the so-called ITER baseline shape [66, 109]. This widening is consistent with a combined Kinetic Ballooning (KB) and PB model where the pedestal width increases during the ELM cycle following a KB gradient limit, until the ELM is triggered when the PB limit is reached [43]. Similar observations were found in MAST where there is also a widening of the pressure pedestal in between ELMs [69, 70]. The extent of the barrier is again found to be limited by KB modes and this was confirmed by local gyrokinetic analysis.

However, in the cases studied here, the inter-ELM evolution of the JET pedestal is different from that typically observed in other tokamaks such as DIII-D and MAST. In the analysis presented above the JET H-mode pedestal width narrows or saturates during the ELM cycle. The difference in the dynamics between MAST and JET is further discussed in [43].

Instead of showing the pressure profiles and corresponding derivatives as a function of normalised flux, as in Figure 4.15, the position of the profiles can be corrected such that the separatrix temperature is 100 eV, see Figure 4.16. This is to be consistent with the two-point model, as described by [110], which relates the upstream temperature to the divertor temperature without modelling the variation in temperature as a function of distance along the scrape off layer. The model assumes strong thermal conduction along flux tubes connecting the upstream and downstream temperature measurements such that there is no particle flows. The only exception is the region at the transition from the plasma to the surface where an electrostatic sheath is formed [110]. Furthermore, the model also assumes there is no particle or energy loss along the flux tubes. This allows the divertor temperature limit to be translated to the upstream separatrix temperature at the bottom of the pedestal resulting in a maximum shift, for the profiles presented here, of ≈ 2.3 % of Ψ. The trends in pedestal position shown in Figure 4.16 are consistent with Figure 4.15. As most notably even after correcting the profile positions the peak gradient for the pure Type I pulse (Figure 4.16(c)) still shifts radially outwards, albeit the magnitude of the shift appears smaller towards the end of the ELM cycle. These corrected profiles are used in the next section when modelling the PB stability boundary using MISHKA-1.

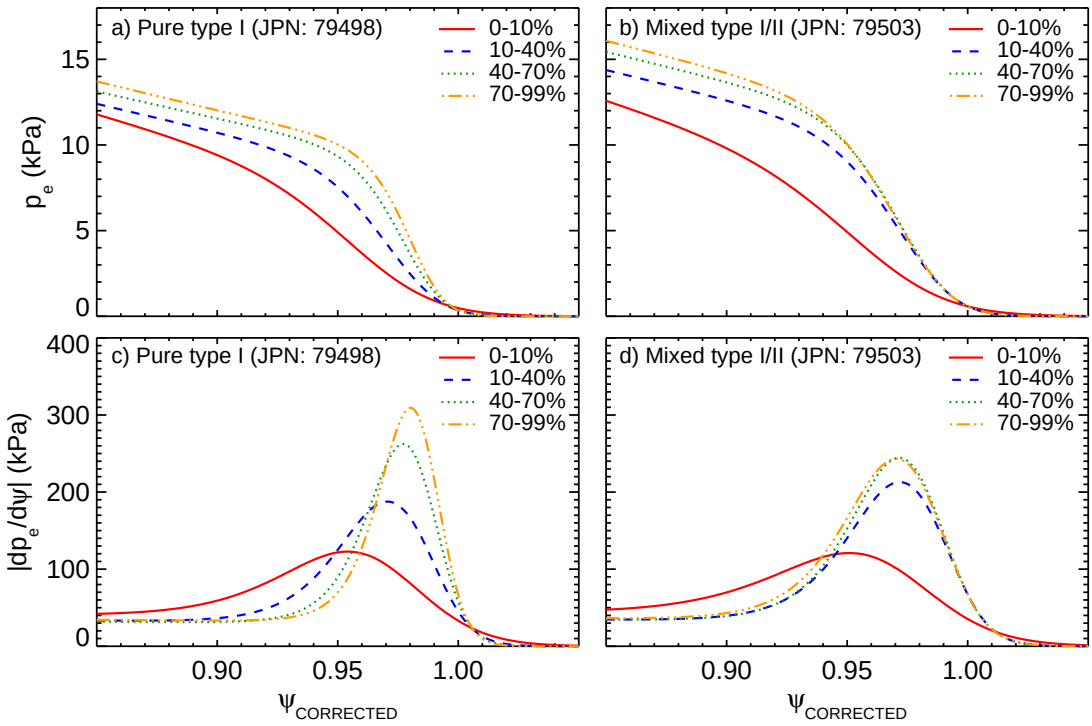

Figure 4.16: (a), (b) Pressure profiles and (c), (d) derivative of pressure profiles throughout ELM cycle for (a), (c) pure Type I and (b), (d) mixed Type I/II JET pulses (similar to Figure 4.15) as a function of normalised flux corrected such that the separatrix temperature is 100 eV.

4.5 Comparison with models

4.5.1 Pedestal stability analysis

Figure 4.17 shows the result of the PB stability analysis performed by MISHKA-1 [27], as described in Section 1.8. The stability diagrams presented in this section use the dimensionless maximum pressure gradient (α_{max}) [111] instead of the p'$_{ped}$. Figure 4.17 (a) and 4.17 (b) show operational points representing the state of a plasma during the ELM cycle for the pure Type I and mixed Type I/II pulses in Figure 4.9.

The change in colour from blue through to red corresponds to an increase in the growth rate of the most unstable mode. A contour of constant growth rate, in this case $\gamma = 0.03\omega_A$, is used to define the stability boundary. The proximity of the point to the stability boundary indicates the stability of the plasma edge at the time corresponding to the input profile. The location of the stability boundary depends on the pedestal width therefore the stability boundary is re-calculated for each input profile.

Figure 4.17 (a) and (b) show the stability boundary and operational point corres-

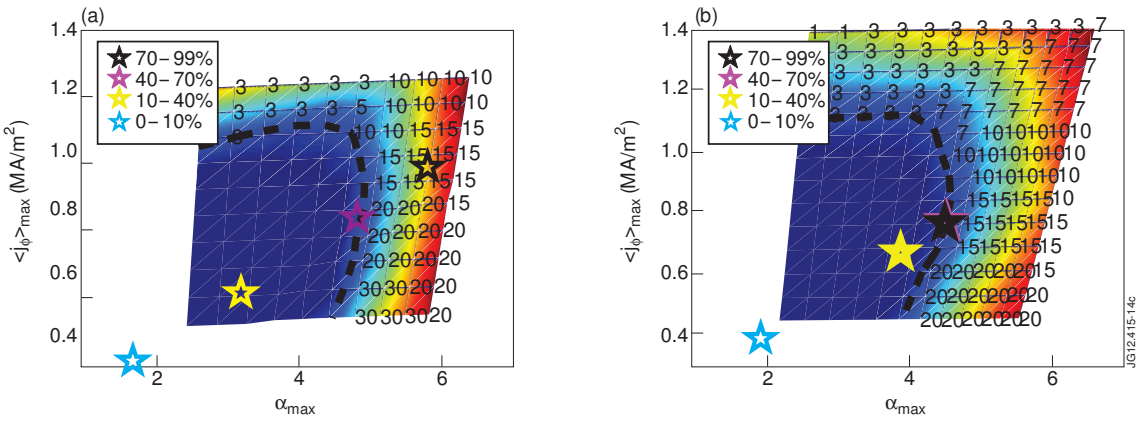

Figure 4.17: Stability analysis for (a) pure Type I (JPN: 79498) and (b) mixed Type I/II (JPN: 79503) pulse. Analysis performed by MISHKA-1, using mtanh fits to HRTS T_e and n_e profiles as an input.

ponding to the plasma state at the last 70-99 % of the ELM cycle. The operational points for 0-10 %, 10-40 % and 40-70 % have been also overlaid to give an indication of relative stability during the ELM cycle but the boundary strictly only applies to the 70-99 % data point, the black star. The proximity of each operational point to its true boundary has been preserved by scaling the position of the operational point just along the normalised pressure gradient axis (as the plasmas are ballooning limited) relative to the 70-99 % boundary.

The pure Type I pulse becomes progressively more unstable during the ELM cycle, as expected from the pedestal evolution shown by Figure 4.14 and 4.15. The pre-ELM operational point for the pure Type I pulse is over the stability boundary, in the unstable region. The operational point for the mixed Type I/II pulse initially evolves towards the stability boundary until the last 40-70 % and 70-99 % of the ELM cycle. These two operational points are similar due to near identical input profiles provided to the code. The pure Type I and mixed Type I/II pulses are both most unstable to the $n = 15$ mode.

A sensitivity analysis has been performed to quantify the uncertainties. Variations in the input to MISHKA-1 have been implemented for the point corresponding to the last 70-99 % of the pure Type I pulse, as shown by Figure 4.18.

The largest deviation from the 70-99 % operational point for the pure Type I pulse, the black star shown by Figure 4.17 (a), is due to a 0.5 % shift in normalised flux of the pressure profile. Figure 4.18 (a) shows both the stability boundary and operational point have shifted closer together and therefore the plasma is not as deeply unstable. Also the operational point is on the ballooning boundary rather than the PB corner.

The total pressure profile, an input to MISHKA-1, is dependent on the effective atomic charge (Z_{eff}) through the ion density, see Equation 4.7.

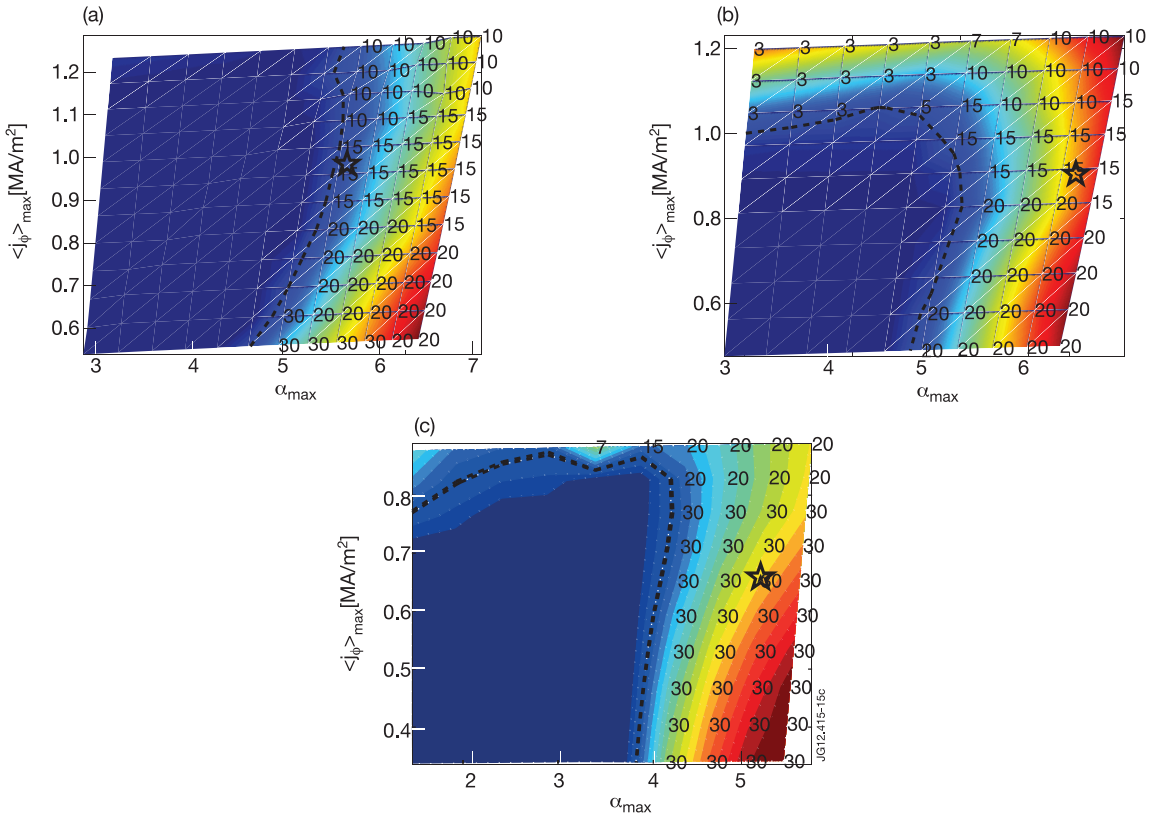

Figure 4.18: Variation in PB stability analysis when (a) applying an inward shift of 0.5 % in poloidal flux, (b) using $Z_{eff} = 1$ and (c) matching the core and pedestal ion temperature (T_i) gradient. The operation point corresponds to the last 70-99 % of the ELM cycle for the pure Type I pulse (JPN: 79498).

$$p = n_e T_e + n_i \left(n_e, Z_{eff}\right) T_i \tag{4.7}$$

Consequently any variation in Z_{eff} would influence the PB stability analysis. Experimentally in hydrogenic plasmas Z_{eff} is found to be ≈ 2 due to impurities. Figure 4.18 (b) shows there is a minimal change in the position of the operational point when Z_{eff} is set to 1.

The results presented by Figure 4.17 all assume the ion temperature is equivalent to the electron temperature ($T_i = T_e$). This is not always the case, particularly in a low collisionality, highly NBI fuelled plasma. An alternative constraint for T_i is assuming the core gradient is maintained into the pedestal region and the ion profiles do not have a steep gradient region at the plasma edge. The resulting profile has a minimal effect on the stability analysis, see Figure 4.18 (c). The operational point moves marginally towards the ballooning region at low J_{sep} and high α.

To summarise, when quantifying the sensitivity of the PB stability analysis, a shift in normalised poloidal flux (0.5 %) of the pressure profile resulted in the only significant deviation of the operational point. The operational point for the pure Type I pulse,

for 70-99 % of the ELM cycle, is still at critical stability. The physical interpretation of the stability analysis has not changed due to the sensitivity analysis. The variation in Z_{eff} and matching core and edge T_i gradient both result in minor deviations.

As shown by Figure 4.12 and 4.13, the mixed Type I/II pulse has a wider pedestal and is able to reach a higher pedestal pressure. In the context of PB theory there are two competing factors influencing the achievable pedestal pressure with respect to a variation in pedestal width. First, a wider pressure pedestal results in a lowering of the PB stability boundary due to PB modes becoming more unstable at lower pressure gradient. However, for a comparable pressure gradient, a wider pedestal can still result in an increased pedestal height. As the mixed I/II pulses from the new JET fuelling database reach a higher pressure when the pedestal widens this suggests the lowering of the stability limit is not the dominating factor.

4.5.2 EPED comparison

The pedestal predictions from two versions of the EPED model, EPED1 and EPED1.62, are presented in this section. For the new fuelling database c_1 ranges between 0.072 and 0.078 with an average of 0.076. This is in good agreement with the value of c_1 used in EPED1. The average ratio of predicted to observed pedestal width is 1.01 ± 0.23 for EPED1 and 1.00 ± 0.20 for EPED1.62. Figure 4.19 shows a comparison of the $\sqrt{\beta_{pol,ped}}$ scaling relationship embedded in EPED1 (black dashed line) and EPED1.62 (blue shaded region) to the experimental measurements (orange and green points). The measured pedestal width increases with increasing measured $\beta_{pol,ped}$ in agreement with the $\sqrt{\beta_{pol,ped}}$ scaling however the broadening of the pedestal width is stronger than expected. Figure 4.19 also shows the EPED1 pedestal width predictions (black diamonds) as a function of predicted $\beta_{pol,ped}$. For the three high resolution pulses in the database a grey line connects the measurement and EPED prediction data points. This highlights that EPED over predicts $\beta_{pol,ped}$ (and consequently Δ) at low fuelling for the pure Type I pulse whereas at high fuelling for the mixed Type I/II pulse EPED under predicts $\beta_{pol,ped}$. This is discussed further below when comparing the observed and predicted pedestal pressure.

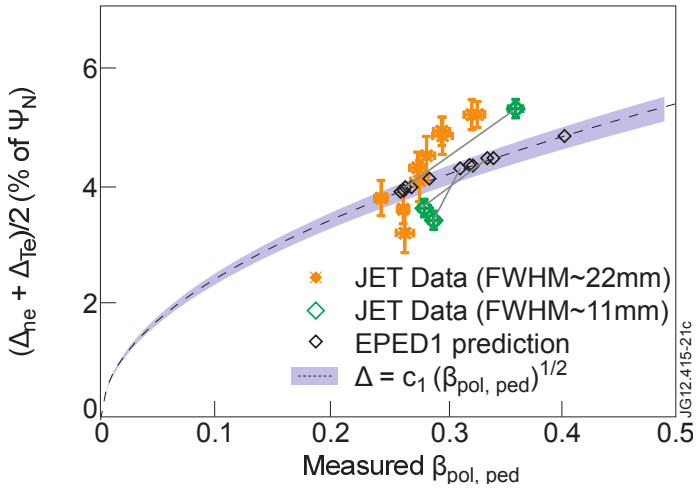

Figure 4.19: Experimental measurements of pedestal width as a function of measured $\beta_{pol,ped}$ (orange and green points) in comparison to $sqrt\beta_{pol,ped}$ scaling relationship embedded in EPED1 (black dashed line) and EPED1.62 (blue shaded region). The blue shaded region reflects the variation in c_1 as calculated using the BCP method. The EPED1 predictions of pedestal width (black diamonds) are shown as a function of predicted $\beta_{pol,ped}$ where the predictions for the three high resolution pulses have been matched up to the corresponding experimental measurements (grey line).

The EPED1 model has previously been compared to a large dataset of low and high triangularity baseline and hybrid discharges on JET [43, 64, 112]. These previous studies have found good statistical agreement with the model, with the average ratio of predicted to observed pedestal pressure of 0.97 ± 0.21. These previous comparisons are shown, along with a comparison to the new fuelling database in Figure 4.20 (a). Figure 4.20 (b) shows both the EPED1 (open red circles) and EPED1.62 (closed green diamonds) pedestal pressure predictions and the measured pedestal pressure (closed blue triangles) as a function of pedestal density for all Type I ELMy H-mode pulses within the new fuelling database. Again on average there is a good agreement between EPED predictions and the measurements as the average ratio of predicted to observed pedestal pressure in the new fuelling database is 1.04 ± 0.22 for EPED1 and 1.04 ± 0.19 for EPED1.62. However, when presented as a function of pedestal density this highlights a systematic trend within the data. For this range of density, EPED1 and EPED1.62 both show a decrease in pedestal pressure as pedestal density increases whereas the experimental measurements show an increase.

More generally, for high triangularity discharges such as those in the new fuelling database, EPED predicts a pedestal pressure that first increases, and then decreases with density [30, 113]. We illustrate this by taking the EPED input parameters from discharge 79498, varying the pedestal density, and calculating the EPED predicted pedestal pressure as a function of density. As the pedestal density is increased, this results in an increasing collisionality at a given pressure. The resulting collisional suppression of the bootstrap current eventually leads to a transition from the

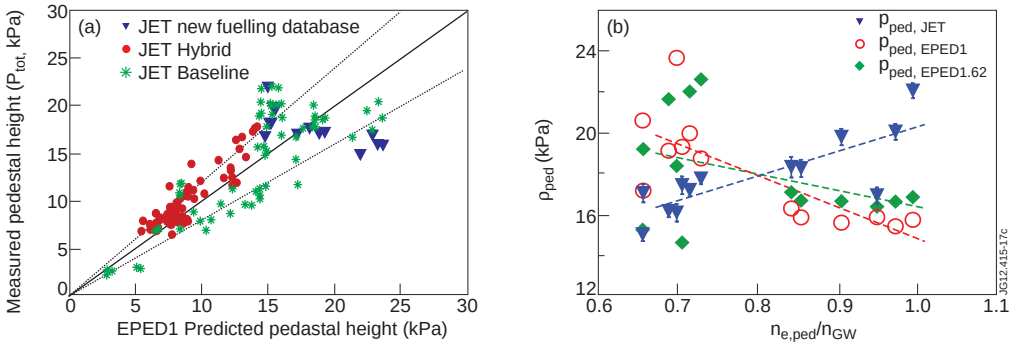

Figure 4.20: (a) Measured JET pedestal pressure is compared to EPED1 predictions for the new fuelling database (closed blue triangles), as well as previously studied hybrid (red circles) and baseline (green asterisks) cases. (b) For all Type I ELM pulses within the new fuelling database, measured JET pedestal pressure (closed blue triangles), EPED1 predictions (open red circles) and EPED1.62 predictions (closed green diamonds) are shown as a function of pedestal density normalized to Greenwald density.

kink/peeling limited regime (where EPED predicted pressure increases with density) to the primarily ballooning-limited regime (where EPED predicted pressure decreases weakly with density), as shown in Figure 4.21 (a). We can define a critical density at which this transition occurs, here $n_{e,ped,crit} \approx 6 \times 10^{19}$ m^{-3}. The corresponding EPED predicted pedestal pressure as a function of normalized density is shown in Figure 4.21 (b). The solid line shows the pedestal height prediction given an integral-line measurement of Z_{eff} of 1.92, the nominal value for 79498. Because the transition shown in Figure 4.21 (a) is related to collision suppression of the bootstrap current, it correlates not just to density, but also to Z_{eff}. Reducing Z_{eff} from 1.92 to 1 (dashed line in Figure 4.21 (b)) results in an increase of the critical density up to a Greenwald fraction near 1. It appears that, at higher pedestal density, EPED maybe under predicting the observed pedestal height due to under predicting the critical density at which the PB stability changes character from kink/peeling to PB limited. If the strong deuterium fuelling near the edge used to reach high density is reducing the value of Z_{eff} within the edge barrier, this could provide an explanation for the continued increase in pedestal pressure with density. Other possible explanations are under further investigation, including more accurate accounting of the impact of ion dilution and impurities on the bootstrap current. It is also important to note that strictly speaking the EPED model was designed for pure Type I ELMy H-mode plasmas. Consequently it may not be appropriate to perform an EPED comparison for all pulses within the new fuelling database. We note that if resistive effects or an effect associated with Type II ELMs were able to hold the pressure gradient slightly below the KB critical value, this would result in a prediction of a somewhat wider and higher pedestal [43, 114], which would be qualitatively consistent with

observations.

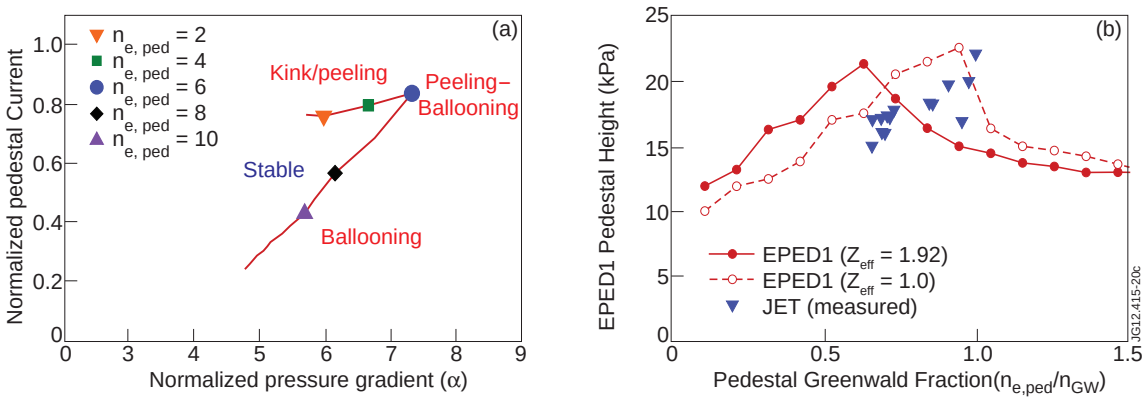

Figure 4.21: (a) Peeling-ballooning stability diagram, where pedestal density in units of $\times 10^{19}$ m^{-3} is indicated by various symbols along the stability boundary (solid line). As density increases, the limiting instability moves from kink/peeling to peeling-ballooning to nearly pure ballooning modes. (b) EPED1 predicted pedestal pressure as a function of density is shown for the same cases as in (a). Predictions are shown both for $Z_{eff} = 1.92$ (solid line) and $Z_{eff} = 1$ (dashed line). Measured values (solid triangles) are shown for comparison.

4.6 Summary and Discussion

The focus of this study is a new JET-C database detailing the pedestal structure and pedestal evolution for ITER relevant, high triangularity, Type I ELMy H-mode plasmas. This study extends [90], exploiting improvements in diagnostic capabilities, primarily due to the installation of the JET High Resolution Thomson Scattering (HRTS) system in 2005, which measures T_e and n_e pedestal profiles.

The plasmas detailed are single null, neutral beam heated and gas fuelled with an average plasma triangularity of ≈ 0.41. There is minimal degradation of plasma performance up to $n_{e,ped}/n_{GW} \approx 1.0$. In the past maintaining good performance at high fuelling has been difficult although, as shown by the new database and [90], it is possible with a large degree of plasma shaping. Further still at high fuelling ($\Gamma_D = 2.6 \times 10^{22}$ el/s), corresponding to a normalised pedestal density $n_{e,ped}/n_{GW} \approx 1.0$, the performance increases as shown by both H_{98} and the stored thermal energy. This is due to an increase in pedestal performance, as shown by the pedestal stored energy.

A mixed Type I/II ELM regime, as originally observed by [90], has been re-established on JET where there is an increased loss between the Type I ELMs. Similar to the 2002 study the Type I ELM frequency decreases with increasing pedestal density. This is due to the increased inter-ELM loss at higher pedestal density prolonging

the build up towards the critical pressure as supported by a difference in the build up of stored energy between a low and high fuelling pulse. Another factor which could influence the ELM frequency, the proximity to the LH threshold, is shown to be constant across the fuelling scan.

Further to [90], this study quantifies the pedestal characteristics throughout the ELM cycle by an mtanh least squares fit to HRTS Te and ne profiles. The change in pedestal structure has been verified by a linear least squares fitting routine and although the obtained widths differ in comparison to the mtanh fits the data trends are similar. The pre-ELM temperature, density and pressure pedestal are wider for an example mixed Type I/II ELMy pulse at high fuelling in comparison to a pure Type I ELMy pulse. Also the pre-ELM pedestal pressure is higher for the mixed Type I/II pulse. The pedestal width for the pure Type I ELMy pulse narrows and the peak pressure gradient increases during the ELM cycle, whereas the width and peak pressure gradient saturate for the mixed Type I/II ELMy pulse. The fits to the HRTS profiles act as an input to the stability and predictive pressure pedestal models.

The PB stability analysis produced by MISHKA-1 shows the plasma edge stability for the mixed Type I/II ELMy pulse moves from stable towards unstable, approaching the ideal ballooning limit of the PB stability boundary. The plasma edge stability saturates towards the last 60 % of the ELM cycle with the pre-ELM operational point located on the stability boundary. In contrast the plasma edge stability for the pure Type I ELMy pulse becomes progressively more unstable during the ELM cycle as the operational point also approaches the ideal ballooning limit of the stability boundary. The pre-ELM operational point for the pure Type I ELMy pulse is over the stability boundary, deep into the unstable region. A deconvolution technique is used to determine the temperature and density pedestal widths from the HRTS profiles. This technique assumes the profiles are truly mtanh and is the current leading method of interpreting the JET HRTS profiles. However, the pre-ELM pedestal width for the pure Type I ELM pulse is particularly narrow and approaches the FWHM of the JET HRTS instrument function (11 mm for the two pulses shown in Figure 4.9). This may result in an underestimate of the pedestal width, which is particularly prominent for the temperature pedestal fit as a weighted deconvolution technique is employed [63]. As the systematic errors are difficult to quantify a complete understanding for the pre-ELM operational point being so deeply in the unstable region for the pure Type I ELMy pulse is yet to be attained.

EPED, based on a combined PB and KB model, predicts the pre-ELM pedestal pressure and width. On average there is good agreement between the model results and the experimental pre-ELM measurements where the average ratio of predicted pedestal height to observed pedestal height is 1.04 ± 0.22 and the average ratio of

predicted pedestal width to observed pedestal width is 1.01 ± 0.23. This spread is within the range of EPED predictive accuracy as observed in a wider multi machine comparison [37, 43, 112, 114]. However the JET results do show a number of differences in comparison to studies on other machines.

The EPED model allows the pressure pedestal width and height to grow unconstrained until the onset of KB modes and PB modes. EPED assumes KB modes limit the pressure gradient in the near steady state at the end of the ELM cycle. For the pedestal height to increase when limited by KB modes the pedestal must widen so as not to exceed the critical pressure gradient. This behaviour is typically observed on DIII-D [66, 109], and MAST [69, 70] throughout the ELM cycle which suggests the pressure gradient is limited by KB modes early on in the ELM cycle. In contrast, the observation that the JET pedestal width becomes narrower during the ELM cycle for the low fuelling pulse (and for the high fuelling pulse in the initial phase of the ELM cycle) suggests that the pressure gradient may not approach KB mode criticality until the latter part of the ELM cycle. This behaviour is still consistent with the EPED premise as long as KB modes do eventually limit the pressure gradient towards the end of the ELM cycle. This is a topic of further research as discussed in [114] which presents a detailed gyrokinetic analysis of the pure Type I ELM and mixed Type I/II ELM pulses presented in this study. Nevertheless EPED predicts the JET pedestal height within a ±20 % error.

A discrepancy between the EPED and experiment observations is the pre-ELM pedestal width as predicted by EPED does not vary as strongly as observed in the new JET fuelling scan. The experimental pre-ELM profile widths from the mtanh fits are $\Delta_{ne} = 1.5 \pm 0.1$ cm and $\Delta_{Te} = 1.9 \pm 0.1$ cm for a low fuelling plasma and $\Delta_{ne} = 2.1 \pm 0.1$ cm and $\Delta_{Te} = 2.9 \pm 0.1$ cm for a high fuelling plasma. This corresponds to an increase, in real space, of 40 % for the density pedestal width and 53 % for the temperature pedestal width from the pure Type I to mixed Type I/II ELMy pulse. Using the expression $\Delta = (\Delta_{Te}+\Delta_{ne})/2$ and converting to normalised poloidal flux coordinates (Ψ) the experimental measurements show an increase in pedestal width from $\Delta_\Psi = 0.034$ to $\Delta_\Psi = 0.053$ corresponding to an increase of ≈ 55 % going from low to high fuelling. Moreover the experimental pre-ELM pressure pedestal height increases by ≈ 20 % for a high fuelling pulse in comparison to low fuelling pulse. The wider pre-ELM pedestal found for the mixed Type I/II ELMy pulse in comparison to the pure Type I ELMy pulse facilitates an increase in pedestal pressure as the steep edge gradient can be sustained over a larger region. This is in spite of a 21 % reduction of the peak pressure gradient. In contrast EPED, given the eight scalar input parameters (B_t, I_p, R, a, δ, κ, $n_{e,ped}$ and $\beta_{N,global}$), predicts a decrease of 25 % in pedestal pressure and a decrease in pedestal width of 20 % in poloidal flux space going from the pure Type I to mixed Type I/II ELMy pulse. The disagreement

between experiment and EPED has two possible explanations. First if we speculate EPED, like MISHKA-1, under-predicts the critical density, which marks the transition from kink-peeling to ballooning limited plasmas, this will account for opposing trends in pedestal pressure. The critical density is a strong function of Z_{eff}, plasma shape and is strongly dependent on the accuracy of neoclassical bootstrap current models. Second, the stronger broadening of the experimental pedestal width than predicted by EPED is an indication that other transport related processes contribute to defining the pedestal width such as enhanced inter-ELM transport as observed at high fuelling, for mixed Type I/II ELMy pulses.

Chapter 5

The H-mode pedestal structure and its role on confinement in JET with a carbon and metal wall

This Chapter builds upon the JET-C pedestal analysis as documented in Chapter 4 by extending the database to incorporate fuelling and seeding ELMy H-mode JET plasmas after the installation of the ITER-Like-Wall (JET-ILW). This study describes the updated database; gives a brief overview of the JET measurements and the EPED model; and then presents the performance and pedestal structure for low and high triangularity plasmas.

5.1 Introduction

The ITER-Like-Wall (ILW) was installed on the JET Tokamak in 2010/11 with the primary aim of demonstrating a reduction in fuel retention [94, 115]. The material composition of the plasma facing components is beryllium for the main chamber and Tungsten for the high heat flux regions, as foreseen for ITER [116]. Measurements from recent JET campaigns with the ILW offer an invaluable opportunity to investigate how the pedestal structure changes with the presence of a metallic wall and its role on confinement. This chapter presents a database consisting of deuterium fuelled and nitrogen seeded Type I ELMy H-mode plasmas on JET with the ILW (JET-ILW) [96, 112, 117–119] with the focus on quantifying the pedestal structure. The pedestal width, gradient and height is determined by fitting a modified hyperbolic tangent (mtanh) function [120] to JET High Resolution Thomson Scattering (HRTS) radial profiles of electron temperature and density [48, 63, 73].

Three high triangularity Type I ELMy H-mode plasmas on JET with the carbon

wall (JET-C), presented in the previous Chapter ([75]), are used within this study as reference plasmas before the installation of the Be/W wall. These three JET-C plasmas have high resolution HRTS measurements at the plasma edge sufficient to quantify the pedestal structure. To summarise, Chapter 4 quantifies the role of pedestal structure on performance across a deuterium fuelling scan. The plasma performance was not only maintained but even improved with increased fuelling up to a density pedestal normalised to the Greenwald density ($n_{e,ped}/n_{GW}$) ≈ 1.0. This improvement in performance was attributed to an increase in pedestal stored energy which coincided with a transition from pure Type I ELMs to mixed Type I/II ELMs [90, 95, 107]. A key result was that the pre-ELM electron temperature and density pedestal width increased from low to high deuterium fuelling.

Results from the 2012 JET-ILW campaign show the high triangularity Type I ELMy H-mode baseline plasmas exhibit an approximate 20-30 % reduction in performance in comparison to JET-C plasmas. This can be attributed to a degraded pressure pedestal height [117, 119, 121]. However, with nitrogen seeding the pressure pedestal height and consequently global performance for JET-ILW plasmas can be partially recovered [117, 119]. These changes in performance coincide with a variation of the peak pedestal gradient and the pedestal width. The reduction in the pressure pedestal height after the installation of the Be/W wall is due to a reduction in temperature pedestal height. The recovery in pressure pedestal height with increasing nitrogen seeding is due to a significant increase in density pedestal height as well as an increase in temperature pedestal height.

A multi-machine review [122] of three possible mechanisms which could account for the changes in performance observed on JET and AUG concluded that the improvement in performance is not due to an improvement in core confinement nor can it be accounted for due to ion dilution. Instead it is most likely the change in pedestal structure results in the improvement in global performance. More specifically, with increasing nitrogen seeding for JET-ILW plasmas the pedestal widens and the peak gradient increases both contributing towards an increase pedestal pressure. Furthermore [122] compares the measurements to preliminary results from the predictive pedestal structure model, EPED.

In [122] only the pressure pedestal structure is discussed for high triangularity JET plasmas. This study extends the JET-ILW pedestal analysis by considering a wider dataset of fuelling and seeding plasmas, incorporating more high triangularity JET-ILW plasmas as well as including low triangularity JET-ILW plasmas. In addition, the relevant contributions of the electron temperature and density pedestal are quantified along with a comparison of measurements with the most recent EPED model predictions.

This chapter is organised as follows: Section 5.2 provides a description of the database and the plasmas presented in this study, Section 5.3 gives an overview of the JET measurements discussed throughout the study along with a detailed introduction to the EPED model; Section 5.4 presents the performance and pedestal structure of the vertical and horizontal target low triangularity JET-ILW plasmas; Section 5.5 presents the performance, ELM characteristics and pressure pedestal structure of the high triangularity JET-C and JET-ILW plasmas as well as a wider database comparison with EPED model predictions; and Section 5.6 provides a summary and discusses the conclusions.

5.2 Description of database

The baseline Type I ELMy H-mode JET plasmas discussed in this study have a magnetic field and plasma current of 2.7 T/2.5 MA where $q_{95} \approx 3.5$. The input power is $\approx 14 - 17$ MW corresponding to $\beta_N \approx 1.2 - 1.5$. The triangularity ($\delta$) ranges between $\approx 0.22 - 0.42$, see Table 1. These plasmas are predominantly from the JET fuelling and seeding experiment before and after the installation of the Be/W ILW [95, 96, 117, 119]. The primary aim of this experiment is to develop a radiative scenario with the introduction of an impurity to mitigate divertor heat loads. As part of the experimental procedure there exists deuterium fuelling and nitrogen seeding scans suitable for investigating the change in pedestal structure. This study also incorporates deuterium fuelled plasmas from the JET baseline scenario development experiments [121].

The 83 plasmas selected for this study can be categorised into four groups: high triangularity JET-C plasmas ($\delta \approx 0.42$), high triangularity JET-ILW plasmas ($\delta \approx 0.38$), low triangularity horizontal target JET-ILW plasmas ($\delta \approx 0.27$) and low triangularity vertical target JET-ILW plasmas ($\delta \approx 0.22$). Figure 5.1(a) demonstrates the EFIT magnetic equilibrium for a high triangularity JET-C (JPN: 79503) and an equivalent JET-ILW (JPN: 82585) plasma. These plasmas are similar apart from a small change in upper triangularity (JET-C $\delta_{UP} \approx 0.44$, JET-ILW $\delta_{UP} \approx 0.39$) to minimise the interaction with the upper inner-wall structure [95, 121]. Figure 5.1(b) and 5.1(c) demonstrate there is a more significant difference between a low triangularity horizontal (JPN: 83177) and vertical (JPN: 83491) target plasma when comparing the magnetic equilibrium reconstruction. The outer strike point for all the high triangularity plasmas (JET-C and JET-ILW) is located on a Horizontal Target (HT); a horizontal tile mounted centrally at the bottom of the divertor, see Figure 5.1(c). As well as the low triangularity HT JET-ILW plasmas, also considered are low triangularity plasmas where the strike point is positioned on a Vertical Target (VT); a vertically mounted tile on the outboard side of the JET divertor, see Figure

Table 5.1: Summary of key parameters defining the plasma scenario for all JET pulses considered in this study. The triangularity δ is the average of the upper and lower triangularity. I_p is the plasmas current. B_t is the toroidal magnetic field strength. P_{NBI} is the input power from neutral beam injection. $D_2\Gamma_{el}$ is the range of deuterium fuelling for the particular pulses included in this study and similarly $N_2\Gamma_{el}$ is the range nitrogen fuelling. $n_{e,ped}/n_{GW}$ is the density pedestal height normalised to the Greenwald density.

	High δ JET-C horiz. target	High δ JET-ILW horiz. target	Low δ JET-ILW horiz. target	Low δ JET-ILW vert. target
No. Pulses	14	60	5	4
δ	0.42	0.38	0.27	0.22
I_P (MA)	2.5	2.5	2.5	2.5
B_t (T)	$2.6 - 2.7$	$2.6 - 2.7$	$2.6 - 2.7$	2.8
P_{NBI} (MW)	$14 - 15$	$15 - 17$	$15 - 17$	16
$D_2\Gamma_{el}$ ($\times 10^{22}$ el/s)	$0.2 - 2.6$	$0.6 - 3.0$	-	$0.6 - 4.3$
$N_2\Gamma_{el}$ ($\times 10^{22}$ el/s)	-	$0.0 - 3.8$	$0.0 - 2.5$	-
$n_{e,ped}/n_{GW}$	$0.75 - 1.05$	$0.67 - 1.06$	$0.59 - 0.70$	$0.59 - 0.74$

5.1(c).

At high triangularity the deuterium fuelling ranges from ≈ 0.2 to 3.0×10^{22} el/s and similarly the nitrogen seeding ranges from $\approx 0.0 - 3.8 \times 10^{22}$ el/s. The nitrogen seeded plasmas are also fuelled with deuterium ranging from ≈ 0.8 to 2.9×10^{22} el/s. The plasmas which make up the two nitrogen scans presented in this study have a similar fixed level of deuterium fuelling of ≈ 0.8 and 1.2×10^{22} el/s. For all high triangularity JET-C and JET-ILW plasmas in the database the electron pedestal density normalised to the Greenwald density ($n_{e,ped}/n_{GW}$) is between ≈ 0.67 to 1.06, see Table 5.1. The plasmas which exhibit an improvement in performance with increased deuterium fuelling (JET-C) [75] and nitrogen seeding (JET-ILW) correspond to a high normalised density ($n_{e,ped}/n_{GW}$) above 1.0. At low triangularity over a similar range of fuelling and seeding the normalised pedestal density ($n_{e,ped}/n_{GW}$) ranges from ≈ 0.59 to 0.74 for JET-ILW plasmas.

In the context of the variation in pedestal structure there is not a suitable nitrogen seeding scan for high triangularity JET-C plasmas due to the lack of high resolution measurements at the time of the experiment or a deuterium fuelling scan for low triangularity horizontal target JET-ILW plasmas or a nitrogen seeding scan for low triangularity vertical target JET-ILW plasmas, (see Table 5.1). There are nitrogen seeded JET-C plasmas [95, 96], however the edge resolution of HRTS is insufficient for this study. The analysis performed for this study has demonstrated it is important to

consider plasmas with the same current, magnetic field, neutral beam input power, gas fuelling configuration and ideally the same machine conditioning. Taking into account these factors results in clearer trends, however this is not always possible hence the limited low triangularity dataset. This study incorporates plasmas from only the first JET-ILW campaign however a more extensive dataset is provided by the most recent JET-ILW campaigns.

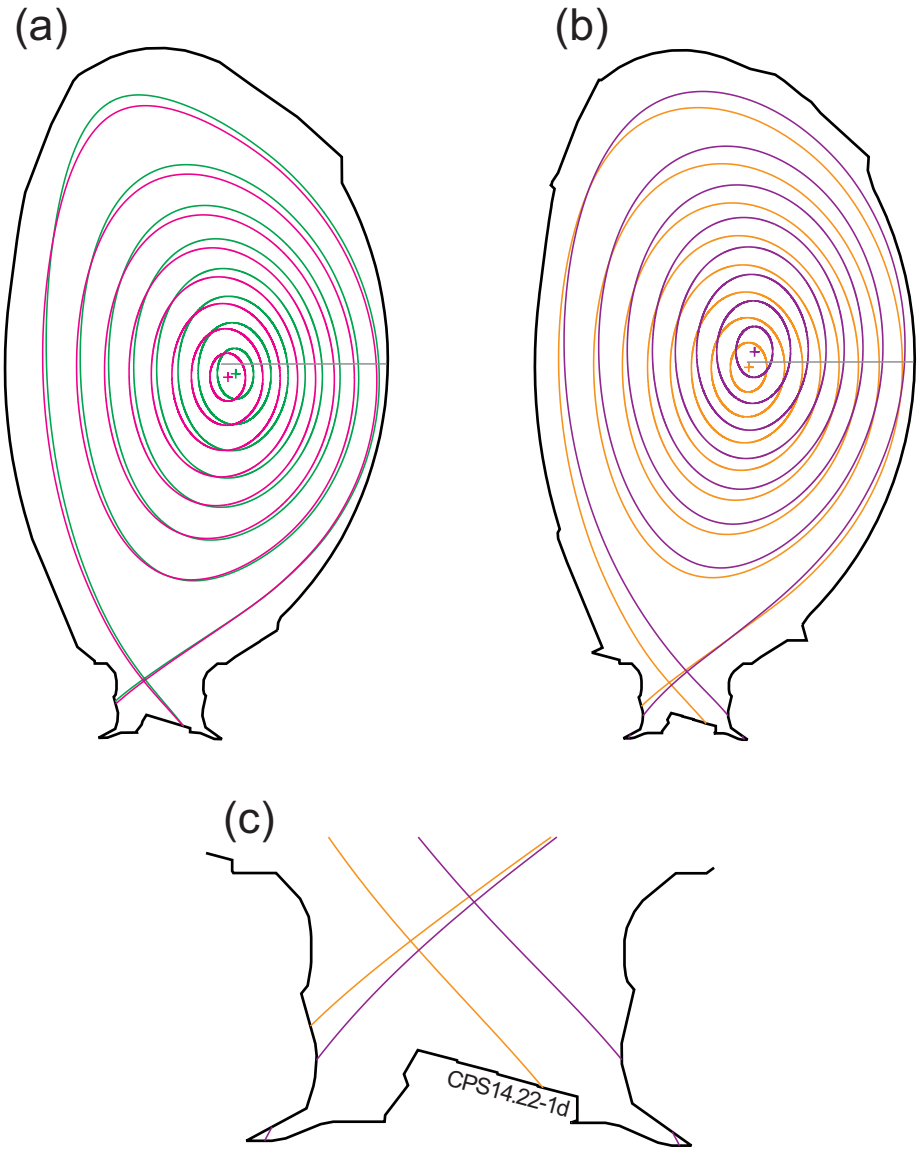

Figure 5.1: EFIT magnetic equilibrium reconstructions for (a) high triangularity JET-C plasma in green (JPN: 79503 at $t = 22.0$ s) and high triangularity JET-ILW plasma in magenta (JPN: 82585 at $t = 15.8$ s). (b) low triangularity horizontal target JET-ILW plasma in orange (JPN: 83177 at 14.8 s) with a low triangularity vertical target JET-ILW plasma in purple (JPN: 83491 at 11.5 s) (c) same as (b) with focus on the divertor region. The horizontal grey line shown on (a) and (b) indicates the location of the HRTS measurement.

5.3 Overview of JET measurements and EPED model

The global performance is quantified by the confinement enhancement factor (H_{98}) and the stored thermal energy (W_{th}). H_{98} is defined as the ratio of the measured energy confinement time for a specific pulse to the energy confinement time as determined from a scaling relation based upon an international multi machine database of H-mode plasmas [99]. The stored thermal energy is calculated from the measured diamagnetic energy corrected for fast ions [101].

The pedestal stored energy (W_{ped}) as given by Equation 4.2 can be more generically expressed in terms of the atomic charge of the dominate impurity (Z_I) as given by the volume integral,

$$W_{ped}(J) \approx \frac{3}{2} \int_V e \left(\frac{(Z_I + 1) - Z_{eff}}{Z_I} \right) n_e T_e dV \tag{5.1}$$

where e is the elementary unit of charge (a constant), Z_{eff} is the average effective atomic charge, n_e is the electron density in m^{-3}, T_e is the electron temperature in eV and V is the plasma volume in m^3. As before, the volume integral is evaluated when the pressure profile is capped at the pressure pedestal top. The electron density and temperature profile utilised by Equation 5.1 are modified hyperbolic tangent fits to the pre-ELM HRTS measured profiles. Equation 5.1 assumes $T_i \approx T_e$ and the relation between n_i and n_e given by Equation 4.3.

For JET-C deuterium fuelled plasmas the dominant impurity is carbon ($Z_I = 6$). For JET-ILW deuterium fuelled plasmas the dominant impurity is beryllium ($Z_I = 4$) whereas for JET-ILW nitrogen seeded plasmas the dominant impurity is assumed to be nitrogen ($Z_I = 7$). Furthermore, it is important to note the average Z_{eff} is incorporated into Equation 5.1 and a flat Z_{eff} profile is assumed.

The pedestal structure is determined by fitting a modified hyperbolic tangent (mtanh) function to ELM synchronised JET High Resolution Thomson Scattering (HRTS) electron temperature and density profiles, see [120]. The HRTS system has a 20 Hz repetition rate resulting in $\approx$ 800 profiles per pulse. Profiles are selected from the stationary ELMy H-mode phase of a pulse, typically $\approx 1.5 - 2.0$ s ($\approx 30 - 40$ profiles). Furthermore, for pre-ELM fits the profiles are selected from the last 70-99 % of the ELM cycle. The size of the percentage window balances selecting a sufficient number of profiles for an accurate fit whilst only selecting profiles representative of the pre-ELM state. The position of the profiles is corrected according to the position of the last closed flux surface as calculated from EFIT. This aligns the steep gradient region (the pedestal) accounting for either an error in the profile position

or small scale fluctuations in plasma position during the ELM cycle. The JET pedestal fitting routine provides a so called classical deconvolved mtanh density fit and a weighted deconvolved temperature fit as determined using the HRTS instrument function [63, 73]. The temperature fit takes into account the variation in density across the scattering volume particularly important in the steep gradient region of the profile. All the JET plasmas considered in this study have high resolution HRTS pedestal measurements where the FWHM of the instrument function is $\approx$ 11 mm [63].

Figure 5.2 shows an example of the deconvolved temperature and density mtanh fit for (a), (c) a pure deuterium fuelled high triangularity JET-ILW plasma (JET Pulse Number: 82585) and (b), (d) a nitrogen seeded high triangularity JET-ILW plasma (JET Pulse Number: 82814). The temperature and density pedestal widens from $\Delta_{Te} \approx 1.7$ to 2.5 cm and $\Delta_{ne} \approx 1.7$ to 2.2 cm respectively with the introduction of nitrogen. The temperature pedestal height remains constant at $T_{e,ped} \approx 0.7$ keV with the introduction of nitrogen whereas the density pedestal height significantly increases from $n_{e,ped} \approx 6.5$ to 10.0×10^{19} m^{-3}. Consequently the nitrogen seeded plasma has a higher electron pressure pedestal height as will be discussed in more detail in Section 5.5. As detailed above the total measured pressure pedestal height is calculated assuming the electron and ion temperature are equal and taking into account ion dilution.

The EPED predictions presented in this study are from the simplified version of the model, EPED1 [30], which currently assumes an up-down symmetric plasma shape for JET runs. Previous studies which discuss EPED1 predictions of the JET pedestal include [37, 75, 118, 123]. The earlier multi machine comparisons (JET, DIII-D measurements [123] and JET, DIII-D, AUG measurements [37]) concluded there is a good agreement between the predicted and measured pedestal height. The conclusion from more recent extensive comparisons, dedicated to JET-C [75] (previous Chapter) and JET-ILW [118] measurements, is more complex as, for example, there are discrepancies between the predicted and measured pedestal height at high deuterium fuelling (JET-C) and high nitrogen seeding (JET-ILW). A possible explanation regarding the discrepancy for highly fuelled JET-C plasmas is due to EPED under-predicting the critical density as a consequence of measurement uncertainty on an additional input parameter to the model, Z_{eff} (see previous Chapter and [75]). The critical density marks the transition from peeling to ballooning limited plasmas.

Further to the eight traditional EPED inputs ($B_t, I_p, R, a, \delta, \kappa, n_{e,ped}, \beta_{N,global}$) the local pedestal effective atomic charge (Z_{eff}) can also be included. This is a particularly important parameter in the context of this study as, for example, the change from a carbon to a metal wall and the variation of nitrogen seeding is incorporated into the EPED model by varying Z_{eff}. However, quantifying the variation of the

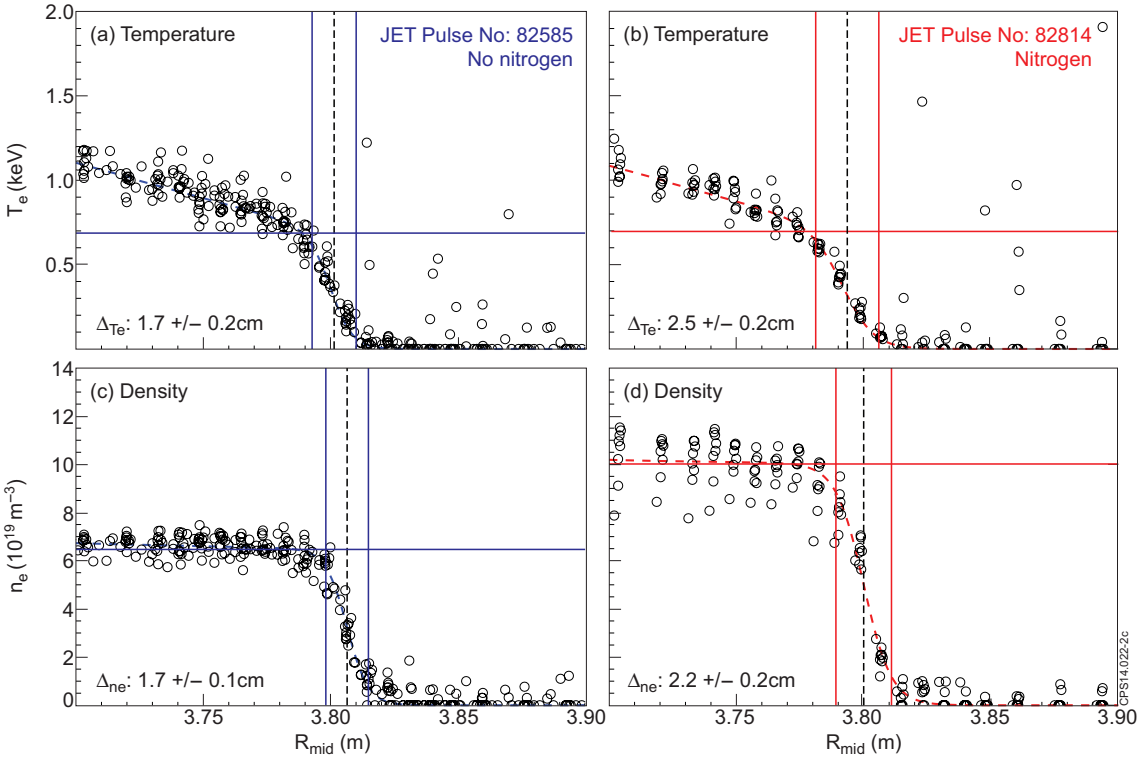

Figure 5.2: Deconvolved modified hyperbolic tangent fits to radial temperature and density HRTS profiles for (a), (c) a pure deuterium fuelled JET-ILW plasma (blue) where $D_2\Gamma_{el} = 1.1 \times 10^{22}$ el/s and (b), (d) a nitrogen seeded JET-ILW plasma (red) where $D_2\Gamma_{el} = 1.3 \times 10^{22}$ el/s and $N_2\Gamma_{el} = 1.3 \times 10^{22}$ el/s.

radial Z_{eff} profile in the pedestal region due to impurity seeding is challenging on JET. There are non-local bremsstrahlung line-integral measurements of Z_{eff} [124], which for JET-C plasmas, decrease from $\approx$ 2.0 to 1.7 with increasing deuterium fuelling demonstrating the plasma becomes purer [95]. After the installation of the Be/W ILW wall it has been shown that the dominant impurity for JET-ILW plasmas is beryllium as opposed to carbon and Z_{eff} decreases from $\approx$ 2.0 to 1.2, as detailed in [125]. Furthermore with the introduction of nitrogen for JET-ILW plasmas Z_{eff} increases from $\approx$ 1.2 up to 1.8 [117, 119]. The EPED1 predictions presented in the previous chapter ([75]) and the most recent EPED1 runs for the low triangularity JET-ILW plasmas presented in this study use bremsstrahlung line-integral measurements of Z_{eff}. The EPED1 runs for high triangularity JET-ILW plasmas as presented in [118] and in this study use a constant Z_{eff} of 2.0. The PB stability sensitivity to Z_{eff} for JET-ILW plasmas is addressed by [126] however, further work is required, particularly for the high triangularity plasmas, to address the role of Z_{eff} on EPED predictions.

5.4 Deuterium fuelling and nitrogen seeding scans in low triangularity JET-ILW plasmas

5.4.1 JET-ILW D-fuelling scan in vertical target, low triangularity configuration

Figure 5.3(a) and 5.3(b) show that for low triangularity VT JET-ILW plasmas there is no significant change in global performance as the confinement enhancement factor (H_{98}) and stored thermal energy (W_{th}) remain constant ($H_{98} \approx 0.7$ and $W_{th} \approx 4.0$ MJ) across a deuterium fuelling scan from 0.6 to 4.3×10^{22} el/s. Figure 5.3(c) shows there is no change in the pedestal stored energy with increasing fuelling. Consequently the ratio of the stored thermal energy to the pedestal stored energy is constant as shown by Figure 5.3(d).

Figure 5.4 presents the measurements of the pressure pedestal structure. Figure 5.4(a) shows an initial widening of the pedestal at low fuelling, however at higher fuelling there is no significant change. Figure 5.4(b) shows the peak pressure gradient decreases with increasing deuterium fuelling saturating at higher fuelling. The resulting total pressure pedestal height is constant across the deuterium scan as shown by Figure 5.4(c). The total pedestal pressure is calculated taking into account ion dilution and is presented to allow a direct comparison to EPED1. The measured average line-integral Z_{eff}, as provided as an input to EPED1, is near constant, from ≈ 1.3 to 1.2, with increasing deuterium fuelling. The EPED1 pedestal width (Figure 5.4(a)) and height (Figure 5.4(c)) predictions are constant with increasing fuelling and therefore in good agreement with measurements considering the experimental and model (± 20 %) uncertainties.

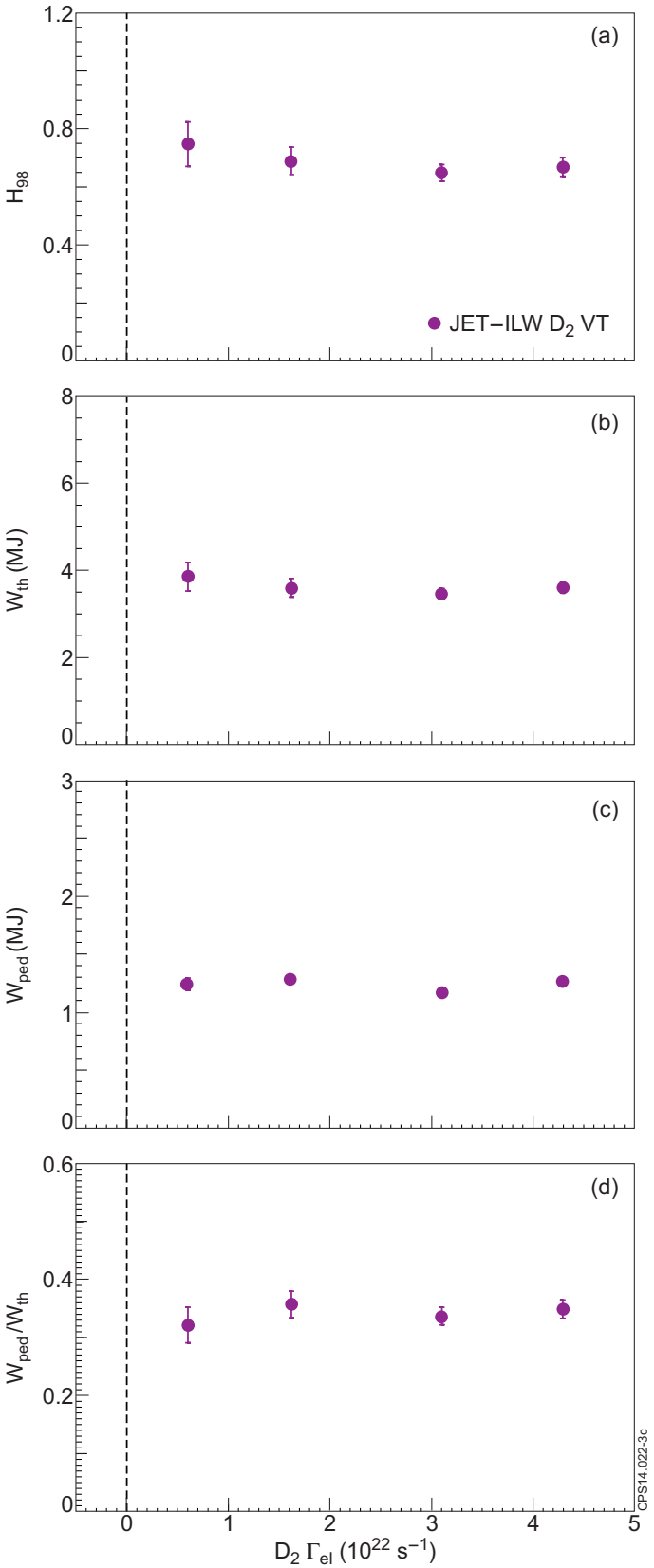

Figure 5.3: Variation of global and edge performance for low triangularity vertical target JET-ILW plasmas across a deuterium fuelling scan. (a) Confinement enhancement factor (H_{98}), (b) total stored thermal energy (W_{th}), (c) pedestal stored energy (W_{ped}) and (d) as a function of deuterium fuelling. The JET pulse numbers in order of increasing D_2 fuelling are 83491 ($Z_{eff} \approx 1.3$), 83490 ($Z_{eff} \approx 1.3$), 83488 ($Z_{eff} \approx 1.2$) and 83487 ($Z_{eff} \approx 1.2$).

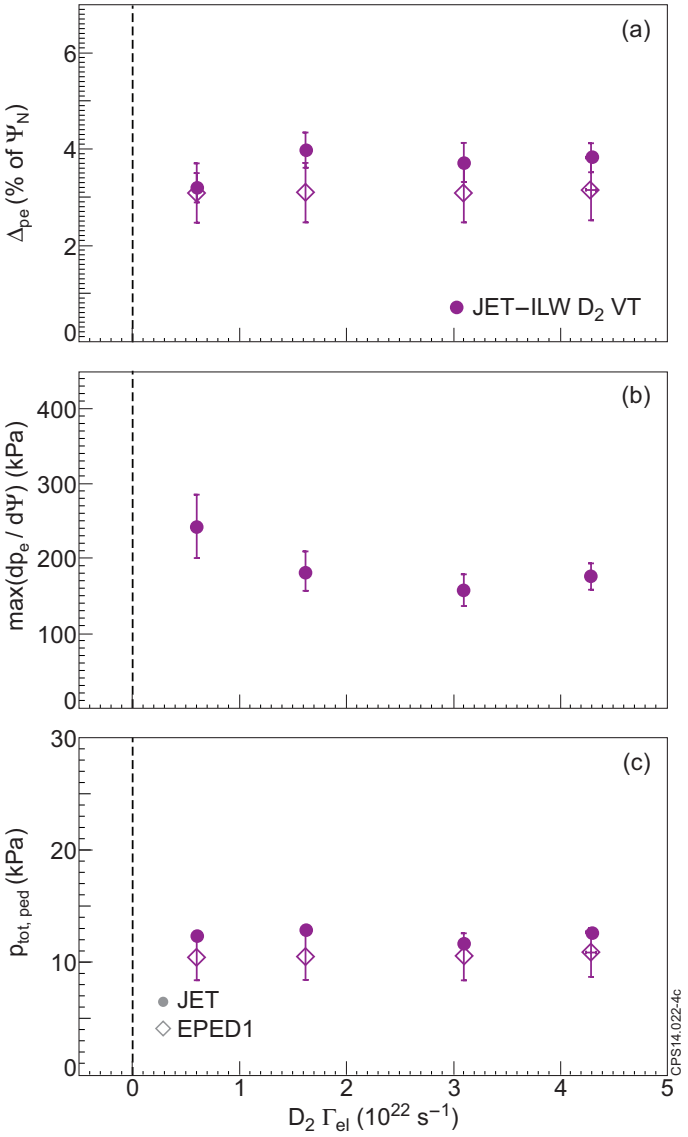

Figure 5.4: Variation in JET measurements of the pressure pedestal structure (circles) and comparison to EPED1 predictions (diamonds) for low triangularity vertical target JET-ILW plasmas across the same deuterium fuelling scan as shown in Figure 5.3. (a) Measured pressure pedestal width (Δ_{pe}) with corresponding EPED1 predictions, (b) peak pressure gradient ($max(d_{pe}/dr)$) and (c) total pressure pedestal height ($p_{tot,ped}$) as a function of deuterium fuelling with corresponding EPED1 predictions. EPED1 runs incorporate average line-integral measurement of Z_{eff}.

5.4.2 JET-ILW N-seeding scan in horizontal target low, triangularity configuration

Figure 5.5(a) and 5.5(b) shows across a nitrogen seeding scan for low triangularity horizontal target JET-ILW plasmas there is no significant change in H_{98} and W_{th} with increasing nitrogen seeding ($H_{98} \approx 0.7$ and $W_{th} \approx 4.0$ MJ). Furthermore, Figure 5.5(c) shows there is no variation in the pedestal stored energy with increasing nitrogen seeding and Figure 5.5(d) shows the ratio of pedestal stored energy to total stored energy is also unchanged.

Figure 5.6 presents the pressure pedestal measurements and EPED1 predictions across the nitrogen seeding scan. Figure 5.6(a) shows the pedestal width is constant with increasing nitrogen seeding. This is the only scan within the study to clearly show that the pedestal width does not increase with increasing gas dosing (deuterium fuelling or nitrogen seeding). Furthermore, the peak pressure gradient (Figure 5.6(b)) and pressure pedestal height (Figure 5.6(c)) show no significant change with increasing nitrogen seeding. The measured line-integral Z_{eff} is modified by the introduction of nitrogen as increases from ≈ 1.2 to 1.5, as incorporated into the EPED1 predictions. The EPED1 width (Figure 5.6(a)) and height (Figure 5.6(c)) predictions are constant with increasing nitrogen seeding and both are in good agreement with the pedestal measurements. It is noted that the EPED1 width predictions are consistently 11 to 16 % lower however this is within the model uncertainty of ± 20 %.

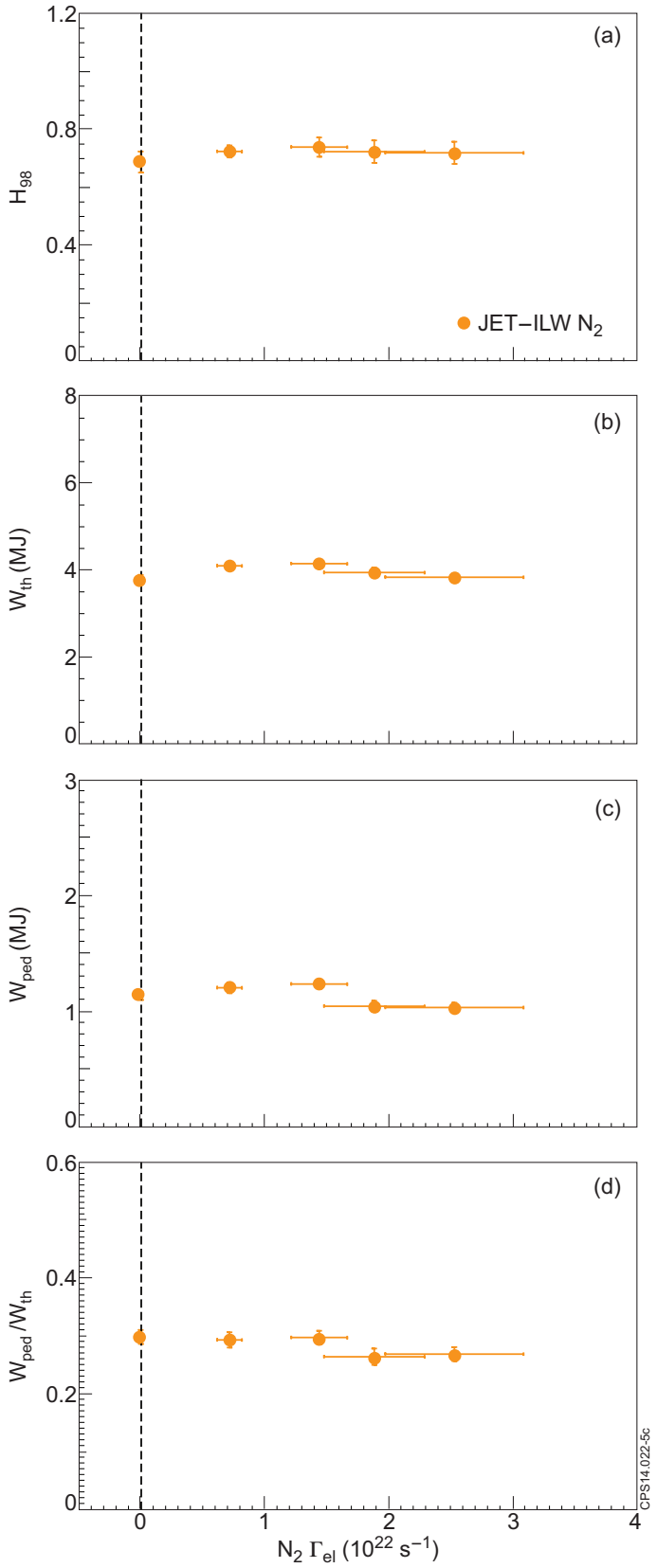

Figure 5.5: Variation in global and edge performance for low triangularity horizontal target JET-ILW plasmas across a nitrogen seeding scan. The deuterium fuelling level is fixed across the nitrogen seeding scan at $D_2\Gamma_{el} \approx 1.4 \times 10^{22}$ el/s. (Continued on next page)

Figure 5.5: (Previous page) (a) Confinement enhancement factor (H_{98}), (b) total stored thermal energy (W_{th}), (c) pedestal stored energy (W_{ped}) and (d) W_{ped}/W_{th} as a function of nitrogen seeding. The JET pulse numbers in order of increasing N_2 seeding are 83177 ($Z_{eff} \approx 1.2$), 83180 ($Z_{eff} \approx 1.3$), 83179 ($Z_{eff} \approx 1.3$), 83182 ($Z_{eff} \approx 1.5$) and 83178 ($Z_{eff} \approx 1.4$).

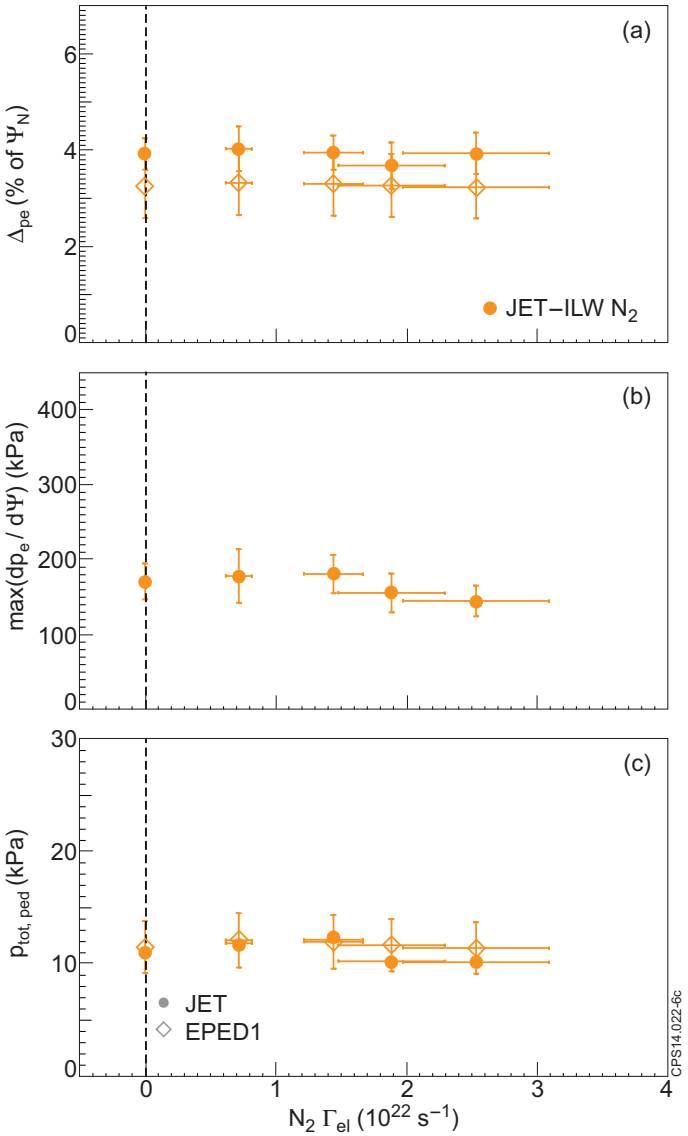

Figure 5.6: Variation in JET measurements of the pressure pedestal structure (circles) and comparison to EPED1 predictions (diamonds) across a across the same nitrogen seeding scan as shown in Figure 5.5. (a) Measured pressure pedestal width (Δ_{pe}) with corresponding EPED1 predictions, (b) peak pressure gradient ($max(d_{pe}/dr)$) and (c) total pressure pedestal height ($p_{tot,ped}$) as a function of nitrogen seeding with corresponding EPED1 predictions. EPED1 runs incorporate average line-integral measurements of Z_{eff}.

5.5 Deuterium fuelling and nitrogen seeding scans in high triangularity JET-C and JET-ILW plasmas

5.5.1 Plasma performance

The left and right hand columns of Figure 5.7 show the performance of high triangularity JET-ILW plasmas with increasing deuterium fuelling and nitrogen seeding respectively. There are two nitrogen scans corresponding to a similar fixed level of deuterium fuelling at $\Gamma_{el} \approx 1.2 \times 10^{22}$ el/s (series 1) and 0.8×10^{22} el/s (series 2).

Figure 5.7(a) and 5.7(c) show there is a $\approx 20 - 30$ % reduction in global performance for equivalent high triangularity plasmas after the installation of the ILW. $H_{98} \approx 0.7 - 0.8$ and $W_{th} \approx 3.7 - 4.5$ MJ for JET-ILW deuterium fuelled plasmas in comparison to equivalent JET-C plasmas where $H_{98} \approx 1.0$ and $W_{th} \approx 6.0$ MJ. Furthermore H_{98} and W_{th} decrease with increasing deuterium fuelling for JET-ILW plasmas unlike the JET-C plasmas. As reported in the previous chapter the JET-C plasmas maintain and even improve overall performance (H_{98} and W_{th}) with increasing deuterium fuelling due to a transition from pure Type I ELMs to the so called mixed Type I/II ELMs [90, 107].

The premise behind mixed Type I/II ELMs is there is an increased continuous loss (Type II ELMs) between the large periodic transient collapses of the pedestal (Type I ELMs) prolonging the build up to criticality and consequently decreasing the ELM frequency. This is consistent with measurements presented in the previous chapter. Furthermore, there is a change in magnetic fluctuation behaviour corresponding to washboard modes which are thought to regulate the build-up in pressure by enhanced inter-ELM transport [102, 106].

The behaviour of global performance is linked to the pedestal stored energy (W_{ped}). Figure 5.7(e) shows W_{ped} (≈ 1.3 MJ) does not improve for the JET-ILW plasmas with increasing deuterium fuelling. The edge performance increases relative to the core performance for equivalent JET-C plasmas with increasing deuterium fuelling as W_{ped}/W_{th} increases from ≈ 0.34 to 0.40, see Figure 5.7(g). However this is not the case for the JET-ILW plasmas as W_{ped}/W_{th} remains approximately constant ≈ 0.33.

Figure 5.7(b) and 5.7(d) shows the global performance initially increases and then saturates ($H_{98} \approx 0.80 - 0.88$ and $W_{th} \approx 4.3 - 5.3$) for both JET-ILW nitrogen seeding scans. This improvement in performance is mostly due to an increase in W_{ped} from

$\approx$ 1.4 to 2.0 MJ (see Figure 5.7(f)). W_{ped} initially increases and then saturates like H_{98} and W_{th}. Figure 5.7(h) shows the ratio of W_{ped}/W_{th} increases and then saturates with increasing nitrogen seeding.

To summarise, the performance behaviour of the JET-ILW high triangularity nitrogen seeded plasmas is akin to the JET-C deuterium fuelled plasmas. This is due to the improvement in overall performance being attributed to the increase in pedestal stored energy at higher gas dosing. In contrast to the JET-C plasmas, the global and edge performance of the JET-ILW plasmas with increasing deuterium fuelling decreases.

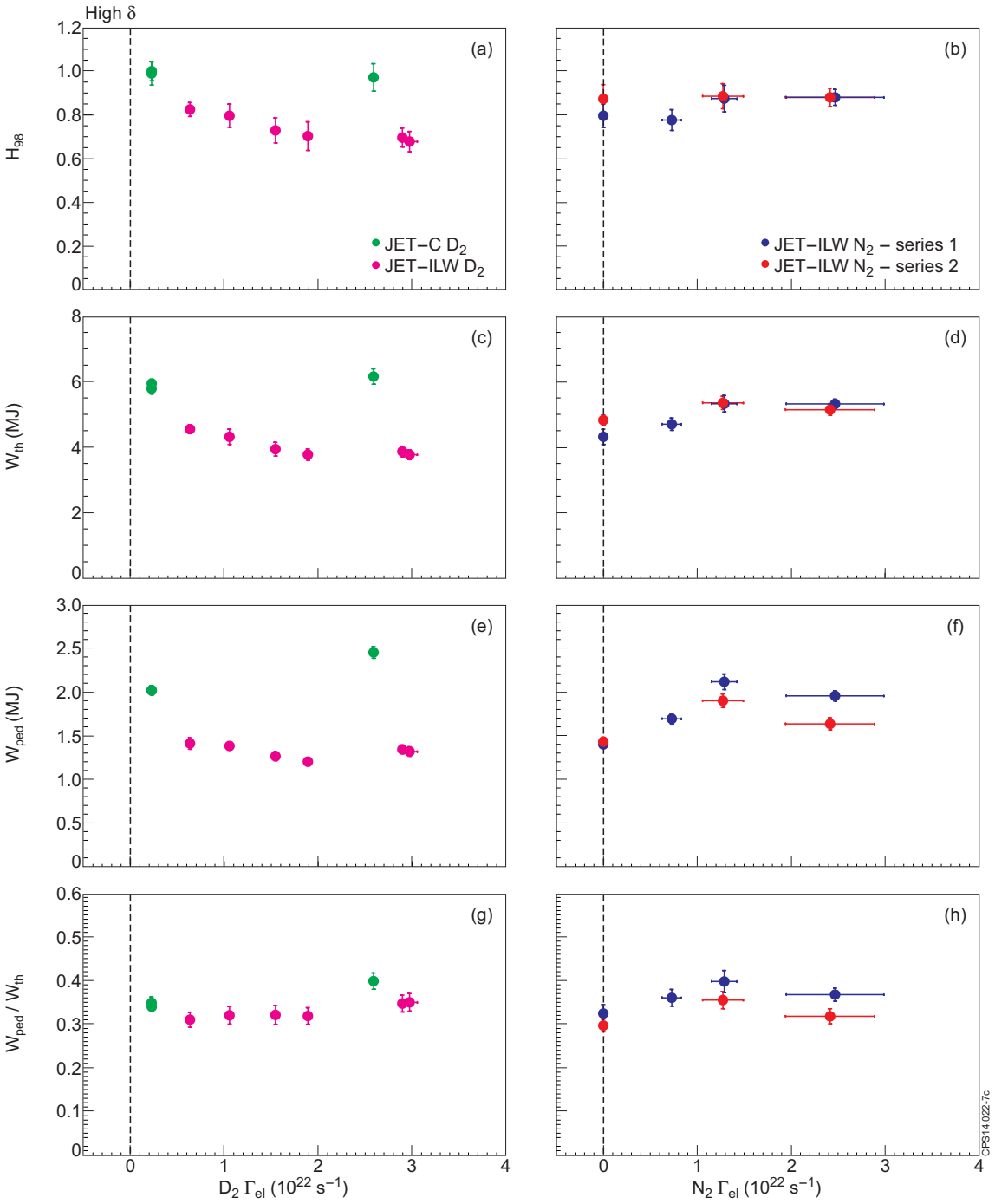

Figure 5.7: (Continued on next page).

Figure 5.7: (Previous page) Variation in core and edge performance for a JET-C deuterium fuelling scan (green), a JET-ILW deuterium fuelling scan (pink) and two JET-ILW nitrogen seeding scans (blue and red). The deuterium fuelling level is fixed across the nitrogen seeding scans at $D_2\Gamma_{el} \approx 1.2 \times 10^{22}$ el/s for series 1 (blue) and $D_2\Gamma_{el} \approx 0.8 \times 10^{22}$ el/s for series 2 (red). Confinement enhancement factor (H_{98}) as a function of (a) deuterium fuelling and (b) nitrogen seeding. Total stored thermal energy (W_{th}) as a function of (c) deuterium fuelling and (d) nitrogen seeding. Pedestal stored energy (W_{ped}) as a function of (e) deuterium fuelling and (f) nitrogen seeding. The JET pulse numbers in order of increasing deuterium or nitrogen seeding are as follows. JET-C D_2 plasmas: 79498 ($Z_{eff} \approx 2.0$), 79499 ($Z_{eff} \approx 1.9$), and 79503 ($Z_{eff} \approx 1.7$). JET-ILW D_2 plasmas; 82586 ($Z_{eff} \approx 1.3$), 82585 ($Z_{eff} \approx 1.3$), 82541 ($Z_{eff} \approx 1.3$), 82540 ($Z_{eff} \approx 1.3$), 82806 ($Z_{eff} \approx 1.3$) and 82751 ($Z_{eff} \approx 1.3$). JET-ILW N_2 series 1 plasmas: 82585 ($Z_{eff} \approx 1.3$), 82816 ($Z_{eff} \approx 1.5$), 82814 ($Z_{eff} \approx 1.5$) and 82813 ($Z_{eff} \approx 1.6$). JET-ILW N_2 series 2: 82588 ($Z_{eff} \approx 1.3$), 82820 ($Z_{eff} \approx 1.5$) and 82819 ($Z_{eff} \approx 1.8$).

5.5.2 ELM characterisation

Figure 5.8 shows the variation in ELM frequency for the high triangularity JET-ILW plasmas shown in Figure 5.7. Figure 5.8(a) shows across the JET-ILW deuterium scan the ELM frequency shows no significant change, in contrast to the equivalent JET-C deuterium scan (see Section 4.3). Figure 5.8(b) suggests across both nitrogen scans there is an initial decrease in ELM frequency up until N_2 $\Gamma_{el} = 1.3 \times 10^{22}$ el/s. After which, the ELM frequency rapidly increases marking the transition towards Type III ELMs.

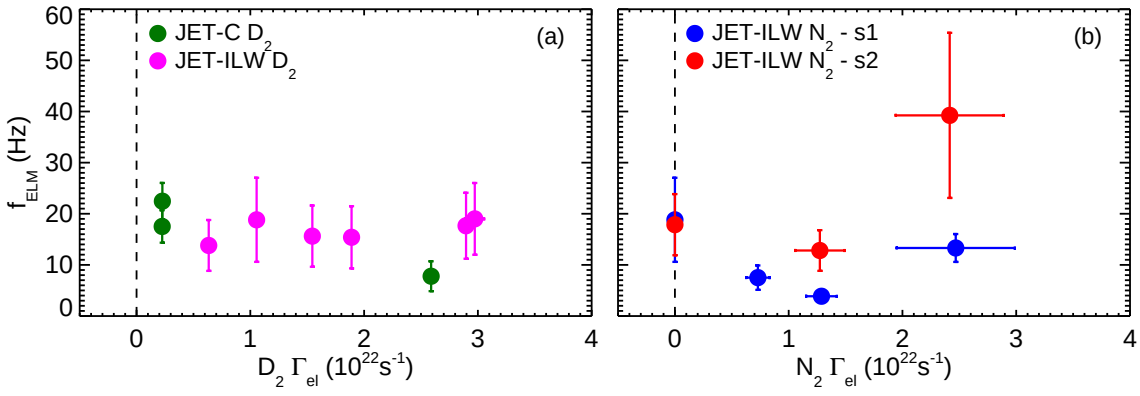

Figure 5.8: Variation in ELM frequency (f_{ELM}) for high triangularity JET-ILW plasmas across the deuterium fuelling and nitrogen seeding scans as shown in Figure 5.7

The initial decrease in ELM frequency and improvement in performance with increasing nitrogen seeding for JET-ILW plasmas is akin to increasing deuterium fuelling for JET-C plasmas. As discussed in Section 4.3, for JET-C plasmas at relatively high deuterium fuelling there is a transition to mixed type I/II ELMs. It is argued that

the decrease in ELM frequency is due to an increase in the inter-ELM loss prolonging the build to critical pressure [75, 90, 95]. This is supported by a difference in the inter-ELM build up of the stored energy, see Figure 4.5.

Similar to Figure 4.5, Figure 5.9 shows the inter-ELM build of the stored energy for the two high triangularity JET-ILW plasmas with and without nitrogen seeding. The nitrogen seeded plasma (red), in comparison to the unseeded plasma (blue), has a slower build up. This is consistent with the premise that the initial decrease in ELM frequency with nitrogen seeding for JET-ILW plasmas is due to a increased inter-ELM loss and suggesting a transition to mixed type I/II ELMs.

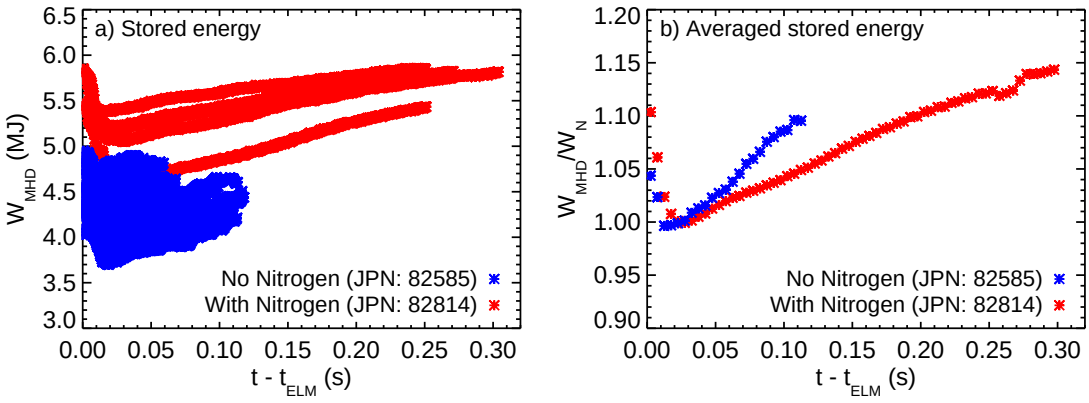

Figure 5.9: Comparison of inter-ELM build up of the stored energy for a high triangularity JET-ILW plasma with (JET pulse no. 82814 in red) and without (JET pulse no. 82585 in blue) nitrogen seeding. These are the same two pulses as shown in Figure 5.2.

It is important to note further analysis is required, such as considering the magnetic fluctuation spectrograms, to confirm consistency with the mixed Type I/II JET-C results. In addition, there are a number of differences between the ELMs in JET-C and JET-ILW plasmas, see [117, 119], which require further understanding in terms of the implications for the mixed Type I/II ELM regime. For example, for JET-ILW plasmas Type I ELMs exist below a critical pedestal temperature height, which, for JET-C plasmas marks the transition to Type III ELMs. Furthermore, the timescale of the ELM crash varies with JET-ILW plasmas as there is a mixture of fast ($\approx$ 2 ms) and slow ($\approx 5-10$ ms) ELM events [118]. In comparison, a typically an ELM crash in JET-C is $\approx 200\mu s$ [127].

5.5.3 Pedestal pressure structure and comparison to the EPED1 model

The left and right hand column of Figure 5.10 shows the pressure pedestal structure and EPED1 predictions for the high triangularity JET-ILW plasmas shown in Figure

5.7.

Figure 5.10(a) and 5.10(c) show the pressure pedestal widens in real and flux space respectively ($\Delta_{pe} \approx 1.5 - 2.7$ cm and 2.9-5.0 % of normalised magnetic flux), across JET-C and JET-ILW deuterium scans [122]. Figure 5.10(e) shows for these plasmas the peak pressure gradient decreases with increasing deuterium fuelling however this decrease is weaker for JET-C plasmas ($dp/d\Psi_N \approx 355 - 280$ kPa) in comparison to JET-ILW plasmas ($dp/d\Psi_N \approx 300 - 170$ kPa). The combination of pedestal width and gradient define the pressure pedestal height which, as shown by Figure 5.10(g), increases from $p_{tot,ped} \approx 20$ to 24 kPa with increasing deuterium fuelling for JET-C plasmas. However, for JET-ILW deuterium fuelled plasmas the stronger reduction in gradient counteracts the pedestal widening resulting in the pressure remaining constant at $p_{tot,ped} \approx 13$ kPa. EPED1 does not predict the increase in pedestal width (Figure 5.10(c)) for JET-C and JET-ILW deuterium fuelled plasmas. EPED1 also does not predict the increase in pressure pedestal height for JET-C plasmas as rationalised in the previous chapter. However EPED1 does predict the pressure pedestal height (Figure 5.10(g)) in the case of the JET-ILW discharges.

Figure 5.10(b) and 5.10(d) show the pressure pedestal also widens with increasing nitrogen seeding for JET-ILW plasmas in real and flux space ($\Delta_{pe} \approx 1.7 - 2.6$ cm and 3.3-5.0 % of normalised magnetic flux). In contrast to the JET-C and JET-ILW deuterium scans, Figure 5.10(f) shows with increasing nitrogen seeding for JET-ILW plasmas the peak pressure gradient initially increases before saturating. Both the increasing width and gradient act to increase the pressure pedestal height with increasing nitrogen seeding, as shown by Figure 5.10(h). EPED1 predicts no change in the pressure pedestal width or height within increasing nitrogen seeding where Zeff is fixed at 2.0. However the integral-line measurements of Z_{eff} range from 1.3 to 1.8 with increasing nitrogen seeding and therefore the injection of an impurity is not accounted for in the model.

In summary, on comparison of JET deuterium (JET-C and JET-ILW) and nitrogen (JET-ILW) scans these measurements highlight two key results. First for plasmas with the presence of a carbon like impurity (carbon for deuterium fuelled JET-C plasmas and nitrogen for nitrogen seeded JET-ILW plasmas) there is an improvement in performance with increasing gas dosing due to the pedestal widening and in the case of JET-C plasmas, a weak reduction in the peak pressure gradient whereas for the JET-ILW plasmas, an improvement in the peak pressure gradient. Second, for the JET high triangularity Type I ELMy H-mode scenario it does not follow that the pedestal widening results in an increase in performance, because for deuterium fuelled JET-ILW plasmas the pressure pedestal widens but the pressure pedestal height remains constant. However, for nitrogen seeded JET-ILW plasmas again the pedestal widens and the pressure pedestal height increases.

Figure 5.11 shows the measured pedestal width (Δ_{pe}) as a function of measured poloidal pedestal normalised pressure ($\beta_{pol,ped}$) reiterating the latter result, as just discussed, in that the increase in width is not necessarily related to pedestal performance. Figure 5.11 also compares measurements with the square root scaling relationship between pedestal width and height which acts as the Kinetic Ballooning constraint in EPED1. The pedestal width increases for the JET-C deuterium scan (green points) with increasing deuterium fuelling and $\sqrt{\beta_{pol,ped}}$ however the pedestal width broadening is greater than expected from the $\sqrt{\beta_{pol,ped}}$ scaling (see previous chapter). The pedestal width for the JET-ILW deuterium scan (pink points) increases with increasing deuterium fuelling. However, unlike JET-C, $\beta_{pol,ped}$ initially decreases with increasing fuelling resulting in a normal deviation from the $\sqrt{\beta_{pol,ped}}$ scaling. Finally, the pedestal width for the two JET-ILW nitrogen scans (red and blue points) increases initially with nitrogen seeding and $\sqrt{\beta_{pol,ped}}$ in good agreement with the $\sqrt{\beta_{pol,ped}}$ scaling. At the highest N_2 seeding rate there is a deviation from the scaling due to the pedestal pressure plateauing. Figure 5.11 highlights that the deuterium fuelling JET-ILW scan is the most challenging for the EPED1 model as, unlike the deuterium fuelled JET-C and nitrogen seeded JET-ILW plasmas, the deuterium fuelling JET-ILW scan deviates from the scaling relation acting as the kinetic ballooning constraint.

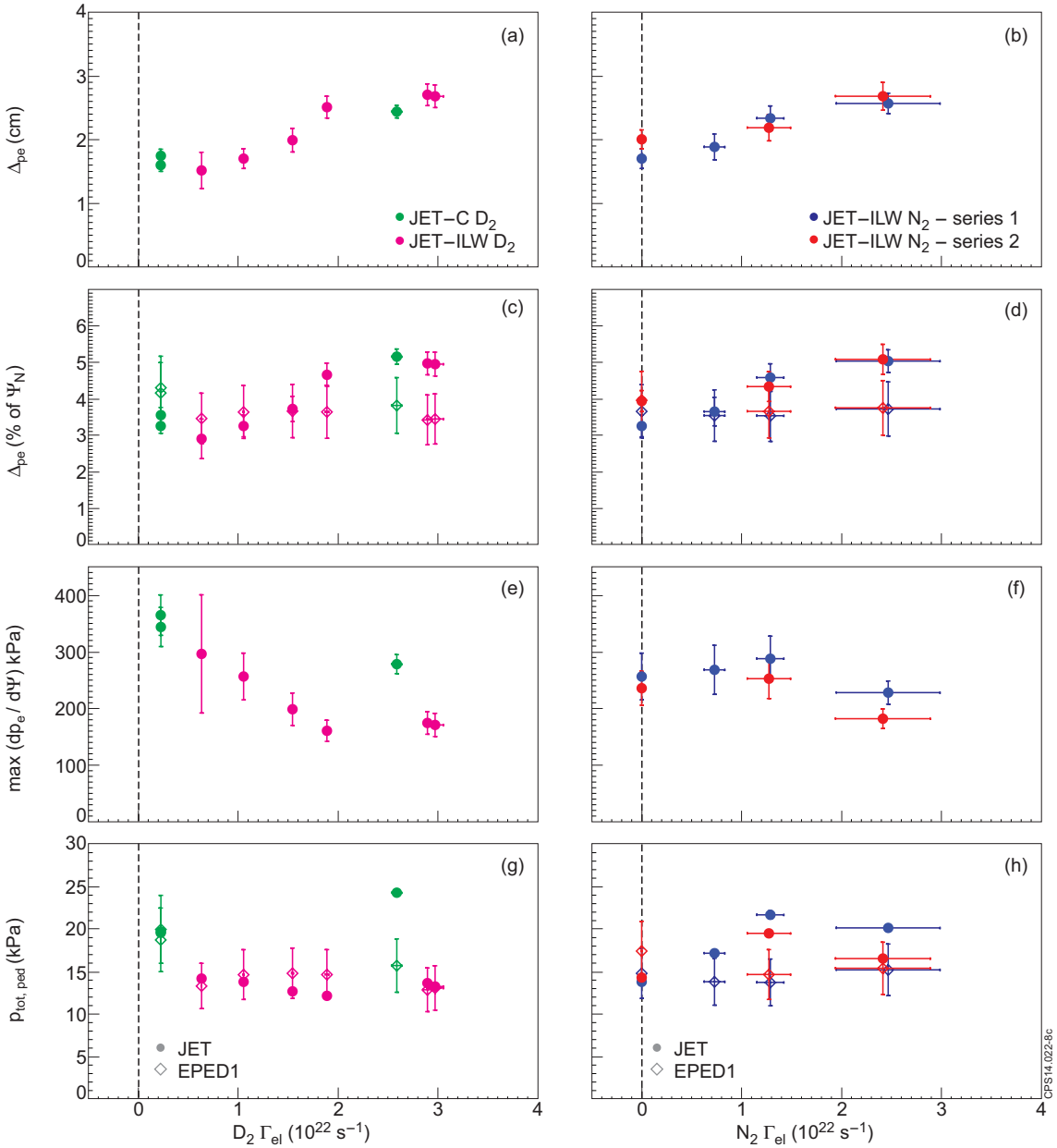

Figure 5.10: Variation in JET measurements of the pressure pedestal structure (circles) and comparison to EPED1 predictions (diamonds) for the deuterium fuelling and nitrogen seeding scans shown in Figure 5.7: JET-C deuterium fuelling scan (green), JET-ILW deuterium fuelling scan (pink) and two JET-ILW nitrogen seeding scans (blue and red). Measured pressure pedestal width (Δ_{pe}) in cm as a function of (a) deuterium fuelling and (b) nitrogen seeding. Measured pressure pedestal width (Δ_{pe}) in percentage of normalised flux and EPED1 predictions as a function of (c) deuterium fuelling and (d) nitrogen seeding. Peak pressure gradient ($max(dp_e/dr)$) as a function of (e) deuterium fuelling and (f) nitrogen seeding. Total pressure pedestal height ($p_{tot,ped}$) as a function of (g) deuterium fuelling and (h) nitrogen seeding. EPED1 runs use fixed value of $Z_{eff} = 2.0$.

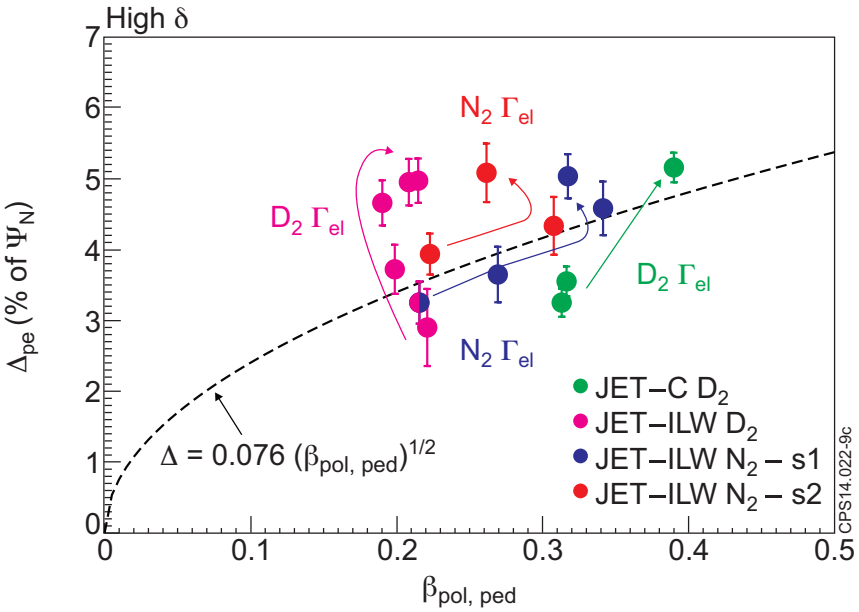

Figure 5.11: Pressure pedestal width in units of normalised flux (Δ_{pe}) as a function of poloidal pedestal normalised pressure ($\beta_{pol,ped}$) for the deuterium fuelling and nitrogen seeding scans shown in Figure 5.7: JET-C deuterium scan (green solid circles), JET-ILW deuterium scan (pink solid circles) and the two JET-ILW nitrogen seeding scan (solid blue and red circles). The black dashed line shows the square root empirical scaling relationship between the pedestal width (Δ_{pe}) and normalised poloidal pedestal pressure ($\beta_{pol,ped}$).

5.5.4 Pre-ELM temperature and density pedestal structure

This section separately examines the variation of the density and temperature pedestal structure. Figure 5.12 presents the temperature pedestal structure and Figure 5.13 presents the density pedestal structure. The left and right hand columns show the pedestal structure with increasing deuterium fuelling and nitrogen seeding, respectively, for the scans shown in Figure 5.7 and 5.10.

Figure 5.12(a) and 5.12(b) show that across both the deuterium fuelling scan (JET-C and JET-ILW plasmas) and the nitrogen seeding scans (JET-ILW plasmas) the temperature pedestal widens, with values ranging from $1.6cm$ at low dosing to $3.2cm$ at high dosing. Figure 5.12(c) and 5.12(d) show the peak temperature gradient decreases across both the deuterium fuelling scan and the nitrogen seeding scans. The reduction of the peak temperature gradient is stronger across the deuterium fuelling scan (Figure 5.12(c)) in comparison to the nitrogen seeding scans (Figure 5.12(d)). The temperature pedestal height across the deuterium fuelling scan marginally decreases for JET-C plasmas and remains approximately constant for JET-ILW plasmas (Figure 5.12(e)). In contrast, for nitrogen seeded plasmas, the temperature pedestal height first decreases and then increases with increasing nitrogen seeding (Figure 5.12(f)). However, overall there is no significant strong change in temperature pedestal height with increasing deuterium fuelling and nitrogen seeding.

Figure 5.13(a) shows that across JET-C and JET-ILW deuterium scans the density pedestal widens ranging from 1.5 cm at low fuelling to 2.8 cm at high fuelling similar to the temperature pedestal width. The peak density gradient, as shown by Figure 5.13(c), remains constant with increasing deuterium fuelling for JET-C plasmas whereas decreases for JET-ILW plasmas. This variation in peak gradient accounts for the increase in density pedestal height with increasing deuterium fuelling for JET-C plasmas whilst the density pedestal height remains constant for JET-ILW plasmas as shown by Figure 5.13(e).

The behaviour of the density pedestal width across the two nitrogen scans (JET-ILW) is not as consistent as the temperature pedestal. Figure 5.13(b) shows the density pedestal width for series 1 (blue) shows no clear trend with increasing nitrogen seeding. However, it is noted that the width does increase from the lowest to highest seeding level. In contrast to series 1 and the deuterium scans the density pedestal width for series 2 shows a weak decrease with increasing nitrogen seeding. The peak density gradient for both nitrogen series initially increases and then saturates as shown by Figure 5.13(d). The pedestal density height shows a strong initial increase after which there is no significant change, see Figure 5.13(f).

The key changes in temperature and density pedestal structure which result in a variation of the pressure pedestal and edge performance for JET-C and JET-ILW

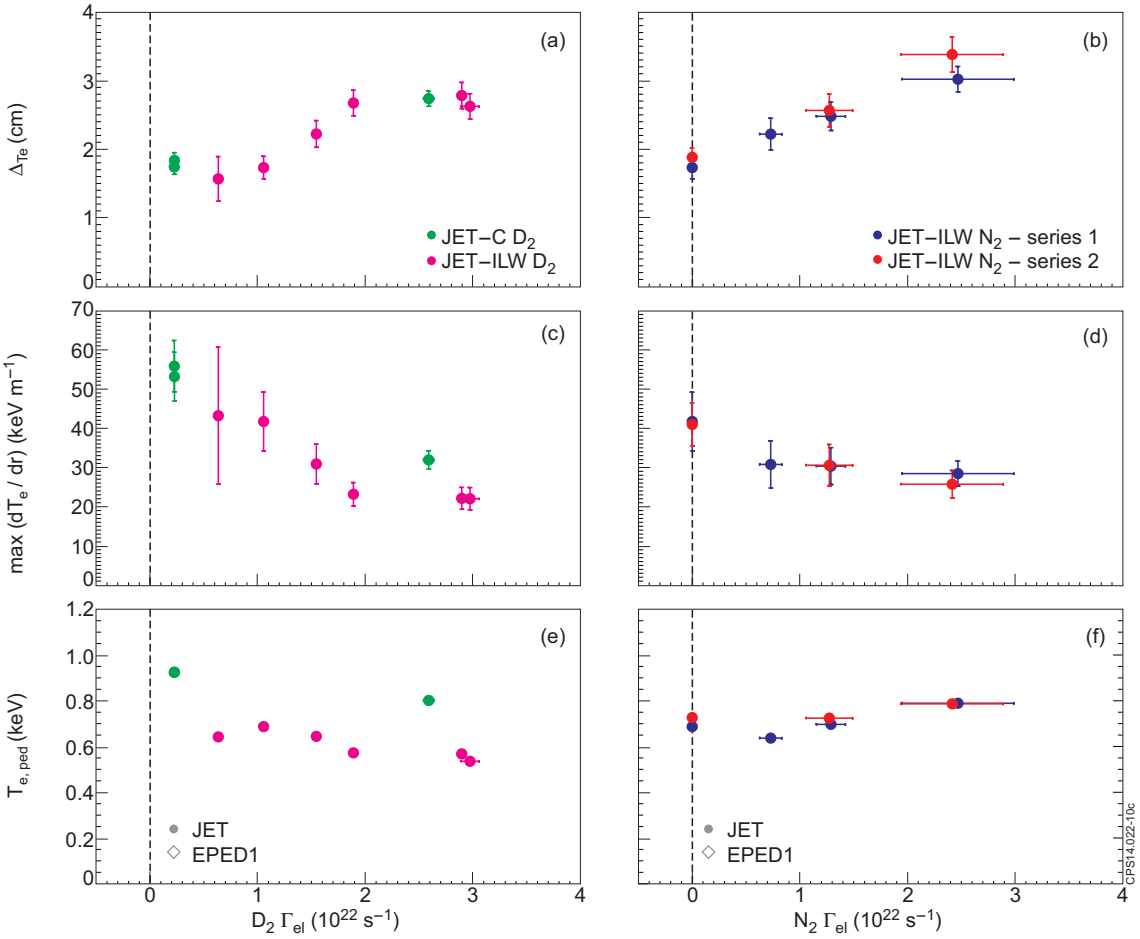

Figure 5.12: Variation in temperature pedestal structure for the deuterium fuelling and nitrogen seeding scans shown in Figure 5.7: JET-C deuterium fuelling scan (green), JET-ILW deuterium fuelling scan (pink) and two JET-ILW nitrogen seeding scans (blue and red). Temperature pedestal width (Δ_{Te}) as a function of (a) deuterium fuelling and (b) nitrogen seeding. Peak temperature gradient ($max(dT_e/dr)$) as a function of (c) deuterium fuelling and (d) nitrogen seeding. Temperature pedestal height ($T_{e,ped}$) as a function of (e) deuterium fuelling and (f) nitrogen seeding.

plasmas are now summarised. First with increasing deuterium fuelling, the pressure pedestal height increases for JET-C plasmas due to a strong increase in the density pedestal height whilst the temperature pedestal height remains constant. Conversely for deuterium fuelled JET-ILW plasmas the pedestal pressure is constant due to the density and temperature pedestal height both remaining constant. The key difference between these plasmas is the variation in the peak density gradient as dn_e/dr is constant for JET-C whereas it decreases for JET-ILW. As a result there is not a strong increase in density pedestal height for JET-ILW plasmas as observed for JET-C plasmas.

For nitrogen seeded plasmas the temperature pedestal behaviour is similar to the deuterium fuelled plasmas in that the pedestal broadens and the peak gradient decreases. The key observation for nitrogen seeded plasmas is the change in the density

pedestal behaviour. The density pedestal shows no monotomous change in width, however the strong increase in peak gradient results in an increase in density pedestal height. The increase in pressure pedestal width is due to the temperature pedestal widening whilst the density pedestal shows no significant change. This increase in pressure pedestal height is due to a strong increase in density pedestal height as well as a relatively small increase in temperature pedestal height.

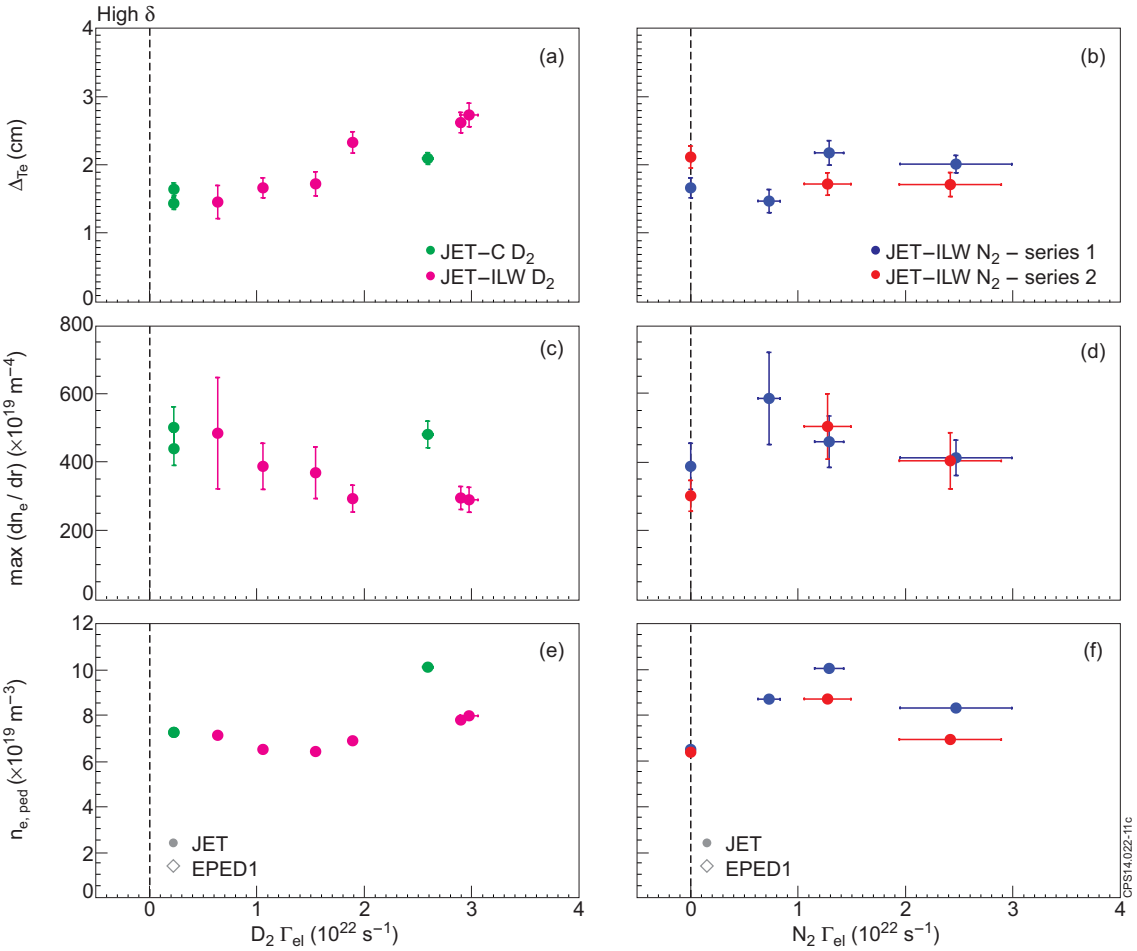

Figure 5.13: Variation in density pedestal structure for the deuterium fuelling and nitrogen seeding scans shown in Figure 5.7: JET-C deuterium fuelling scan (green), JET-ILW deuterium fuelling scan (pink) and two JET-ILW nitrogen seeding scans (blue and red). Density pedestal width (Δ_{ne}) as a function of (a) deuterium fuelling and (b) nitrogen seeding. Peak density gradient ($max(dn_e/dr)$) as a function of (c) deuterium fuelling and (d) nitrogen seeding. Density pedestal height ($n_{e,ped}$) as a function of (e) deuterium fuelling and (f) nitrogen seeding.

5.5.5 Comparison of EPED1 predictions to larger JET database

Throughout this study deuterium fuelling and nitrogen seeding scans, typically consisting of three to six carefully selected pulses, have been considered. The premise behind focusing on these scans is so any variations in, for example, machine parameters (e.g. use of different gas injection modules) or a variation in machine conditioning between experiments is mitigated as much as possible to improve the clarity of the trends in performance and pedestal structure. However it is essential to consider these scans in the context of a wider set of pulses to provide further confidence in the conclusions. This is particularly important for the comparison of measurements to EPED1 predictions for the high triangularity plasmas where the largest discrepancies are observed.

Figure 5.14 presents the measured pressure pedestal height and width as a function of the equivalent EPED1 prediction for high triangularity deuterium fuelled JET-C plasmas (triangles), deuterium fuelled JET-ILW plasmas (diamonds) and nitrogen seeded JET-ILW plasmas (circles). Figure 5.14(a) and 5.14(b) detail a larger database of JET plasmas whilst Figure 5.14(c) and 5.14(d) demonstrate where the scans presented in this Chapter overlay in the context of this larger dataset. The dashed lines shown in Figure 5.14 indicate where the measurement is equal to EPED1 and the dotted dashed lines indicate the extremity of EPED1 predictive accuracy (± 20 %).

Figure 5.14(a) compares the pressure pedestal height measurements and EPED1 predictions. There is a larger scatter for the JET-C D_2 fuelled plasmas, see previous Chapter, where a systematic deviation is found for the highest deuterium fuelling levels. The cluster of deuterium fuelled JET-ILW plasmas are centred on the black dashed line indicating good agreement between the JET measurements and EPED1. However the cluster of nitrogen seeded JET-ILW plasmas is centred along the upper dotted line at the extremity of the EPED1 accuracy. EPED1 under predicts the pressure pedestal height relative to the measurement as shown in detail by Figure 5.10 when considering the nitrogen scans.

EPED1 is a combined height and width model and therefore it is important to consider the width as shown in Figure 12(b) along with Figure 5.14(a). Figure 5.14(b) demonstrates that for high triangularity plasmas the measurements all show a significant range of pedestal widths corresponding to an increase in deuterium fuelling or nitrogen seeding as concluded from the scans. This is not captured by the EPED1 predictions as reflected by a vertical scatter of each group of pulses (deuterium fuelled JET-C plasmas, deuterium fuelled JET-ILW plasmas and nitrogen seeded JETÂň-ILW plasmas) with points spanning the full extent of the EPED1

predictive accuracy and above. This implies the square root relationship between width (Δ) and normalised pressure ($\beta_{pol,ped}$) is not always applicable for JET plasmas and may depend on factors such as the density regime, impurity content (Z_{eff}), position on PB stability diagram and ELM type.

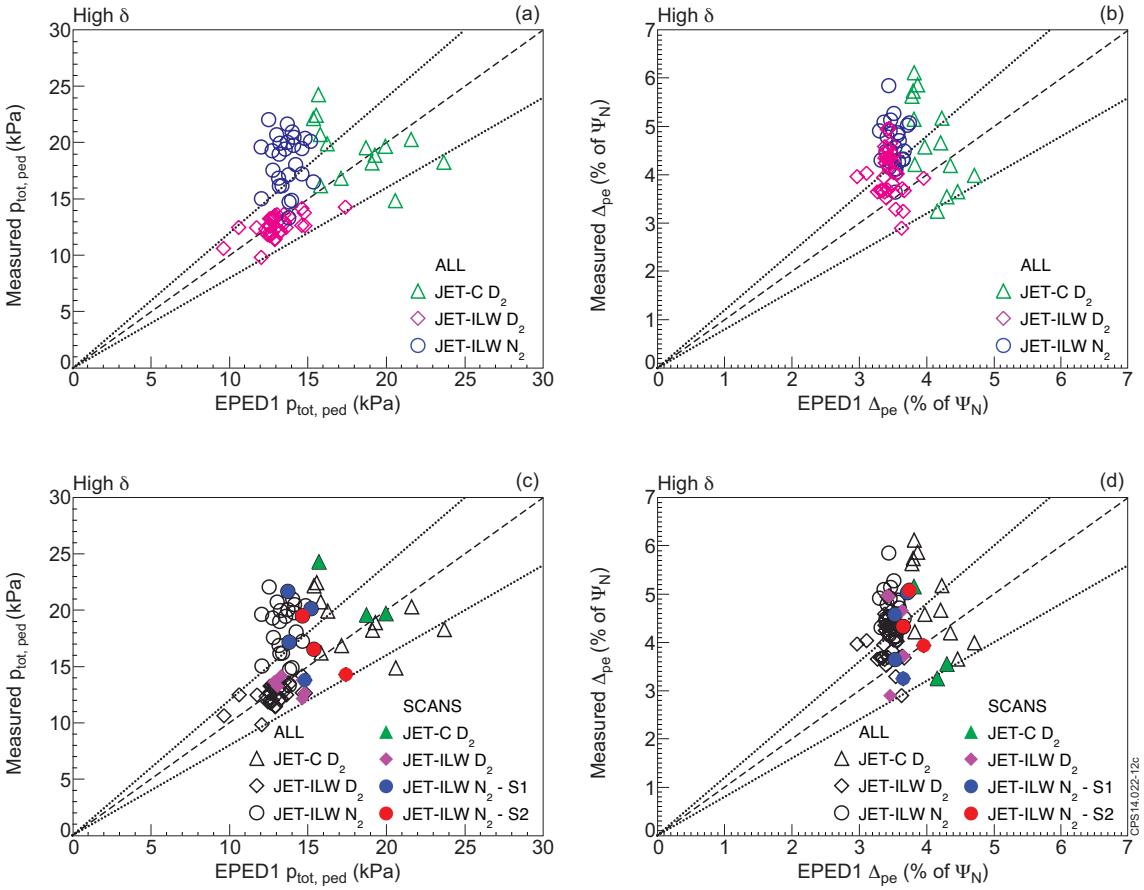

Figure 5.14: (a), (c) Measured pedestal pressure as a function of EPED1 prediction for pedestal pressure and (b), (d) measured pedestal width as a function of EPED1 prediction for pedestal width all for high triangularity JET-C D2 fuelled plasmas (triangles), JET-ILW D2 fuelled plasmas (diamonds) and JET-ILW N_2 nitrogen seeded plasmas (circles). (a), (b) Larger database of JET plasmas for 15 JET-C D_2 (green), 36 JET-ILW D_2 (magenta) and 30 JET-ILW N_2 (blue) plasmas. (c), (d) Comparison of larger database (open grey) to fuelling and seeding scans (closed coloured symbols) as presented throughout this study. The dashed line indicates where measurement is equal to the EPED1 prediction and the dotted dashed lines indicate accuracy of the EPED1 predictions, ±20 %. EPED1 runs use fixed value of $Z_{eff} = 2.0$.

Figure 5.14(c) and 5.14(d) show the scans detailed throughout this study (coloured symbols) overlaid onto the larger dataset (grey symbols). Each scan follows the larger cluster of equivalent plasmas demonstrating that the scans reflect the trends observed in the larger database comparison.

5.6 Summary and conclusions

This Chapter reports on the JET pedestal structure with the new ITER-Like-Wall, comparing both high and low triangularity plasma performance with equivalent JET carbon wall plasmas. Furthermore there is a comparison of the pedestal measurements to EPED1 predictions.

Low triangularity JET-ILW plasmas in both vertical and horizontal target strike point configurations show no significant change in performance (H_{98}, W_{th}, W_{ped}) and pedestal structure (Δ_{pe}, $p_{e,ped}$) with the gas puff level and these results are in good agreement with EPED1 predictions.

For the high triangularity discharges, deuterium fuelling and nitrogen seeding scans with the ITER-like wall have revealed a number of new features in pedestal behaviour on JET. Pure deuterium fuelled discharges with the JET-ILW show an overall 20-30 % reduction in performance when compared with equivalent JET carbon wall discharges. Furthermore, it is observed that there is no improvement in performance and the ELM frequency is constant with increasing deuterium fuelling levels, in contrast with the carbon wall. HRTS data from these fuelling scans reveals an apparent increase in the pedestal width as the deuterium fuelling levels are increased but, crucially, this increase in pedestal width appears not to be consistent with previous scaling observations (e.g. $\Delta = 0.076\sqrt{\beta_{pol,ped}}$ scaling [30]) as the overall pedestal performance does not correspondingly increase. This result has important implications for the physics constraints that determine the pedestal width (for example KBM constraints within EPED models) and is a topic that will require further study in future work.

In contrast to the deuterium fuelled plasmas, the addition of nitrogen seeding to JET-ILW plasmas does show an increase in the pressure pedestal height, restoring performance to the levels previously observed with the JET carbon wall. Furthermore, the ELM frequency decreases and the timescale of the inter-ELM build up of stored energy increases with nitrogen seeding consistent with a transition to mixed Type I/II ELMs. Additional analysis is required to support the premise of a transition to mixed Type I/II ELMs. Measurements of the electron temperature and density pedestal structure for these pulses reveal that the reduction in performance for deuterium fuelled plasmas after the installation of the Be/W ILW wall is primarily due to a reduction in the temperature pedestal height. However, the recovery of the pressure pedestal height with increasing nitrogen seeding is predominately due to the increase in density pedestal height whilst the temperature pedestal height also marginally increases. The increase in pressure pedestal height is accompanied by a widening of the pressure pedestal that is primarily attributed to an increase in temperature pedestal width as the corresponding density pedestal width shows no

clear trend and the behaviour varies between different scans with increasing nitrogen seeding.

EPED1 predictions for the JET-ILW deuterium fuelled plasmas show very good agreement with the measured pressure pedestal height. However, for the pulses considered here, the observed systematic increase in the pedestal width with increased deuterium fuelling levels (at constant $\beta_{pol,ped}$) is not predicted. The JET measurements suggest the pressure pedestal formation is not purely governed by the plasma edge as the scrape-off-layer, neutral recycling and wall interactions could all play a role. If this is the case, further work is required to determine how to incorporate these effects into current models. For the JET-ILW nitrogen seeded plasmas, EPED1 predictions appear to underestimate the measured pressure pedestal height and, as with the pure deuterium fuelled discharges, the observed widening of the pedestal pressure is not captured by the model. Further work is required to identify the origins (for example, the role of Z_{eff} profiles) and significance of these discrepancies, as well as further refining and understanding the uncertainties associated with the measurements and the model.

Chapter 6

Conclusions and future work

6.1 Conclusions

This thesis is focused on the JET HRTS system with particular interest in a number of different aspects, spanning hardware improvements to pedestal fitting. This section presents the key conclusions from each chapter.

Chapter 2 provides an introduction to the HRTS system, which measures electron temperature and density profiles across a large part of the plasma radius, along an outer radial chord close to the magnetic mid-plane. This chapter also discusses the improvements made to address the under-performance of the HRTS polychromators. In their original configuration, the HRTS polychromators were found to suffer from loss of signal, fibre-to-fibre sensitivity and input numerical aperture sensitivity. This severely compromised the ability to provide independently calibrated HRTS temperature profiles. By realigning the polychromators and installing plastic shims to correct the position of the APDs, these shortcomings have been successfully resolved. A comparison of averaged temperature profiles before and after the work demonstrates that the systematic point-to-point fluctuations in electron temperature across the profile have been reduced to acceptable levels. Consequently, all the JET electron temperature data collected after this optimisation (after the installation of the new ITER-Like-Wall) is now independently calibrated (whereas previously the systematic errors were corrected via cross calibration to JET's ECE diagnostic).

One of the key aims of the JET HRTS system is to measure the steep pressure gradient at the plasma edge; the pedestal. The process of fitting an mtanh function to ELM synchronised HRTS radial electron temperature and density profiles, in order to extract the pedestal structure, is described in Chapter 3. In addition to statistical errors, the mtanh parameters also contain systematic errors from the deconvolution methods, which incorporate the HRTS instrument function. This is discussed in

detail by [63, 73]. Chapter 3 also quantifies the systematic error arising from the ELM synchronisation of the selected HRTS profiles. A Monte-Carlo simulation that replicates the fitting technique uses synthetic HRTS-like profiles to demonstrate that this systematic error is negligible in comparison to the statistical uncertainty.

The process of creating a synthetic HRTS-like profile is explained in Chapter 3. In this, the photon throughput of the HRTS system is estimated, approximating the system transmission losses and comparing this to the number of photons collected during the Raman calibration (which offers a continuous stable measurement of known density). The measured number of Raman scattered photons, as determined by the signal-to-noise ratio is found to be correct to within a factor of 1.7, with good agreement in the radial profile shape. By correcting the number of Thomson scattered photons for a given temperature and density by a factor of 1.7 and comparing with the Thomson scattered wavelength distribution, given by the Selden-Naito expression at a given temperature, the number of photons in each spectral channel can be accurately evaluated. The synthetic measured temperature and density is then determined by fitting to the response of each channel incorporating errors from photon noise (Poisson statistics) in addition to the amplifier and background light noise. The spread of temperature and density measurements when performing the fit numerous times is used as the corresponding overall error in the fit. Analysis of the effect of vignetting for the two possible HRTS lines-of-sight show that there is a degradation of measurement quality for three more edge spatial points on the upper line-of-sight.

Chapter 3 also provides a description of the procedure undertaken to perform an mtanh fit to ELM synchronised data. This involves selecting the stationary phase of a pulse, selecting the timing of the ELMs, and then, assessing the quality of the resulting fits (and repeating the initial steps if necessary). It is also shown that comparing fits covering different regions of the ELM cycle provides a useful insight into whether the mtanh parameters conform to overall trends.

The primary focus of this thesis has been to utilise the JET pedestal fitting routine to quantify the pedestal structure. Chapters 4 and 5 document a JET-C and JET-ILW pedestal study respectively.

The JET-C pedestal study, presented in Chapter 4, details the results from the analysis of a fuelling scan database comprising of 14 high triangularity ($\delta \approx 0.41$), Type I ELMy H-mode JET plasmas. These results show as the fuelling level is increased from low, ($\Gamma_D \approx 0.2 \times 10^{22}$ el/s, $n_{e,ped}/n_{gw} = 0.7$), to high dosing ($\Gamma_D \approx 2.6 \times 10^{22}$ el/s, $n_{e,ped}/n_{gw} = 1.0$) levels the variation in ELM behaviour shows consistency with a transition from 'pure Type I' to 'mixed Type I/II' ELMs [90]. In contrast, the pulses in the new JET-C database are better diagnosed in comparison to previous

studies (such as [90]) and most notably have pedestal measurements provided by the JET High Resolution Thomson Scattering (HRTS) system. This study focuses on the role of the pedestal structure, as quantified by a least squares mtanh fit to the HRTS profiles, on the plasma performance across the fuelling scan.

A key result from this work is the pedestal width narrows and the peak pressure gradient increases during the ELM cycle for low fuelling plasmas, whereas, at high fuelling, the pedestal width and peak pressure gradient is found to saturate towards the latter half of the ELM cycle. An ideal MHD stability analysis shows that both low and high fuelling plasmas move from stable to unstable approaching the ideal ballooning limit of the finite peeling ballooning stability boundary. Comparison to EPED predictions show, that on average, there is good agreement with experimental measurements for both pedestal height and width. However, when presented as a function of pedestal density, experiment measurement and model predictions show opposing trends. The measured pre-ELM pressure pedestal height increases by ≈ 20 %, while results from EPED predict a 25 % decrease from low to high fuelling. Similarly, the measured pressure pedestal width widens by ≈ 55 %, in poloidal flux space, whereas EPED predictions show a 20 % decrease from low to high fuelling. Two possible explanations for the disagreement are provided. First, it may be that EPED under-predicts the critical density, which marks the transition from kink-peeling to ballooning limited plasmas. Second, the stronger broadening of the measured pedestal width, than predicted by EPED, is an indication that other transport related processes may contribute to defining the pedestal width, such as enhanced inter-ELM transport as observed at high fuelling, for mixed Type I/II ELMy pulses.

The JET-ILW pedestal study, presented in Chapter 5, extends the JET-C database to include low and high triangularity ($\delta \approx 0.22 - 0.39$) 2.5 MA, Type I ELMy H-mode JET plasmas from the first campaign performed after the installation of the new ITER-like Wall (JET-ILW) with a view to explain the observed changes in performance (edge and global). The database explores the effect of increasing deuterium fuelling ($D_2\Gamma_{el} \approx 0.6 - 4.3 \times 10^{22}$ el/s) and nitrogen seeding ($N_2\Gamma_{el} \approx 0.0 - 3.8 \times 10^{22}$ el/s). A comparison to equivalent JET carbon wall (JET-C) plasmas is made as well as considering predictions from EPED1.

The low triangularity vertical target JET-ILW deuterium scan and low triangularity horizontal target JET-ILW nitrogen scan both show no significant change in performance ($H_{98} \approx 0.7$, $W_{th} \approx 4.0$ MJ and $W_{ped} \approx 1.2$ MJ) and pedestal structure ($\Delta_{pe} \approx 4$ % of Ψ_N, $p_{e,ped} \approx 12$ kPa) with increasing gas dosing of either deuterium or nitrogen. These results are in good agreement with EPED1 predictions.

At high triangularity the JET-ILW plasmas have revealed a number of new features regarding the pedestal behaviour. For pure deuterium fuelled JET-ILW plasmas a

20-30 % reduction in performance is observed in comparison with JET-C plasmas. Measurements of the electron temperature and density reveal that the reduction in performance from JET-C to JET-ILW is primarily due to a degradation of the temperature pedestal height. With increasing deuterium fuelling there is no measurable improvement in performance or pedestal pressure for JET-ILW plasmas, in contrast to high triangularity JET-C plasmas. However, the pedestal still widens with increasing deuterium fuelling for JET-ILW plasmas, which is inconsistent with the $\Delta = 0.076\sqrt{\beta_{pol,ped}}$ scaling. The performance and pedestal pressure of JET-ILW plasmas can be partially recovered to that of JET-C plasmas with additional nitrogen seeding. The increase in pressure pedestal height for JET-ILW plasmas with nitrogen seeding is predominately due to a significant increase in density pedestal height in addition to an increase in the temperature pedestal height. Furthermore, the increase in pedestal width is found to result from to the temperature pedestal widening whilst there is no significant change observed in the density pedestal width. The comparison between EPED1 predictions and measurements at high triangularity is intriguing as, for example, pure deuterium fuelled plasmas show very good agreement in terms of pedestal height but not in width. EPED1 results under-predict the pedestal height and width at high nitrogen seeding levels for JET-ILW plasmas, however, further work is required to determine the significance of these deviations as discussed in detail in the next section. Understanding this is essential as it provides further insight to the physical mechanisms that govern the pedestal structure and edge performance.

6.2 Future work

There are currently no imminent hardware modifications planned for the HRTS system. The lower line of sight is preferred due to the better edge measurements of the pedestal (at the detriment of the radial extent of the core measurements). One of the challenges the HRTS system faces when operating with a metal wall is increased stray light due to reflections in the vessel. Stray light affects only a few spatial points, however, these tend to (unfortunately) be key points in the pedestal region. This will be interesting to further quantify and monitor as the wall tiles are pushed to operational limits and the characteristics of the reflections potentially change. In the long term, the HRTS system will need to ensure compatibility with the planned JET DT campaign. Since the JET HRTS system was installed long after JET's previous DT campaign a full and detailed avaluation of the system hardware is necessary in order to determine if it will be able to withstand the high energy neutron flux and to determine what modifications (if any) must be implemented.

In terms of the JET pedestal analysis tool, potential future enhancements include

converting to a Bayesian technique (instead of the χ^2 minimisation) and developing a fitting tool which incorporates multiple diagnostic data with the corresponding instrument function. The challenge with developing a Bayesian tool is this would require greater integration to the diagnostic analysis software. With regards to a multiple diagnostic fit, the challenges lie in rigorously incorporating the instrument function of each diagnostic. In the long term, the focus should shift from the development of the tool to the routine use of the tool.

To further exploit the existing fuelling and seeding pedestal database additional areas of interest include quantifying the inter-ELM dynamics of the pedestal structure for JET-ILW plasmas, similar to the analysis performed in Chapter 4 for JET-C plasmas. Initial progress has been made in that the pedestal fits have been performed. It would also be interesting to understand the difference between the density and temperature pedestal structure and explore how to incorporate this knowledge into the pedestal models. For example, the relative position of the temperature pedestal is radially further inward in comparison to the density pedestal (see Figure 5.2).

There have been more recent fuelling and seeding JET-ILW experimental sessions resulting in plasmas which have not yet been incorporated into the database presented in this thesis. The fuelling and seeding pedestal database should be extended, particularly as the most recent JET-ILW plasmas incorporate a variation in divertor configuration at high and low triangularity. Furthermore, the type of plasmas and scenarios considered should be expanded beyond the ITER baseline fuelling and seeding plasmas, which have previously been the focus of recent JET pedestal structure studies. Experiments have been conducted on hybrid plasmas where β_N extends much higher than the plasmas presented in this thesis. There has already been some analysis of the pedestal structure for these hybrid JET-ILW plasmas but systematic nitrogen seeding scans have not yet been completed. In addition, the JET-ILW measurements should be compared to their equivalent measurements on DIII-D and ASDEX-Upgrade (AUG) to establish the machine dependence of the pedestal structure variations explored in this thesis. This has already been started. Comparison of JET and AUG measurements, as detailed in [122], show the effect of a metal wall is variable as AUG with a Tungsten wall does not show a reduction in confinement as experienced by equivalent JET high triangularity plasmas. Furthermore, there is no strong improvement in confinement with nitrogen seeding. To facilitate the comparison of DIII-D and JET measurements there has been a recent dedicated DIII-D experiment to study the role of collisionality and effective charge on the H-mode pedestal structure through means of deuterium fuelling, nitrogen seeding and lithium dropping. An advantage of performing a multi-machine comparison is the study benefits from the diagnostic strengths of each machine.

There are a number of possible actions that would serve to improve the comparison

between the JET measurements and EPED predictions. For the existing database, a scan of the Z_{eff} input to the EPED model will be particularly insightful, for even just one JET-ILW nitrogen seeded plasmas. This should demonstrate whether the variation in Z_{eff} required to get measurements and predictions to agree is physically possible. For future JET-EPED comparisons it would be invaluable to improve the Z_{eff} and impurity measurements on JET such that a reliable local pedestal Z_{eff} measurement can be provided as an input to the model. The edge current is an important quantity in the context of the PB pedestal stability and EPED predictions. For JET plasmas this is calculated by the equations documented in [29] or other models. An improvement would be to develop the capability on JET to measure the edge current. Another consideration relating to EPED is that it is important to understand the significance of those JET plasmas that deviate from the $\Delta = 0.076\sqrt{\beta_{pol,ped}}$ scaling, which acts as the KB constraint within the model. A more extensive database would highlight where this scaling does and does not apply for JET plasmas. Furthermore, signatures of KB modes should be identified to better understand the pedestal width and height limits. These actions may result in further developments to the EPED model.

Another possible area of interest would be to improve the ion kinetic profiles, particularly at the plasma edge in the pedestal region, to determine if the trends in the pedestal structure reported in this thesis for the electron profiles are observed in the ion profiles. Also, these profiles would confirm whether the assumption that $T_e = T_i$ is valid and this could improve the uncertainty on the EPED comparison (since the model calculates the total pressure profile).

In terms of the general long term goal of better understanding the H-mode pedestal and it's role on confinement, it is important to strive towards a more integrated approach. This will involve combining expertise and knowledge of the SOL, pedestal and core regions when analysing measurements and implementing models as the plasma behaviour within JET's new metallic wall has demonstrated these can strongly impact upon each other.

Appendix A

The evolution of electron density and temperature following the H-mode transition

The main focus of this thesis is exploiting JET HRTS measurements during the stationary phase of a pulse to quantify the H-mode pedestal structure. However, HRTS profiles are also utilised for numerous other physics studies for example, as now discussed, the evolution of electron temperature and density following H-mode transition and in the termination phase. The overriding aim of this study is to understand the transport processes which govern the build up and decay of stored energy and then assess the implications for ITER. This appendix section focuses on the analysis of JET density profiles after the H-mode transition completed by M. Leyland as part of a wider study convened and published by A. Loarte (ITER Organization) [128].

A.1 Introduction

Fusion power (alpha particle heating P_α) is proportional to the plasma density [12] as,

$$P_\alpha = R_{DT} E_\alpha = n_D n_T < \sigma\upsilon > V E_\alpha \tag{A.1}$$

where R_{DT} is the deuterium-tritium reaction rate (as given by Equation 1.1), E_α is the energy of the resulting alpha particle from a deuterium-tritium reaction (≈ 3.5 MeV), n_D is the deuterium density, n_T is the tritium density and $< \sigma\upsilon >$ is the reactivity. Consequently, the formation and shape of the density profile is particu-

larly important when establishing a burning plasma on future devices such as ITER [87].

The stationary baseline regime foreseen for ITER, where $Q_{DT} \geq 5$ operation, is an ELMy H-mode [81, 89]. An H-mode plasma is formed by a spontaneous transition from a heated low confinement region (L-mode) when achieving a sufficient edge power flow (P_{loss}), as defined by [128],

$$P_{loss} = P_{\alpha} + P_{add} - P_{rad}^{core} - \frac{dW_{plasma}}{dt} \geq P_{L-H} \tag{A.2}$$

where P_{alpha} is the heating power due to the energetic alpha particles, P_{add} is the power due to additional heating, P_{rad}^{core} is the radiated power, $\frac{dW_{plasma}}{dt}$ is the change in plasma stored energy and P_{L-H} is the L-H loss power threshold as determined from a multi-machine database [105]. In the build-up phase following the H-mode transition controlling the density profile by gas fuelling (edge), pellet injection (edge) and negative neutral beam injection (core) is particularly important in terms the resulting stationary H-mode global performance (H_{98}, W_{th}) and fusion gain (Q_{DT}). For example if the density is increased too quickly the plasma is cooled reducing the reactivity ($< \sigma\upsilon > \propto T$) and resulting in less alpha particle heating. This could ultimately result in the plasma dropping out of H-mode back into L-mode. Conversely, if the density is increased too slowly the build-up phase is unnecessarily prolonged as external heating is required to heat the plasma before the alpha particle heating can fully establish.

Gaining an insight into the physical mechanisms which govern the formation of the density profile requires solving the 1-dimensional diffusion equation, as given by [10],

$$\frac{\partial n}{\partial t} + \frac{\partial \Gamma}{\partial r} = S \tag{A.3}$$

where n is the density, Γ is the outward particle flux and S is the source term. This equation can be used to describe the particle transport along a radial chord within a Tokamak plasma. The outward particle flux (Γ) is typically defined as[87],

$$\Gamma = -D\nabla n + nV \tag{A.4}$$

where D is the diffusion coefficient, n is the density and V is the convection velocity. The aim of transport research is to solve this particle diffusion equation along with a similar set of equations describing energy and magnetic flux diffusion. In terms of the particle diffusion, the rate of change in the density profile ($\frac{\partial n}{\partial t}$) and the source term (S)

can be determined from measurements whereas the spatial variation of the particle flux ($\frac{\partial \Gamma}{\partial r}$) is unknown. Models, such as JETTO, solve the diffusion equation to find a particle flux consistent with the other terms of the diffusion equation. However, obtaining a solution is non-trivial due to, first, there are two particle sources (plasma core and scrape-off-layer). Second, the requirement of a convection term (nV) as when analysing experimental measurements, [129–131] an inward pinch (negative V) is necessary to account for a peaked density profile in the absence of core particle fuelling [87]. These studies quantify D and V in the stationary established phase of a pulse however this study is interested in the transient phase after the H-mode transition.

This chapter documents the behaviour of the density profile following the L-H transition for JET plasmas with the carbon wall (JET-C) database covering a range of plasma currents [88]. Of particular interest is quantifying the relative timescale of the core and edge density evolution. These measurements are used to constrain transport modelling by means of the JETTO code.

A.2 Description of database and example JET pulse

This study considers two data sets corresponding to low ($\delta \approx 0.26$) and high ($\delta \approx 0.41$) triangularity type I ELMy H-mode JET-C plasmas, see Table A.1. The plasma current (I_P) ranges from ≈ 1.0 to 4.3 MA (low δ) and ≈ 1.0 to 3.5 MA (high δ). The magnetic field increases with current from ≈ 1.1 to 3.4 T (low δ) and ≈ 1.0 to 3.2 T (high δ). These plasmas are predominately NBI heated where the average heating power (P_{NBI}) ranges from 4.5 to 22.7 MW with increasing plasma current. There is additional RF heating up to 4.0 MW for the pulses with the highest NBI heating. The pedestal density normalised to the Greenwald density ($n_{e,ped}/n_{GW}$) ranges from 0.3 to 0.7 (low δ) and 0.6 to 1.1 (high δ). The highest values of q_{95} and β_N, see Table A.1, correspond to the lower current plasmas.

Figure A.1 shows the typical evolution of the build-up phase after the H-mode transition for a high current ($I_P \geq 3.0$ MA) JET-C plasma. The high current plasmas are of particular relevance to ITER as the plasma density approaches ITER values ($\approx 1.0 \times 10^{20}$ m^{-3}) whilst maintaining a relatively high plasma core temperature (≈ 5 keV). For this particular pulse the NBI heating is applied at ≈ 9.00 s after which the D_α emission begins to rise. The H-mode transition occurs at 9.38 s as indicated by the small reduction in D_α emission. The stored thermal energy ramps up from 2 to 10 MJ in ≈ 2 s. There is strong initial deuterium fuelling ($\Gamma_D \approx 5.0$ el s^{-1}) coinciding with the beginning of NBI heating however during the stationary phase of the pulse

Table A.1: Comparison plasma parameters for low and high triangularity type I ELMy H-mode JET-C plasmas where δ_{up} is the upper triangularity, δ_{low} is the lower triangularity and δ is the average trianglarity all averaged over the low and high triangularity data set. B_t is the magnetic field in T, I_p is the plasma current in MA, q_{95} is the safety factor at 95 % of the minor radius, P_{NBI} is the neutral beam injection (NBI) heating power and $n_{e,ped}/n_{GW}$ is the pedestal density normalised to the Greenwald density.

	Low triangularity	High triangularity
No. pulses	20	18
$(\delta_{up} + \delta_{low}) = \delta$	$(0.18 + 0.33)/2 = 0.26$	$(0.43 + 0.40)/2 = 0.41$
B_t	$1.1 - 3.4$ T	$1.1 - 3.2$ T
I_p	$1.0 - 4.3$ MA	$1.0 - 3.5$ MA
q_{95}	$2.6 - 3.7$	$2.9 - 3.7$
P_{NBI}	$4.5 - 22.7$ MW	$4.5 - 20.5$ MW
P_{ICRH}	$0.0 - 4.0$ MW	$0.0 - 2.2$ MW
β_N	$1.5 - 2.2$	$1.3 - 2.5$
$n_{e,ped}/n_{GW}$	$0.3 - 0.7$	$0.6 - 1.1$

the Γ_D is reduced to ≈ 3.5 el s^{-1}.

The core ($\rho \equiv r/a = 0.2$) temperature shows the most significant increase ($\Delta T_{e,i} \approx 2$ keV) with NBI heating before the H-mode transition. The edge ($\rho \equiv r/a = 0.8$) temperature also increases. Shortly after the H-mode transition the core and edge temperature does not evolve any further whereas the core and edge density begins to increase. The variation in density occurs just after the H-mode transition due to the formation of the edge transport barrier. The edge density increases over a timescale similar to the energy confinement time (τ_E) in the stationary phase. Of particular interest in the context of this study and ITER is the core density increases over a longer timescale of $(4 - 5\tau_E)$. Consequently there is initially a hollow density profile as shown by Figure A.2(c) and (d).

Figure A.2 demonstrates this hollow profile is less pronounced the longer after the H-mode transition until it is flattened by a sawtooth event 1.15 s after the H-mode transition. Hollow density profiles have been observed towards the end of a long ELM free period [132], such as before the first ELM, due to the influx of impurities at the plasma edge modifying the peaking (de-peaking) of the density profile. The hollow density profiles discussed here are not due to impurity accumulation as the ion and electron density and temperature measurements are comparable. At high edge densities ($\approx 8.0 \times 10^{19}$ m^{-3}) the NBI deposition profile also become hollow (see Figure A.2(e)) resembling the lack of core fuelling as expected on ITER.

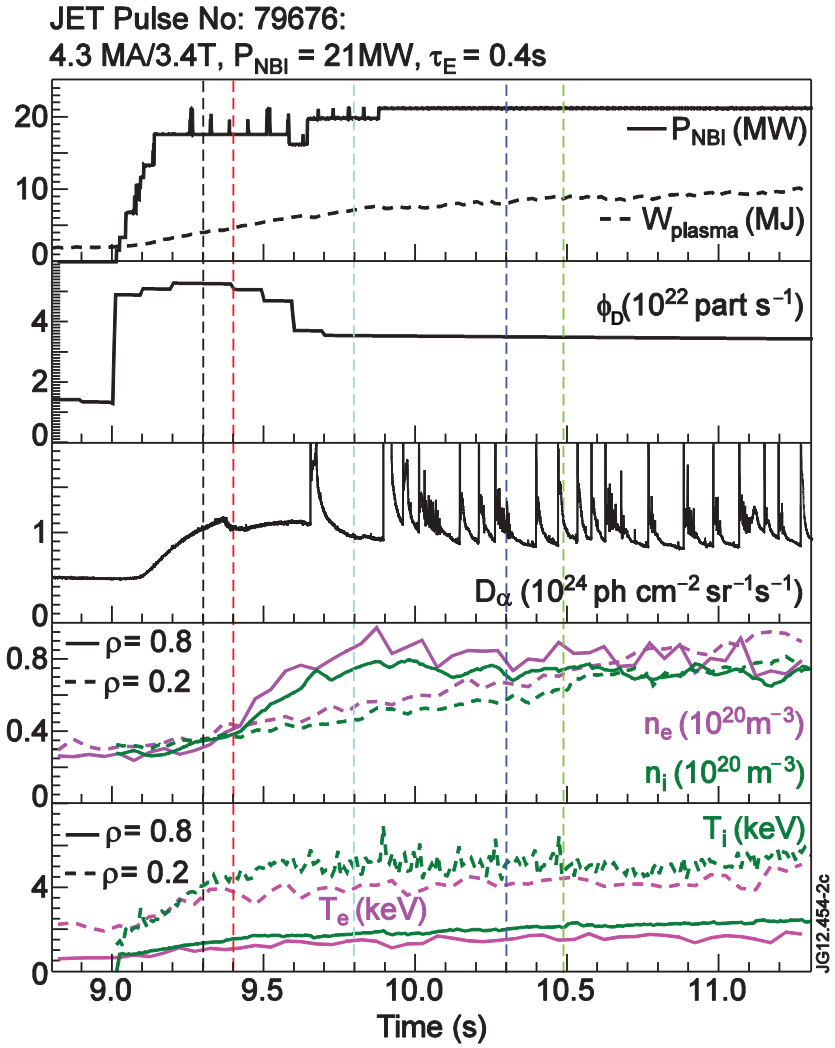

Figure A.1: Evolution of Neutral Beam Heating (NBI) (P_{NBI}), plasma energy (W_{plasma}), gas fuelling rate (ϕ_D), divertor D_α emission and evolution of core ($\rho = 0.2$) and edge ($\rho = 0.8$) electron and ion density and temperature for JET Pulse Number 79676 in the build-up phase following the H-mode transition. Dashed vertical lines indicate timing of profiles as shown by Figure A.2. Figure as published in [128].

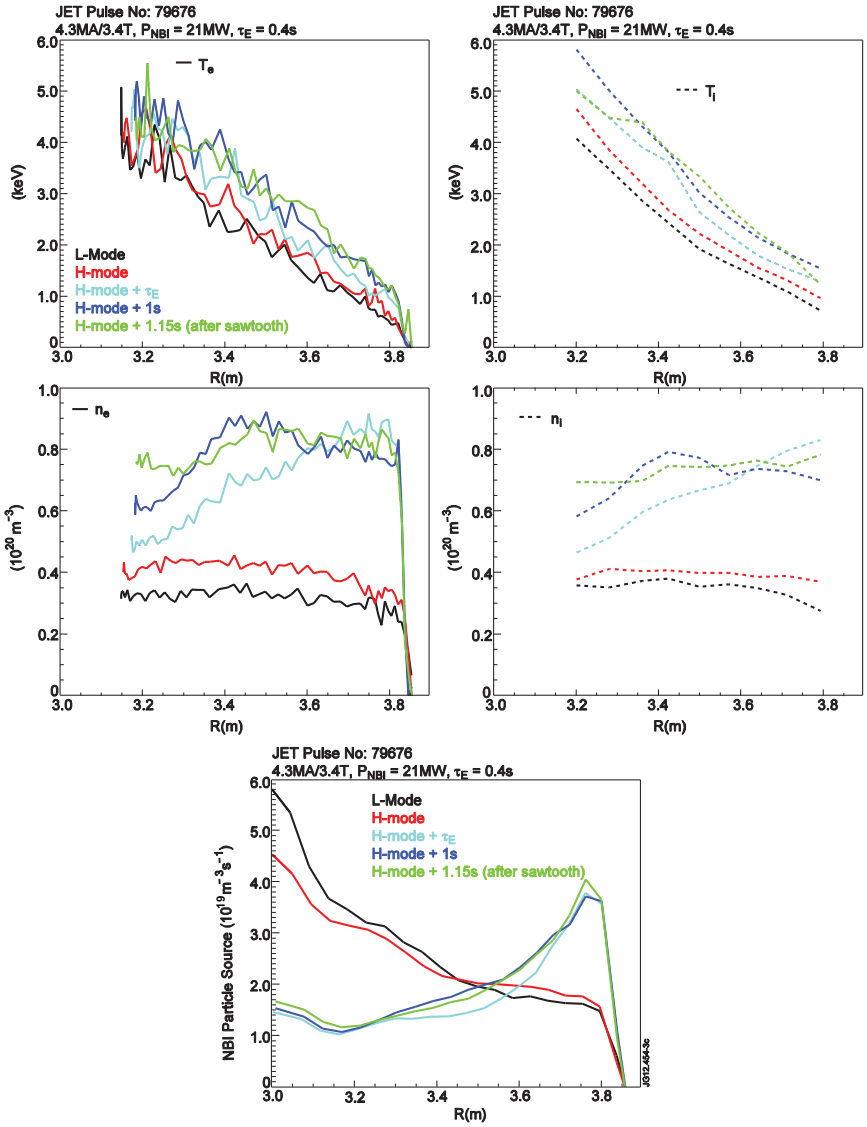

Figure A.2: (a) Electron temperature, (b) ion temperature, (c) electron density, (d) ion density and (e) NBI particle deposition profile as a function of major radius (R) at $t = 9.3$ s (black), 9.4 s (red), 9.8 s (grey), 10.3 s (blue) and 10.5 s (green), as indicated by the vertical dashed lines in Figure A.1. Profiles show L-mode, H-mode build-up phase with hollow density and NBI deposition profiles along with flattening of profiles after first sawtooth. Figure as published in [128].

A.3 Hollow density profiles

The duration of the hollow density profile and magnitude of the so-called de-peaking can be quantified by fitting a Gaussian to the ratio of edge ($\rho = 0.8$) to core ($\rho = 0.2$) density, see Figure A.3(a). These locations are chosen because the edge the measurement is sufficiently unaffected by the collapse of the pedestal due to ELMs [64, 133]. Whereas for the innermost measurement, the HRTS line of sight does not always pass through the plasma core and so $\rho = 0.2$ is a reliable choice to provide coverage. Figure A.3(a) shows the edge to core density ratio raises above 1.0 indicating the degree and duration of the hollow density profiles. In contrast, Figure A.3(b) shows the edge to core ratio for temperature remains below 1.0 indication the temperature profile remains peaked in the build-up phase following the L-H transition.

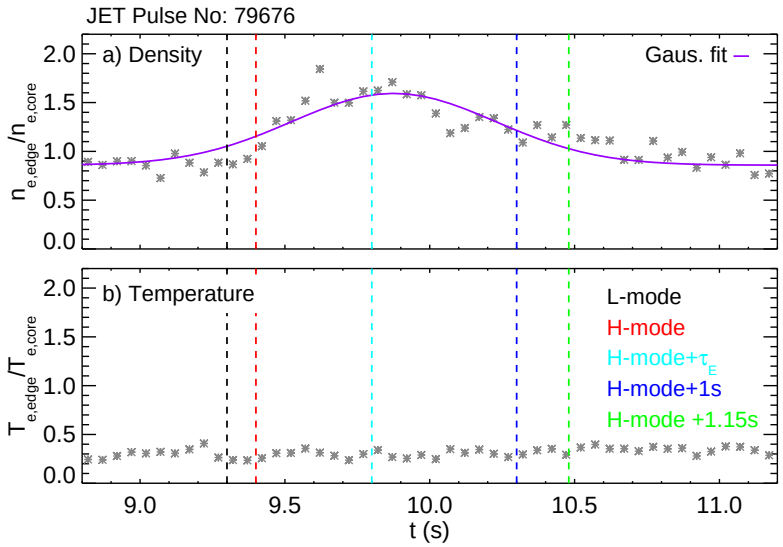

Figure A.3: (a) Ratio of the edge ($\rho = 0.8$) to core ($\rho = 0.2$) electron density and similarly (b) the ratio of the edge to core electron temperature for JET Pulse Number 79676, as in Figure A.1 and A.2.

The result of the Gaussian fit to $(n_{e,edge}/n_{e,core})$ for the high and low triangularity JET-C plasmas is summarised in Figure A.4. Both the magnitude of the de-peaking and duration of the hollow density profiles increase with plasma current however there is a large scatter particularly at high plasma current.

The formation of the hollow density profiles coincide with a hollow NBI particle deposition profiles as shown by the profiles for JET Pulse Number 79676, see Figure A.2. With increasing plasma current for low and high triangularity plasmas the de-peaking of the NBI deposition profile increases however the high triangularity plasmas can become hollow at lower plasma current. This is due to the plasma current not being the primary governing parameter. High triangularity plasmas are able to achieved a stronger transport barrier resulting in a higher edge density. An

increase in edge density results in a more de-peaked NBI particle deposition profile, see Figure A.5.

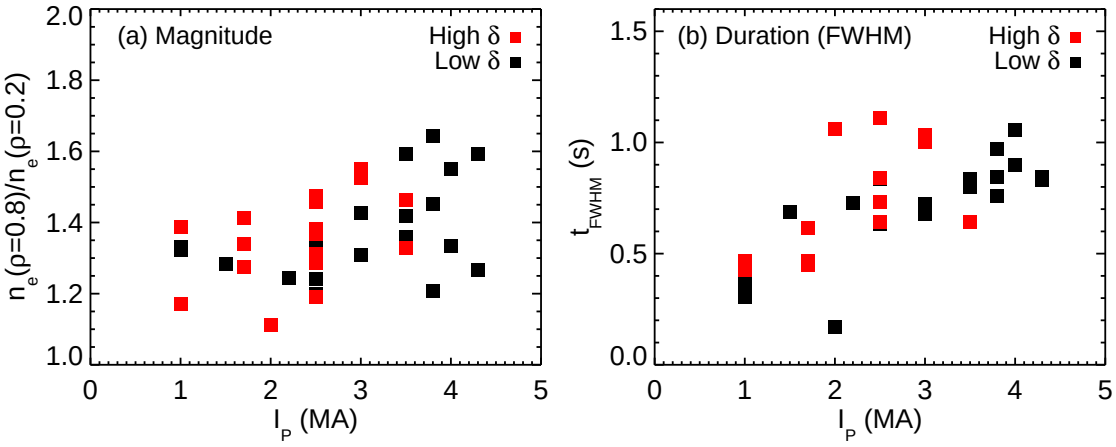

Figure A.4: (a) Magnitude of electron density de-peaking and (b) duration of hollow electron density profile (right) as determined by fitting a Gaussian fit to the ratio of the edge ($\rho = 0.8$) to core ($\rho = 0.2$) electron density for high (red) and low (blue) triangularity JET-C pulses.

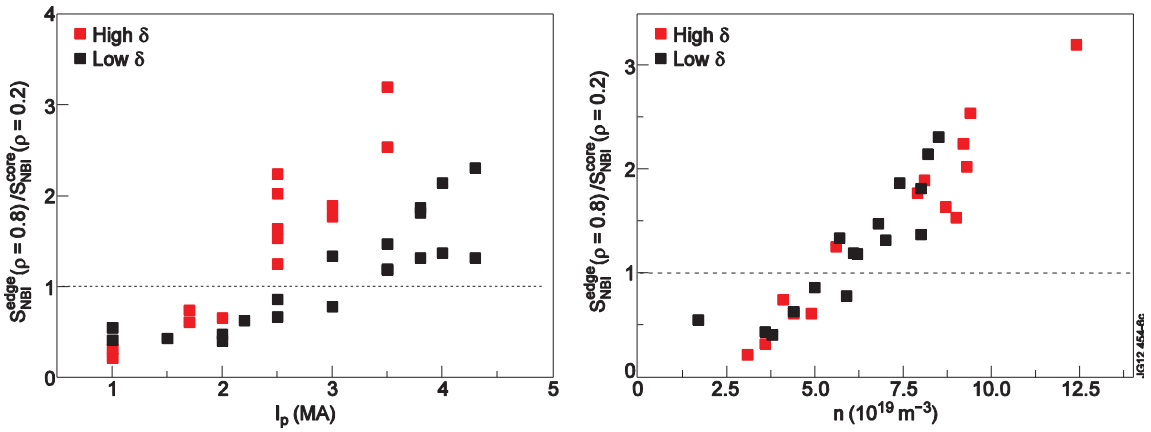

Figure A.5: Ratio of edge to core NBI particle deposition for both low and high triangularity JET plasmas as a function of plasma current (left) and edge density (right). Figure as published in [128].

A.4 Timescale of plasma build-up

The timescale of the density build-up phase is particularly important with regards to the alpha particle heating, as described in the introduction. This timescale is quantified by fitting a modified hyperbolic tangent (mtanh) function with respect to time instead of space [120], see Figure A.6. An mtanh function is convenient as the parameters defining the function can be related to physical quantities. More specifically, the offset is the L-mode density; the width is the timescale of the build-up; the height is the H-mode density; and the position is a time mark for the density build-up.

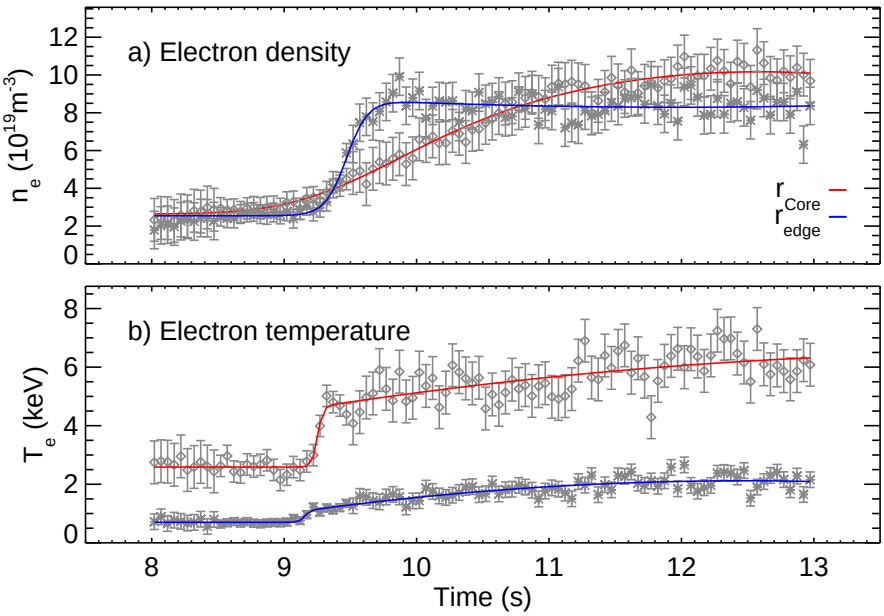

Figure A.6: Example of modified hyperbolic tangent (mtanh) fit to the evolution of core (red) and edge (blue) electron (a) density and (b) temperature for JET Pulse Number 79676, as in Figure A.1 and A.2.

Figure A.7 shows the core and edge temperature and density build-up timescale for all low triangularity JET-C pulses considered in this study. The electron timescales, as shown by Figure A.7(a), are determined from High Resolution Thomson Scattering measurements whereas the ion timescales, as shown by Figure A.7(b), are determined from charge exchange measurements. The electron and ion timescales for the core temperature, edge temperature and edge density show no variation with increasing plasma current and are comparable to the energy confinement time ($\tau_E \approx 0.3 - 0.4$ s). In contrast, the electron and ion timescale for the core density increases with increasing plasma current from $\approx \tau_E$ to $6\tau_E$. Similar behaviour is found for the for the high triangularity plamsas A.8 however it is noted the data quality is not as good in comparison to the low triangularity data-set, particularly for the ion measurements.

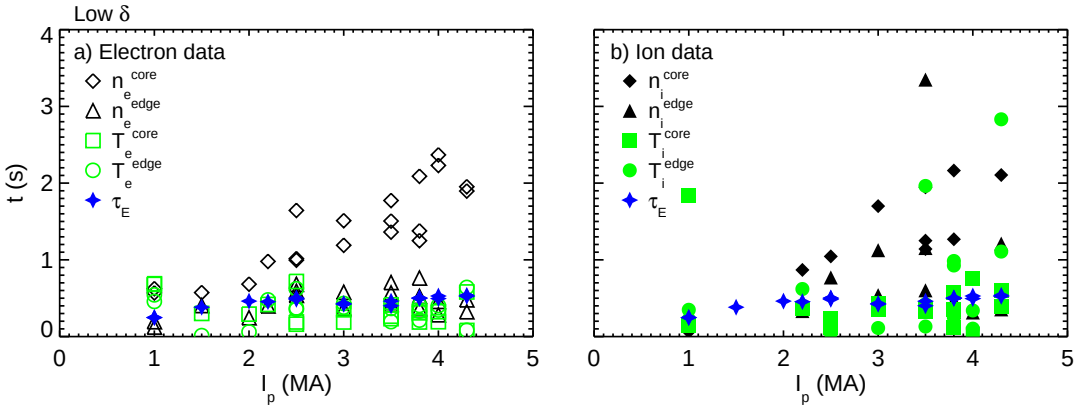

Figure A.7: Build-up timescale of core and edge temperature and density as determined by a modified hyperbolic tangent (mtanh) fit. (a) Electron and (b) ion measurements for low triangularity JET-C plasmas.

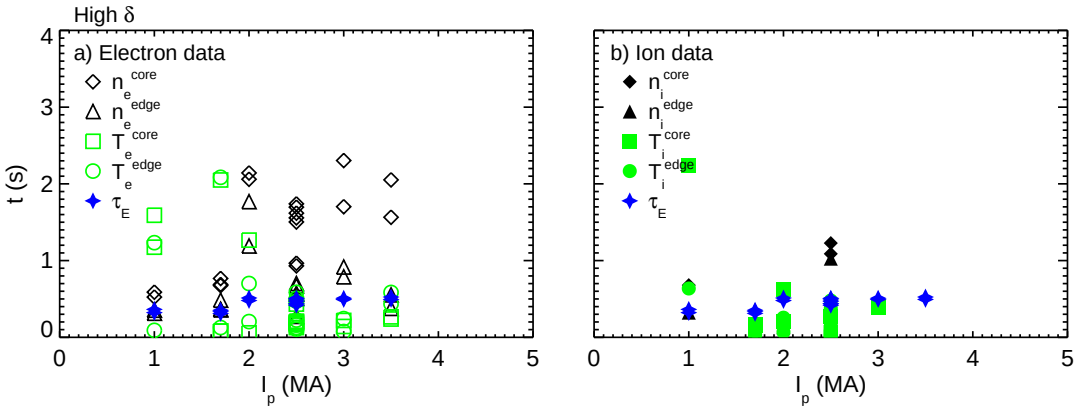

Figure A.8: Build-up timescale of core and edge electron temperature and density as determined by a modified hyperbolic tangent (mtanh) fit for high triangularity JET-C plasmas.

A.5 Summary

Hollow density profiles are observed on JET in the build-up phase following the H-mode transition. JET-C plasmas show the duration and magnitude of the de-peaked profiles increases with plasma current. Furthermore the core temperature, edge temperature and edge density all build up over a timescale comparable to the energy confinement time (τ_E). However, the build up of core density is prolonged at higher plasma current. These hollow density profiles coincide with hollow NBI deposition profiles.

JETTO, a 1.5 dimensional fluid transport model specific to the JET Tokamak [134], has been used to model the build-up phase following the H-mode transition on JET, as detailed by [128]. A key result is the timescale of the density and temperature build-up following the H-mode transition can be replicated by JETTO modelling when assuming no inward particle pinch. This is in contrast to previous modelling results, such as [135], which suggests there is a particle pinch of the order ($\nu_{pinch} =$

$0.5D\rho/a$). Furthermore, the diffusion coefficients are a factor of two to four smaller than expected in comparison to the stationary modelling. This could be due to the density gradient, as a result of the hollow density profile, altering the balance of particle transport. A complete discussion along with the implications for ITER is discussed in [128].

Bibliography

[1] United Nations Department of Economic and Social Affairs Population Division 2013 World Population Prospects The 2012 Revision: Highlights and Advance Tables Tech. rep. United Nations New York URL http://esa.un.org/wpp/Documentation/pdf/WPP2012_HIGHLIGHTS.pdf

[2] European Fusion Development Agreement 2012 Fusion Electricity A roadmap to the realisation of fusion energy Tech. rep. EFDA URL http://www.efda.org/wpcms/wp-content/uploads/2013/01/JG12.356-web.pdf

[3] International Energy Agency 2013 Key world energy statistics Tech. rep. IEA URL http://www.iea.org/publications/freepublications/publication/KeyWorld2013.pdf

[4] International Energy Agency 2013 World Energy Outlook: Executive Summary Tech. rep. IEA URL http://www.iea.org/publications/freepublications/publication/WEO2013_Executive_Summary_English.pdf

[5] Intergovernmental Panel on Climate Change 2013 Climate change 2013: The Physical Science Basis - Summary for Policymakers Tech. rep. IPCC URL http://www.climatechange2013.org/images/uploads/WGI_AR5_SPM_brochure.pdf

[6] International Energy Agency 2011 Generation from Coal Generation: Measuring and Reporting Efficiency Performance and CO2 Emissions Tech. rep. IEA URL http://www.iea.org/publications/freepublications/publication/power_generation_from_coal.pdf

[7] International Energy Agency 2010 Technology Roadmap: Nuclear Energy Tech. rep. IEA

[8] International Atomic Energy Agency 2009 Classification of Radioactive Waste Tech. rep. IAEA Vienna

[9] International Energy Agency 2013 Technology Roadmap: Wind Energy Tech. rep. IEA URL http://www.iea.org/publications/freepublications/publication/Wind_2013_Roadmap.pdf

[10] Freidberg J 2007 *Plasma Physics and Fusion Energy* (Cambridge University Press)

[11] Tipler P and Mosca G 2008 *Physics for Scientists and Engineers* (W.H. Freeman and Company)

[12] Wesson J 2004 *Tokamaks* 3rd ed (Clarendon Press)

[13] Chen F 1984 *Introduction to Plasma Physics and Controlled Fusion Volumn 1: Plasma Physics* 2nd ed (Plenum press)

[14] Lindl J, Atherton L, Amednt P, Batha S, Bell P, Berger R, Betti R, Bleuel D, Boehly T, Bradley D, Braun D, Callahan D, Celliers P, Cerjan C, Clark D, Collins G, Cook R, Dewald E, Divol L, Dixit S, Dzenitis E, Edwards M, Fair J, Fortner R, Frenje J, Glebov V, Glenzer S, Grim G, Haan S, Hamza A, Hammel B, Harding D, Hatchett S, Haynam C, Herrmann H, Herrmann M, Hicks D, Hinkel D, Ho D, Hoffman N, Huang H, Izumi N, Jacoby B, Jones O, Kalantar D, Kauffman R, Kilkenny J, Kirkwood R, Kline J, Knauer J, Koch J, Kozioziemski B, Kyrala G, La Fortune K, Landen O, Larson D, Lerche R, Le Pape S, London R, MacGowan B, MacKinnon A, Malsbury T, Mapoles E, Marinak M, McKenty P, Meezan N, Meyerhofer D, Michel P, Milovich J, Moody J, Moran M, Moreno K, Moses E, Munro D, Nikroo A, Olson R, Parham T, Patterson R, Peterson K, Petrasso R, Pollaine S, Ralph J, Regan S, Robey H, Rosen M, Sacks R, Salmonson J, Sangster T, Sepke S, Schneider D, Schneider M, Shaw M, Spears B, Springer P, Stoeckl C, Suter L, Thomas C, Tommasini R, Town R, VanWonterghem B, Vesey R, Weber S, Wegner P, Widman K, Widmayer C, Wilke M, Wilkens H, Williams E, Wilson D and Young B 2011 *Nuclear Fusion* **51** 094024 ISSN 0029-5515 URL http://stacks.iop.org/0029-5515/51/i=9/a=094024?key=crossref.62b03360f12c151b128af8a9e38b68be

[15] Wagner F 1982 *Physical Review Letters* **49** 1408–1412

[16] Jacquinot J, Bhatnagar V, Cordey J, Horton L, Start D, Barnsley R, Breger P, Christiansen J, Clement S, Davies S, Ehrenberg J, Eriksson L G, Fishpool G, Gadeberg M, Harbour P, Jäckel H, Lawson K, Lingertat J, Lowry C, Maggi C, Matthews G, Monk R, O'Brien D, Righi E, Saibene G, Sartori R, Schunke B, Sips A, Stamp M, Stork D, Strachan J, Tanga A and Thomsen K 1999 *Nuclear Fusion* **39** 235–253 ISSN 0029-5515 URL http://stacks.iop.org/0029-5515/39/i=2/a=307?key=crossref.934bcd67b7de99c725bc570e0eea6793

[17] Aymar R 2002 *Plasma Physics and Controlled Fusion* **44** URL http://iopscience.iop.org/0741-3335/44/5/304

[18] Shaing K and Crume E J 1989 *Physical Review Letters* **63** 2369–2372

[19] Meyer H, Bunting C, Carolan P, Conway N, Dunstan M, Kirk A, Scannell R, Temple D and Walsh M 2008 *Journal of Physics: Conference Series* **123** 012005 ISSN 1742-6596 URL http://stacks.iop.org/1742-6596/123/i=1/a=012005?key=crossref.0d29a752301a6c4272a59c34f44f0e14

[20] LaBombard B, Rice J, Hubbard A, Hughes J, Greenwald M, Granetz R, Irby J, Lin Y, Lipschultz B, Marmar E, Marr K, Mossessian D, Parker R, Rowan W, Smick N, Snipes J, Terry J, Wolfe S and Wukitch S 2005 *Physics of Plasmas* **12** 056111 ISSN 1070664X URL http://link.aip.org/link/PHPAEN/v12/i5/p056111/s1&Agg=doi

[21] Loarte A 2006 *Nature Physics* **2** 369–370

[22] Greenwald M 2002 *Plasma Physics and Controlled Fusion* **44** R27–R80

[23] Greenwald M, Terry J, Wolfe S, Ejima S, Bell M, Kaye S and Neilson G 1988 *Nuclear Fusion* **28** 2199–2207

[24] Snyder P, Wilson H, Ferron J, Lao L, Leonard A, Mossessian D, Murakami M, Osborne T, Turnbull A and Xu X 2004 *Nuclear Fusion* **44** 320–328 ISSN 0029-5515 URL http://stacks.iop.org/0029-5515/44/i=2/a=014?key=crossref.89835c4cb4068995f80cd693912eebc5

[25] Snyder P, Wilson H, Ferron J, Lao L, Leonard A, Osborne T, Turnbull A, Mossessian D, Murakami M and Xu X 2002 *Physics of Plasmas* **9** 2037 ISSN 1070664X URL http://link.aip.org/link/PHPAEN/v9/i5/p2037/s1&Agg=doi

[26] Snyder P, Wilson H, Osborne T and Leonard A 2004 *Plasma Physics and Controlled Fusion* **46** A131–A141 ISSN 0741-3335 URL http://stacks.iop.org/0741-3335/46/i=5A/a=014?key=crossref.ba3b5f7cf77604cad361753bdedacf15

[27] Mikhailovskii A 1998 *Plasma Physics and Controlled Fusion* **40** 1907–1921

[28] Saarelma S, Alfier A, Beurskens M, Coelho R, Koslowski H, Liang Y and Nunes I 2009 *Plasma Physics and Controlled Fusion* **51** 035001 ISSN 0741-3335 URL http://stacks.iop.org/0741-3335/51/i=3/a=035001?key=crossref.cb533bb78aeb89cab2ac59765e0cfb77

[29] Sauter O, Angioni C and Lin-Liu Y 1999 *Physics of Plasmas* **6** 2834 ISSN 1070664X URL http://link.aip.org/link/PHPAEN/v6/i7/p2834/s1&Agg=doi

[30] Snyder P, Groebner R, Leonard A, Osborne T and Wilson H 2009 *Physics of Plasmas* **16** 056118 ISSN 1070664X URL http://link.aip.org/link/PHPAEN/v16/i5/p056118/s1&Agg=doi

[31] Snyder P B and Hammett G W 2001 *Physics of Plasmas* **8** 744 ISSN 1070664X URL http://scitation.aip.org/content/aip/journal/pop/8/3/10.1063/1.1342029

[32] Candy J 2005 *Physics of Plasmas* **12** 072307 ISSN 1070664X URL http://scitation.aip.org/content/aip/journal/pop/12/7/10.1063/1.1954123

[33] Schneider P, Wolfrum E, Groebner R, Osborne T, Beurskens M, Dunne M, Ferron J, Günter S, Kurzan B, Lackner K, Snyder P and Zohm H 2012 *Plasma Physics and Controlled Fusion* **54** 105009 ISSN 0741-3335 URL http://stacks.iop.org/0741-3335/54/i=10/a=105009?key=crossref.b8ef5bcd0dd3d19b481ce1e4208242de

[34] Osborne T, Groebner R and Lao L 1998 *Plasma Physics and Controlled Fusion* **40** URL http://iopscience.iop.org/0741-3335/40/5/054

[35] Osborne T, Burrell K, Groebner R, Lao L, aW Leonard, Maingi R, Miller R, Porter G, Staebler G and aD Turnbull 1999 *Journal of Nuclear Materials* **266-269** 131–137 ISSN 00223115 URL http://linkinghub.elsevier.com/retrieve/pii/S0022311598008149

[36] Groebner R, Osborne T, aW Leonard and Fenstermacher M 2009 *Nuclear Fusion* **49** 045013 ISSN 0029-5515 URL http://stacks.iop.org/0029-5515/49/i=4/a=045013?key=crossref.43da841f09906bafcfc9ffd88ad7267d

[37] Beurskens M, Osborne T, Schneider P, Wolfrum E, Frassinetti L, Groebner R, Lomas P, Nunes I, Saarelma S, Scannell R, Snyder P B, Zarzoso D, Balboa I, Bray B, Brix M, Flanagan J, Giroud C, Giovannozzi E, Kempenaars M, Loarte A, de la Luna E, Maddison G, Maggi C, McDonald D, Pasqualotto

R, Saibene G, Sartori R, Solano E, Walsh M and Zabeo L 2011 *Physics of Plasmas* **18** 056120 ISSN 1070664X URL http://link.aip.org/link/PHPAEN/v18/i5/p056120/s1&Agg=doi

[38] Urano H, Takizuka T, Kamada Y, Oyama N and Takenaga H 2008 *Nuclear Fusion* **48** 045008 ISSN 0029-5515 URL http://stacks.iop.org/0029-5515/48/i=4/a=045008?key=crossref.69e9e7b9bd7bc8ac7621ae170cbfce4f

[39] Kirk A, O'Gorman T, Saarelma S, Scannell R and Wilson H 2009 *Plasma Physics and Controlled Fusion* **51** 065016 ISSN 0741-3335 URL http://stacks.iop.org/0741-3335/51/i=6/a=065016?key=crossref.207e4f1c95564463d399eeb39eb5cb56

[40] Diallo A, Maingi R, Kubota S, Sontag A, Osborne T, Podestà M, Bell R, LeBlanc B, Menard J and Sabbagh S 2011 *Nuclear Fusion* **51** 103031 ISSN 0029-5515 URL http://stacks.iop.org/0029-5515/51/i=10/a=103031?key=crossref.5416d2de4485d7624dd63d961058ffae

[41] Snyder P, Groebner R, Hughes J, Osborne T, Walk J, Beurskens M, Candy J, Staebler G and Wilson H 2011 The EPED pedestal model: model extensions and validation *13th International Workshop on H-mode Physics and Transport Barriers* (Oxford, UK)

[42] Snyder P, Groebner R, Hughes J, Osborne T, Beurskens M, aW Leonard, Wilson H and Xu X 2011 *Nuclear Fusion* **51** 103016 ISSN 0029-5515 URL http://stacks.iop.org/0029-5515/51/i=10/a=103016?key=crossref.334289a0972991b200871ad1b82fa95c

[43] Snyder P, Osborne T, Beurskens M, Burrell K, Groebner R, Hughes J, Maingi R, Nazikian R, Orlov D, Schmitz O, Wade M, Walk J and Wilson H 2012 The EPED Pedestal Model: Extensions, Application to ELM-Suppressed Regimes, and ITER Predictions *International IAEA Conference on Fusion Energy* 1 (San Diego, US) pp 1–7

[44] Hutchinson I 2002 *Principles of plasma diagnostics* 2nd ed (New York: Cambridge University Press)

[45] Fiocco G and Thompson E 1963 *Physical Review Letters* **10** 89–91

[46] Peacock N, Robinson D, Forrest M, Wilcock P and Sannikov V 1969 *Nature* **224** 488–490

[47] Salzmann H, Bundgaard J, Gadd A, Gowers C, Hansen K, Hirsch K, Nielsen P, Reed K, SchroÌĹdter C and Weisberg K 1988 *Review of Scientific Instruments* **59** 1451 ISSN 00346748 URL http://link.aip.org/link/RSINAK/v59/i8/p1451/s1&Agg=doi

[48] Pasqualotto R, Nielsen P, Gowers C, Beurskens M, Kempenaars M, Carlstrom T and Johnson D 2004 *Review of Scientific Instruments* **75** 3891 ISSN 00346748 URL http://link.aip.org/link/RSINAK/v75/i10/p3891/s1&Agg=doi

[49] Carlstrom T, Campbell G, DeBoo J, Evanko R, Evans J, Greenfield C, Haskovec J, Hsieh C, McKee E, Snider R, Stockdale R, Trost P and Thomas M 1992 *Review of Scientific Instruments* **63** 4901 ISSN 00346748 URL http://link.aip.org/link/RSINAK/v63/i10/p4901/s1&Agg=doi

[50] Carlstrom T, Foote J, Nilson D and Rice B 1995 *Review of Scientific Instruments* **66** 493 ISSN 00346748 URL http://link.aip.org/link/RSINAK/v66/i1/p493/s1&Agg=doi

[51] Murmann H, GoÌĹtsch S, RoÌĹhr H, Salzmann H and Steuer K 1992 *Review of Scientific Instruments* **63** 4941 ISSN 00346748 URL http://link.aip.org/link/RSINAK/v63/i10/p4941/s1&Agg=doi

[52] Kurzan B and Murmann H 2011 *The Review of scientific instruments* **82** 103501 ISSN 1089-7623 URL http://www.ncbi.nlm.nih.gov/pubmed/22047288

[53] Yoshida H, Naito O, Yamashita O, Kitamura S, Sakuma T, Onose Y, Nemoto H, Hamano T, Hatae T, Nagashima a and Matoba T 1999 *Review of Scientific Instruments* **70** 751 ISSN 00346748 URL http://link.aip.org/link/RSINAK/v70/i1/p751/s1&Agg=doi

[54] Hughes J, Mossessian D, Hubbard A, Marmar E, Johnson D and Simon D 2001 *Review of Scientific Instruments* **72** 1107 ISSN 00346748 URL http://link.aip.org/link/RSINAK/v72/i1/p1107/s1&Agg=doi

[55] Hughes J, Mossessian D, Zhurovich K, DeMaria M, Jensen K and Hubbard A 2003 *Review of Scientific Instruments* **74** 1667 ISSN 00346748 URL http://link.aip.org/link/RSINAK/v74/i3/p1667/s1&Agg=doi

[56] Scannell R, Walsh M, Carolan P, Darke A, Dunstan M, Huxford R, McArdle G, Morgan D, Naylor G, O'Gorman T, Shibaev S, Barratt N, Gibson K, Tallents G and Wilson H 2008 *The Review of scientific instruments* **79** 10E730 ISSN 1089-7623 URL http://www.ncbi.nlm.nih.gov/pubmed/19044546

[57] Scannell R, Walsh M, Dunstan M, Figueiredo J, Naylor G, O'Gorman T, Shibaev S, Gibson K and Wilson H 2010 *The Review of scientific instruments* **81** 10D520 ISSN 1089-7623 URL http://www.ncbi.nlm.nih.gov/pubmed/21033875

[58] Johnson D, Bretz N, LeBlanc B, Palladino R, Long D and Parsells R 1999 *Review of Scientific Instruments* **70** 776 ISSN 00346748 URL http://link.aip.org/link/RSINAK/v70/i1/p776/s1&Agg=doi

[59] Naito O, Yoshida H and Matoba T 1993 *Physics of Fluids B* **4256** 4256–4258

[60] Steane A 2012 *Relativity made relatively easy* 1st ed (Oxford: Oxford University Press)

[61] Beausang K 2011 *The consistency of electron temperautre measurements by Thomson scattering at the JET Tokamak* Ph.D. thesis University College Cork

[62] Flanagan J 2010 Alternative calibration techniques for thomson scattering diagnostics on large fusion devices via an integrated data approach *IOP plasma physics conference*

[63] Frassinetti L, Beurskens M, Scannell R, Osborne T, Flanagan J, Kempenaars M, Maslov M, Pasqualotto R and Walsh M 2012 *The Review of scientific instruments* **83** 013506 ISSN 1089-7623 URL http://www.ncbi.nlm.nih.gov/pubmed/22299950

[64] Beurskens M, Alfier A, Alper B, Balboa I, Flanagan J, Fundamenski W, Giovannozzi E, Kempenaars M, Loarte A, Lomas P, de La Luna E, Nunes I,

Pasqualotto R, Pitts R, Saibene G, Walsh M and Wiesen S 2009 *Nuclear Fusion* **49** 125006 ISSN 0029-5515 URL http://stacks.iop.org/0029-5515/49/i=12/a=125006?key=crossref.9ac9aef93201c3e7c9898aa77e2629f5

[65] Maggi C, Groebner R, Angioni C, Hein T, Horton L, Konz C, aW Leonard, Petty C, aCC Sips, Snyder P, Candy J and Waltz R 2010 *Nuclear Fusion* **50** 025023 ISSN 0029-5515 URL http://stacks.iop.org/0029-5515/50/i=2/a=025023?key=crossref.07b0dd51dec770195f8650c88e525916

[66] Groebner R, Snyder P, Osborne T, Leonard A, Rhodes T, Zeng L, Unterberg E, Yan Z, McKee G, Lasnier C, Boedo J and Watkins J 2010 *Nuclear Fusion* **50** 064002 ISSN 0029-5515 URL http://stacks.iop.org/0029-5515/50/i=6/a=064002?key=crossref.365f51942fb04314ada33b64debfafa6

[67] Hughes J, Hubbard A, Mossessian D, Labombard B, Biewer T, Porkolab M, Rice J, Snipes J, Terry J, Wolfe S and Zhurovich K 2007 *Fusion Science And Technology* **51** 317–341

[68] Hubbard A, Boivin R, Granetz R, Greenwald M, Hughes J, Hutchinson I, Irby J, LaBombard B, Lin Y, Marmar E, Mazurenko A, Mossessian D, Nelson-Melby E, Porkolab M, Snipes J, Terry J, Wolfe S, Wukitch S, Carreras B, Klein V and Pedersen T 2001 *Physics of Plasmas* **8** 2033 ISSN 1070664X URL http://link.aip.org/link/PHPAEN/v8/i5/p2033/s1&Agg=doi

[69] Dickinson D, Saarelma S, Scannell R, Kirk A, Roach C and Wilson H 2011 *Plasma Physics and Controlled Fusion* **53** 115010 ISSN 0741-3335 URL http://stacks.iop.org/0741-3335/53/i=11/a=115010?key=crossref.9b85834584d7adce7ff6e0f3a1d84cd4

[70] Dickinson D, Roach C, Saarelma S, Scannell R, Kirk A and Wilson H 2012 *Physical Review Letters* **108** 135002 ISSN 0031-9007 URL http://link.aps.org/doi/10.1103/PhysRevLett.108.135002

[71] Kirk A, Counsell G F, Cunningham G, Dowling J, Dunstan M, Meyer H, Price M, Saarelma S, Scannell R, Walsh M and Wilson H 2007 *Plasma Physics and Controlled Fusion* **49** 1259–1275 ISSN 0741-3335 URL http://stacks.iop.org/0741-3335/49/i=8/a=011?key=crossref.abf01452153d276a4a9ae03880e09b6f

[72] Hatae T, Sugihara M, Hubbard A, Igitkhanov Y, Kamada Y, Janeschitz G, Horton L, Ohyabu N, Osborne T, Osipenko M, Suttrop W, Urano H and Weisen H 2001 *Nuclear Fusion* **41** URL http://iopscience.iop.org/0029-5515/41/3/305

[73] Scannell R, Beurskens M, Carolan P, Kirk A, Walsh M, O'Gorman T and Osborne T 2011 *The Review of scientific instruments* **82** 053501 ISSN 1089-7623 URL http://www.ncbi.nlm.nih.gov/pubmed/21639498

[74] Arends E 2003 *Density gradients in spherical tokamak plasmas* Ph.D. thesis Technische Universiteit Eindhoven

[75] Leyland M, Beurskens M, Frassinetti L, Osborne T, Snyder P, Giroud C, Jachmich S, Maddison G, Lomas P, Perez von Thun C, Saarelma S, Saibene G and Gibson K 2013 *Nuclear Fusion* **53** 083028 ISSN 0029-5515 URL http://stacks.iop.org/0029-5515/53/i=8/a=083028?key=crossref.e50f9cef7df35cbf5d6893d618a8f7a6

[76] Barlow R 1989 *Statistics: A Guide to the Use of Statistical Methods in the Physical Sciences* (John Wiley and Sons Ltd)

[77] Beurskens M 1999 *Filamentation of tokamak plasmas* Ph.D. thesis Technische Universiteit Eindhoven

[78] Scannell R 2007 *Investigation of H-mode edge profile behaviour on MAST using Thomson scattering* Ph.D. thesis University College Cork

[79] Flanagan J 2013 HRTS calibration report: ILW shutdown and restart Tech. rep. Culham Centre for Fusion Energy

[80] O'Gorman T 2012 *Investigation of neoclassical tearing modes on MAST using Thomson scattering* Ph.D. thesis University of Cork

[81] Shimada M, Campbell D, Mukhovatoc V, Fujiwara M, Kirneva N, Lackner K, Nagami M, Pustovitov V, Uckan N, Wesley J, Asakura N, Costley A, Bonne A, Doyle E, Fasoli A, Gormezano C, Gribov Y, Gruber O, Hender T, Houlberg W, Ide S, Kamada Y, Leonard A, Lipschultz B, Loarte A, Miyamoto K, Mukhovatov V, Osborne T, Polevoi A and Sips A 2007 *Nuclear Fusion* **47** S1–S17

[82] Hubbard A 2000 *Plasma Physics and Controlled Fusion* **42** URL http://iopscience.iop.org/0741-3335/42/5A/302

[83] Onjun T, Bateman G, Kritz A and Hammett G 2002 *Physics of Plasmas* **9** 5018 ISSN 1070664X URL http://link.aip.org/link/PHPAEN/v9/i12/p5018/s1&Agg=doi

[84] Osborne T, Cordey J, Groebner R, Hatae T, Hubbard A, Horton L, Kamada Y, Kritz A, Lao L, Leonard A, Loarte A, Mahdavi M, Mossenssian D, Onjun T, Ossenpenko M, Rognlien T, Saibene G, Snyder P, Sugihara M, Shurygin R, Thomsen K, Wade M, Wilson H, Xu X and Yatsu K 2002 Characteristics of the H-mode pedestal and extrapolation to ITER *19th IAEA International Conference on Fusion Energy* November (Lyon) URL http://www.iaea.org/programmes/ripc/physics/fec2002/html/node52.htm

[85] Connor J, Hastie R, Wilson H and Miller R 1998 *Physics of Plasmas* **5** 2687 ISSN 1070664X URL http://link.aip.org/link/PHPAEN/v5/i7/p2687/s1&Agg=doi

[86] Ryter F, Leuterer F, Pereverzev G, Fahrbach H U, Stober J and Suttrop W 2001 *Physical Review Letters* **86** 2325–2328 ISSN 0031-9007 URL http://link.aps.org/doi/10.1103/PhysRevLett.86.2325

[87] Doyle E, Houlberg W, Kamada Y, Mukhovatov V, Osborne T, Polevoi A, Bateman G, Connor J, Cordey J, Fujita T, Garbet X, Hahm T, Horton L, Hubbard A, Imbeaux F, Jenko F, Kinsey J, Kishimoto Y, Li J, Luce T, Martin Y, Ossipenko M, Parail V, Peeters A, Rhodes T, Rice J, Roach C, Rozhansky V, Ryter F, Saibene G, Sartori R, Sips A, Snipes J, Sugihara M, Synakowski E, Takenaga H, Takizuka T, Thomsen K, Wade M and Wilson H 2007 *Nuclear Fusion* **47** S18–S127

[88] Nunes I, Lomas P, McDonald D, Saibene G, Sartori R, Voitsekhovitch I, Beurskens M, Arnoux G, Boboc a, Eich T, Giroud C, Heureux S, de la Luna

E, Maddison G, aCC Sips, Thomsen H and Versloot T 2013 *Nuclear Fusion* **53** 073020 ISSN 0029-5515 URL http://stacks.iop.org/0029-5515/53/i=7/a=073020?key=crossref.4b84d0122bbd9633de348ed1a31582fa

[89] ITER Physics Basis Editors 1999 *Nuclear Fusion* **39** 2137

[90] Saibene G, Sartori R, Loarte A, Campbell D, Lomas P, Parail V, Zastrow K, Andrew Y, Sharapov S, Korotkov A, Becoulet M, Huysmans G, Koslowski H, Budny R, Conway G, Stober J, Suttrop W, Kallenback A, Hellermann M V and Beurskens M 2002 *Plasma Physics and Controlled Fusion* **44** URL http://iopscience.iop.org/0741-3335/44/9/301

[91] Saibene G, Horton L, Sartori R, Balet B, Clement S, Conway G, Cordey J, Esch H D, Ingesson L, Lingertat J, Monk R, Parail V, Smith R, Taroni A, Thomsen K and Hellermann M V 1999 *Nuclear Fusion* **39** 1133–1156 ISSN 0029-5515 URL http://stacks.iop.org/0029-5515/39/i=9/a=307?key=crossref.0830e20ad5f69229f986c2ae4e975b19

[92] Kirk A, Wilson H, Counsell G, Akers R, Arends E, Cowley S, Dowling J, Lloyd B, Price M and Walsh M 2004 *Physical Review Letters* **92** 245002 ISSN 0031-9007 URL http://link.aps.org/doi/10.1103/PhysRevLett.92.245002

[93] Maggi C 2010 *Nuclear Fusion* **50** 066001 ISSN 0029-5515 URL http://stacks.iop.org/0029-5515/50/i=6/a=066001?key=crossref.bbf752fb35b2a1124782f574d424bc21

[94] Philipps V, Mertens P, Matthews G and Maier H 2010 *Fusion Engineering and Design* **85** 1581–1586 ISSN 09203796 URL http://linkinghub.elsevier.com/retrieve/pii/S0920379610001894

[95] Giroud C, Maddison G, McCormick K, Beurskens M, Brezinsek S, Devaux S, Eich T, Frassinetti L, Fundamenski W, Groth M, Huber A, Jachmich S, Järvinen A, Kallenbach A, Krieger K, Moulton D, Saarelma S, Thomsen H, Wiesen S, Alonso A, Alper B, Arnoux G, Belo P, Boboc A, Brett A, Brix M, Coffey I, de la Luna E, Dodt D, Vries P D, Felton R, Giovanozzi E, Harling J, Harting D, Hawkes N, Hobirk J, Jenkins I, Joffrin E, Kempenaars M, Lehnen M, Loarer T, Lomas P, Mailloux J, McDonald D, Meigs A, Morgan P, Nunes I, Perez van Thun C, Riccardo V, Rimini F, Sirinnelli A, Stamp M and Voitsekhovitch I 2012 *Nuclear Fusion* **52** 063022 ISSN 0029-5515 URL http://stacks.iop.org/0029-5515/52/i=6/a=063022?key=crossref.e338770a9f20d9b58de0321e3770a039

[96] Maddison G, Giroud C, McCormick G, Alper B, Arnoux G, da Silva Aresta Belo P, Beurskens M, Boboc A, Brett A, Brezinsek S, Coffey I, Devaux S, Devynck P, Eich T, Felton R, Fundamenski W, Harling J, Huber A, Jachmich S, Joffrin E, Lomas P, Monier-Garbet P, Morgan P, Stamp M, Telesca G, Thomsen H and Voitsekhovitch I 2011 *Nuclear Fusion* **51** 082001 ISSN 0029-5515 URL http://stacks.iop.org/0029-5515/51/i=8/a=082001?key=crossref.6ea18c5fdda4ea21c2442c93379df575

[97] Pamela J and Solano E 2003 *Nuclear Fusion* **1540** 1540–1554

[98] Schmuck S, Fessey J, Gerbaud T, Alper B, Beurskens M, de la Luna E, Sirinelli A and Zerbini M 2012 *The Review of scientific instruments* **83** 125101 ISSN 1089-7623 URL http://www.ncbi.nlm.nih.gov/pubmed/23282107

[99] ITER Physics Basis Expert Groups on Confinement and Transport and Confinement Modelling and Database ITER Physics Basis Editors 1999 *Nuclear Fusion* **39** 2175

[100] Sartori R, Saibene G, Horton L, Becoulet M, Budny R, Borba D, Chankin A, Conway G, Cordey G, McDonald D, Guenther K, Hellermann M V, Igithkanov Y, Loarte A, Lomas P, Pogutse O and Rapp J 2004 *Plasma Physics and Controlled Fusion* **46** 723–750 ISSN 0741-3335 URL http://stacks.iop.org/0741-3335/46/i=5/a=002?key=crossref.71688515a798c62fad8f1cb0db472b00

[101] ITER H-mode database working group 1994 *Nuclear Fusion* **34** 131

[102] Perez von Thun C, Maraschek M, da Graça S, Buttery R, Herrmann A, Stober J, Conway G, Eich T, Fuchs J, Horton L, Igochine V, Kallenbach A, Loarte A, Müller H, Nunes I, Saibene G, Sartori R, Sips A, Suttrop W and Wolfrum E 2008 *Plasma Physics and Controlled Fusion* **50** 065018 ISSN 0741-3335 URL http://stacks.iop.org/0741-3335/50/i=6/a=065018?key=crossref.90c7804433fd01c413413fc97b693a01

[103] Wolfrum E, Bernert M, Boom J, Burckhart A, Classen I, Conway G, Eich T, Fischer R, Gude A, Herrmann A, Luhmann N, Maraschek M, McDermott R, Park H, Pütterich T, Vicente J, Wieland B and Willensdorfer M 2011 *Plasma Physics and Controlled Fusion* **53** 085026 ISSN 0741-3335 URL http://stacks.iop.org/0741-3335/53/i=8/a=085026?key=crossref.b48f6936cc2c13d9258fad4057f706c4

[104] Sartori R, Saibene G, Becoulet M, Lomas P, Loarte A, Campbell D, Andrew Y, Budny R, Beurskens M, Kallenbach A, Parail V, Suttrop W, Stober J, Zastrow K, Zerbini M and Monk R 2002 *Plasma Physics and Controlled Fusion* **44** 1801–1813

[105] Martin Y, Takizuka T and The ITPA CDBM H-mode Threshold Database Working Group 2008 *Journal of Physics: Conference Series* **123** 012033 ISSN 1742-6596 URL http://stacks.iop.org/1742-6596/123/i=1/a=012033?key=crossref.433acb98b7d8b044ce2b33de88f46da5

[106] Perez C, Koslowski H, Hender T, Smeulders P, Loarte A, Lomas P, Saibene G, Sartori R, Becoulet M, Eich T, Hastie R, Huysmans G, Jachmich S, Rogister A and Schüller F 2004 *Plasma Physics and Controlled Fusion* **46** 61–87 ISSN 0741-3335 URL http://stacks.iop.org/0741-3335/46/i=1/a=005?key=crossref.99f264e4c8340fb67f2ce5d286dcda51

[107] Saibene G, Lomas P, Sartori R, Loarte A, Stober J, Andrew Y, Arshad S, Conway G, de la Luna E, Günther K, Ingesson L, Kempenaars M, Korotkov A, Koslowski H, Lönnroth J, McDonald D, Meigs A, Monier-Garbet P, Parail V, Perez C, Rimini F, Sharapov S and Thomas P 2005 *Nuclear Fusion* **45** 297–317 ISSN 0029-5515 URL http://stacks.iop.org/0029-5515/45/i=5/a=001?key=crossref.6f9ef33859faadc9c36b2e35c8a375f8

[108] Dodt D, Brix M, Beurskens M, Flanagan J, Kempenaars M and Maslov M 2012 Pedestal Density Profiles from the Upgraded Lithium Beam Diagnostic at JET and Comparison to Expectations from Neutral Penetration *39th European Physical Society Conference on Plasma Physics* 1 (Stockholm, Sweden) pp 1–4

[109] Osborne T, Beurskens M, Callen J, Frassinetti L, Groebner R, Hughes J, Saarelma S, Schneider P, Smith R, Snyder P, Wolfrum E and Yan Z 2011 Scaling of H-mode Pedestal and ELM Characteristics from a Multi- Tokamak Database and Comparison to Theoretical Models *13th International Workshop on H-mode Physics and Transport Barriers* (Oxford, UK) p 56118

[110] Stangeby P 2000 *The Plasma Boundary of Magnetic Fusion Devices* (Taylor and Francis Group)

[111] Miller R, Chu M, Greene J, Lin-Liu Y and Waltz R 1998 *Physics of Plasmas* **5** 973 ISSN 1070664X URL http://link.aip.org/link/PHPAEN/v5/i4/p973/s1&Agg=doi

[112] Beurskens M, Frassinetti L, Challis C, Osborne T, Snyder P, Alper B, Angioni C, Bourdelle C, Buratti P, Crisanti F, Giovannozzi E, Giroud C, Groebner R, Hobirk J, Jenkins I, Joffrin E, Leyland M, Lomas P, Mantica P, McDonald D, Nunes I, Rimini F, Saarelma S, Voitsekhovitch I, de Vries P and Zarzoso D 2013 *Nuclear Fusion* **53** 013001 ISSN 0029-5515 URL http://stacks.iop.org/0029-5515/53/i=1/a=013001?key=crossref.239b1649eaa6d6338435d6ce2c7e7f64

[113] Snyder P, Burrell K, Wilson H, Chu M, Fenstermacher M, aW Leonard, Moyer R, Osborne T, Umansky M, West W and Xu X 2007 *Nuclear Fusion* **47** 961–968 ISSN 0029-5515 URL http://stacks.iop.org/0029-5515/47/i=8/a=030?key=crossref.e315015157354730c97ccf03803b56de

[114] Saarelma S, Beurskens M, Dickinson D, Frassinetti L, Leyland M and Roach C 2013 *Nuclear Fusion* **53** 123012 ISSN 0029-5515 URL http://stacks.iop.org/0029-5515/53/i=12/a=123012?key=crossref.7af6ec789be5a4852011043fb437e329

[115] Matthews G, Beurskens M, Brezinsek S, Groth M, Joffrin E, Loving A, Kear M, Mayoral M L, Neu R, Prior P, Riccardo V, Rimini F, Rubel M, Sips G, Villedieu E, de Vries P and Watkins M 2011 *Physica Scripta* **T145** 014001 ISSN 0031-8949 URL http://stacks.iop.org/1402-4896/2011/i=T145/a=014001?key=crossref.0af5621e75d3c560c1ba3bda6a0ccf02

[116] Pitts R, Kukushkin A, Loarte A, Martin A, Merola M, Kessel C, Komarov V and Shimada M 2009 *Physica Scripta* **T138** 014001 ISSN 0031-8949 URL http://stacks.iop.org/1402-4896/2009/i=T138/a=014001?key=crossref.d5086d04ddbd8759295ea68d2dee8238

[117] Giroud C, Maddison G, Jachmich S, Rimini F, Beurskens M, Balboa I, Brezinsek S, Coelho R, Coenen J, Frassinetti L, Joffrin E, Oberkofler M, Lehnen M, Liu Y, Marsen S, McCormick K, Meigs A, Neu R, Sieglin B, van Rooij G, Arnoux G, Belo P, Brix M, Clever M, Coffey I, Devaux S, Douai D, Eich T, Flanagan J, Grünhagen S, Huber A, Kempenaars M, Kruezi U, Lawson K, Lomas P, Lowry C, Nunes I, Sirinnelli A, Sips A, Stamp M and Wiesen S 2013 *Nuclear Fusion* **53** 113025 ISSN 0029-5515 URL http://stacks.iop.org/0029-5515/53/i=11/a=113025?key=crossref.b25f5cabfe1eb9a1df537a555d386b64

[118] Beurskens M, Frassinetti L, Challis C, Giroud C, Saarelma S, Alper B, Angioni C, Bilkova P, Bourdelle C, Brezinsek S, Buratti P, Calabro G, Eich T,

Flanagan J, Giovannozzi E, Groth M, Hobirk J, Joffrin E, Leyland M, Lomas P, de la Luna E, Kempenaars M, Maddison G, Maggi C, Mantica P, Maslov M, Matthews G, Mayoral M L, Neu R, Nunes I, Osborne T, Rimini F, Scannell R, Solano E, Snyder P, Voitsekhovitch I and de Vries P 2014 *Nuclear Fusion* **54** 043001 ISSN 0029-5515 URL http://stacks.iop.org/0029-5515/54/i=4/a=043001?key=crossref.ba45b365f8ae97a8c4a242cbf0c86022

[119] Maddison G, Giroud C, Alper B, Arnoux G, Balboa I, Beurskens M, Boboc A, Brezinsek S, Brix M, Clever M, Coelho R, Coenen J, Coffey I, da Silva Aresta Belo P, Devaux S, Devynck P, Eich T, Felton R, Flanagan J, Frassinetti L, Garzotti L, Groth M, Jachmich S, Järvinen A, Joffrin E, Kempenaars M, Kruezi U, Lawson K, Lehnen M, Leyland M, Liu Y, Lomas P, Lowry C, Marsen S, Matthews G, McCormick G, Meigs A, Morris A, Neu R, Nunes I, Oberkofler M, Rimini F, Saarelma S, Sieglin B, Sips A, Sirinelli A, Stamp M, van Rooij G, Ward D and Wischmeier M 2014 *Nuclear Fusion* **54** 073016 ISSN 0029-5515 URL http://stacks.iop.org/0029-5515/54/i=7/a=073016?key=crossref.ec60f82729207fdc0068079bef46cf82

[120] Groebner R and Carlstrom T 1998 *Plasma Physics and Controlled Fusion* **40** URL http://iopscience.iop.org/0741-3335/40/5/021

[121] Joffrin E, Baruzzo M, Beurskens M, Bourdelle C, Brezinsek S, Bucalossi J, Buratti P, Calabro G, Challis C, Clever M, Coenen J, Delabie E, Dux R, Lomas P, de la Luna E, de Vries P, Flanagan J, Frassinetti L, Frigione D, Giroud C, Groth M, Hawkes N, Hobirk J, Lehnen M, Maddison G, Mailloux J, Maggi C, Matthews G, Mayoral M, Meigs a, Neu R, Nunes I, Puetterich T, Rimini F, Sertoli M, Sieglin B, aCC Sips, van Rooij G and Voitsekhovitch I 2014 *Nuclear Fusion* **54** 013011 ISSN 0029-5515 URL http://stacks.iop.org/0029-5515/54/i=1/a=013011?key=crossref.a89225aa2fe9903cd9fbfdef9d11dca9

[122] Beurskens M, Schweinzer J, Angioni C, Burckhart A, Challis C, Chapman I, Fischer R, Flanagan J, Frassinetti L, Giroud C, Hobirk J, Joffrin E, Kallenbach A, Kempenaars M, Leyland M, Lomas P, Maddison G, Maslov M, McDermott R, Neu R, Nunes I, Osborne T, Ryter F, Saarelma S, Schneider P, Snyder P, Tardini G, Viezzer E and Wolfrum E 2013 *Plasma Physics and Controlled Fusion* **55** 124043 ISSN 0741-3335 URL http://stacks.iop.org/0741-3335/55/i=12/a=124043?key=crossref.a32eee93a7bb754c7b41d5b03dd0386f

[123] Beurskens M, Osborne T, Horton L, Frassinetti L, Groebner R, Leonard A, Lomas P, Nunes I, Saarelma S, Snyder P, Balboa I, Bray B, Crombé K, Flanagan J, Giroud C, Giovannozzi E, Kempenaars M, Kohen N, Loarte A, Lönnroth J, de la Luna E, Maddison G, Maggi C, McDonald D, McKee G, Pasqualotto R, Saibene G, Sartori R, Solano E, Suttrop W, Wolfrum E, Walsh M, Yan Z, Zabeo L and Zarzoso D 2009 *Plasma Physics and Controlled Fusion* **51** 124051 ISSN 0741-3335 URL http://stacks.iop.org/0741-3335/51/i=12/a=124051?key=crossref.cac2fb962e8306b32e674f731fa092eb

[124] Morgan P, Behringer K, Carolan P, Forrest M, Peacock N and Stamp M 1985 *Review of Scientific Instruments* **56** 862 ISSN 00346748 URL http://scitation.aip.org/content/aip/journal/rsi/56/5/10.1063/1.1138074

[125] Brezinsek S, Jachmich S, Stamp M, aG Meigs, Coenen J, Krieger K, Giroud C, Groth M, Philipps V, Grünhagen S, Smith R, van Rooij G, Ivanova D and

Matthews G 2013 *Journal of Nuclear Materials* **438** S303–S308 ISSN 00223115 URL http://linkinghub.elsevier.com/retrieve/pii/S002231151300130X

[126] Saarelma S, Beurskens M, Bottino A, Frassinetti L, Giroud C, Kirk A, Leyland M, Scannell R and Roach C 2013 Global ideal MHD and gyrokinetic pedestal stability of JET with a carbon and metal wall and a comparison with MAST H-mode plasmas *14th International Workshop on H-mode Physics and Transport Barrier* (Fukuoka, Japan)

[127] Loarte A, Saibene G, Sartori R, Campbell D, Becoulet M, Horton L, Eich T, Herrmann A, Matthews G, Asakura N, Chankin A, Leonard A, Porter G, Federici G, Janeschitz G, Shimada M and Sugihara M 2003 *Plasma Physics and Controlled Fusion* **45** URL http://iopscience.iop.org/0741-3335/45/9/302

[128] Loarte A, Leyland M, Mier J, Beurskens M, Nunes I, Parail V, Lomas P, Saibene G, Sartori R and Frassinetti L 2013 *Nuclear Fusion* **53** 083031 ISSN 0029-5515 URL http://stacks.iop.org/0029-5515/53/i=8/a=083031?key=crossref.b274d239fd9dc3968a97fd64f18929cb

[129] Baker D, Wade M, Jackson G, Maingi R, Stockdale R, DeGrassie J, Groebner R, Forest C and Porter G 1998 *Nuclear Fusion* **38**

[130] Efthimion P, von Goeler S, Houlberg W, Synakowski E, Zarnstorff M, Batha S, Bell R, Bitter M, Bush C, Levinton F, Mazzucato E, McCune D, Mueller D, Park H, Ramsey A, Roquemore A and Taylor G 1998 *Physics of Plasmas* **5** 1832 ISSN 1070664X URL http://scitation.aip.org/content/aip/journal/pop/5/5/10.1063/1.872853

[131] JET Team (prepared by K-D Zastrow) 1999 *Nuclear Fusion* **39** 1891–1896

[132] Scotti F, Soukhanovskii V, Bell R, Guttenfelder W, Kaye S, Gerhardt S, Kaita R and LeBlanc B 2012 Study of neoclassical core transport of intrinsic impurities in the National Spherical Torus Experiment *39th European Physical Society Conference on Plasma Physics* (Stockholm, Sweden)

[133] Loarte A, Becoulet M, Saibene G, Sartori R, Campbell G, Eich T, Herrmann A, Laux M, Suttrop W, Alper B, Lomas P, Matthews G, Jachmich S, Ongena J and Innocente P 2002 *Plasma Physics and Controlled Fusion* **44** URL http://iopscience.iop.org/0741-3335/44/9/303

[134] Cenacchi G and Taroni A 1988 JETTO: A free-boundary plasma transport code (basic version) Tech. rep. JET Joint Undertaking Report JET-IR(88)03

[135] Angioni C, Weisen H, Kardaun O, Maslov M, Zabolotsky a, Fuchs C, Garzotti L, Giroud C, Kurzan B, Mantica P, aG Peeters and Stober J 2007 *Nuclear Fusion* **47** 1326–1335 ISSN 0029-5515 URL http://stacks.iop.org/0029-5515/47/i=9/a=033?key=crossref.0dc28c6d14ede5ab2abd117bf7e96533